Unique Mechanisms of Colloidal Stability Probed by Surface-Specific Vibrational Spectroscopy

by

Ashley N. Mapile

A dissertation accepted and approved in partial fulfillment of the

requirements for the degree of

Doctor of Philosophy

in Chemistry

Dissertation Committee:

Jeffrey Cina, Chair

Lawrence Scatena, Advisor

Carl Brozek, Advisor

Cathy Wong, Core Member

Daniel Steck, Institutional Representative

University of Oregon

Summer 2024

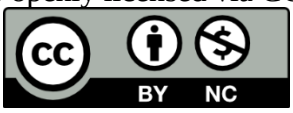

DISSERTATION ABSTRACT

Ashley N. Mapile

Doctor of Philosophy in Chemistry

Title: Unique Mechanisms of Colloidal Stability Probed by Surface-Specific Vibrational Spectroscopy

The stability of nanoparticles suspended in a solution, known as colloids, is crucial for their application in drug delivery systems, the solution processibility required for drop-casting films, and the long-term storage or transport of sensitive chemical materials. While current mechanisms for colloidal stability include implicit models of solvation – namely Derjaguin-Landau-Verwey-Overbeek (DLVO) and Flory-Huggins theories – these classical approaches neglect the role of specific solvent-surface interactions. Analyzing these surface-specific interactions in colloidal stability becomes increasingly relevant for nanosized particles, which have a highly accessible surface area compared to their bulk counterparts.

This dissertation seeks to understand unconventional mechanisms of colloidal stability that are not explained by traditional theories alone, with oil-in-water emulsions and nanoparticles of metal-organic frameworks (nanoMOFs) as model materials. Leveraging the surface-specific spectroscopic technique, vibrational sum frequency scattering spectroscopy (VSFSS), this work provides a molecular-level understanding of the specific surface interactions that contribute to colloidal stability. In particular, emulsions can be stabilized by a steric layer of polymer alone, with colloidal behavior tunable by pH, electrolyte concentration, molecular weight, and temperature. These sterically-stabilized emulsions find applications in drug delivery systems that must withstand extreme physiological conditions. For bare nanoMOFs, an ordered solvation shell and solvent-metal surface binding contribute to unforeseen long-term stability in common solvents. Additionally, nanoMOFs coated with a polymeric binding agent – similar to those used in the paint industry – yield ultra-strong mixed-matrix membranes for gas separation technologies. Ultimately, this work bridges molecular interfacial chemistry with material properties, emphasizing the importance of understanding mechanisms of colloidal stability.

This dissertation includes previously published co-authored material.

CURRICULUM VITAE

NAME OF AUTHOR: Ashley N. Mapile

GRADUATE AND UNDERGRADUATE SCHOOLS ATTENDED:

University of Oregon, Eugene, OR
University of Puget Sound, Tacoma, WA

DEGREES AWARDED:

Doctor of Philosophy, Physical Chemistry, 2024, University of Oregon
Master of Science, Physical Chemistry, 2021, University of Oregon
Bachelor of Science, Chemistry, 2019, University of Puget Sound

AREAS OF SPECIAL INTEREST:

Vibrational Spectroscopy
Colloids and Soft Matter
Interfacial Chemistry

PROFESSIONAL EXPERIENCE:

Co-Chair, Gordon Research Seminar in Vibrational Spectroscopy, August 2024
Associate Editor, Journal of Emerging Investigators, 2023-Present
Newsletter Complier, Society for Applied Spectroscopy, 2023-Present
Graduate Research Assistant, University of Oregon Department of Chemistry and Biochemistry, 2019-2024
Graduate Teaching Assistant, University of Oregon Department of Chemistry and Biochemistry, 2019-2024
Undergraduate Researcher, National Science Foundation Research Experience for Undergraduates (NSF-REU), University of Oregon, Summer 2018
Undergraduate Researcher, NSF-REU, University of Washington, Summer 2017

GRANTS, AWARDS, AND HONORS:

Honorable Mention, National Science Foundation Graduate Research Fellowship Program, 2021

PUBLICATIONS:

1. Mapile, A. N.; Scatena, L.F. Bulking Up: The Impact of Polymer Sterics on Emulsion Stability. *In Review.* **2024**

2. Mapile, A. N.; Svensson Grape, E.; Brozek, C. K. Solvation of Nanoscale Materials. *Chem. Mater.* **2024**. https://doi.org/10.1021/acs.chemmater.4c01518.

3. Mapile, A. N.; LeRoy, M. A.; Fabrizio, K.; Scatena, L. F.; Brozek, C. K. The Surface of Colloidal Metal–Organic Framework Nanoparticles Revealed by Vibrational Sum Frequency Scattering Spectroscopy. *ACS Nano* **2024**, *18* (20), 13406–13414. https://doi.org/10.1021/acsnano.4c03758.

4. Mapile, A. N.; Scatena, L. F. Stabilizing Strands: Exploring the Kinetic Stability of Polymer-Coated Emulsions with Surface Specific Spectroscopy. *Colloids Surfaces A* **2024**, *697*, 134414. https://doi.org/10.1016/j.colsurfa.2024.134414.

5. LeRoy, M. A.; Perera, A. S.; Lamichhane, S.; Mapile, A. N.; Khaliq, F.; Kadota, K.; Zhang, X.; Ha, S.; Fisher, R.; Wu, D.; Risko, C.; Brozek, C. K. Colloidal Stability and Solubility of Metal–Organic Framework Particles. *Chem. Mater.* **2024**. https://doi.org/10.1021/acs.chemmater.3c03191.

6. Huang, J.; Marshall, C. R.; Ojha, K.; Shen, M.; Golledge, S.; Kadota, K.; McKenzie, J.; Fabrizio, K.; Mitchell, J. B.; Khaliq, F.; Davenport, A. M.; LeRoy, M. A.; Mapile, A. N.; Debela, T. T.; Twight, L. P.; Hendon, C. H.; Brozek, C. K. Giant Redox Entropy in the Intercalation vs Surface Chemistry of Nanocrystal Frameworks with Confined Pores. *J. Am. Chem. Soc.* **2023**, *145* (11), 6257–6269. https://doi.org/10.1021/jacs.2c12846.

7. Carpenter, A. P.; Christoffersen, E. L.; Mapile, A. N.; Richmond, G. L. Assessing the Impact of Solvent Selection on Vibrational Sum-Frequency Scattering Spectroscopy Experiments. *J. Phys. Chem. B* **2021**, *125* (12), 3216–3229. https://doi.org/10.1021/acs.jpcb.1c00188.

8. Tran, E.; Mapile, A. N.; Richmond, G. L. Peeling Back the Layers: Investigating the Effects of Polyelectrolyte Layering on Surface Structure and Stability of Oil-in-Water Nanoemulsions. *J. Colloid Interface Sci* **2021**, *599*, 706–716. https://doi.org/10.1016/j.jcis.2021.04.115.

9. Wilson, K. S.; Mapile, A. N.; Wong, C. Y. Broadband Single-Shot Transient Absorption Spectroscopy. *Opt. Express, OE* **2020**, *28* (8), 11339–11355. https://doi.org/10.1364/OE.390938.

ACKNOWLEDGMENTS

I am extremely grateful to receive the support of so many passionate and dedicated individuals over the course of my chemistry career. From starting as a music major to finishing a Ph.D. it's been quite a journey, and I couldn't have done it without help.

First and foremost, thank you to Geri Richmond for inspiring me to study at the University of Oregon and providing me with a home in the Richmond Lab. I still remember when I introduced myself to Geri at my first ACS conference in New Orleans as a scared little undergraduate unaware of my future. After an REU in the Richmond lab (and meeting Geri's chickens), I was sold on Eugene and pursuing a graduate degree. I truly wouldn't be here if it wasn't for her. Geri's efforts to promote equality in science and her ability to craft engaging presentations are two aspects that I hope to carry on in my own career.

Second, thank you to my advisors Larry Scatena and Carl Brozek who took me under their wing and directed me through the difficult, winding path of graduate school. Larry, thank you for your tough conversations that challenged me to think deeper about my results and push myself as a researcher. I had a great time writing these manuscripts and flushing out the ideas with you (even despite the tough peer review process!). I'm honored to have learned from one of the best laser brains around. Carl, to think that we've only worked together for three years! We've cranked out a lot of impressive work (and more on the way!). Thank you for making the scientific process fun in a time when I was feeling discouraged and drained. Brainstorming in your office, drawing out figures, making two-week plans, analyzing data...to the regular person, these might seem like boring tasks, but our discussions helped me realize what I loved most about science: the investigative process and collaborating with others. Diamonds are made under pressure, right? Just like the perspective we wrote at the last minute! We make a great scientific team and I hope we get to work together again.

Thank you to my committee members Jeff Cina, Cathy Wong, and Daniel Steck who asked difficult questions and pushed me to be the best researcher I could be. I also appreciated the advice and teachings of the UO faculty, particularly Marina Guenza, Jim Prell, Andy Marcus, Scott Hansen, Julia Widom, Mark Lonergan, Chris Hendon, Karl Reasoner, Mike Haley (and Rocky), and Amanda Cook (and Pyewacket). Thank you to the chemistry office, especially Leah O'Brien and Christi Mabinuori whose helpful smiles always brightened my day. Thank you to Priscilla

Lewis (and Shiloh) who made the logistics of graduate school so much easier and helped me be involved in the PURS and REU program. I am also grateful to my professors at the University of Puget Sound who inspired me to pursue graduate school and enriched my education in more ways than they will ever know. Thank you especially to Dan Burgard, Amanda Mifflin, Steven Neshyba, Eric Scharrer, Jo Crane, Luc Boisvert, Gerard Morris, and Jennifer Nelson. Hack hack chop chop!

To my lab mates past, present, and future: Andrew Carpenter, Rebecca Altman, Brandon Schabes, Emma Tran, Marc Foster, Konnor Jones, Checkers Marshall, Kevin Fabrizio, Jiawei Huang, Erik Svensson Grape, Michael LeRoy, Jacob McKenzie, Audrey Davenport, Faiqa Khaliq, Quinn Valentine, Golnaz Navidi, Racheal Fisher, Rachel Galfo, Dario Nunez, and Adam Mather, thank you for being there every day for a good laugh, a tough conversation, or just a coffee walk. For the Richmond Lab members, thank you for providing me with the foundations for graduate school and inspiring me to be just like you! To the Brozek group, thank you for the fun, wild times, and for welcoming a physical chemistry person like me into your materials world.

Finally, the biggest thank you to the four most important beings in my life. A huge thank you and all the love to my partner, Cassidi Howard. Thank you for being there at the exciting and stressful times, the times when I was grumpy and grumbling with Adobe Illustrator, and for all the times that I've practiced my talks for you. Thank you to my parents, Kim Mapile and Todd Mapile, without a doubt, I wouldn't be finishing this crazy thing if it wasn't for your unwavering support. And to Pepper, thank you for your kisses and cuddles! I love you all so much.

For Nibbler.

TABLE OF CONTENTS

Chapter Page

LIST OF FIGURES

Figure Page

LIST OF TABLES

Table Page

CHAPTER I: INTRODUCTION

This introduction provides a background on the traditional theories used to describe solvation and stability of common colloids (nanoparticles, polymers, and proteins) whose mechanistic details are important for application to our nano-sized emulsions and MOFs. Next, this introduction specifies the unique characteristics of the systems studied here – namely the kinetic stability of emulsions and the porosity of nanoMOFs – and presents avenues for measuring colloidal behavior.

The introduction contains material published in *Chemistry of Materials* as a Perspective written with co-authors Erik Svensson Grape and Carl K. Brozek in 2024. Chapter II provides a technical background on vibrational sum frequency scattering spectroscopy (VSFSS) and details the experimental setup used in this work. Chapters III and IV describe two research projects that study the role of steric bulk from a polymer layers as a mechanism for stability of hexadecane emulsions. The role of pH- and salt-sensitivity is introduced in Chapter III and molecular weight dependence is probed in Chapter IV. Chapter III was published in *Colloids and Surfaces A: Physiochemical and Engineering Aspects* in 2024 and Chapter IV is currently submitted to *Soft Matter*, with both manuscripts supervised and written with Lawrence F. Scatena. Chapter V was published in *ACS Nano* in 2024 in collaboration with Michael A. Leroy, Kevin Fabrizio, Lawrence F. Scatena, and Carl K. Brozek and introduces VSFSS as an emerging technique to measure the surface of bare, colloidally stable MOF nanoparticles. Chapter VI contains unpublished work in preparation for submission co-authored with Michael A. Leroy, Audrey M. Davenport, Lawrence F. Scatena, and Carl K. Brozek that combines the two main aspects of this dissertation, nanoMOF particles and polymer coatings, where the surface structure of carbonyl polymers at very low concentrations is measured and proposed as a solution to homogenously disperse nanoMOF particles in a polymeric membrane. Finally, Chapter VII details unpublished work in collaboration with Adam P. Mather and Carl K. Brozek that connect the fundamentals of colloidal stability discovered in this work, namely solvation shells, to the relevant parameter of critical aggregation concentration of both porous and non-porous inorganic colloids. Chapter VIII will conclude this dissertation with remarks on the exciting and broad future of VSFSS for studying buried, colloidal surfaces.

I.A. SOLVATION AT NON-POROUS INTERFACES

I.A.1. Colloidal Stability and Solvation

In the 1940s, two teams of researchers independently studied the forces contributing to particle colloidal stability. Boris Derjaguin and Lev Landau in the Soviet Union presented their theory of colloidal stability that invoked short-range van der Waals attractions between particles overcome by electrostatic surface repulsions.[1] While the electrical double layer had previously been introduced by Hermann von Helmholtz (1853),[2] Louis Georges Gouy (1910),[3] David Leonard Chapman (1913),[4] and Otto Stern (1924),[5] Derjaguin and Landau pioneered the notion of electrostatic potentials at curved interfaces where the surface electric field decays as a function of the particle radius. Meanwhile, in the Netherlands, Evert Verwey and Theodoor (Jan) Overbeek developed the now-ubiquitous potential energy curves of two interacting spherical particles as a function of interparticle distance and electrolyte concentration.[6,7] Ultimately, a model of the forces governing nanoparticle stability in solution was named DLVO theory for the four authors involved.[8] DLVO theory has been thoroughly derived to describe the colloidal stability of hard-shell nanoparticles in a variety of electrolyte concentrations,[9,10] surface charge composition,[11,12] solvent environments,[13] and many other scenarios.[13–18] DLVO theory can be summarized by Eq. 1:

$$W(D) = W_{vdw} + W_{elec} \tag{1}$$

where W(D) represents the interaction energy between neighboring particles, W_{vdw} is the attractive energy due to van der Waals interactions and W_{elec} is the repulsive electrostatic energy (**Figure I.1A**). The entropy and steric pressures of the system have been incorporated into extended DLVO theory (XDLVO)[19,20] as described by Eq. 2:

$$W(D) = W_{vdw} + W_{elec} + W_{osmotic} + W_{entropic} \tag{2}$$

where the addition of the $W_{osmotic}$ term accounts for the repulsive energy caused by neighboring nanoparticles with an increased overlap region (typically due to increased surface sterics), while the $W_{entropic}$ term accounts for the attractive energy arising from an increase in solvent entropy upon particle coalescence. This entropy-driven aggregation is often termed the hydrophobic effect.

Although developed as a general model, DLVO theory applies best to “hard” colloidal systems, such as colloidal quantum dots, core-shell metallic nanoparticles, or metal oxides with

well-defined boundaries between the nanoscale object and the suspending solution. Whereas hard-shelled colloids maintain their rigidity in solution, "soft-shelled" particles stretch and adapt to nearby fluid interfaces (**Figure I.1B**).[21–24] Hard-shell particles are convenient systems to study as short-range van der Waals interactions decay exponentially as a function of distance from the particle without the need to consider interfacial charge-screening. On the other hand, soft-shell particles, such as oil droplets, metal nanoparticles coated with a polymer layer, proteins clusters, and even living cells,[25] present complications to DLVO theory as solvent intercalation, ion adsorption,[26] spontaneously ordered solvation shells , and surface roughness,[15] together comprising so-called "non-DLVO forces". Experimental attempts to bridge these two types of systems, such as core-shell colloids with soft exteriors and hard interiors,[21,27] impart improved thermodynamic stability and, in some cases, unique optical behavior.[28,29] Theoretical models of

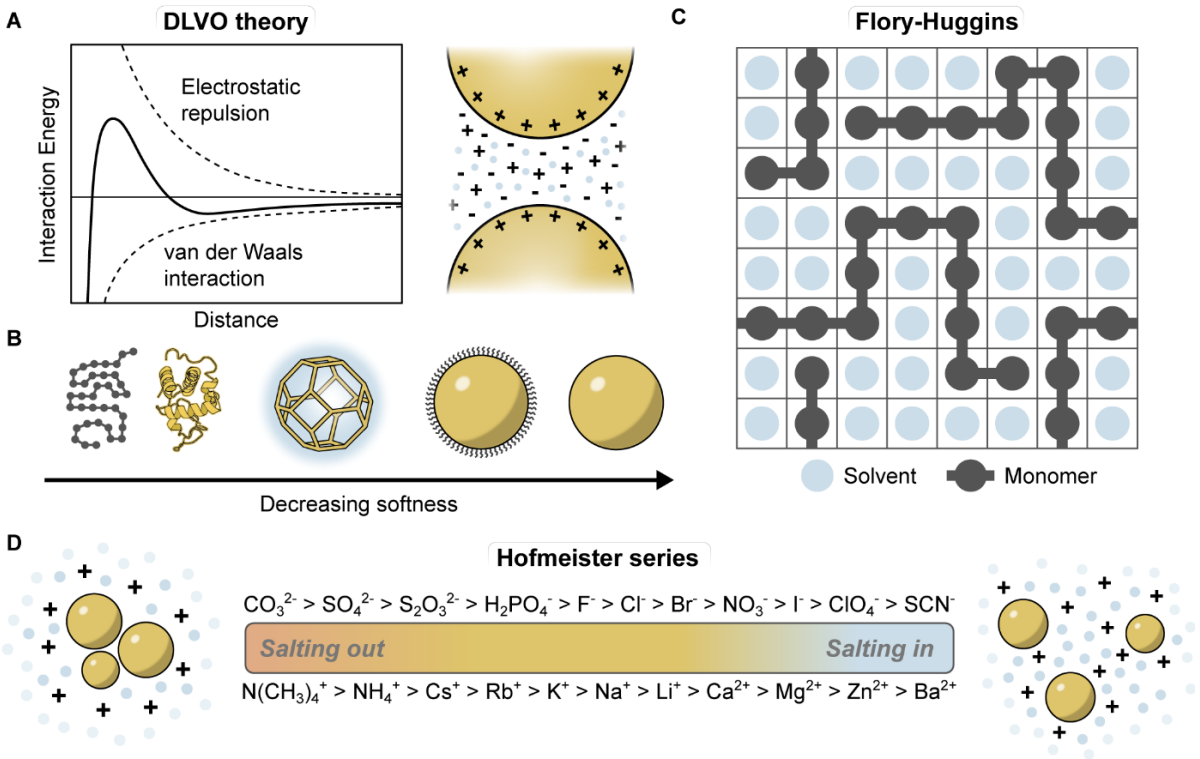

Figure I. 1 A) Typical DLVO graph showing the interaction energy as a sum of electrostatic repulsion and attractive van der Waals interactions. B) Illustration of the soft-to-hard range of nanoscale materials ranging from polymers/proteins to hard spheres, such as metal oxide nanoparticles. C) The lattice model of polymer solvation as described by Flory-Huggins theory. D) Illustration and ion examples in relation to the Hofmeister series of solvation.

such systems account only for the hard-soft interface, while neglecting the possibility of low density and heterogeneous surfaces and their associated energetics.

According to the IUPAC definition, a colloid involves a "molecule or polymolecular particle dispersed in a medium" with "at least in one direction a dimension roughly between 1 nm and 1 μm".[30] Examples of colloids include a solid in a gas (smoke), a liquid in a gas (aerosol), or a liquid in a liquid (emulsion), in addition to many other dispersion types that do not require solvent as a medium. Understanding the stability of heterogeneous mixtures in solution is critical to their implementation in displays, coatings, or membranes, but the clear phase boundary creates significant challenges because of the difficulty in studying the chemistry that emerges at the colloidal interface. The process of dissolution, by contrast, involves the formation of a single, homogeneous phase.[31] Unlike solutions, the heterogeneity of colloidal dispersions creates thermodynamic instability resulting in their eventual phase separation. Suspended particles can be filtered out or mechanically separated, whereas separating dissolved particles requires additional chemical transformations.[32,33] In the following sections, we provide a brief overview of the chemistry underlying the colloidal stability of non-porous inorganic nanoparticles with and without functionalized surfaces, and how it critically involves solvent.

I.A.2. Capped Colloidal Nanoparticles

Nearly all non-porous inorganic nanoparticles require surface functionalization for long-term stability. The strong van der Waals attractions between bare metallic surfaces results in nearly instantaneous aggregation and sedimentation. Semiconductor nanocrystals, specifically quantum dots, the topic of the Nobel Prize in Chemistry in 2023,[34,35] represent another key example of nanoparticles that find utility only by surface functionalization. Attaching surfactant ligands to prevent Ostwald ripening[36,37] allows semiconductor nanoparticles to remain stable at precise sizes that dictate their tunable optical properties.[38–40] Functionalizing quantum dots with either an inorganic shell also diversifies the available solvents for dispersion.[41,42] Most notably, the addition of water-soluble ligands, such as citrates,[43] polymers,[44,45] or other small molecules[46,47] allows for the use of metallic nanoparticles within cellular media. A wide variety of ligands have been studied for their interaction with various solvent media.[48,49] By contrast, nearly all porous colloidal materials, as described below, require no surface functionalization for colloidal stability.

Therefore, for context, we must understand the mechanism of colloidal stability for nanoparticles prepared without capping agents.

I.A.3. Bare Nanoparticle Solvation

Few reports have documented bare nanoparticles exhibiting long-term colloidal stability. The examples described below are restricted in their industrial applications due to highly defective surfaces, the necessity of a stabilizing supporting material, and the need for post-synthetic cleaning or filtration. For example, while it has been shown that metallic nanoparticles can be stabilized by a partially oxidized surface,[50] this chemical decomposition generates a heterogeneous and rough surface with mixed valence sites.[51,52] An alternate approach that avoids surface oxidation was achieved by synthesizing bare copper nanoparticles with an electron-donating gadolinium support.[53] Implementing nanoparticles in biological sensing applications cannot be achieved, however, with a bulky and potentially toxic supporting material. Another approach involves "sterilization" of bare gold nanoparticles by autoclave.[54] Studies suggest that < 5-nm particles assemble into larger 10-30 nm particles during this process. This size-focusing serves as a form of filtration to achieve a narrow size dispersity, but size selection does not always ensure colloidal stability.[55] Because these few examples of bare nanoparticles are short-lived colloids, they are often quickly drop-casted back to their solid state.[56–59]

In the few studies of bare metallic nanoparticles in solution without a stabilizing support, the ionic structure of the supporting electrolyte and the resulting electrical double layer at the surface has proven to be a key, but poorly understood feature contributing to colloidal stability. Simulations suggest that facet-specific ion adsorption and an ordered primary solvation shell promote gold nanoparticle stability in water.[52,60] Experimental studies also suggest water stability of bare nanoparticles arises from ion adsorption dependent on electrolyte concentration and following the so-called Hofmeister series for anions.[54,61–63] The colloidal stability of nanoparticles in solvents without electrolyte, however, have only been studied as computational simulations of bare particles[64] or through weakly ligated experimental systems where a portion of the surface remains deliberately exposed.[65] Thus, achieving a metal nanoparticle colloid stabilized by solvation forces alone remains an open challenge and would open an avenue for tuning the opto-electronic and electrochemical electrical properties of metallic nanoparticles in a wide variety of

solutions. To understand the colloidal stability of bare nanomaterials, therefore, we instead turn to the supramolecular solvation chemistry of polymers and proteins.

I.B. SOLVATION AT PSEUDO-POROUS INTERFACES

I.B.1. Polymer Solubility

At nearly the same time that Derjaguin, Landau, Verwey, and Overbeek developed their model of colloidal stability, Paul Flory and Maurice Huggins independently considered how polymers could dissolve despite distinct differences in molecular size from the surrounding solvent.[66,67] While the entropy of mixing a simple molecule in solution can be described by Gibbs energy of mixing:

$$\Delta G_{mix} = \Delta H_{mix} - T\Delta S_{mix} \quad (3)$$

where *H* is enthalpy, T is temperature, and *S* is entropy, this relationship only considers the gross interaction between a molecule and its surroundings. It neglects synergistic behavior between individual units within a chain, such as in a polymer (**Figure I.1C**). Flory and Huggins adapted the Gibbs energy of mixing for polymers as:

$$\Delta G_{mix} = RT(n_1 ln\phi_1 + n_2 ln\phi_2 + n_1\phi_2\chi_{12}) \quad (4)$$

which now considers the number of moles (n) and the volume fraction (ϕ) of the solvent (component 1) and polymer (component 2). χ_{12} is material-specific and describes the synergistic interaction between the polymer and the solvent, allowing for specific descriptions of polymer solubility.

We introduce the term "pseudo-porosity" to describe the solvation of polymers and related systems. While polymers lack permanent porosity (the ability to maintain a rigid, porous structure when suspended in solution), their solvation mechanism depends on the large solvent accessible surface areas carved out by the wrapping of individual monomer units. In Flory-Huggins theory, a polymer solution is modeled as a lattice of cells containing either polymer monomer units or a solvent molecule. Based on this image, the individual mixing components of a monomer unit with the polymer is well described by equation 4. However, realistic intermolecular forces from hydrophobicity,[68] ionic screening,[69] and other polymer or solvent-specific interactions[70,71] integral to solvation and polymer conformation are absent from eq. 4.

In addition to the pseudo-porosity of conventional polymers, intrinsically porous polymers and porous polymer membranes also exist. Typical examples of porous polymer membranes include polycarbonate, polyester, or cellulose with pore diameters ranging from nanometers to 10s of μms. The narrow, one-dimensional confinement of these pores within a membrane have led to a versatile platform for studying solvent-controlled ion-transport under spatial confinement akin to the ion-transport across cellular membranes and carbon nanotubes.[72,73] Chemical functionalization of these materials leads to specific ion effects, such as appended carbonate groups showing preferential binding of metal cations.[74] Polymers of intrinsic microporosity (PIMs), on the other hand, contain voids of 2 nm or less.[75] Controlling the solubility of PIMs is critical for creating robust films with consistent pore sizes.[76] The commonly used PIM-1, however, dissolves only in tetrahydrofuran (THF) and chloroform ($CHCl_3$), leading to reduced solution processability and restricting the incorporation of fillers or other composites. Recent work has introduced post-synthetic modifications of PIMs to improve their solubility,[77] with the key result that specific solvent interactions with appended moieties improves solubility. In understanding the solvation of porous materials discussed in Section 3, these reports of porous polymers offer the insight that solution stability of nanoscale materials benefits from monomer units accessible to solvent.

I.B.2. Hydration of Proteins

Proteins comprise another class of macromolecules whose solvation depends on solvent interacting with accessible building blocks, yet with the added compositional diversity of amino acid mixtures and H-bonding networks. For proteins, solvation can be described as monomer-by-monomer solubility or by secondary structure solvation via protein folding to bury hydrophobic moieties. As a result, proteins arrange into secondary structures, like helices or sheets, and fold into native states to satisfy solvent interactions with their respective amino acid chains. Numerous studies have quantified surface interactions between proteins and water in solution,[78,79] with one notable computational investigation into the hydrogen bonding of a protein in water as a function of solvent accessible surface area and protein conformation.[80] These authors report that the solvation free energy of a protein decreases linearly as a function of the solvent accessible surface area of the protein. This finding suggests that an increase in the surfaces available for solvation promote stability in solution. As the basis of Flory-Huggins theory, leveraging enthalpically favorable

solvent-material interactions is critical for solubility and stability. In a permanently porous material, as explained below, the unparalleled solvent accessible surface areas provide increased sites for solvation interactions via internal and external surfaces.

The unique folding ability of a protein allows it to adapt to an otherwise thermodynamically unstable environment. In contrast, porous framework materials, such as metal-organic frameworks (MOFs), cannot protect select components by geometrical reconfiguration. Protein folding or unfolding can be induced by addition of ions that "salt-in" or "salt-out" the macromolecule of interest (protein, polymer, nanoparticle, etc.) *vis-à-vis* the Hofmeister series (**Figure I.1D**). Ion specific effects in protein precipitation was introduced by Franz Hofmeister in the late 1880s to describe how different salts impact the solubility of proteins despite possessing the same net charges.[81,82] Kosmotropes, or "structure-makers" are ions that interact more strongly with water than with the protein themselves, causing the protein to remain in its native folded state and salt-out of solution. Common examples of kosmotropes include citrate, sulfate, and phosphate anions or magnesium, calcium, or lithium cations. On the other hand, chaotropes, or "structure-makers" interact closely with individual protein units, promoting an unfolded, solubilized state of the protein. Chaotropes include iodide, nitrate, and tetrafluoroborate anions or calcium, magnesium, and aluminum cations. Polyoxometalates (POMs), for example, are super-chaotropes due to their large, delocalized charge and low surface densities.[83] While Hofmeister's initial experiments provide a basis for harnessing specific-ion effects, recent work has produced a more detailed understanding of salts and their impact on colloidal stability and solubility, especially cooperative contributions from ion pairs.[84–87] Vibrational spectroscopy and molecular dynamic simulations reveal that cations follow the Hofmeister series through strong backbone-salt interactions and weaker interactions with negatively charged side chains.[88] Anions, however, despite following the Hofmeister series at the backbone, exhibit a reversed trend on positively charged amino acid residues. For this reason, the Hofmeister series for anions holds only when the backbone-salt interactions outweigh the salt interactions with side chains. Tuning the colloidal stability of metal-based nanoparticles requires understanding the specific-ion effect in solvents beyond water.[89,90] A comprehensive study of the ion effects in non-aqueous solvents found that water is not unique in its role in the Hofmeister series.[91] In fact, aprotic solvents also show an ion specificity due to the inherent molar volume and electrostriction of the ion, or the ability of the ion to slightly deform.

These results confirm that a Hofmeister trend persists regardless of solvent identity, thereby providing a basis for tailoring the colloidal stability of non-aqueous materials.

Specific ion effects are critical to the colloidal stability of bare nanoparticles. In one study, gold nanoparticles without any organic ligands at the surface were stabilized by as little as 10 μM of a chaotropic anion.[61] The electrolyte solutions were added during nanoparticle synthesis, thereby acting as a non-organic capping ligand. Additional electrolyte may destabilize colloids, however. Reports indicate that increasing salt concentration to the mM regime often leads to nanoparticle aggregation, as exhibited by metallic nanosheets titrated with potassium salts of varying valency anions[92] and other metal nanoparticles.[93,94] A likely causes is that with increased salt concentrations electrolyte ions screen the effective charge density that normally prevents aggregation. Nevertheless, tuning salt concentrations could serve as a promising strategy for controlling the solvation of porous nanoparticles with bare surfaces.

I.C. SOLVATION OF OIL-IN-WATER EMULSIONS

I.C.1. Emulsion Kinetic Stability

Formulating stable emulsions and understanding the mechanism of oil droplet stability has far reaching implications, from the development and enhancement of new cosmetic products, to the efficacy of drug delivery systems and oil spill remediation technologies.[95–97] Traditionally, oil droplets with diameters of 20-200 nm are classified as nanoemulsions while larger droplets with diameters of 200-1000 nm in diameter can be referred to as miniemulsions.[98] Regardless of the size, surfactant-coated emulsions are useful laboratory analogues for modeling commercially-used dispersants that reduce the surface tension of a large oil patch and enable the formation of stable, small oil droplets that are continuously distributed by waves and eventually biodegraded by marine microbes.[99] However, these oil droplets require high energy mixing for formation and are thermodynamically unstable leading to eventual phase separation given enough time.[100–103] In practice, ultrasonication is necessary to input the energy required for the system to enter the kinetically trapped state (**Figure I.2**). The addition of surfactants, electrolyte, polymers, and/or proteins can provide a protective layer that prevents particle coalescence over time. DLVO theory explains that particle-particle repulsion in emulsions is commonly accounted for by balancing

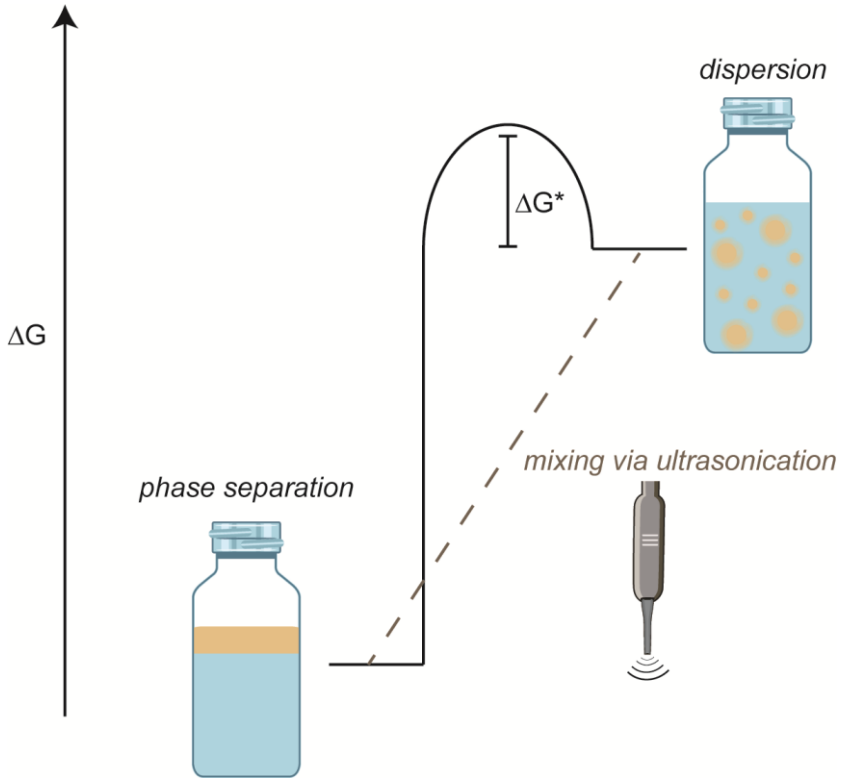

Figure I. 2. Illustration of emulsion formation from a phase separated state to a dispersion via ultrasonication. The dispersed emulsion is kinetically trapped and will eventually return to the phase separate state.

attractive van der Waals interactions with repulsive electrostatic forces, such as those typically achieved by an ionic surfactant. A zeta potential, or surface charge, of about ± 30 mV is typically necessary to a stabilize a colloid. Extended DLVO theory further accounts for steric effects with the addition of a destabilizing osmotic pressure term and a stabilizing entropic term. In most applications, emulsion stabilization is ensured by surface functionalization that provides electrostatic or steric repulsion, or a combination of the two.

Beyond oil remediation, the curved interface of emulsions have proven to be of interest to measure the molecular packing behavior as compared to planar oil/water interfaces. The Richmond/Scatena lab and others have postulated that the geometry of the interface and the thermodynamic instability of emulsions are responsible for the observed differences in molecular orientation and conformation at the two interfaces.[104–106] In one regard, ultrasonication forces both the formation of oil into small droplets *and* the adsorption of surfactants or polymers to the interface. The addition of ultrasonicating energy can cause unexpected interfacial behavior as compared to what has been exhibited at a planar oil/water interface where small molecules

thermodynamically adsorb to the interface at an equilibrium time scale. Not only do emulsions differ from their planar counterparts in terms of kinetic stability, but they exhibit a curved geometry, instead of flat. While the droplet geometry increases overall interfacial surface area for chemical adsorption, it also enhances steric and electrostatic crowding effects which can reduce interfacial coverage of surfactants, polymers, or ions.[107] Keeping these aspects of thermodynamic and kinetic stability in mind for the planar and droplet oil/water interfaces, respectively, are important when interpreting VSFS spectra from each chemical environment.

I.C.2. Steric Stabilization of Emulsions

While non-toxic surfactants are useful for environmental applications, the introduction of proteins as colloid stabilizers have the potential to encapsulate and selectively deliver hydrophobic drugs.[108–112] It is hypothesized that colloids are stabilized by protein coronas through steric hinderance or, in other words, a thick protein shell prevents droplets from coalescing. While recent work using 2D-IR spectroscopy and sum frequency scattering spectroscopy have investigated the newfound importance of protein-stabilized colloids, the molecular conformation and detailed mechanism of stability remain difficult to probe due to the complicated nature of long-chain proteins and their resulting coronas.[113,114]

Polyelectrolytes are useful analogues for studying protein coronas as both macromolecules have varying functional groups along a repeating backbone, a nuanced folding or coiling structure with the ability to hydrogen bond or form secondary structures, and charge localization along the chain dictated by environmental pH. Yet, polyelectrolytes are often easier to study than proteins due to their known monomer units and simple tunability of molecular weight, percent protonation, and secondary structure. In addition to their pH-dependent behavior in bulk solution, acids and polyelectrolytes adsorbed at interfaces are known to have a surface pK_a ~1 unit more alkaline than the bulk pK_a due to interfacial solvent dielectrics reducing the solvation energy of the acid functional groups.[115–120] This pH-dependence is critical for materials such as polyelectrolyte coarcervates, where stabilization across a variety of conditions can be a challenge.[121,122] The adsorption behavior of polymers has generated both theoretical[123] and experimental[124,125] studies that seek to understand interfacial conformation. In particular, a “train, loop, tail” representation has been developed that describes how polymers lie flat at the surface (train), coil beyond the surface into the bulk (loop) and extend at the ends of the polymer chains (tail) to emphasize

favorable surface-polymer interactions or bulk-polymer interactions, dependent on the polymer identity and interface.[126–128] Here, VSFSS is a powerful tool to probe polymer conformation at interfaces.

Previous work from Marc Foster in the Richmond Laboratory investigated the role of carboxylic acid surfactants at the curved oil/water interface.[106] These experiments were fundamental in developing a rigorous experimental procedure to measure the carbonyl and carboxylate modes via VSFSS. A non-resonant contribution from the CaF_2 windows used in VSFSS contribute to a large background that requires de-timing of the visible pulse to deconvolute the resonant vibrational modes of interest.[129] Additionally, Marc found that the carbonyl and carboxylate modes at the oil/water droplet interface differed in both spectral line shape and peak position then the same modes measured at a planar oil/water interface or the planar air/water interface.[104,130] These differences were attributed to the difference in solubility of the hydrophobic phases with the alkyl chains of the surfactant. The improved solubility of the surfactant in the CH-rich oil phase as compared to air, for example, would increase the ordering of the head group at the droplet interface. At the same time, it was proposed that the curved geometry of the droplet resulted in charge repulsion across the droplet that caused a lower population of surfactants at the droplet surface. With this increased surfactant head group area, the carbonyl and carboxylate modes exhibited improved ordering at the oil/water droplet interface.

In this dissertation, the ability of a low-charge polymer to stabilize emulsions without the assistance of a surfactant is explored. The colloidal stability of this polymer system was further probed by adjusting the pH, salt identity and concentration, molecular weight of the polymer, backbone substitution, and temperature. The adjustment of these variables provide insight into the physiological robustness of polymer-stabilized emulsions with tunable parameters that can improve drug delivery platforms.

I.D. SOLVATION AT POROUS INTERFACES

To understand the solubility and stability of porous colloids, we suggest using the aforementioned models of solvation, namely electrostatic or steric repulsion, the hydrophobic effect, monomer-by-monomer solubility, and specific ions interactions. By possessing both internal and external surfaces, porous colloids exhibit surface area-to-volume ratios and accessible void spaces far

exceeding any class of non-porous or pseudo-porous material.[131] For example, the surface density of the commonly studied zeolitic imidazolate framework ZIF-8 (Zn(2-methylimidazolate)$_2$), has a surface density of 7 atoms/nm^2 while non-porous ZnO has a surface density of 78 atoms/nm^2 (**Appendix F**). Additionally, as illustrated by the example above, the internal and external surfaces of porous materials resemble the heterogeneous surfaces of proteins. We expect the surface of porous materials to be susceptible to specific solvent-surface interactions as opposed to generalized hard-shell interactions between a homogeneous nanoparticle surface or surfactant ligands and the supporting solvent. In the following sections, we describe common permanently porous materials (*i.e.*, materials that retain porosity in solution) and propose mechanisms for their colloidal stability and solubility. This research field is nascent, without consensus around theory that explains the colloidal stability of porous materials. We propose, given the examples below, that specific solvent-surface interactions, such as through ordered solvation shells and chemical interactions between the material building blocks and the solvent provide the colloidal stability of porous materials.

I.D.1. Simple Porous Structures

As a starting point, nanotubes serve as a basis for understanding the solvation of a one-dimensional porous material (**Figure I.3A**). The pores, or tunnels, of nanotubes can range from 0.5-2 nm in diameter and are typically grown from a metal catalyst via chemical vapor deposition. One might assume that water should be excluded from the nanotube interior due to its hydrophobicity and because water absorption is entropically disfavored.[132] Surprisingly, water adsorbs inside the pores of carbon nanotubes, leading to the phenomenon of "water wires".[133] One explanation proposes that water wires and carbon nanotube solubility results from the entropy of water flowing through the pores and from free rotation of water molecules. Studies also suggest dissolution in water does not involve favorable enthalpic interactions between water and the nanotube, suggesting water solubility of other hydrophobic materials through entropy-favored interactions. Changing the nanotube polarity, via simulations or experimental crystal engineering, allows for tuning of the water wire mobility, specifically in terms of water migration from one opening of the tube to the other, functioning as a nanosized garden hose. Carbon nanotubes also dissolve in ionic liquids,[134,135] where both solvation shells and internal hydrogen bonding are postulated to stabilize the particles. Similar solvation behavior has been observed for carbon nanotubes in benzene,[136]

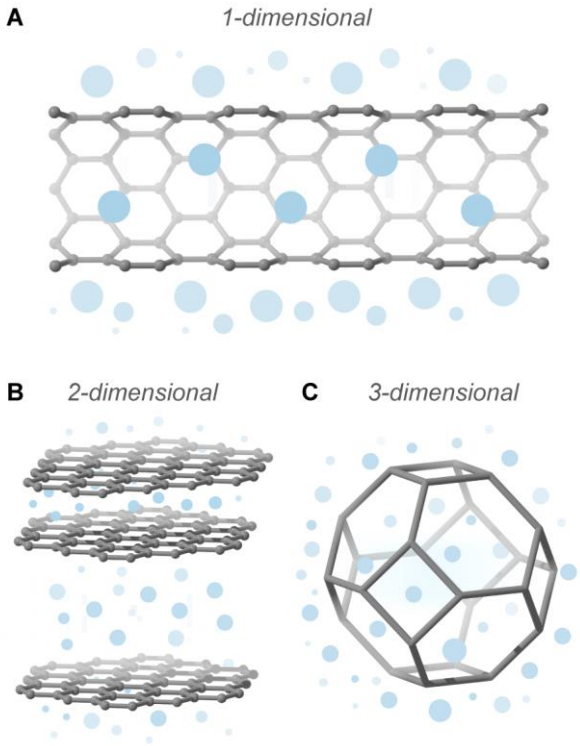

Figure I. 3 Illustration of A) 1-dimensional (polymers, nanotubes), B) 2-dimensional (layered or sheet-like materials), and C) 3-dimensional structures (porous materials) and their possible solvent interactions.

alcohols,[137] and polymer solutions,[138] however nearly all studies are computational. Although challenging, experimental studies of nanomaterials solvation will lay the foundation for designing their application in solution state applications, such as drug delivery or membranes.

Whereas nearly all nanotubes are homogenous and comprised of carbon, the solvation of 2D materials introduces the probability of surface heterogeneity (**Figure I.3B**). In addition to the atomically homogeneous example of graphene, 2D materials include the heterogeneous boron nitride, metal chalcogenides, or metal oxides. In these materials, solvent accessible surface areas exist between sheets (interlayer), introducing another unique solvation environment in addition to interior and exterior pores. Despite their enhanced surface areas, most nanosheets require a surfactant or post-synthetic modification for long-term colloidal stability, similar to 3D, non-porous inorganic analogs.[139–141] As illustrated by the examples below, electrical double layers are thought to spontaneously assemble at the surface of nanosheets, providing a large electrostatic surface repulsion (as measured by zeta potential) and site-specific water interactions at the surface. These results suggest that in high-surface area materials without deliberately added surface

capping agents, specific solvent interactions are important for colloidal stability. Surprisingly, hydrophobic 2D materials, including graphene and MoS_2, disperse in aqueous solutions via exfoliation-induced oxidation.[142,143] Studies suggest that ultrasonication causes etching of edge-groups that improves the solubility in water. In a notable study, graphene ultrasonicated at high-temperatures exhibited long-term colloidal stability in water while the sample sonicated at low-temperatures maintained a pristine morphology and was unstable in water.[144] The introduction of edge-site functionalization to graphene oxide in the form of hydroxyl and carboxyl groups also contributes to the increased water stability. However, for heterogeneous nanosheets of hexagonal boron nitride, MoS_2, WS_2, and $MoSe_2$, colloidal stability in water was achieved after sonication at both high- and low-temperatures and no surface functionalization was observed.

3D porous materials with relatively simple compositions include microporous nanoparticles such as silica and zeolites (**Figure I.3C**). Mesoporous silica (SiO_2) has pore diameters of 2-50 nm, while microporous silica has much smaller pores below 2 nm. Zeolites are aluminosilicates with even smaller pore diameters ranging from 0.3-0.8 nm. As with colloidal nanoparticles, polymers, and proteins detailed above, the colloidal stability of 3D porous nanomaterials depends on proper electrolyte concentration,[145] surfactant surface coverage,[146,147] and polymer coatings.[148] Studies remain largely empirical and an underlying mechanism of colloidal stability remains unclear. Representative studies include the finding that mesoporous silica is typically synthesized with a surfactant like hexadecyltrimethylammonium bromide (CTAB) acting as both a structure-directing molecule (to synthesize a specific shape) and a stabilizing capping ligand.[149–151] These surfactant-capped materials can be stable for upwards of a year in water.[152] Mesoporous silica nanoparticles can also be surface functionalized as hydrophobic, which renders them useful drug delivery agents.[153,154] Little is known about the solvation and colloidal stability of mesoporous silica, although recent work suggests that performing dialysis solvent exchange or coating the nanoparticles with proteins improves dispersability.[155,156]

A potential method for probing mechanisms of colloidal stability in porous materials would rely on surface functionalization. Although porous, silica and zeolites lack chemical tunability beyond their typical inorganic compositions (**Figure I.4B**). Instead, organic-inorganic framework materials assemble from a wide variety of metallic and organic-compounds, resulting in a diverse

range of pore diameters, aperture shapes, solvent-accessible surface area, morphology, and well-developed methods for post-synthetic modulation of surface compositions.

I.D.2. Porous Frameworks

Understanding the colloidal stability of porous frameworks attracts intense recent attention, in part because 3D porosity challenges conventional mechanisms of solvation, such as the notion of electrostatic forces between smooth, uniform, hard spheres. Porous framework materials metal-organic frameworks (MOFs) are pursued for a wide range of applications due to their unparalleled performance at selective gas separation, water filtration, carbon sequestration, and other areas leveraging tunable guest-host interactions (**Figure I.4A**). Practical implementation as solution processible and reusable materials, such as thin film membranes, demands their ability to suspend as uniform, stable colloids in a range of solvents. Stability in water would facilitate their utility in biological applications, for example, while compatibility with low-boiling solvents would render them amenable to spraying coating and other forms of industrial production at-scale. In addition to a lack of knowledge of solvation structure, few studies exist for any form of surface functionalization. Reported surface ligands deviate from those well studied with conventional quantum dots.[157] Solvent interactions likely dictate the interaction of porous materials with polymers in the so-called mixed matrix membranes envisioned for chemical separation technologies. Little is known about microscopic aspects of the polymer-porous colloid interface, except that great care must be taken to prevent polymers from intercalating and clogging pores,[158,159] which can be detrimental to gas sorption and chemical separation applications. In this section, we will describe the current theories of colloidal stability for porous frameworks and the challenges in studying them.

Unlike typical, nonporous nanoparticles, MOFs exhibit colloidal stability without the need for conventional capping ligands.[160] In fact, while traditional surfactants such as dodecanoic acid or cetyltrimethylammonium bromide can be included in a MOF synthesis to impart size or shape control,[161,162] these ligands do not remain with the MOF nanoparticles after washing, as we have observed by nuclear magnetic resonance spectroscopy, thermogravimentric analysis, and other analytical techniques.[160,163] Instead, while post-synthetic addition of ligand dyes[157] or DNA/protein coronas[164] leads to functionalized surfaces, few if any studies detail how they impact colloidal stability. Instead, we recently demonstrated that the solvent identity plays a greater role in

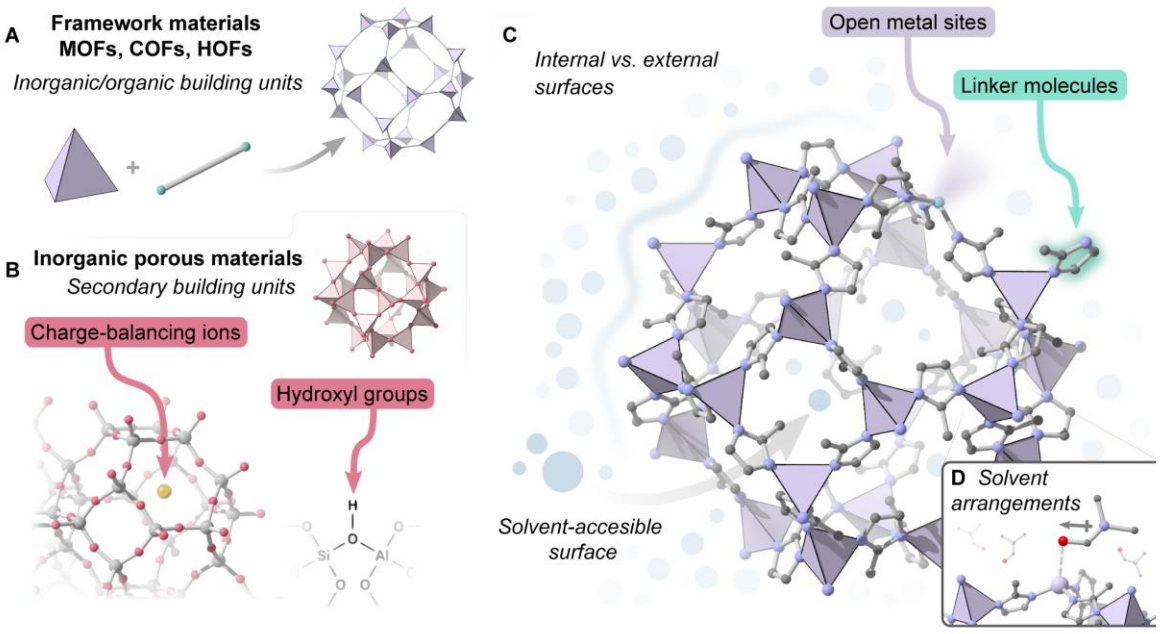

Figure I. 4 Representation of A) framework materials, comprised of inorganic/organic building units that are assembled into porous frameworks and B) inorganic porous materials, which are made up of secondary building units. In C) both material classes show distinct internal vs. external surfaces due to their high solvent-accessible surface areas. Direct functional groups or open metal sites within the materials D) may induce different solvent arrangements.

stabilizing the surface as only solvents that can dissolve the organic linker can suspend the MOF nanoparticle.[160] This result strongly suggests that the interaction of MOF nanoparticles resembles the dissolution of cage molecules, polymers, and other macromolecules systems where solubility depends solvent-monomer energetics and accessible void spaces (**Figure I.4C,D**).

In addition to specific solvent-surface interactions, classical electrostatic arguments of DLVO theory could explain the stability of uncapped MOF nanoparticles, where surface charges would arise from deprotonated linker molecules or open metal sites. Electrostatics alone is unlikely to account for the full mechanism of colloidal stability, however.[165] Recent reports of zeta potentials—indicators of net surface charge— typically at the border (±30 mV) of values required for colloidal stability by DLVO theory.[160,166] These reduced zeta potentials can be attributed to the low surface density of porous nanoparticles and the weak, short-range electrostatic fields produced by surface defects that quickly decayed through porous channels.[167] Binding of solvent or polymers to open metal sites at the surface of MOF nanoparticles improves colloidal stability,

while also reducing the apparent surface charge.[159,163] In other words, zeta potentials may not relate directly to MOF colloidal stability.

Instead of traditional electrostatics, we suggest the intrinsic porosity of nanoMOFs improves colloidal stability through entropic effects. For nonporous colloids, entropy favors aggregation because it removes solvation shells and disorders excluded solvent. This process is termed the "hydrophobic effect" and was introduced as a mechanism to describe porous nanoparticles,[168] where the total amount of ordered solvent must be lower than nonporous colloids due to the low density surfaces. As a result, the potential energy favoring aggregation decreases as well. To examine the interaction of solvent with porous interfaces, we use VSFSS to measure the orientation of *N*,*N*-dimethylformamide (DMF) or water solvation shells at the exterior of Zn(2-methylimidazolate)$_2$ (ZIF-8) colloids. Although predicted to exist, solvation shells of colloids were previously documented only by atomic force microscopy and x-ray studies.[169–173] In addition to providing a protective shell of steric repulsion, we propose that solvent interactions with open metal sites and linker monomer units improves solvation energetics akin to Flory-Huggins theory. We also observed that the bridging 2-methylimidazolate linkers spontaneously align at the solvent interface in a manner that expands the internal pore volumes. This lattice flexibility, like a protein, may further enhance favorable solvent interactions and colloidal stability. Taken together, these recent reports provide a roadmap for preparing and stabilizing porous materials in solution.

This thesis describes research which probes the surface structure of colloidal materials that are stabilized by non-DLVO forces, including factors like steric stabilization, low electrostatic potential, sparse surface density, particle porosity, and surface heterogeneity. A background on the surface-specific technique of vibrational sum frequency scattering spectroscopy is provided in the following chapter, laying the groundwork for using this powerful tool to study the interfaces of uniquely stable colloidal materials.

CHAPTER II: VIBRATIONAL SUM FREQUENCY SCATTERING SPECTROSCOPY (VSFSS)

II.A.VSFSS THEORY

Developed by Roke *et. al.*,[174] vibrational sum frequency scattering spectroscopy (VSFSS) is a scattering adaptation of the reflection-based vibrational sum frequency spectroscopy introduced by Shen *et. al.*.[175] While reflection VSFS has been commonly used to probe planar air/water[176], oil/water[177], oxide/water [178], and silica/water[179] interfaces, the scattering variation of this technique enables investigation into the interface of nano-sized colloids.[180,181] In the scattering experiment, a visible and tunable infrared (IR) pulse are overlapped spatially and temporally at the

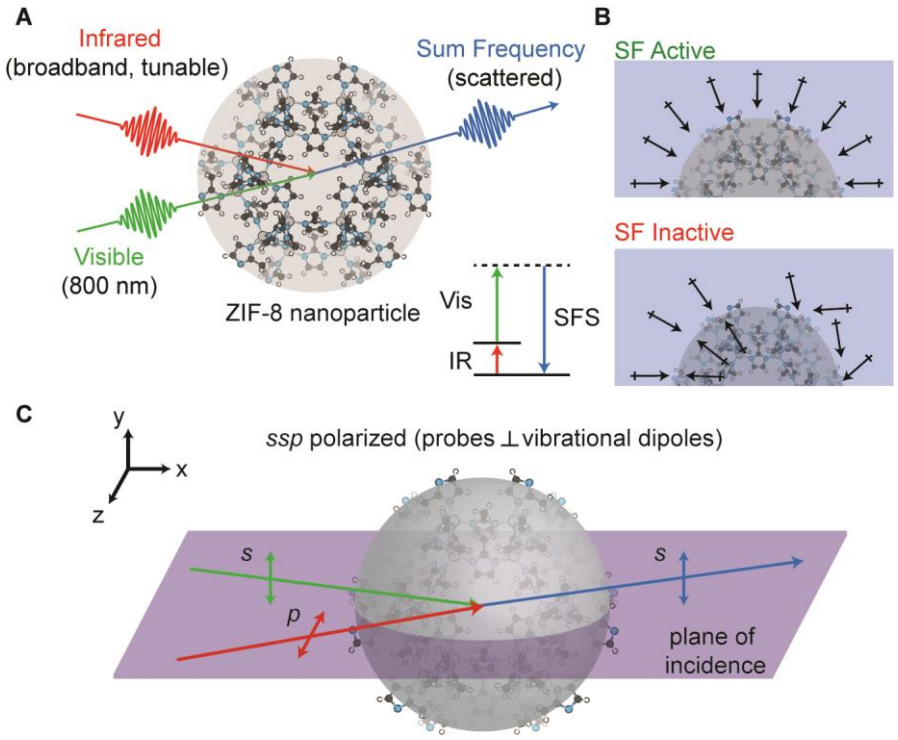

Figure II. 1 A) Schematic of VSFSS, in which a scattered sum frequency response (blue) is generated by overlapping a visible (green) and IR (red) pulse spatially and temporally at a curved interface. The energy level diagram of VSFSS is shown in the bottom right. B) Cartoon representation of the possible scenarios in which a sum frequency signal could be expected. IR transition dipoles at anisotropic surfaces (top) are sum frequency active while mismatched or directly opposing transition dipoles (bottom) are sum frequency inactive. C) Schematic of the ssp polarization scheme in which the sum frequency, visible beams, and IR beams are s, s, and p polarized, respectively. This polarization combination probes vibrational dipoles perpendicular to an interface.

curved interface to generate a scattered sum frequency response that is the sum of the two incoming beams (**Figure II.1A**). VSFSS directly probes vibrational modes at interfaces due to selection rules under the electric dipole approximation prohibiting contributions from a centrosymmetric environment such as a bulk liquid phase. The signal indicates two main attributes of the chemical environment: the population of molecules at the interface and the average molecular orientation of vibrational modes, also referred to as net molecular ordering. Only highly ordered resonant vibrations generate a sum frequency response (**Figure II.1B**).

In VSFSS, the intensity of the scattered SF response is proportional to the intensities of the incoming visible and IR beams ($I_{IR}I_{vis}$) and the square modulus of the second-order nonlinear susceptibility ($X^{(2)}$) as shown in Equation 5.

$$I_{SF} \propto I_{IR}I_{Vis}\left|\chi^{(2)}\right|^2 \tag{5}$$

In a centrosymmetric environment where all directions are equivalent, $\chi^{(2)}_{ijk}$ is identical in two opposite directions such as: $\chi^{(2)}_{ijk} = \chi^{(2)}_{-i-j-k}$. Additionally, $\chi^{(2)}_{ijk}$ is a third rank tensor and obeys the property that changing the sign of the three subscripts is the same as reversing the axis system like: $\chi^{(2)}_{ijk} = -\chi^{(2)}_{-i-j-k}$. To satisfy both of the above symmetry properties, $\chi^{(2)}_{ijk}$ must equal 0, and thus a SF response in a centrosymmetric environment is forbidden. Therefore, VSFS is a surface specific technique as the interface of two materials in non-centrosymmetric and results in non-zero tensor elements. VSFS involve 3 electric fields (visible, IR, and SF), thus $\chi^{(2)}$ is a 3x3x3 tensor with 27 elements. These elements are reduced through symmetry considerations to result in seven non-zero elements that contribute to a SF response. Only four of these elements are unique. These contributions physically represent different orientations of the vibrational mode dipoles relative to the interface and can be probed through a variety of polarization combinations. The possible polarization combinations and the respective $\chi^{(2)}_{ijk}$ element(s) that contribute to the spectrum are: *pss* ($\chi^{(2)}_{zyy}$), *sps* ($\chi^{(2)}_{yzy}$), *ssp* ($\chi^{(2)}_{yyz}$), and *ppp* ($\chi^{(2)}_{zzz}$, $\chi^{(2)}_{zxx}$, $\chi^{(2)}_{xzx}$, $\chi^{(2)}_{xxz}$), where the polarizations are listed in the order of SF, visible, and infrared. The resonant portion of the second-order susceptibility is dependent on both the net orientation and population of molecules at the interface (Equation 6).

$$\chi_R^{(2)} = \frac{N}{\varepsilon_0}\langle\beta_V\rangle \tag{6}$$

Where N is the number of molecules at the interface, ε_0 is the vacuum permittivity, and $\langle\beta_V\rangle$ is the average macroscopic hyperpolarizability which accounts for the orientation of molecules at the interface.

The $X^{(2)}$ has non-resonant and resonant terms which are accounted for in the fitting equation (7) as developed by Bain *et al.*

$$\left|X(\omega)^{(2)}\right|^2 = \left|X_{NR}^{(2)}e^{i\phi} + \sum_v \int_{-\infty}^{+\infty} \frac{A_v e^{i\phi v} e^{-\left(\frac{\omega_L-\omega_v}{\Gamma_v}\right)^2}}{\omega_L - \omega_{IR} + i\Gamma_L} d\omega_L\right|^2 \tag{7}$$

where the amplitude of the non-resonant susceptibility is described by $X_{NR}^{(2)}$ with a phase ϕ.[182] The summation of all vibrational transitions that are SFG active describes the resonant susceptibility, where A_v is the peak amplitude, ϕ is the phase, Γ_L is the Lorentzian linewidth describing homogenous broadening, and Γ_v is the Gaussian linewidth describing inhomogeneous broadening. Equation 5 is used to fit all experimental spectra.

A practical aspect of VSFSS is the ability to change the polarization of the incoming and collected beams to isolate vibrational responses from unique molecular orientations relative to the interface. A three-letter nomenclature denotes the polarization of the beams in the sum-frequency, visible, and IR beams, respectively (**Figure II.1C**). In this dissertation, *ssp*, *sps*, and *ppp* polarization schemes are used. The *ssp* polarization scheme probes IR transition moments perpendicular to the interface while the *sps* polarization probes IR transition moments aligned parallel to the interface. The *ppp* polarization combination probes a combination of transition moments in both the perpendicular and parallel contributions.

II.B. LASER SETUP

The VSFSS system used to collect the data presented in this dissertation is engineered as follows and in **Figure II.2**. A Ti:Sapphire regenerative amplifier laser (Coherent Libra) generates an 800 nm, ~80 fs fundamental pulses with a 1 kHz repetition rate. A portion of that beam is used as the visible pulse while the remaining is sent through an optical parametric amplifier (Coherent OPerA Solo) to generate a broadband infrared (IR) beam through difference frequency

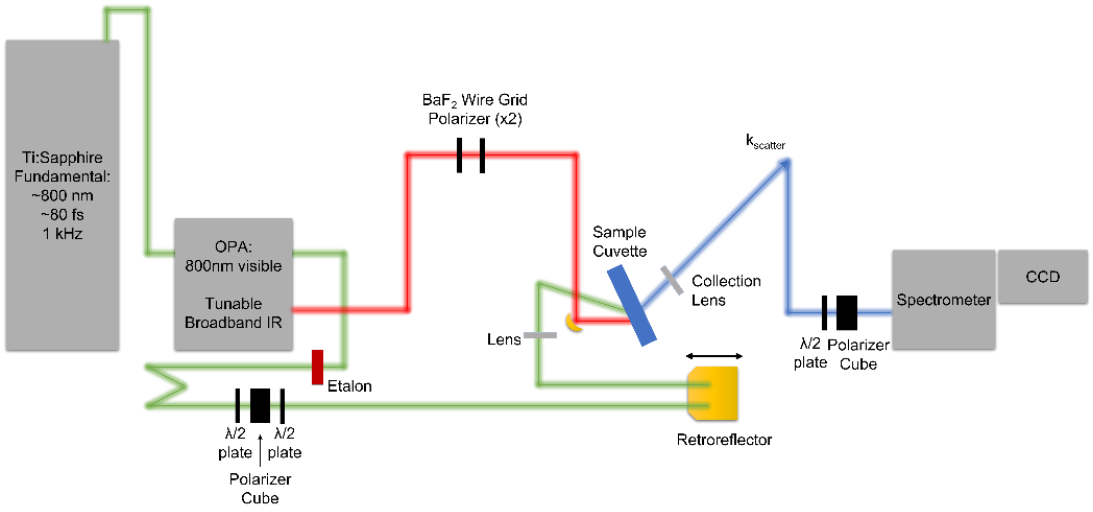

Figure II. 2 Schematic of the VSFSS experiment utilized in this dissertation with visible (green), IR (red), and SF (blue) beam paths. Mirrors are omitted for clarity.

generation. The visible and IR pulses are then directed along a series of mirrors, lenses, and polarizers to become spatially and temporally overlapped at the sample stage. The sample cell is composed of a CaF_2 window in the front and a quartz cuvette in the back (Helma QS) with an optical path length of 200 μm. The IR beam is focused at the sample to a spot size of ~80 μm with a parabolic gold mirror, while the visible beam is focused right after the sample cell to a ~500 μm spot size. The scattered SFG response is collected at an angle of ~60°, collimated with a plano-convex lens, and focused into a spectrograph and accompanying charge-coupled device intensifier (Princeton Instruments IsoPlane SCT320 and PI-MAX4). For all experiments, the visible pulse energy was 25 μJ while the IR pulse energies were 2-3 μJ and 5 μJ for the C=O and C-H stretching regions, respectively.

To account for daily fluctuations in laser power, a single trace in a figure is the result of at least 3 averaged trials across different days. One trial consists of 2 signal and 2 background measurements. Each trial is averaged, background subtracted, and normalized by a non-resonant response from $KNbO_3$ to account for changes in IR spectral shape. In the C-H region, spectra are further normalized by the integrated SFG intensity (from 2800-3000 cm^{-1}) generated from a d-hexadecane emulsion in D_2O stabilized with 1 mM AOT. Each trial is further normalized by the size of the droplet (determined by a monomodal distribution from DLS) through a scattering pattern developed by Roke *et. al.* that accounts for the percentage of scattered signal collected at 60° which is dependent on droplet size and beam polarizations.[183,184] More details on the

normalization procedure for VSFSS utilized in the Richmond/Scatena laboratory can be seen in a in **Appendix G**.[185] Additionally, a calculation of the particle concentration necessary to overcome the signal to noise threshold for VSFSS is provided in **Appendix H**.

The above procedure was used to collect all of the VSFS spectra presented in this dissertation and are not repeated in the experimental sections of each chapter for clarity. Chapter III begins the experimental section of this thesis by using VSFSS to study the surface structure of emulsions stabilized with a steric layer of polymer.

CHAPTER III: EMULSIONS STABILIZED BY POLY(ACRYLIC ACID)

This work was published in volume 697 of the journal *Colloids and Surfaces A: Physiochemical and Engineering Aspects* in June 2024. Ashley N. Mapile is credited with conceptualization, formal analysis, investigation, writing – original draft, writing – review and editing, and visualization. Lawrence F. Scatena assisted in conceptualization, writing – review and editing, supervision, and funding acquisition. Supplementary information for this chapter is provided in Appendix A

III.A. AN INTRODUCTION TO POLY(ACRYLIC ACID)

As explained in the introduction to this thesis, polyelectrolytes are useful analogues to studying protein coronas that are known to stabilize colloids due to the tunable nature of polymers. Many characteristics of polymers, such as the chain length (via molecular weight), chemical functionality, % protonation, and morphology can all be adjusted synthetically or by environmental conditions. Poly(acrylic acid) (PAA, **Figure III.1)** is a simple polyelectrolyte that can mimic protein behavior at interfaces. PAA, which contains a single carboxylic acid repeating group, can expand in solution when deprotonated or hydrogen bond with itself to form coils when protonated and is a useful material in forming zwitterionic polymer coarcervates.[186–190] Through pH-dependent zeta potential measurements (**Appendix A, Figure A1**) the interfacial pK_a of PAA at the hexadecane/water emulsion interface was determined to be ~5.3, about 0.8 units more alkaline

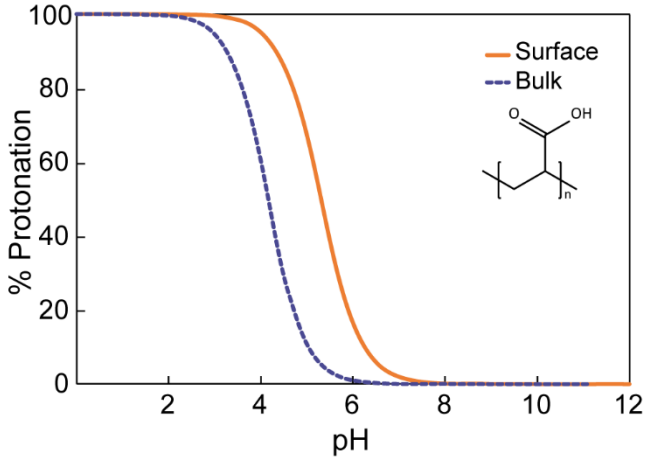

Figure III. 1 Chemical structure of poly(acrylic acid) and percent protonation curve as a function of pH for surface (solid, orange line) and bulk (dotted, purple line). Percent protonation was calculated with the Henderson-Hasselbalch equation, the known bulk pKa (4.5), and the experimentally derived interfacial pK_a (5.3).

than the bulk pK_a (**Figure III.1**). Therefore, studying the pH-dependent conformational behavior of PAA adsorbed at the emulsion interface can provide insight into droplets stabilized by pH-sensitive protein coronas as well as a detailed understanding of the mechanisms of colloidal stability.

The adsorption behavior of PAA without the addition of a surfactant, has been studied at both the planar CCl_4/water and air/water interfaces using vibrational sum frequency spectroscopy (VSFS). These studies found that in conditions above the pK_a (pH >4.5), the polymer is interfacially inactive, but the addition of charge-screening cations promotes adsorption of the polymer to the interface.[105,191–194] Below pH 4.5, the polymer is interfacially active and exhibits a well-ordered structure as evident by strong CH and C=O VSFS spectral features. At a planar interface, molecular dynamics are thermodynamically determined by equilibrium surface activity and surface-active molecules develop a stable configuration given time. On the other hand, emulsions require the input of external energy to form droplets resulting in a kinetically trapped interface.[98,101] During the formation of emulsions, surface-active molecules initially adsorb to the interface via ultrasonication but subsequently adsorb/desorb through equilibrium thermodynamics after formation of the curved interface. Thus, the conformational ordering of interfacial molecules adsorbed to emulsions is dictated by the thermodynamic equilibrium of molecular adsorption and the kinetic energy encouraging the platform of these colloids to destabilize and coalesce. Stabilization of emulsions is best described by the theory developed by Derjaguin, Landau, Verwey, and Overbeek (DLVO) which states that both electrostatic and steric repulsion prevents droplet coalescence and keeps the emulsions in a kinetically trapped state.[8,98,101,195] Reports of emulsions coated with solid polymer particles (such as Pickering emulsions),[196] nanoparticles with a polymeric coating,[197] and emulsions formed with surfactant/polymer mixtures[198] suggest unique behavior at curved hydrophobic interfaces as opposed to their planar counterparts. While there have been reports of emulsions stabilized with polymer alone, observed through Janus particles[199] or magnetic nanoemulsions,[200] and specifically emulsions coated with diblock copolymers,[201,202] they lack insight into the detailed mechanism of stability promoted by polymers or the molecular level information to provide a structural understanding of the droplet interface.

Here, we demonstrate the stability of emulsions coated with PAA and provide a picture of polymer molecular conformation with the surface-specific vibrational sum frequency scattering spectroscopy (VSFSS). Despite the lack of surface charge thought to be necessary for droplet

stabilization, PAA-coated emulsions prepared at pH 2 are stable and exhibit interfacial polymer ordering. Surprisingly, the highly charged pH 6 polymer does not stabilize emulsions and exhibits no molecular organization. With the addition of salt, we observe charge screening at the interface and a disruption to polymer ordering because of localized electrostatics. We propose that emulsions are stabilized through the steric hindrance of an adsorbed PAA layer, whose molecular conformation and charge-dependent behavior can provide insight to protein corona-stabilized droplets and their application as drug delivery vehicles.

III.B. MATERIALS AND METHODS

III.B.1. Materials

All materials were used as delivered without further purification. Hexadecane (≥99%), dioctyl sodium sulfosuccinate (AOT, ≥97%), poly(acrylic acid) (PAA, average M_v ~ 450,000), calcium chloride ($CaCl_2$, anhydrous, ≥97%), magnesium chloride ($MgCl_2$, anhydrous, ≥98%), sodium chloride (NaCl, BioXtra, ≥99.5%), and ammonium chloride (NH_4Cl, ACS reagent, ≥99.5%) were purchased from Sigma-Adrich. Deuterated hexadecane (n-hexadecane-d_{34}, 98.6% D), sodium deuteroxide (NaOD, 99.5% D), and deuterium chloride (DCl, 99.8% D) were purchased from CDN Isotopes. Deuterium oxide (D_2O, 99.9% D) was purchased from Cambridge Isotope Labs. All glassware was copiously cleaned in a bath containing sulfuric acid (98% Sigma-Aldrich) and AlNOCHROMIX oxidizer from Godax Laboratories Inc. After sitting in the acid bath for at least 24 hours, glassware was rinsed for at least 2 min. with 18.2 MΩ-cm water and dried in an oven.

III.B.2. Emulsion Formation

Emulsions consisting of hexadecane (or d-hexadecane) suspended in water (or D_2O) were prepared by ultrasonication (Branson Sonifier 250) of the sample at 5% output power (~12.5%) at 20 kHz for 5 minutes at a constant duty cycle. The ultrasonication probe tip was placed at the interface of the aqueous solution and oil layer to ensure homogenous mixing. The AOT-coated emulsion standard was formed by ultrasonicating AOT stock solution with oil to give a 1mM AOT emulsion with 2.5% v/v oil in water. PAA-stabilized emulsions were formed in the same fashion with DCl or NaOD added to reach the desired pD (pH). Emulsion pH was measured using MilliporeSigma MColorpHast pH strips and an Oakton Instruments Portable Meter Kit. The detection of pH values can differ from pD values by 0.43,[203] however for ease of communication, pH is used in this paper.

III.B.3. Dynamic Light Scattering and Zeta Potential

Emulsion hydrodynamic diameter (Z-average), polydispersity index (PDI), and zeta potential were measured by a Malvern Zetasizer Nano ZS. Details regarding the theory and practice of dynamic light scattering (DLS) and zeta potential can be found elsewhere.[204,205] From DLS measurements, hydrodynamic diameter and PDI was reported from an average of at least three measurements. DLS and zeta potential measurements were collected by pipetting 1 mL of emulsion solution into a Malvern folded capillary zeta cell, therefore maintaining consistent v/v oil concentrations. Zeta potential values were reported from an average of at least five measurements. Determination of the surface pK_a using zeta potential measurements is detailed in the supporting information (Figure S1) and follows a procedure developed by Haes *et. al.*[206]

III.C. RESULTS AND DISCUSSION

III.C.1. Impact of PAA Concentration

Emulsions were formed with concentrations of PAA ranging from 1 ppm to 4000 ppm in the natural pH conditions of PAA (pH 4) and measured by dynamic light scattering and zeta potential (**Figure III.2**). For context, previous experiments at the CCl_4/water interface used 5 ppm PAA while air/water interface experiments used 4500 ppm.[105,191] **Figure A2** and **Table A1** demonstrate that emulsions prepared at or below 250 ppm PAA were unstable after 1 week (**Appendix A**). Bare emulsions (those without deliberately added surface active agents) are known to have a negative zeta potential due to miniscule amounts of surface active contaminants.[180,207] The zeta potential of our hexadecane/water emulsions (-32 mV) suggest minor surface active impurities. The presence

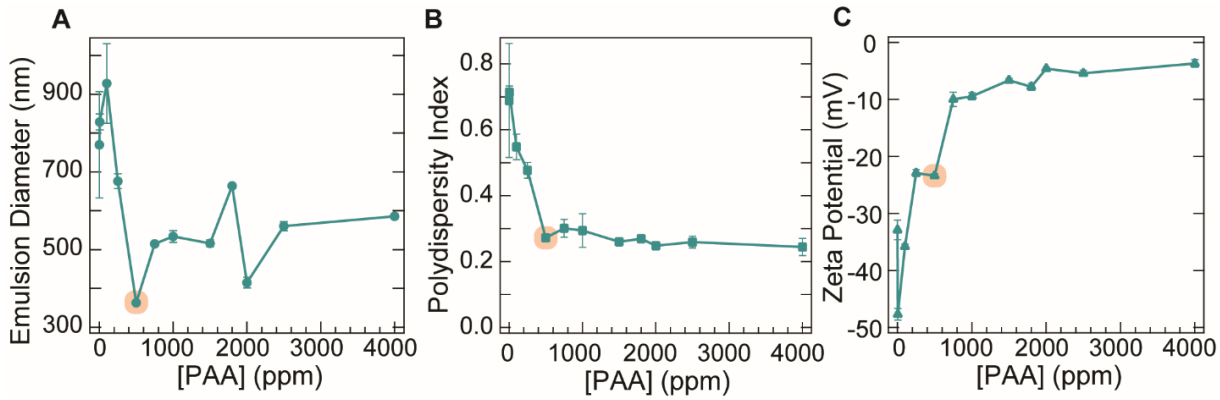

Figure III. 2 Characteristics A) hydrodynamic diameter, B) polydispersity index, and C) zeta potential) of emulsions coated with varying amounts of PAA at pH 4. Points shaded orange indicate 500 ppm PAA.

of these impurities were identified in previous emulsion studies from our laboratory that employed meticulous and extensive cleaning procedures to minimize their presence.[180] After PAA addition, the polymer is much more surface active than the impurities and displaces any contaminants that contributed to the negative surface charge. As additional PAA is added, charge screening and hydrogen bonding causes a reduction in the magnitude of the zeta potential.

At a concentration of 500 ppm, PAA-stabilized emulsions exhibit good colloidal stability, moderately polydisperse size distributions, and a highly charged surface layer as indicated by the orange shaded points in **Figure III.2**. Additionally, as confirmed by pendant drop surface tensiometery, discussed in **Appendix A** and **Figure A3**, PAA adsorbs to the hexadecane/water interface at a concentration of 500 ppm. Emulsions formed using 250 ppm PAA and below resulted in unstable droplets presumably due to a lack of surface population. Despite a remarkably high magnitude zeta potential (≥30 mV) emulsions stabilized with 100 ppm PAA or below are unstable and crash out quickly after formation, likely due to a thin or completely absent polymer layer. While the addition of PAA at concentrations above 500 ppm leads to more stable emulsions, as indicated by the long-term stability, significant charge screening occurs making them difficult targets for measuring the interplay between electrostatics and steric repulsion when salt ions are added. The slight increase in emulsion size and reduction in zeta potential with increasing concentration of PAA is due to polymer layering at the surface which extends the hydrodynamic diameter and charge screens the surface as is consistent with other polymer-layering studies.[16,201,208,209] Emulsions stabilized with 1500 ppm PAA or higher have a low zeta potential (~-7 mV) and are colloidally stable up to a week, solidifying the observation that sterics alone are enough to stabilize emulsions. Due to the desire to study the impact of surface charge screening, the emulsions used in this paper are formed with 500 ppm PAA as they have long-term colloidal stability, are moderately polydisperse and have appreciable interfacial charge.

III.C.2. Emulsions Stabilized by PAA Alone

Emulsions coated with 500 ppm PAA were formed at pH 2, pH 4, and pH 6 via ultrasonication of 2.5% v/v hexadecane in water. Pendant drop surface tensiometery measurements indicate that high amounts of PAA adsorb to the hexadecane/water interface at pH 2 and pH 4 while little adsorption is observed at pH 6 (**Figure A4**). Emulsions at pH 2 and pH 4 maintained colloidal stability after one week, as evident by their visual turbidity, while pH 6 oil droplets phase separated (**Figure**

A4). Dynamic light scattering of pH 2, pH 4, and pH 6 colloids measured 20 minutes after formation revealed hydrodynamic diameters of 477.7, 363.2, and 761.0 nm, respectively, demonstrating that the average size of emulsions prepared at pH 2 and 4 are in the nanosized regime while pH 6 emulsions are inherently larger. Narrow, monodisperse colloids have a PDI < 0.1, while polydisperse systems have a PDI > 0.1.[210] Moderate polydispersity is defined by a PDI from 0.1-0.4 and describes the pH 2 and pH 4 emulsions studied `here (PDIs of 0.247 and 0.272, respectively), while the pH 6 emulsions have broad polydispersity (PDI of 0.628). Similarly, size distribution plots from DLS measurements are monomodal for emulsions at pH 2 and pH 4, but multimodal for pH 6 (**Figure A5**). Table S2 lists the PDI of each emulsions system studied by VSFSS which are in line with recent studies on emulsion formulations.[201,211–213] To be acceptable for drug delivery applications, monodisperse colloids are defined to have a PDI < 0.3 while polydisperse systems have a PDI > 0.3, however stricter criterion of monodispersity may require a PDI < 0.1.[98,214,215] The zeta potential of pH 2 emulsions was measured to be only -3.08 mV, while at pH 4 zeta potential measurements reveal a charge of -23.4 mV. At only 16.7% protonation of PAA at pH 6 (**Figure III.1**), oil droplets have a significantly charged interface with a zeta potential -45.0 mV. Doping-in acid or base to an emulsion initially prepared at the natural conditions (pH 4) has little impact on the resulting size, PDI, or zeta potential of pH 2 or pH 4 droplets (Figure S6) suggesting that emulsion stability is pH reversible and dependent on polymer adsorption.

The long-term stability of emulsions prepared at pH 2 is remarkable considering that polymers *and* surfactants/salt or post-functionalized emulsions are typically required to stabilize emulsion oil droplets due to the necessity of interfacial charge.[216–218] For example, reports of low-charge emulsions such as those coated by the surfactant sodium decanoate in acidic conditions, have a zeta potential of about -5 mV and destabilize within one hour.[106] The appreciable change in zeta potential can be attributed to the ~5% of deprotonation difference between PAA at pH 2 (~99.9% protonated) and pH 4 (~95.2% protonated). The instability of the pH 6 oil droplets is surprising considering that the degree of zeta potential for these droplets is similar to that experienced by hexadecane-in-water emulsions stabilized with 10 mM sodium decanoate where the zeta potential is about -50 mV.[106] Due to this strong electrostatic repulsion, decanoate-stabilized emulsions can be stable upwards of months with slight Ostwald ripening. The stability of this PAA-coated emulsion system contradicts what is displayed by surfactant-stabilized

emulsions, thus, we examine this system with VSFSS to gain a molecular-level understanding of the polymer conformation at the emulsion interface that gives rise to this unique colloid stability.

VSFSS spectra of the colloids coated with PAA in pH 2, pH 4, and pH 6 conditions were measured in the C-H stretching region (2800-3000 cm^{-1}). Two major peaks were observed at pH 2 and pH 4 while no signal was measured for pH 6 (**Figure III.3**). In accordance with previous heterodyne-detected SFG experiments at the planar air/water interface, as well as complementary bulk IR and Raman spectroscopies, the broad feature at 2877 cm^{-1} is assigned to the methine (CH) stretch and the feature at 2929 cm^{-1} is assigned to the methylene (CH_2) symmetric stretch.[105,219] The higher frequency feature also contains contributions from the methylene asymmetric overtone and Fermi Resonance.[105] The broad full width at half maximum present in the methine stretch at pH 4 (53 cm^{-1} and 16 cm^{-1} for the methine and methylene stretch, respectively) can be attributed to different solvation environments for the CH mode that is tethered to the carbonyl group.[220] At pH 4, methylene modes presumably lie strictly in the oil phase while the carbonyl groups pull the methine modes further away from the interface, comparable to what was observed to

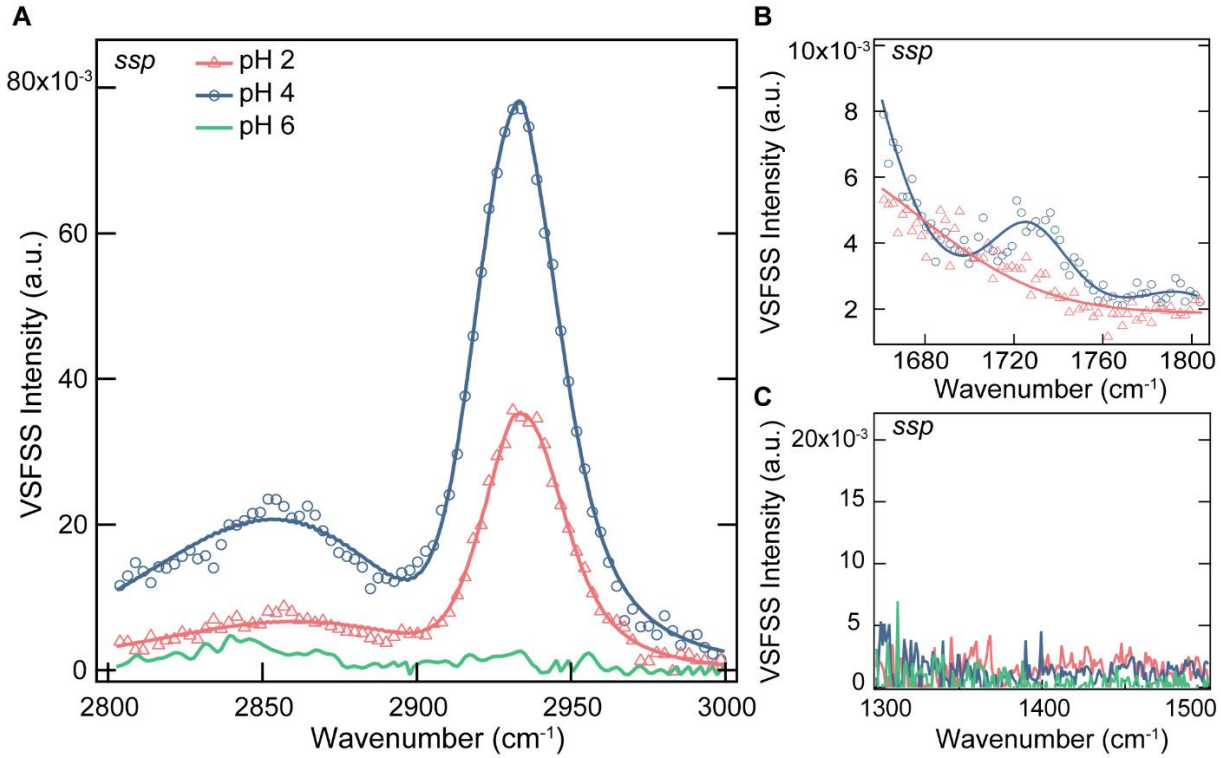

Figure III. 3 VSFSS measurements (ssp polarization) of d-hexadecane oil droplets in D2O stabilized with 500 ppm PAA at varying pH conditions in the A) C-H stretching region, B) carbonyl (C=O) stretching region, and C) the carboxylate (COO-) symmetric stretching region. Solid lines represent fits of the data.

poly(methacrylic) acid at the planar CCl_4/water interface.[221] The variety of oil- and water-solvated environments of the methine results in the peak broadening. At pH 2, the methine feature is nearly absent. SFG experiments with hydrolyzed polyacrylamide (HPAM) and detailed Fourier-transform IR spectra of PAA show an increase in the CH_2 intensity while the CH feature broadens and decreases in intensity with increasing amount of polymer due to a higher population of methine modes being solvated in the water phase.[219,220] For PAA, as more polymer saturates the interface from pH 4 to pH 2, as indicated by the increase in surface pressure (**Figure A3**), it is likely that some of the methine CH modes are solvated in the oil while others are solvated in the water.

At pH 4, the presence of two distinct and high intensity CH modes (**Figure III.3A)** suggests that the polymer adopts a conformation at the interface with a well-ordered backbone. At pH 2 the methine stretch is nearly absent and the methylene stretch is reduced, suggesting a less ordered conformation of PAA as compared to pH 4. These differences in signal intensity can be explained as the result of slight differences in polymer organization and protonation. At pH 2, PAA is ~99.9% protonated at the interface while at pH 4 PAA is ~95.2% protonated (**Figure III.1**). While the ~5% difference in protonation might seem insignificant, it has been observed that uncharged polyelectrolytes in bulk aqueous environments develop a random coil conformation.[186] This coiling is promoted by acidic conditions where intramolecular H-bonding between carboxylic acid moieties is most favorable. Extending this behavior to the interface, where the interfacial pK_a of 5.3 (as compared to the bulk pK_a of 4.5) promotes the formation of acidic polymer, the decrease in polymer backbone signal moving to acidic conditions is attributed to random coiling of polymer and forming intramolecular hydrogen bonds at the interface.[105] At pH 2, decreasing the persistence length of the polymer through coiling is thermodynamically favorable and akin to protein folding, in which the hydrophobic moieties favor intramolecular hydrogen bonding as opposed to aqueous solvation. In contrast, oil droplets prepared at pH 6 have PAA molecules that are ~16.7% protonated. It has been observed in bulk aqueous solutions that as ionization of a carboxylic acid polymers increases, the persistence length increases.[188,222] In a similar fashion to a protein unfolding, uncoiling of the highly charged polymer allows for charge solvation within the aqueous phase. While our experiments cannot conclusively determine the location of PAA at pH 6, we hypothesize that the polymer is either located near the interface (within the boundaries of a solvation shell) or at the interface in a low or disordered population. While the lack of signal observed for PAA at pH 6 could be attributed to the extended polymer solvated in the aqueous

phase, as in previous SF experiments of PAA at the planar CCl_4/water interface, the surface pressure and high magnitude negative zeta potential measurements suggests that PAA is near the oil droplet surface. Therefore, we will assume that at pH 6 PAA has minimal ordered surface population resulting in the absence of VSFSS signal.

The pendant groups of PAA were also measured by VSFSS in the C=O stretching region (**Figure III.3B**) to determine the orientation of the pH-sensitive functional groups at pH 2 and pH 4. Experimentally, a large non-resonant background is experienced in the C=O region, likely due to the CaF_2 window.[106,129] De-timing of the visible beam is used to reduce the non-resonant response, however, weak C=O signals also reduce in intensity and result in noisy spectra in this region. A small feature is seen in the C=O region for pH 4 at 1735 cm^{-1} assigned to the C=O stretching mode on the polymer pendant group consistent with VSFS experiments of PAA at the CCl_4/water interface.[193] Data from PAA-coated oil droplets at pH 6 is omitted from this graph for clarity, as the signal resembled the non-resonant background exhibited at pH 2. The absence of a C=O vibrational mode at pH 2 and pH 6 indicates that the functional groups are disordered. At pH 2, a slightly disordered backbone (compared to pH 4) results in a disordered pendant group exhibiting no measurable VSFSS signal. While at pH 4, the highly ordered backbone contributes to minor organization of the carbonyl. In addition to disorder, the lack of signal could be attributed to low surface population as described above. To confirm the presence of a C=O vibrational mode at pH 4, emulsions stabilized with 1000 ppm PAA were measured in the C=O stretching region (**Figure A7**). A strong feature with good signal to noise with 1000 ppm PAA was measured at the same frequency as the emulsions measured with 500 ppm PAA. These results suggest that the C=O group of PAA at 500 ppm concentration at pH 4 are ordered but lack the interfacial population necessary to elucidate a strong SFG response.

VSFSS measurements in the COO- stretching region were made to determine if the deprotonated functional group is ordered (**Figure III.3C**). However, no signal was observed in the carboxylate stretching region for any pH conditions. For pH 2 and pH 4, the percent protonation at the interface indicates that the carboxylic acid group is dominating the surface population. Thus, any carboxylate groups, if present, are in too little in population to be visible by VSFSS and/or not well ordered. At pH 6, although the polymer is significantly deprotonated and COO- groups are present (~16.7% protonation), the polymer is predominately solvated in the water phase as suggested by low surface pressure (<10 mN/m) measured by pendant drop surface tensiometery

data (**Figure A4**). Therefore, there will be no carboxylate organization at the interface, consistent with the conclusions suggested above by surface tension and VSFSS C-H region data and with VSFS experiments at the CCl_4/water planar interface.[193]

The adsorption of PAA to the hexadecane/water interface can also be rationalized by the hydrophilic-lipophilic balance (HLB), a metric commonly used for surfactants to describe their relative oil or water solubility. Surfactants with a lower HLB value (closer to 0) have better oil solubility while surfactants with a higher HLB value (closer to 20) exhibit better water solubility. Generally, oil in water emulsifiers have an HLB between 8 and 16. Using the methods proposed by Davies,[223] we calculated HLB values for PAA at pH 2, 4, and 6 using our experimentally derived % protonation values (**Eq. A2**, **Appendix A**). We found that at pH 2 and 4, PAA has an HLB or 8.17 and 8.97, respectively, indicating that the polymer is fairly oil-soluble and acts as a good oil-in-water emulsifier. However, the HLB value for PAA at pH 6 is 22.3 suggesting that the polymer does not have sufficient surfactant characteristics and prefers to be solubilized in water, consistent with our spectroscopic analysis.

From these results exploring PAA at the emulsion interface at pH conditions with low deprotonation (<5%), it appears that sterics play a significant role in dictating the colloidal stability of these emulsions as the electrostatic repulsion and consequential colloidal stability experienced in this system is not what would be predicted by DLVO theory. Emulsions prepared at pH 2, despite having almost zero surface charge are colloidally stable, while pH 6 oil droplets have a high surface charge but are unstable. At pH 4, the natural pH of the system, the polymer is largely protonated (~95%), has high surface pressure, and was a well-ordered chain at the interface. Presumably, the CH backbone is aligned into the oil phase while the carboxylic acid groups are slightly aligned in the water phase. With the addition of acid (~99% protonation at pH 2), PAA is still present at the interface in high population but experiences less chain organization as compared to pH 4 due to intramolecular hydrogen bonding between acid groups and subsequent coiling of the polymer. On the other hand, at pH 6 (~17% protonated) the polymer is not ordered at the interface and a higher population of the polymer prefers to be solvated in the water phase as an extended, charged chain. **Figure III.6** summarizes the molecular picture of PAA-coated oil droplets.

III.C.3. Addition of Salt to PAA-stabilized Emulsions

In an effort to charge screen PAA and promote interfacial activity, in particular for pH 6, the impact of chloride salts on emulsion stability was studied. Upon the addition of chloride-based cations, the size, PDI, and zeta-potential of PAA-stabilized emulsions were measured (**Figure III.4**). Concentrations of salt ranged from 0-2 mM for the divalent cations (Ca^{2+} and Mg^{2+}) and 0-6 mM for the monovalent cations (Na^{+} and NH_4^{+}) to keep the ionic strength of the solution consistent

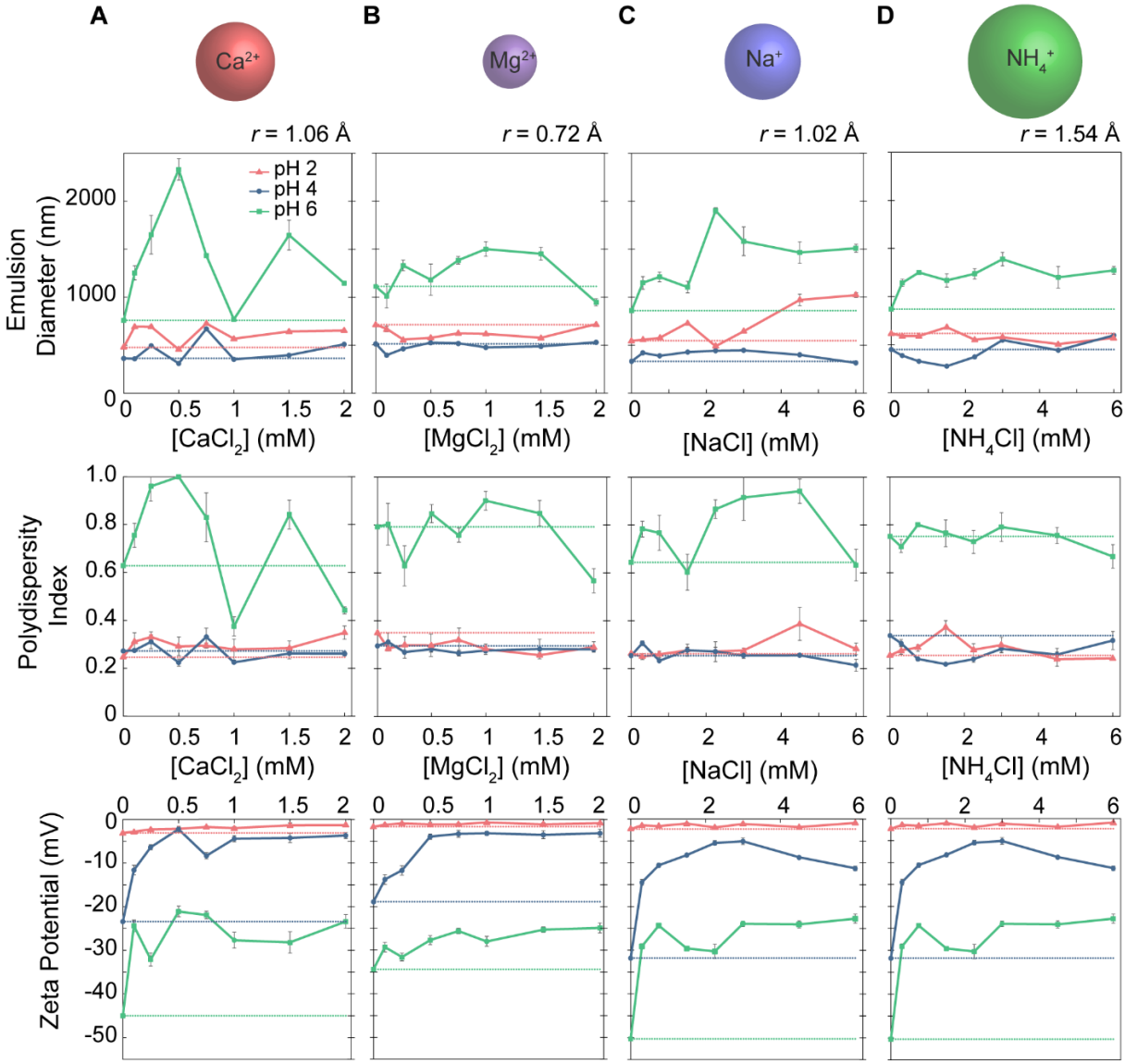

Figure III. 4 Characteristics (top panel: hydrodynamic diameter, middle panel: polydispersity index (PDI), bottom panel: zeta potential) of d-hexadecane oil droplets in D2O stabilized with 500 ppm PAA at varying pH conditions with the addition of A) CaCl2, B) MgCl2, C) NaCl, and D) NH_4Cl. Ionic radii and scaled cation sizes are provided at the top. Dotted colored lines are a guide to the eye for emulsions made without salt.

between varying cations. In general, the addition of salt causes minor changes to the size or PDI of the emulsion. To ensure consistent normalization of the scattered light generated and collected from VSFSS experiments, colloid radius must be within 100-900 nm.[224] At pH 2 and pH 4, emulsions generally stayed within this size regime except for the addition of NaCl at high concentrations at pH 2 which could be attributed to PAA crowding at the interface. At pH 2 and pH 4, PDI exhibits no trend with the addition of salt. The negligible change in size or PDI of the emulsions at pH 2 and pH 4 with the addition of salt suggests that no additional polymer layers are absorbed to the surface. At pH 6, size and PDI change drastically but without any clear trend. The wide range in these values are attributed to unstable emulsions that contain little, if any, polymer at the interface, and do not favorably stabilize the oil droplets. These results suggest that the salt ions do not bring pH 6 polymer to the surface as observed at the planar interface, which could be attributed to the different chemical nature of the interfaces and solubility of CCl_4.[193] In all pH conditions the addition of salt causes a reduction in the magnitude of the zeta potential. This is most noticeable at pH 4 and pH 6 where charge screening reduces the zeta potential by almost 20 mV with the addition of only 0.3 mM ionic strength salt. Significant charge screening occurs for ionic strengths up to ~1.5 mM before the zeta potential plateaus with the addition of salt up to 6 mM ionic strength. Despite the addition of salt and subsequent charge screening, the pH 6 oil droplets are never stabilized, as evident by the large diameter and high PDI. This suggests that at pH 6, even with charge screening at the interface promoting the zeta potential akin to stable pH 4 emulsions (<30 mV), the polymer would rather be solvated in the water phase than oriented at the interface.

To better understand how the presence of salt impacts polymer conformation and promotes charge screening VSFSS studies were conducted on PAA-coated colloids with the addition of the various salts. An ionic strength of 2 mM was chosen for all VSFSS salt studies because emulsions stabilized with $CaCl_2$ at 2 mM ionic strength (1 mM $CaCl_2$) exhibited the most stable size and PDI at pH 6 and because charge screening plateaus by 2 mM ionic strength. Upon the addition of 2 mM ionic strength salt, the VSFSS intensity of PAA in the CH stretching region decreases at pH 4 to a signal intensity on the same scale as emulsions at pH 2 (**Figure III.5A-B**). At pH 2, adding NaCl and NH_4Cl promotes a slight change in the overall intensity, while at pH 6, no spectral features are observed with added salt (**Figure III.5C**) A small population of PAA does adsorb to the interface at pH 6 with the addition of salt, as observed through interfacial pressure data (**Figure**

A3) suggesting that salt decreases the hydrophilic character of the carboxylic acid group therefore reducing the HLB (**Appendix A**) and promoting surface adsorption. However, as seen spectroscopically, the addition of salt does not cause ordering of the polymer chain at the interface. The VSFSS response of the carbonyl group was also measured with the addition of 2 mM ionic strength salt and no increase in signal was observed (**Figure A8**). Peak position shifts are potentially present in the C=O spectra, however the signal to noise is so low in this region that no conclusions can be made with confidence.

In general, adding salt changes the structure of the polymer at pH 4 more drastically than at pH 2 as more of the polymer is deprotonated at pH 4 and thus there are more carboxylate sites for the cations to bind. The binding of the cation to carboxylate sites disrupts polymer organization at the surface as the polymer likely needs to readjust and coil at the confined emulsion interface to

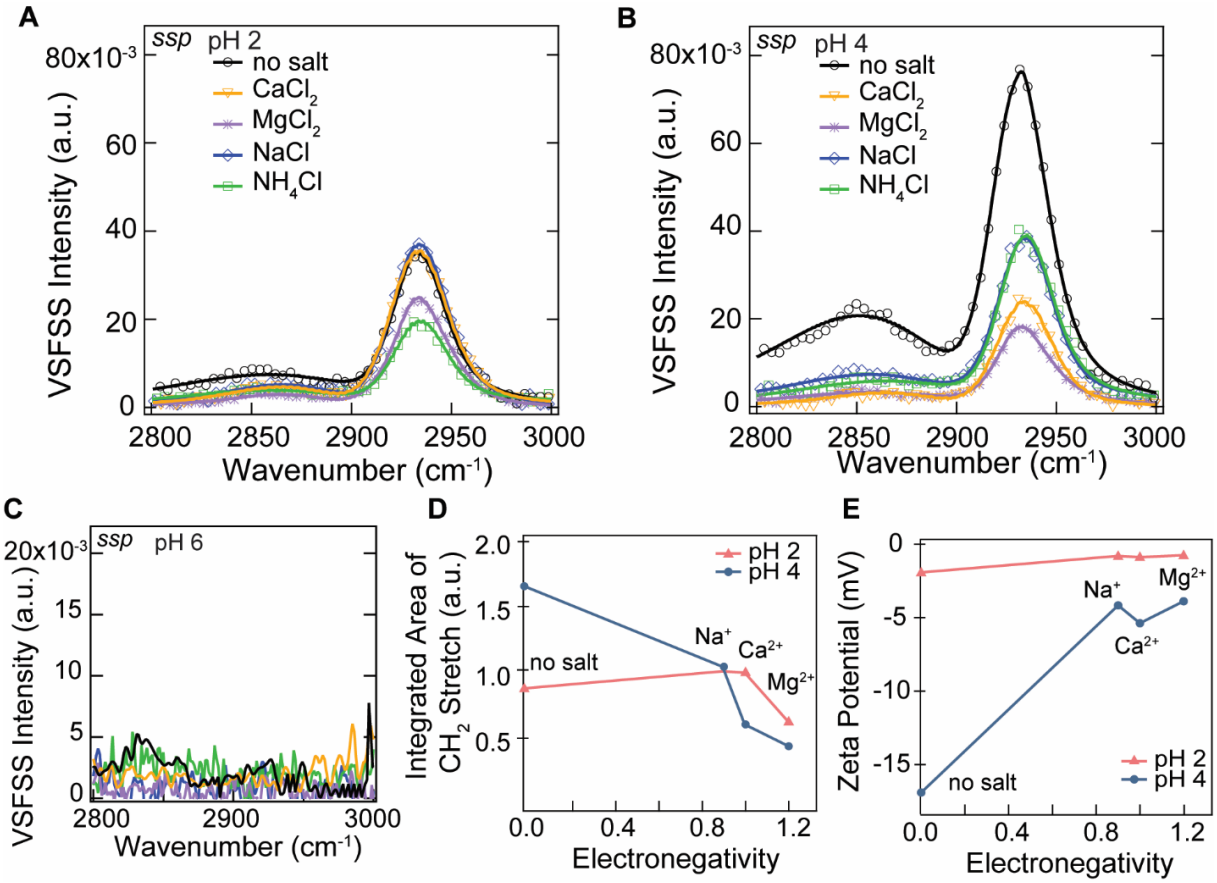

Figure III. 5 VSFSS (ssp polarization) of d-hexadecane oil droplets in D2O stabilized with 500 ppm PAA and 2 mM ionic strength salt at A) pH 2, B) pH 4, and C) pH 6. Solid lines represent fits of the data. Electronegativity of cations defined by the Pauling scale are compared to D) the integrated area of the CH_2 stretch and E) zeta potential.

create cationic bridging between acid groups.[220] As best exemplified in the pH 4 condition, the addition of salt promotes the polymer to develop a more random coil backbone conformation, that mimics that of the natural pH 2 polymer, resulting in a decrease in the VSFSS signal with the addition of salt. The impact of chloride counterion at the surface can be neglected due to the inherent negative zeta potential of PAA-stabilized emulsions without salt. With the addition of chloride salts, the surface charge is reduced in magnitude suggesting that the cations are more attracted to the negatively charged interface than the anions which are assumed to be solvated in the water phase.

A quantitative look at the VSFSS spectral changes with addition of salt shows that as the electronegativity of the cation increases, as determined by the Pauling scale, we see a corresponding decrease in CH_2 integrated area and zeta potential magnitude (**Figure III.5D-E**) The CH_2 area was calculated by integrating the area from the full width half max of a Gaussian fit of the CH_2 feature centered around 2930 cm^{-1}. As NH_4^+ is a molecular ion and does not have electronegativity, it is excluded from this trend. The decreasing CH_2 intensity with increasing electronegativity is present regardless of pH but is clearer at pH 4 due to the higher number of carboxylic acid groups available to interact with the cations. As the electronegativity of the cation increases, it has an increased ability to pull the electron density away from the carboxylic acid groups on the polymer and promote solvation in the water phase. Cations with a higher electronegativity promote polymer coiling, as demonstrated by the decrease in CH signal intensity and effectively charge screening the zeta potential. This results in a disruption of the CH backbone conformation and a decrease in the polymer persistence length at pH 4 (**Figure III.6**). Slight change in the polymer structure is observed at pH 2 due to the minimal population of carboxylate groups that can interact with the cation (**Figure III.6**).

The absence of signal from PAA with salt at pH 6 are in contrast with observations at the planar oil/water interface where the addition of salt increased the C=O signal and had negligible impact on the CH stretching modes. At a planar interface, the dynamics of adsorbed molecules are dominated by the thermodynamics of positive enthalpic interactions while slightly limited by kinetic diffusion through the medium. Thus, over time, a polymer at the planar oil/water interface can stretch and extend to adopt a thermodynamically favorable state that allows for stabilizing complexation with metal cations. Despite the significant charge screening exhibited at pH 6, the absence of VSFSS signal suggests that PAA is not complexing with ions at the oil droplet interface.

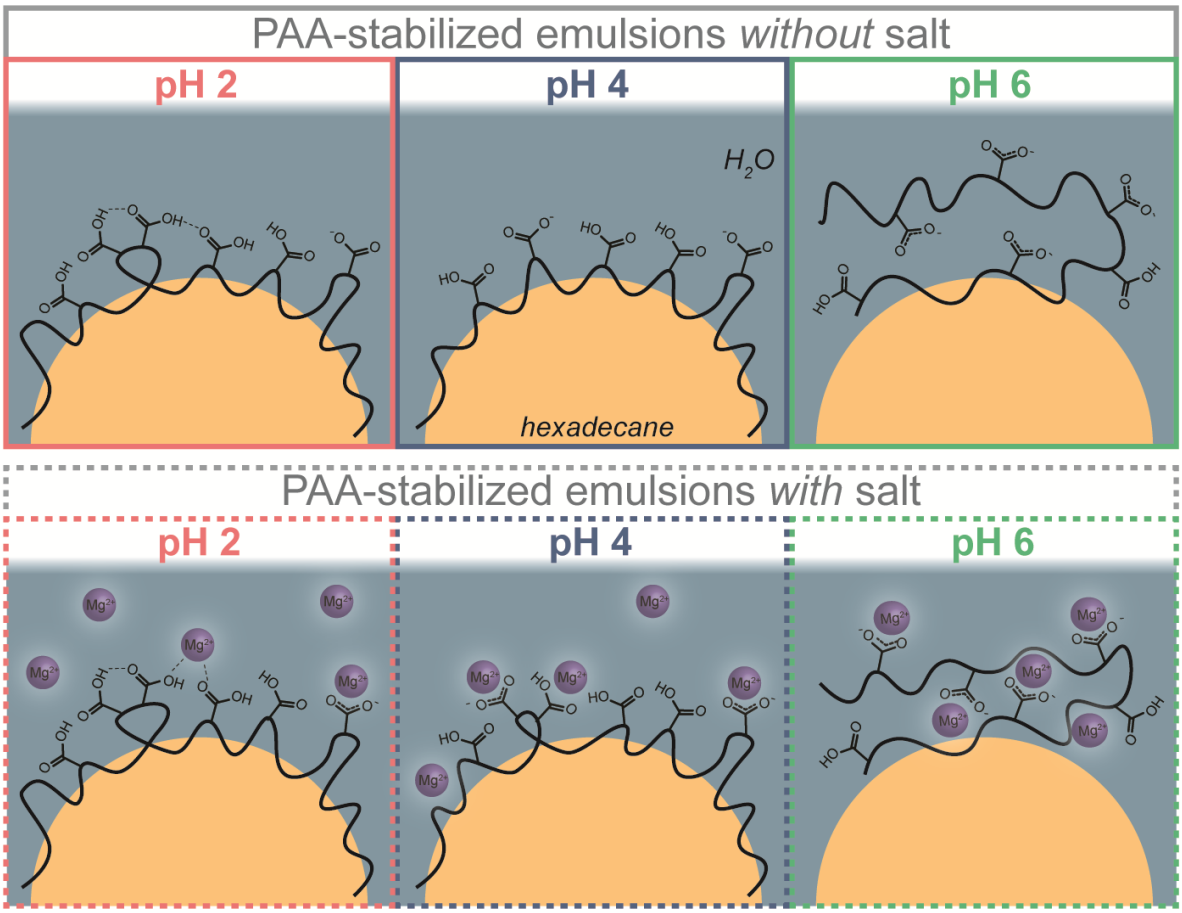

Figure III. 6 Illustration depicting the behavior of PAA at the hexadecane/water droplet interface in varying pH conditions without (above) and with (below) the presence of salt, the example of MgCl2 shown here. Chloride anions have been omitted for clarity and are solvated in the water phase.

Independent of pH or salt addition, in the kinetically trapped emulsion system, the adsorbed PAA layer will adopt a thermodynamically stable orientation that is different from that at the planar interface due to the competing kinetic energy driving oil droplets to coalescence. To carefully consider molecular adsorption at interfaces, we cannot neglect how the factors that contribute to colloidal stability, namely sterics and charge, impact the conformation of the surface-active species. The competition between polymer adsorption and droplet coalescence has implications on molecular structure when variables such as pH and ionic strength are varied. For PAA at pH 6 at the oil/water droplet interface, the energy released from droplet aggregation overcomes the slight polymer adsorption that is present with the addition of cations and the polymer remains solvated in the aqueous phase (**Figure III.6**), while at pH 2 and pH 4 PAA can stabilize emulsions through sterics alone due to the adsorption of the highly surface-active protonated polymer.

III.D. CONCLUSIONS

The interface-specific vibrational spectroscopy employed here along with complementary emulsion characteristic measurements provides a molecular-level picture of PAA at the hexadecane/water emulsion interface, which has previously been explored only at planar interfaces. VSFSS spectra in the CH stretching region suggest an ordered PAA backbone at pH 2 and pH 4 (**Figure III.6**), while at pH 6, the polymer prefers to be solvated in the aqueous phase with minimal, disordered chain adsorption. With the addition of salt, no PAA adsorption was observed at pH 6 which contrasts with findings at the planar CCl_4/water interface where salt addition promotes polymer adsorption. While the addition of salt causes charge screening at the hexadecane/water emulsion interface, the pH 6 polymer does not become more interfacially ordered resulting in a unstable colloid. At pH 2, the influence of cations has minimal impact on the conformation of PAA due to the low % protonation, however, at pH 4, the addition of salt causes a decrease in persistence length and increase in polymer coiling, resulting in an ordered backbone that mimics the conformational structure of the pH 2 polymer. While there have been previous reports of sterically-stabilized emulsions, our results provide a molecular level understanding of the stability mechanism.

Due to the kinetically trapped state of emulsions as compared to the thermodynamically stable planar interface, polymer conformation and colloidal stability are closely intertwined. While classical DLVO theory suggests that a large surface charge is necessary to stabilize colloids, these results show that a surface active, steric layer is enough to maintain emulsion stability for upwards of 1 week at pH 2 and pH 4, while too much charge on the polyelectrolyte (at pH 6) causes unstable oil droplets with polymers solvated in the bulk phase. Chapter IV will detail how varying polymer molecular weight can tune the steric character, with the intention that polymers of a very low molecular weight could behave like surfactants. Additionally, this work provides a basis for understanding other pH-dependent polymers, such as those stable in a basic regime. In particular, emulsion stability via pH-tunable polymers can be applied to targeted drug delivery, allowing for dissolution of a drug in specific conditions. The ability to stabilize emulsions with a polymer alone aids in forming colloidally stable systems, such as those coated by proteins coronas or polymer coacervates and broadens our understanding of traditional DLVO theory.

CHAPTER IV: IMPACT OF POLYMER STERICS ON EMULSION STABILITY

This work is currently under review in the journal *Soft Matter*. Ashley N. Mapile is credited with conceptualization, formal analysis, investigation, writing – original draft, writing – review and editing, and visualization. Lawrence F. Scatena assisted in conceptualization, writing – review and editing, supervision, and funding acquisition. Supplementary information for this chapter is provided in Appendix B.

IV.A. AN INTRODUCTION TO POLYMER STERIC HINDRANCE

The inherent hydrophobicity of pharmaceutical ingredients remains a challenge in delivering drugs through the aqueous-rich human body. It was estimated in 2007 that 40% of drugs on the market were water-insoluble with a surge of hydrophobic drug candidates in the development pipeline (~90%) expected to have increased the prevalence of oil-soluble pharmaceuticals in the current age.[225] In addition to transporting inherently hydrophobic drugs, using oil-soluble delivery agents protects sensitive ingredients. The recent employment of lipid nanoparticles for delivering the COVID-19 vaccine, for example, protected the mRNA nucleotides from metabolic enzymes and other harsh environments in the body.[226] Current mechanisms for hydrophobic drug delivery include inorganic-based nanocarriers,[227,228] lipid-based nanoparticles,[229] nanoemulsions coated with surfactants or gelling polymers,[230–232] and protein coronas.[233] While these systems efficiently encapsulate hydrophobic drugs, the mechanism of stabilization is largely unknown. In one respect, these systems defy common theories of colloidal stability (i.e. DLVO) that require a substantial surface charge to prevent particle aggregation. Additionally, in the case of proteins or diverse lipid bilayers, specific probing of the moieties that give rise to colloidal stability is difficult due to the chemical complexity of the stabilizing units and buried nature of droplet interfaces. We recently demonstrated that small emulsion droplets suspended in water exhibit long-term colloidal stability when coated with poly(acrylic acid) (PAA) at pH 2 and 4.[234] With surface-specific spectroscopy, it was determined that low-charge PAA stabilizes emulsions through an ordered backbone that provides steric repulsion between droplets. These emulsions are resistant to acidic conditions and the addition of electrolyte. Using a simple polymer like PAA allows for a detailed experimental view of molecular ordering at the droplet interface with insight that can be applied to more complicated polymers or proteins that contain many different chemical functionalities.

Due to their tunable molecular weight, pH sensitivity, and unique architectures of synthetic polymers,[235] kinetically stable droplets coated with polymer are becoming increasingly useful for biosensing applications.[236] While changing the macromolecular concentration can impact emulsion stability,[237] many polymers exhibit poor solubility at higher concentrations. Instead, probing different chemical architectures or conformational orientation at an interface is achieved through polymer morphology (i.e. linear,[238] block,[239,240] or core-shell[241]), chemical identity/compatability,[242,243] and layer thickness.[244,16,245] In particular, the thickness of a polymer layer at an interface is adjusted by modifying the polymer molecular weight or by adding chemical moieties to the polymer backbone, both of which increase steric hindrance and have the ability to stabilize emulsions. Understanding how polymers with varying steric properties orient at an interface will provide insight into developing novel drug delivery platforms, especially with polymers that have pH tunability relevant to physiological conditions.

The adsorption behavior of polymers has generated both theoretical[123] and experimental[124,125] studies that seek to understand interfacial conformation. In particular, a "train, loop, tail" representation has been developed that describes how polymers lie flat at the surface (train), coil beyond the surface into the bulk (loop) and extend at the ends of the polymer chains (tail) to emphasize favorable surface-polymer interactions or bulk-polymer interactions, dependent on the polymer identity and interface.[126–128] To probe polymer conformation at interfaces, vibrational sum frequency spectroscopy (VSFS), a surface-specific vibrational spectroscopy that provides insight to molecular ordering at buried interfaces, has been employed. Previous sum frequency studies have investigated the influence of polymer molecular weight on backbone ordering at the planar polystyrene/silver interface,[246] air/water interface,[247] and oil/water interface.[192] These studies found that polymer ordering was highly dependent on a balance between enthalpic and entropic contributions to polymer adsorption. It is more favorable for ionic polymers to be solvated in bulk solution to solvate charged functional groups and emphasize entropic disorder of the chain. Thus, enthalpically induced adsorption and solvation of the side chain functional groups must overcome this barrier to drive polymer adsorption to surfaces.[248] Specifically, enthalpic contributions from backbone/substrate interactions would increase interfacial ordering while entropic contributions from polymer coiling would reduce interfacial ordering.[246] While delivering a useful mechanistic groundwork for understanding polymer

adsorption, a key limitation of the previous sum frequency studies is that only 2-3 different molecular weights were studied thus, limiting the breadth of steric hindrance applied to the system.

In addition to tuning molecular weight, polymer steric hindrance can be increased with the addition of bulky groups to the polymer backbone. The few studies that have investigated the interfacial ordering of a sterically hindered polymer backbone through methyl substitution (i.e. poly(acrylic acid) vs. poly(methacrylic acid) or poly(methyl methacrylate)) have only been conducted via bulk infrared spectroscopy[249] or at planar air/water[250,251] or oil/water interfaces[221,252] with VSFS. These studies found that the addition of a methyl group on the polymer backbone improves solvation of the polymer into the hydrophobic phase. Additionally, changing the stereo configuration of the polymer, through the use of isotactic and syndiotactic poly(methacrylic acid), for example, can result in distinct oil- and water-rich C=O environments. For simplicity, this work uses isotactic poly(methacrylic acid), but future work will seek to understand the influence of backbone substitution orientation on polymer conformation at curved interfaces.

In this work, poly(acrylic acid) of five different molecular weights (2, 10, 450, 1000, and 4000 kDa) was used to probe the influence of steric hindrance on polymer molecular ordering at a droplet interface. The hexadecane/water emulsion interface used in this work mimics drug delivery platforms where a hydrophobic drug is incapsulated in the oil-core. Vibrational sum frequency scattering spectroscopy (VSFSS) is used to provide molecular-level detail of ordered vibrational modes at the curved interface while complementary dynamic light scattering (DLS) provides insight to emulsion stability. Additionally, we investigated the role of an additional methyl group on polymer ordering by measuring emulsions coated with poly(methacrylic acid) at varying concentrations. Based on rheological and thermal testing of bulk polymers,[253–256] it is hypothesized that at the oil/water droplet interface polymers of a low molecular weight will exhibit surface activity similar to that of surfactants and exhibit minimal polymer-polymer interactions. At higher molecular weights, it is projected that the polymer will have interchain crosslinks that contribute to layering on the droplet. At any molecular weight, the balance between enthalpically favorable polymer-substrate or polymer-polymer interactions and entropically favorable polymer disorder in the aqueous phase will determine the interfacial conformation of the polymer and the resulting emulsion stability. Finally, pH- and temperature-dependent DLS measurements of emulsion stability connects the microscopic understanding of polymer steric hindrance on interfacial ordering to macroscopic insight leading to the development of stable drug delivery systems.

IV.B. MATERIALS AND METHODS

IV.B.1. Materials

All materials were used as delivered without further purification. Hexadecane (≥ 99%), dioctyl sodium sulfosuccinate (AOT, ≥ 97%), and poly(acrylic acid) (PAA, average M_v ~ 450 kDa) were purchased from Sigma-Aldrich. PAA of varying molecular weight (ultra pure 2 kDa, ultra pure 10 kDa, 1000 kDa, and 4000 kDa) and poly(methacrylic acid) (PMAA, 100 kDa) were purchased from Polysciences, Inc. Deuterated hexadecane (n-hexadecane-d_{34}, 98.6% D), sodium deuteroxide (NaOD, 99.5% D), and deuterium chloride (DCl, 99.8% D) were purchased from CDN Isotopes. Deuterium oxide (D_2O, 99.9% D) was purchased from Cambridge Isotope Labs. All glassware was cleaned with a sulfuric acid bath (98%, Sigma-Aldrich) containing ALNOCHROMIX oxidizer from Godax Laboratories Inc. Glassware was submerged in the acid bath for at least 24 hours before being rinsed with 18.2 MΩ-cm water and dried in an oven.

IV.B.2. Emulsion Formation

Hexadecane (or D-hexadecane) emulsions suspended in water (or D_2O) were prepared by ultrasonication from a Branson Sonifer 250 at 5% output power of 20 kHz for 5 minutes at a constant duty cycle. The ultrasonicating probe tip was aligned at the interface of the aqueous solution and oil layer to ensure homogenous mixing. The AOT-coated emulsion standard was formed by ultrasonicating an AOT stock solution with D-hexadecane to generate an emulsion with 1 mM AOT and 2.5% v/v oil in water. Polymer-coated emulsions were formed in the same fashion with DCl or NaOD added to reach the desired pD (pH). Emulsion pH was measured using Millipore Sigma MColorpHast pH strips. While the detection of pH values can differ from pD values by 0.43,[203] pH instead of pD is used for clarity and accurately describes the pH-dependent phenomenon at three regions studied as confirmed by previous work from this group.

IV.B.3. Dynamic Light Scattering and Zeta Potential

Hydrodynamic diameter (Z-average), polydispersity index (PDI), and zeta potential of the emulsions was measured with a Malvern Zetasizer Nano ZS. The size and PDI are reported from an average of at least three measurements while zeta potential values are an average of at least five measurements. Room temperature DLS and zeta potential measurements were collected by pipetting 1 mL of the emulsion solution into a Malvern folded capillary zeta cell without dilution.

For variable temperature DLS, 1 mL of emulsion solution was pipetted into a glass cuvette and capped. The samples are prepared at room temperature and equilibrated for at least 20 minutes before the first measurement occurs at 0 °C. DLS measurements are taken at 10 °C increments (up to 90 °C) with sufficient equilibration time at each temperature step to ensure temperature accuracy with 0.1 °C.

IV.C. RESULTS AND DISCUSSION - EMULSIONS COATED WITH PAA OF VARYING MOLECULAR WEIGHT

IV.C.1. Emulsion Characteristics

A solution of poly(acrylic acid) (PAA) in D_2O at varying molecular weight (2, 10, 450, 1000, and 4000 kDa) was ultrasonicated with 2.5% D-hexadecane to form kinetically stable emulsions with a final polymer concentration of 500 ppm. Our previous study investigated the influence of concentration on emulsion stabilization.[234] Briefly, 500 ppm was chosen as enough polymer concentration to coat the interface but reduce the amount of polymer layering that causes charge screening. We seek to limit charge screening so that approximately a single layer of polymer is at the interface. This allows for zeta potential to be used as a metric for understanding polymer adsorption. The size, polydispersity index (PDI), and zeta potential of the resulting emulsions prepared at pH 2, 4, and 6 are summarized in **Figure IV.1**. Stable emulsions were formed at pH 4 with all molecular weights and at pH 2 for low molecular weights (≤ 450 kDa) as indicated by the small size and visual turbidity. At pH 2, large unstable oil droplets were formed with high

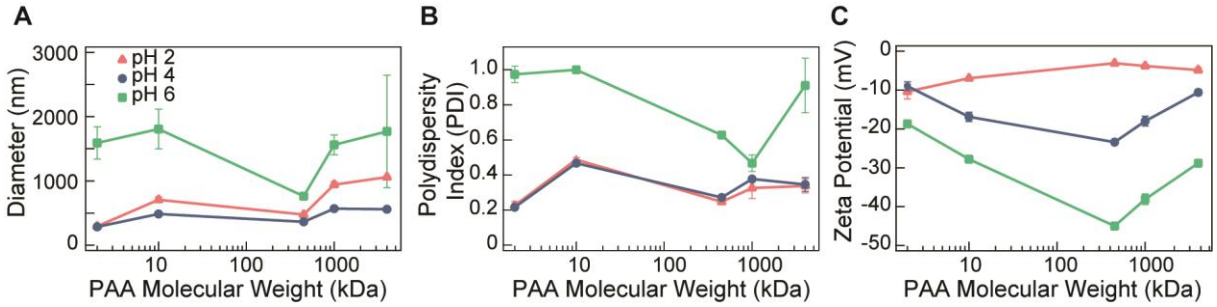

Figure IV. 1 A) Hydrodynamic diameter, B) polydispersity index, and C) zeta potential of emulsions coated with 500 ppm poly(acrylic acid) at varying molecular weights and pH conditions.

molecular weights (1000 and 4000 kDa) as indicated by the large size and PDI. No stable emulsions were formed at pH 6.

At pH 4 and 6, an absolute minimum of the zeta potential was observed at 450 kDa. With shortening or lengthening of the polymer chain the zeta potential is decreased in magnitude. At lower molecular weights, the decline in surface charge is attributed to the reduced polymer surface coverage given the same concentration as higher molecular weights counterparts.[257] At higher molecular weights, charge screening of multiple polymer layers causes a reduction in zeta potential. At pH 2, very little change in zeta potential was observed due to the low percent deprotonation in these conditions (1%).[234] The hydrodynamic diameter and zeta potential are important parameters for contextualizing our spectral results below, while size distribution was used to account for the scattered signal collected by VSFSS.

IV.C.2. Entropy and Enthalpy Favored Adsorption

To understand the changes in PAA conformation as a function of molecular weight, we turned to well-known mechanisms of polymer adsorption to analyze the VSFS spectral trends below. Unlike surfactants, polymers are not inherently surface active as they do not always possess distinct hydrophilic and hydrophobic regions as these regions are continuously tethered. In a similar fashion to denatured proteins, polymers would rather be solvated in the bulk, aqueous phase to emphasize entropic disorder, solvate ionic functional groups, and protect hydrophobic moieties. Therefore, to promote polymer adsorption to surfaces, the strong polymer-water interaction must be overcome by favorable polymer-substrate or polymer-polymer (layering) connections, which are closely tied to polymer length. Previous work has demonstrated that at high molecular weights, long polymer chains can extend at surfaces. This extension emphasizes favorable polymer-polymer and polymer-substrate van der Waals forces which results in an ordered backbone.[246] On the other hand, at low molecular weight, the conformation of the adsorbed polymer favors entropic disorder. With less repeat units, there are fewer backbone/substrate interactions as compared to higher molecular weight systems, thus entropy must compensate. These behaviors are described as entropy and enthalpy-driven adsorption, describing the driving force that dictates polymer conformation of the interface.

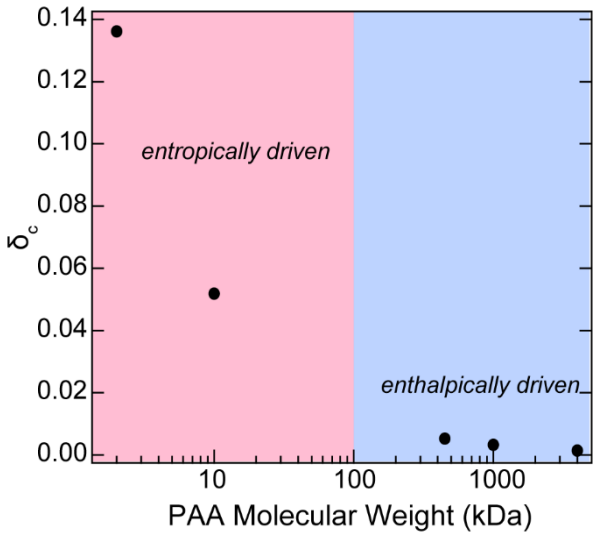

Figure IV. 2 Critical adsorption parameter (δc) as a function of poly(acrylic acid) molecular weight. δc ~ N-3/5 where N is the degree of polymerization.

The mechanism for adsorption is described quantitatively by the unit-less critical adsorption parameter, δ_c, and was calculated for the PAA system studied here (**Figure IV.2)** where $\delta_c \sim N^{-3/5}$ and N is the degree of polymerization. A larger δ_c suggests more entropic contributions to adsorption while a lower δ_c indicates more enthalpic contributions. We find that PAA adsorption is entropically driven at low molecular weights (2 and 10 kDa) and enthalpically driven at high molecular weights (450, 1000, and 4000 kDa). This analysis suggests that at low molecular weight, a preference towards disorder is expected and at higher molecular weights, an extended ordered backbone is favored.

IV.C.3. VSFSS of Varying Molecular Weight PAA Emulsions at pH 4

A conformational analysis of PAA at the oil/water droplet interface as a function of molecular weight was probed with vibrational sum frequency scattering spectroscopy (VSFSS). This technique provides a molecular picture of droplet interfaces by probing interfacial vibrations, where the presence of sum frequency signal indicates population and net orientation of the vibrational transition moments being probed. The polarization scheme *ssp* (relating to the polarization of the sum frequency, visible, IR pulses, respectively) was used to probe vibrational transition moments perpendicular to the oil/water interface, as consistent with previous experiments.[234] **Figures IV.3 and IV.5** show the interfacial vibrational response of the PAA backbone in the C-H stretching region as a function of molecular weight at pH 4 and pH 2,

respectively. As stable emulsions were not formed in pH 6 conditions, no VSFSS measurements were conducted.

At pH 2 and 4, a narrow feature at 2932 cm^{-1} is attributed to the methylene (CH_2) symmetric stretch on the backbone of PAA while the broad feature at 2871 cm^{-1} is assigned to the methine (CH) stretch. These fitting assignments are consistent with previous literature and fitting parameters are summarized in **Table B2**.[105,234] To deconvolute the influence of polymer molecular weight on interfacial ordering, the peak amplitude and Gaussian linewidth were compared as a function of molecular weight (**Figure IV.3B-C**). As the oscillator probed in these experiments is kept consistent for each measurement, the peak amplitude provides information on the population and orientation of vibrational modes while the Gaussian linewidth provides insight into the variety of chemical environments present for these vibrations at the droplet interface. For example, a large amplitude suggests a high population of ordered surface vibrational modes and a small Gaussian linewidth suggests a limited chemical environment of those moieties. The higher intensity of the methylene symmetric stretch, as compared to the methine stretch, makes it a better probe for determining interfacial ordering as a function of polymer molecular weight. However, the trends

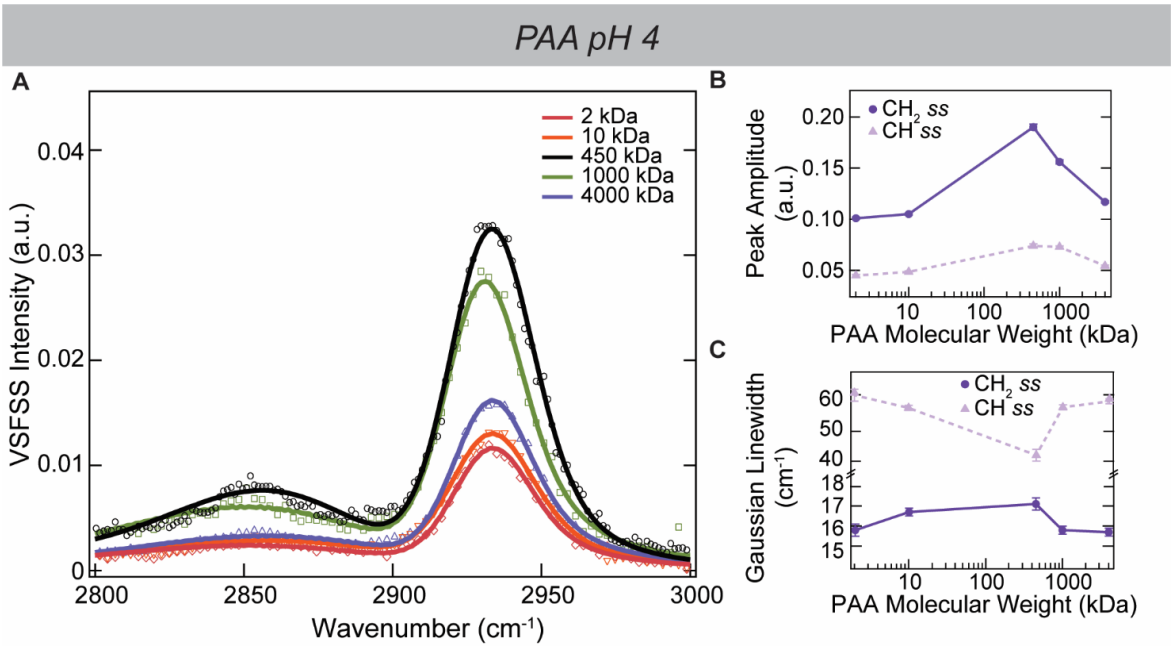

Figure IV. 3 VSFSS measurements (ssp polarization) of D-hexadecane emulsions in D2O stabilized with 500 ppm PAA of varying molecular weight at pH 4 in the C-H stretching region. Solid lines represent fits of the data. Panels B and C demonstrate the relationship between peak amplitude and gaussian linewidth obtained from the fits as a function of PAA molecular weight for the CH_2 and CH symmetric stretch.

for the methine stretch were included to show that the conclusions generated on polymer ordering is consistent regardless of the vibrational probe chosen for analysis.

At pH 4, the peak amplitude of the CH_2 symmetric stretch (*ss*) exhibits a maximum at 450 kDa and decreases with either the lengthening or shortening of the polymer chain (**Figure IV.3A-B**) These results closely resemble the trend exhibited with zeta potential as a function of molecular weight, where high molecular weight polymers layer at the surface and charge screen the slipping plane. In general, the conformation of PAA at pH 4, as compared to pH 2, is driven by the polymer's preference to solvation the ionic species. As detailed below, the conformational changes as a function of molecular weight at pH 4 are much more dramatic than at pH 2. The high intensity VSFS signal for the CH_2 *ss* at 450 kDa suggests a very ordered polymer backbone, consistent with previous interfacial studies.[234] When increasing the polymer molecular weight, the peak amplitude decreases due to disordered interchain crosslinks. While some layering can be ordered, the necessity to accommodate deprotonated acid groups results in incomplete and random polymer sheets, which is not seen at pH 2. This PAA layering is supported by the increase in hydrodynamic size measured by DLS (**Figure IV.1A**) Interchain interactions are frequently exhibited for high molecular weight polymers in bulk solution, where an increase in mechanical robustness and viscosity is attributed to crosslinking.[255,256] At lower molecular weights, the CH_2 peak amplitude decreases due to conformational adjustment of the polymer that is necessary to solvate the deprotonated carboxylic acids on the short chain and is entropy favored. Additionally, it is likely that lower molecular weight PAA is less surface active and thus there is less interfacial population that would give rise to VSFS amplitude.[257] Whereas at higher molecular weights (450 kDa and above), cooperative, long-chain ordering allows for accommodation of the ionic species. Previous studies have demonstrated that long-chain polymers emphasize the positive enthalpic interactions between the polymer backbone and the substrate (in this case, hexadecane).[192,258] At low molecular weights, this long-range communication is disrupted and thus shorter PAA chains cannot utilize the strong enthalpic interactions leveraged by longer chain polymers. Instead, it is hypothesized that low molecular PAA is coiled at the interface in a disordered orientation that is both entropy favored and solvates the deprotonated acid.

The change in Gaussian linewidth for the CH_2 *ss* at pH 4 is minimal (± 2 cm^{-1}) as a function of molecular weight (**Figure IV.3C**) due to this vibrational mode being solvated completely in the oil phase. However, the methine stretch exhibits a unique trend and is inherently broader than the

methylene stretch, as this mode is tethered to the water-soluble carboxylic acid group whose solvation environment varies significantly. The increase in Gaussian linewidth for the CH stretch as we move to the lower and higher extremes of molecular weight suggest a wider variety of C=O solvation environments.[220,234] The broadening of the methine mode at higher concentrations is caused by C=O modes being solvated at varying distances and degrees of hydrophobicity as the long chain polymer layers at the surface. At lower molecular weights, the deprotonated acid pulls the short chain further into the water phase, causing the polymer to be adsorbed to the surface like a surfactant (**Figure IV.4**). The different solvation environments due to this ionic group result in linewidth broadening. A similar behavior was observed for short chain zwitterionic polymers at the planar hexadecane/water interface, where the ionic species were solvated in the water and the polymer chain was suspended in the oil, but the intertwined nature of the polymer resulted in mixed solvation phases.[259]

In general, for pH 4 at low molecular weights, PAA adsorption mimics that of a surfactant with a distinct hydrophobic and hydrophilic region, whereas at higher molecular weights polymer-polymer layering is induced by interchain crosslinking (**Figure IV.4**). These results are similar to a physiologically-relevant study that found that Pickering emulsions coated with the polysaccharide, dextran sulphate, were more stable with a molecular weight of 500 kDa than 40 kDa.[260] Our results expand on the influence of polymer steric bulk by finding that at high molecular weights interchain crosslinks cause polymer layering at the surface.

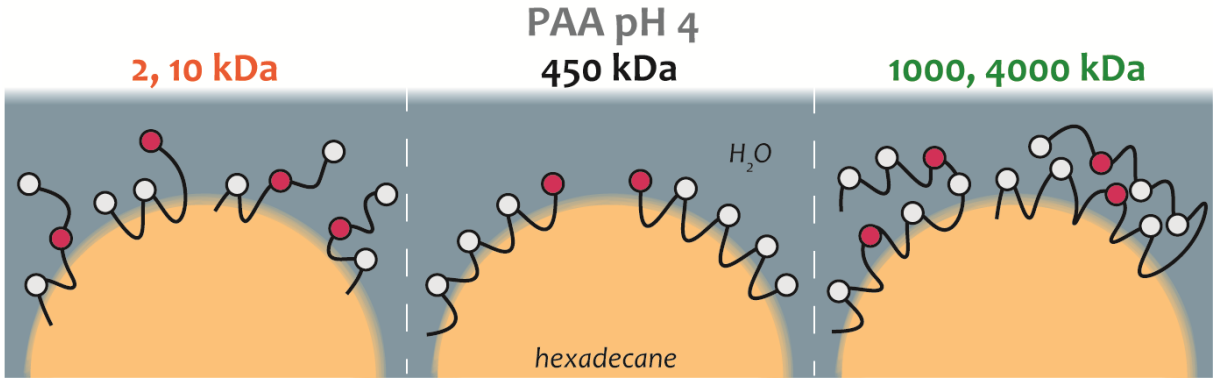

Figure IV. 4 Molecular picture of the hexadecane/water droplet interface of PAA at low (2 and 10 kDa), medium (450 kDa), and high (1000 and 4000 kDa) molecular weight at pH 4.

IV.C.4. VSFSS of Varying Molecular Weight PAA Emulsions at pH 2

At pH 2 (**Figure IV.5**), the interfacial ordering trend as a function of molecular weight is not as clear as at pH 4. However, these minimal changes are not surprising considering that there is such little surface charge on the PAA-coated emulsion at pH 2 (**Figure IV.1C**). Ultimately, the differences in adsorbed PAA conformation arising between pH 4 and pH 2 are dictated by the necessity for the pH 4 system to solvate the deprotonated acid. Nearly all of the carboxylic acid is protonated at pH 2 (99%), therefore the conformational adjustments needed to accommodate that charge at pH 4 are not observed. Additionally, there is more surface coverage at pH 2 as compared to pH 4 due to the increase in protonation as confirmed by surface tension measurements (**Figure B3**) and the higher CH_2 *ss* signal intensity.

At low molecular weight, the entropically-induced adsorption of PAA at pH 2 results in a slight decrease in methylene and methine peak amplitudes as compared to 450 kDa (**Figure IV.5B**). However, this amplitude is still higher than seen at pH 4, as the impacts of entropy are not

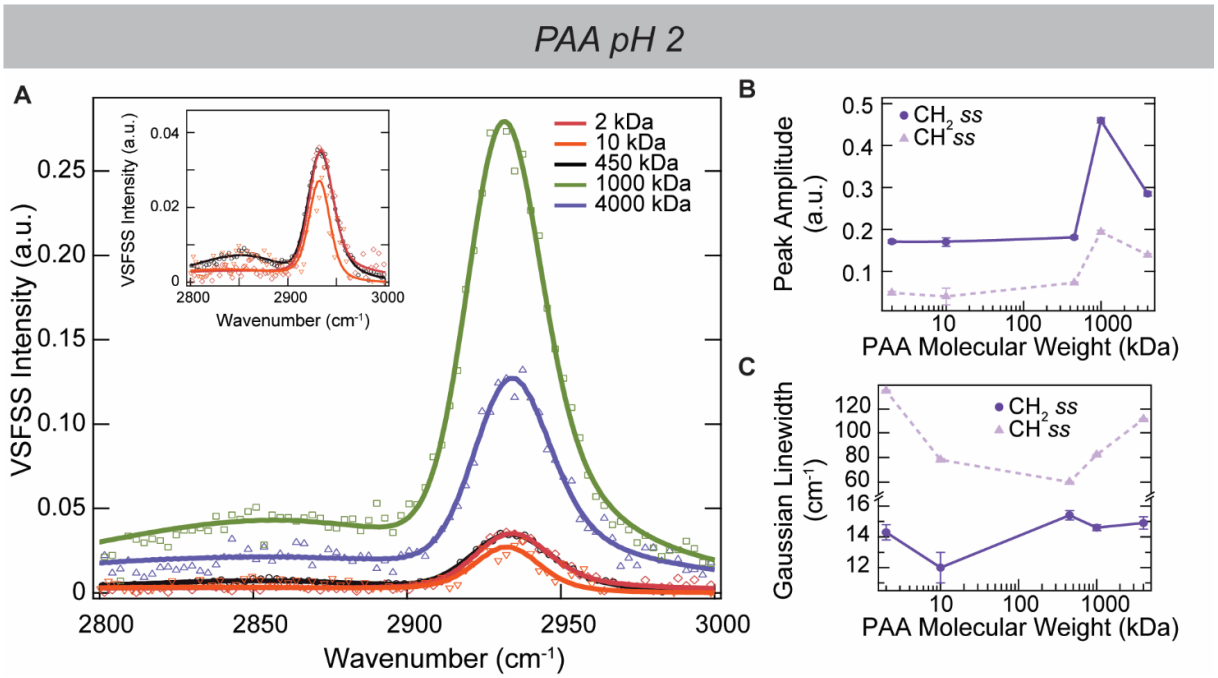

Figure IV. 5 VSFSS measurements (ssp polarization) of D-hexadecane emulsions in D2O stabilized with 500 ppm PAA of varying molecular weight at pH 2 in the C-H stretching region. Solid lines represent fits of the data. Panel A inset provides a zoom-in of the 2, 10, and 450 kDa traces. Panels B and C demonstrate the relationship between peak amplitude and gaussian linewidth obtained from the fits as a function of PAA molecular weight for the CH_2 and CH symmetric stretch.

as dramatic when the polymer is nearly 100% protonated at pH 2. Therefore, despite being entropically driven, the protonation of almost all the acid groups allows PAA to develop a more elongated conformation at pH 2 to better emphasize polymer-substrate interactions as compared to pH 4.

At high molecular weight PAA in pH 2, we attribute the methyl signal intensity to an increase in polymer layers at the emulsion surface. It is known that crosslinking is favorable at pH 2 due to the low percentage of deprotonation, resulting in a high number of polymer-polymer enthalpic interactions. While at pH 4, the addition of polymer layers reduced SFG signal due to disordered packing needed to accommodate the deprotonated acid, PAA at pH 2 can form nearly perfect layers of ordered polymers without ionic functional group disruption. SFG studies of poly(methyl methacrylate) at the planar polymer/silica surface also find that at high molecular weight, the methylene groups on the backbone are closely packed into the hydrophobic phase and are well oriented.[261] Additionally, nonionic polymers, like poly(N-vinyl acetamide) are known to exhibit well-ordered layers beyond the droplet surface.[16] This analysis is supported by the fact that DLS reports large diameters (> 900 nm) for droplets formed at pH 2 with high molecular weight PAA. The increase in hydrodynamic diameter is attributed to an increase in polymer layering at the surface, as was seen in previous emulsion studies.[262] At pH 2, the change in CH_2 *ss* linewidth is minimal (±2 cm^{-1}) (**Figure IV.5C**), however, the CH stretch linewidth increases at higher molecular weights. Like in pH 4 conditions, the broadening of this feature is due to the methine mode being solvated in a variety of chemical environments and becoming disordered. Ultimately, the conformational differences between PAA molecular weights at pH 2 is not as striking as pH 4

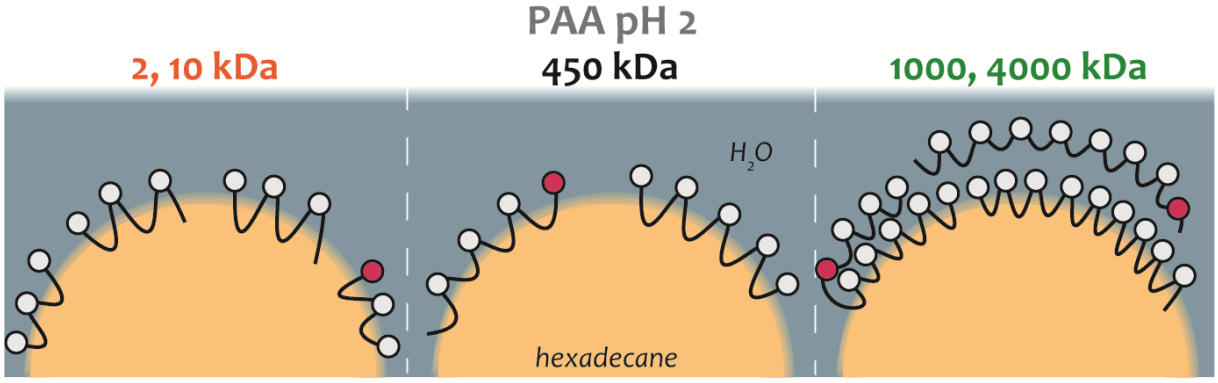

Figure IV. 6 Molecular picture of the hexadecane/water droplet interface of PAA at low (2 and 10 kDa), medium (450 kDa), and high (1000 and 4000 kDa) molecular weight at pH 2.

due to the polymer being nearly 100% protonated and thus no ionic species require water solvation. A detailed interpretation of the data though, shows that increased surface coverage of PAA is exhibited at lower molecular weights resulting in a fairly ordered backbone, while at higher molecular weights, the increase in spectral intensity is due to polymer layers increasing the ordered population (**Figure IV.6**).

IV.C.5. C=O Region and Summary

To determine the influence of polymer molecular weight on carboxylic acid ordering at the oil/water emulsion interface, VSFSS was used in the C=O stretching region (**Figure B1**). As stable emulsions were not formed at pH 6, no VSFSS measurements were conducted. This region requires de-timing of the visible beam to reduce a non-resonant response caused by the windows used in the experiment and detailed in previous publications.[129,163] To account for the elevated non-resonant background, two additional broad peaks were used in fitting (**Table B3**). A single resonant feature around 1740 cm^{-1} is attributed to the C=O stretching mode on PAA. At pH 2 and 4, there seems to be no correlation between the ordering of the C=O mode on PAA and the molecular weight. Global fitting and subsequent analyses of the peak position, Gaussian linewidth, and peak amplitude were all considered (**Figure B2**). We hypothesize that carboxylic acid ordering is independent of polymer backbone ordering and is nearly undetectable at the oil/water emulsion interface at a concentration of 500 ppm, as shown previously.[234] While increasing the concentration of polymer could improve the signal intensity measured by VSFSS, the solubility of high molecular weight PAA decreases dramatically with increasing concentration. Complementary surface-specific techniques, such as vibrational sum frequency spectroscopy at a planar oil/water interface which has increased resolution and input power, could provide better insight into the molecular ordering of the carboxylic acid group on PAA but directly probing this mode on a curved interface at this concentration remains elusive.

Ultimately these results suggest that at pH 4, PAA exhibits the highest amount of interfacial ordering and subsequent emulsions stability (as indicated by size, PDI, and zeta potential) at 450 kDa. At lower molecular weights, PAA is less-ordered due to poor chain communication resulting in less enthalpically-favored polymer-substrate interactions and greater entropy-favored disorder. At higher molecular weights, PAA becomes less ordered due to enhanced opportunities for crosslinking of polymer chains. Similar behavior is exhibited at pH 2, but with less dramatic

interfacial effects as a function of PAA molecular weight due to the lower degree of deprotonation. It was observed that at low molecular weights, PAA adsorption at pH 2 is well-ordered. At pH 2 with higher molecular weights, the crosslinking-induced environment results in a thick polymer chain at the surface. While not accounted for in the critical adsorption parameter, δ_c, these results suggest that specific chemical nature, tuned by pH in this case, impacts polymer adsorption characteristics.

IV.D. RESULTS AND DISCUSSION - EMULSIONS COATED WITH PMAA

IV.D.1. Emulsion Characteristics

Probing the impact of backbone sterics on interfacial ordering was achieved by ultrasonicating a solution of poly(methacrylic acid) (PMAA, molecular weight = 100 kDa) with D_2O and D-hexadecane to form kinetically stable emulsions with a final PMAA concentration of 500 or 2687 ppm. 500 ppm was chosen to maintain the same concentration as the PAA studies, while 2687 ppm was chosen to result in the same number of monomer units of PMAA as compared to PAA at 500 ppm. The surface activity of PAA and PMAA at 500 ppm are similar at pH 2, 4, and 6 (**Figure B3**) as measured by pendant drop surface tensiometery. Stable emulsions were formed with both 500 and 2687 ppm PMAA at pH 2 and pH 4 (**Table B1**). No stable emulsions were formed at pH 6 regardless of PMAA concentration, however a short-lived emulsion could be formed at pH 6 with 2687 ppm PMAA, likely due to a high surface coverage of the polymer.

IV.D.2. VSFSS of PMAA Coated Emulsions

To determine the influence of steric hindrance on polymer backbone ordering at the oil/water droplet interface, VSFSS was used to measure the interfacial ordering of PMAA as compared to PAA. **Figure IV.7** shows the interfacial vibrational response of PMAA as a function of pH and concentration in the C-H and C=O stretching regions for both 500 and 2687 ppm. As stable emulsions were not formed at pH 6, no VSFSS measurements were conducted on those samples. In the C-H stretching region, the feature at ~2939 cm^{-1} is attributed to the methyl symmetric stretch on the backbone of PMAA (**Figure IV.7A**). A small, broad feature at ~2890 cm^{-1} was necessary

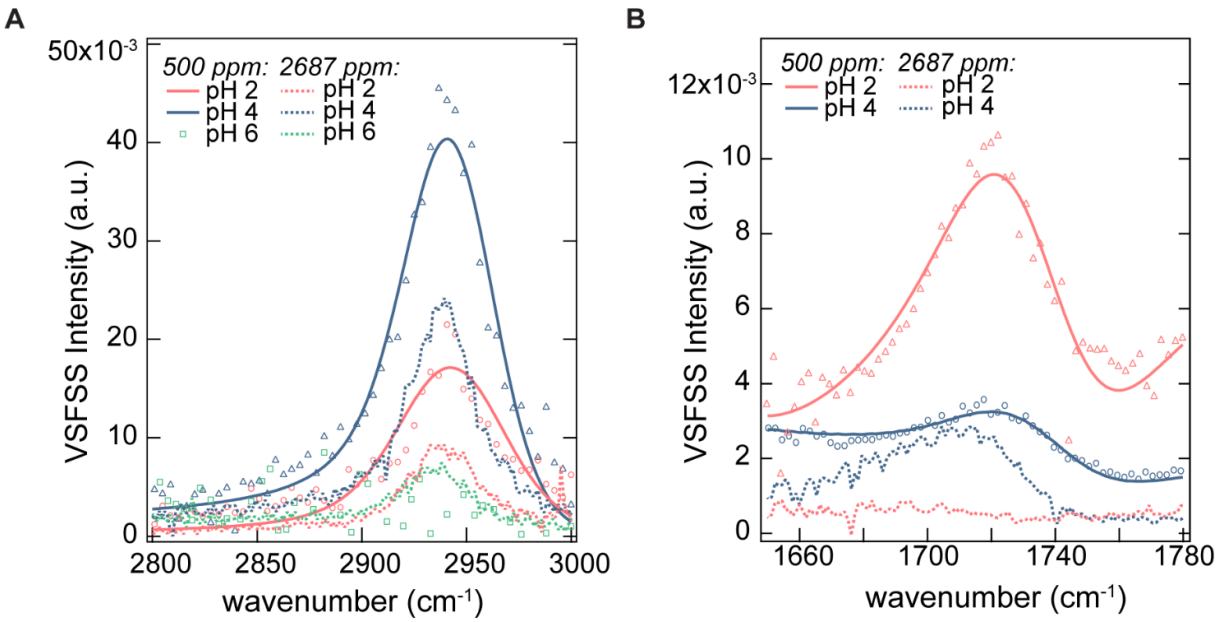

Figure IV. 7 VSFSS measurements (ssp polarization) of D-hexadecane emulsions in D2O stabilized with PMAA in the A) C-H and B) C=O stretching regions in varying pH conditions. Solid lines represent fits to the spectra measured with 500 ppm PMAA. Spectra measured with 2687 ppm PMAA are plotted with dashed lines.

when fitting the spectra and is assigned to the methyl symmetric stretch at the end of the polymer tail. Fitting parameters are summarized in **Tables B4-B5** and are consistent with previous literature.[221,250,263]

As the fitting assignments differ for PAA and PMAA, and therefore individual peak intensities cannot be compared between systems, the integrated intensity in the C-H stretching region was used as a metric for polymer backbone ordering (**Table IV.1).** The integrated intensity provides a general representation of polymeric backbone ordering at the emulsion interface. With the same concentration of polymer (500 ppm) at pH 4, adding a methyl group to the polymer backbone results in an increase in the integrated C-H stretching region area. This increase in signal could be attributed to the methyl group on PMAA increasing the solubility of the polymer backbone into the oil phase, therefore improving the polymer ordering. The improved hydrophobic solubility was previously observed by studies of PMAA at the planar oil/water interface.[221] However, once increasing the concentration to keep the number of monomer units consistent between PAA and PMAA (2687 ppm), we see a decrease in the integrated area, interpreted as a decrease in the polymer ordering due to the methyl group causing steric hindrance

Table IV. 1 Integrated area of VSFSS spectra collected from PAA and PMAA in the C-H stretching region from 2800-3000 cm-1, corresponding to Figure IV.7A.

pH	*PAA 500 ppm*	*PMAA 500 ppm*	*PMAA 2687 ppm*
2	1.62	1.34	0.559
4	1.87	2.84	1.41

within the polymer backbone. At a lower concentration (500 ppm), PMAA has more space to lengthen and accommodate the additional methyl group, while at a higher concentration (2687 ppm), the methyl group causes a steric disruption to the backbone ordering. At pH 2, we see an overall decrease in the integrated area from PAA to PMAA, regardless of polymer concentration. As PAA is known to form loops and coils at pH 2, the addition of a methyl group increases the favorability to reduce hydrophobic backbone-water interactions through coiling, ultimately reducing the interfacial ordering.

Interestingly at pH 6, slight VSFS signal in the C-H stretching region is observed from emulsions coated with 2687 ppm PMAA (**Figure IV.7A**). As this emulsion exhibits short-lived colloidal stability, VSFS spectra measured nearly immediately after formation of the emulsion (20 minutes) was necessary to observe ordered polymer at the interface. The presence of PMAA signal at pH 6 is due to the methyl group on PMAA increasing the oil solubility at the interface, in contrast to PAA at pH 6 which prefers to be solvated in the water phase due to the deprotonated carboxylic acid groups. While still exhibiting a large negative zeta potential indicative of a deprotonated polymer, the additional methyl group on PMAA aids in oil solvation at the interface leading to a slightly ordered and metastable droplet.

In the C=O stretching region, a single feature at 1736 cm^{-1} is assigned to the carbonyl stretching mode on the acid (**Figure IV.7B**). With 500 ppm PMAA at both pH 2 and 4, we see a higher intensity for PMAA than was observed for PAA, similar to what was exhibited in the C-H stretching region. The lower polymer concentration, as compared to 2687 ppm, allows for accommodation of the increase in steric bulk at the interface and improves the solubility of the methyl group into the oil phase, causing a subsequent ordering of the carboxylic acid group tethered to the backbone. Once the monomer concentration is increased (to 2687 ppm), the C=O mode becomes disordered as a result of the polymer backbone steric hindrance causing looping of PMAA. Ultimately, while increasing the hydrophobicity of a polymer improves its solubility at an

oil-rich interface at low concentrations, the steric hindrance of the backbone results in enhanced coiling and disorder in conditions where that behavior is already favorable, such as at low pH and high concentration.

IV.E. RESULTS AND DISCUSSION - EMULSION THERMAL STABILITY

To be suitable for drug delivery applications, emulsion vessels must withstand variable environments in storage, transport, and infusion into the human body. For example, delivering drugs into the gastrointestinal tract is challenging due to the intense acidity (pH 1-2) of the stomach.[264,265] Additionally, temperature tunability, such as through phase change materials which selectively deposit an agent at a given temperature, is useful for drug delivery systems.[266,267] Here, we show the robust stability of this PAA-coated emulsion system at pH 2 and 4 with varying molecular weights, by measuring the hydrodynamic diameter at a variety of temperatures (**Figure IV.8**). Temperature-dependent PDI is shown in **Figure B4**.

Emulsions at pH 4 remain relatively stable across a wide temperature range (20-90 °C, **Figure IV.8A**) as indicated by their invariant size. While the emulsions are not particularly resistant to cold temperatures (0-20 °C) and coagulate in solution, they exhibit strong thermal robustness at high temperatures. In fact, when moving from room temperature (~20 °C) to physiological temperatures (~36 °C), emulsions coated with 450 kDa PAA and lower molecular

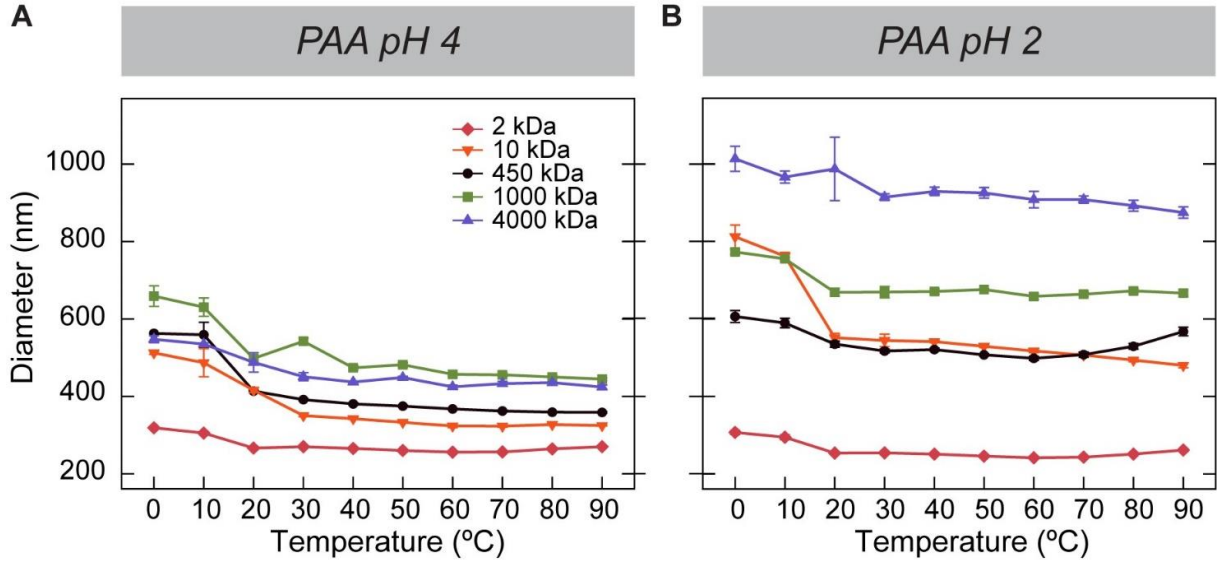

Figure IV. 8 Temperature-dependent diameter of emulsions coated with 500 ppm PAA of varying molecular weight as a function of temperature at A) pH 4 and B) pH 2.

weight, exhibit improved colloidal stability as indicated by the smaller size, suggesting that these emulsions approach a thermodynamically stable diameter in physiologically relevant conditions. These results are in contrast to other temperature-dependent emulsion studies which observe phase change behaviors at higher temperatures (~60 °C).[231] Emulsions coated with 1000 and 4000 kDa PAA have a larger diameter than the shorter chain counterparts, likely due to thick polymer layers at the surface extending the measured hydrodynamic diameter. At pH 2, emulsions only exhibit temperature stability across the entire temperature range when coated with 2 kDa PAA (**Figure IV.8B**). At higher molecular weights, the increasing tendency for looping and coiling results in emulsion destabilization and larger droplet sizes. These results corroborate the VSFS spectra demonstrating that polymer disorder and crosslinking that occurs at pH 2 does not promote colloidal stability. Only at low molecular weights, where less crosslinking is expected to occur and the polymer behaves more like a surfactant, do we see thermal stability. Meanwhile, at pH 4, where very little crosslinking of the polymer is expected as compared to pH 2, emulsions remain relatively stable across a wide temperature range. We hypothesize that in addition to forming a steric layer that facilitates colloidal stability at room temperature, the PAA layer provides additional thermal protection, making it a relevant choice for drug delivery. Expanding these results to consider the impact of physiological saline buffers would be useful,[268] but we predict from previous work that the addition of electrolyte at low concentrations has minimal impact on the resulting emulsion stability.[234]

IV.F. CONCLUSIONS

Via linear and non-linear light scattering techniques, the influence of PAA molecular weight and the addition of a methyl group on the backbone (PMAA) on polymer conformation at the curved hexadecane/water interface was probed. The readily available 450 kDa molecular weight of PAA is considered a standard likely due to its ability to form well-ordered chains at the oil/water interface. At higher molecular weights (1000 and 4000 kDa), enthalpically favored van der Waals interactions between the polymer backbone and the oil as well as hydrogen bonding between polymer chains results in an ordered backbone with multiple polymer layers extending beyond the surface. This surface layering lengthens the hydrodynamic diameter and charge screens the zeta potential. At lower molecular weights (2 and 10 kDa), shorter polymer chains act like surfactants and rely on entropic disorder to solvate the deprotonated groups. This general behavior is exhibited

at the natural pH of PAA, pH 4. With PAA at pH 2, the conformational differences as a function of molecular weight are not as distinct due to the nearly 100% protonation of PAA at pH 2 reducing the need for ionic solvation.

For PMAA, with an additional methyl group on the backbone as compared to PAA, no steric hindrance is faced at low concentrations as the polymer has more surface area to extend and form an ordered backbone. In fact, the improved oil solvation of PMAA results in a short-lived emulsion formed at pH 6 with a concentration of 500 ppm PAA. With higher concentration (2687 ppm), making the number of repeat units for PAA and PMAA the same, the additional methyl group causes steric disruption and results in a more disordered configuration as compared to PAA.

The unveiling of polymer conformation at the curved hexadecane/water interface can help design efficient drug delivery emulsions with long-term colloidal stability. In particular, we demonstrate the size stability of these emulsions in physiologically relevant pH and temperature conditions. Another way to tune emulsion stability could be with the incorporation of both short- and long-chain polymers which have been shown to be impactful for physical properties.[269] Combining polymers of varying molecular weight could improve interfacial surface coverage due to efficient packing capability, similar to surfactant mixtures and surfactant-polymer composites.

This work also provides another example of non-DLVO forces, namely steric bulk without surface charge, that contribute to colloidal stability. In the following chapters, the unique colloidal stability of bare metal-organic framework nanoparticles are studied to better understand other forms of non-DLVO interactions that give rise to stable dispersions.

CHAPTER V: COLLOIDAL STABILITY OF ZIF-8

This work was published in volume 18, issue 20 in the journal *ACS Nano*. Ashley N. Mapile is credited with conceptualization, formal analysis, investigation, writing – original draft, writing – review and editing, and visualization. Michael A. LeRoy is credited with formal analysis and investigation. Kevin Fabrizio assisted in data visualization. Lawrence F. Scatena assisted in conceptualization, writing – review and editing, supervision, and funding acquisition. Carl K. Brozek assisted in conceptualization, writing – review and editing, supervision and funding acquisition. Supplementary information for this chapter is provided in Appendix C.

V.A. AN INTRODUCTION TO BARE MOF NANOPARTICLES

Solvation shells dictate the interactions between colloidal materials and their surroundings. The activity of proteins, for instance, derives from the structure and dynamics of hydration shells often nanometers thick and with behavior distinct from bulk water.[270,271] The properties of nanoparticles, from catalysis and particle growth mechanisms to plasmonics and colloidal stability, also depend on how solvent molecules structure around a particle surface.[169,272,273] Classically, according to continuum solvation models and Derjaguin-Landau-Verwey-Overbeek (DLVO) theory, colloidal stability depends only on electrostatic repulsion overcoming van der Waals attraction between particle surfaces.[8] When attractive interactions outweigh repulsion, as with metal nanoparticles and quantum dots, capping ligands provide additional steric and entropic repulsion.[274] Colloids without capping ligands and weak electrostatic forces are postulated to be stabilized by solvation shells that act as protective coatings.[60,275,276]

Available analytical tools reveal important, but more general information about solvation shell structure and ordering. Atomic force measurement techniques, pioneered by Israelachvili, detect the presence of multi-layer hydration shells on mica surfaces through oscillations in the steric friction upon approaching the particle surface.[172,277] Pair distribution function analysis of X-ray scattering data similarly suggests water self-assembles into ordered nanometer-thick layers at the surface of metal oxide nanoparticles, even when surfactant ligands are added to cap the particle surface.[169] Recently, second harmonic generation scattering experiments reveal pH- and salt-dependent ordering of water at the interface of colloidal SiO_2 and TiO_2 nanoparticles.[278,279] While these studies lay foundational evidence for ordered solvation shells, they lack the specificity necessary to identify both the chemical nature *and* molecular conformation of solvation shells near

metal nanoparticles. Such insights will be critical in understanding the chemistry of solvation shells assembled at complex interfaces. In particular, porous colloids pose considerable challenges and opportunities for studying interfacial phenomena due to their low surface-charge densities, the presence of both internal and external surfaces, and because void spaces comprise a significant portion of the nanoparticle-solvent electrical double layer. Preliminary investigations of porous colloids include calculations that reveal significant fluctuations in the electrostatic potential of bare, mesoporous silica nanoparticles that are highly dependent on pore size.[167,280–283] Related studies have shown that the morphology of porous particles influences the ordering of solvation shells and overall colloidal stability.[284] To understand how factors such as pore topology, molecular composition, and particle size influence the colloidal stability of porous materials spectroscopic techniques are needed to uncover the arrangement of molecules at solvated nanoparticle surfaces.

While VSFSS has been used extensively to study surfactant-stabilized nanoemulsions and ligand-capped particles, here we use VSFSS to probe a free-standing nanoparticle-solvent interface. Not only does our work assign discrete vibrational modes to solvent molecules and their relative orientation to the interface, but we also provide insight into the interfacial structure of both traditional metal oxide nanoparticles and the largely uninvestigated porous metal-organic framework nanoparticles whose surface is significantly less dense than their metal oxide counterparts.

Colloidal nanocrystals of porous solids stand in stark contrast with the "hard-shell" colloids well-suited to conventional models of interfacial chemistry. Metal-organic frameworks (MOFs), in particular, possess the highest accessible surface areas of any known material.[285] Unlike conventional nanoparticles, void spaces of nanometer-sized pores dominate the external surfaces of MOF nanoparticles (nanoMOFs). This scarcity of nanoparticle material at the interface should consequently lower the electrostatic repulsion and van der Waals attraction that dictate colloidal stability according to DLVO theory. Such low-density architectures also create complex surfaces for the self-assembly of solvation shells due to their heterogeneous compositions and to the presence of both internal and external surfaces accessible to solvent. In the few existing synthetic methods for nanoMOFs, "modulators", rather than the typical surfactant ligands found in the quantum dot literature, direct the size of nanoMOFs. Unlike surfactant ligands, evidence suggests modulators rarely incorporate onto the exterior or interior surfaces. Instead, as described by the

"seesaw" model we reported recently, modulators influence particle sizes by affecting the metal-linker binding and linker deprotonation equilibria.[286,287] With this predictive model, we demonstrated a nanoparticle synthesis of the conductive MOF Fe(1,2,3-triazolate)$_2$ with diameter sizes controllable to just 6 nm—the smallest nanoMOFs to-date.[288] Size-dependent optical and charge-transport behavior emerged from this class of semiconductor nanocrystals distinct from traditional quantum dots. Despite the lack of surfactant additives and the absence of incorporated modulator, the particles exhibited indefinite colloidal stability in *N*,*N*-dimethylformamide (DMF) under anaerobic conditions. These observations suggest a mechanism of colloidal stability involving solvation shells, despite the minimal amount of material at the particle surfaces where solvent could potentially bind. Nanoparticles of the commonly studied Zn-based MOF, ZIF-8 (Zn(2-methylimidazolate)$_2$), also demonstrated long-term colloidal and air stability[289] (unlike Fe(TA)$_2$) in DMF, making them ideal candidates to study solvation shell chemistry. While ZIF-8 and other MOF species are known to be colloidally stable[290], and are frequently used in drug delivery platforms due to this attribute[291], most cases require post-synthetic modification in the form of capping ligands, surfactants, or polymers to provide long-term stability and efficacy[292–294]. The mechanism of colloidal stability for bare nanoparticles, especially those with a low surface density such as MOF nanoparticles, remains unknown. In applications, the ability to functionalize these nanoMOFs into polymer matrices to meet industrial demands for chemical separations and carbon capture will depend on surface interactions that contribute to this surfactant-free colloidal stability.[295,296] While others have studied the ligands of surface-coated nanoparticles[174,297,298] or bulk-sized MOF materials[299] through sum frequency techniques, herein, we investigate the solvent-particle interface of bare colloidal nanoparticles with long-term colloidal stability via VSFSS. Our results demonstrating the necessity of an ordered solvation shell for MOF colloidal stability are important for the varied uses of bare MOF nanoparticles where the addition of a surface agent could have unintended consequences on optical properties, solution processibility, solubility, and self-assembly.

V.B. MATERIALS AND METHODS

V.B.1. Materials

All chemicals were used as purchased unless otherwise stated. Zinc nitrate hexahydrate (99%, metal basis, crystalline, Thermo Fisher Scientific), 2-methylimidzole (99%, Acros Organics), methanol (certified ACS, Fisher Chemical), *N*,*N*-dimethylformamide (certified ACS, Fisher Chemical), and N,N-dimethylformamide-d_1, (99 atom % D, CDN Isotopes). All glassware used in VSFSS experiments is copiously cleaned in a concentrated sulfuric acid bath (98% Sigma-Aldrich) containing AlNOCHROMIX oxidizer (Godax Laboratories Inc.) for at least 24 hours before being rinsed for at least 2 min. with MilliQ water and dried in an oven.

V.B.2. Synthesis of nanoZIF-8 Particles

ZIF-8 nanoparticles (nanoZIF-8) were synthesized following literature procedure.[300] In general, to synthesize 36 nm nanoZIF-8, zinc nitrate hexahydrate (2 g, 6.72 mmol) in 136 mL of methanol was poured into to a 2-methylimidazole solution (2.7596 g, 33.61 mmol) in 136 mL of methanol stirring at 500 rpm and left to react for 1 hour. After 1 hour, the resulting nanoparticles were centrifuged and washed 3x with methanol by sonication and centrifugation. The resulting particles were then dried at 100˚C under vacuum for 24 hours. For different sizes the ratio of Zn:2Mim:MeOH was adjusted by a scale of 1:X:1000 with X = 2, 3, and 5 equivalents for large, medium, and small sizes of nanoZIF-8, respectively.

V.B.3. nanoZIF-8 Sample Preparation for VSFSS

SEM images of nanoZIF-8 are shown in **Figure C1**. Unless mentioned otherwise, 316 nm sized particles (96 nm crystallite domain) were used in all experiments described in this paper whose hydrodynamic diameter averages between 300-400 nm as measured by dynamic light scattering.

Each VSFSS sample consists of 80 μL of freshly sonicated nanoparticle suspension prepared at a concentration of 5 mg/mL. The ZIF-8 particles measured here exhibit crystallite domain sizes of 96 nm as determined by Scherrer analysis (**Figure C2**). By SEM, particle sizes average to 316 nm. When suspended in DMF, H_2O, or solvent mixtures, all samples exhibit slight swelling to hydrodynamic diameters of ~300-400 nm. This increase in hydrodynamic diameter arises from the presence of self-assembled solvation shells with finite diameters in solution.

Because the DLS sizes appear only slightly larger than the SEM sizes, we conclude that size contributions from particle aggregation is minor.

V.B.4. Powder X-Ray Diffraction

Sample purity was verified by powder X-Ray diffraction (PXRD) with a Bruker D2 Phaser benchtop diffractometer. Using the PXRD, Scherrer analyses were conducted to analyze crystallite size of the nanoMOFs and are shown in **Figure C2**.

V.B.5. FT-IR Spectroscopy

FT-IR spectra were collected on a Thermo Fisher Nicolet 6700 FT-IR spectrometer using the Smart iTR diamond ATR accessory. Bulk FT-IR spectroscopy assisted in analysis of VSFSS spectra and is shown in **Figure C3**.

V.B.6. Dynamic Light Scattering and Zeta Potential Measurements

Particle size average (Z-average), polydispersity index, and zeta potential were measured with a Malvern Zetasizer Nano ZS. Through dynamic light scattering, the Brownian motion of nanoMOF particles is observed by irradiating the sample with a 633nm laser and measuring the intensity fluctuations in the light scattered by the particle[204,301]. The Stokes-Einstein equation correlates the size of the particles with the speed of their Brownian motion. Instrumental software measures the rate of scattered light intensity fluctuations, generates a correlation function, determines the decay rate of the correlation function, and uses that decay rate to calculate a particle size distribution. A cumulant analysis determines mean particle size (Z-average) and the polydispersity index.

Zeta potential measurements characterize the potential at the slipping plane boundary of nanoparticles which indicates surface charge[205,302]. Laser Doppler Velocimetry is used to measure the electrophoretic mobility, or the velocity of particles moving under the influence of an electric field. Henry's equation describes the relationship between electrophoretic mobility and zeta potential.

V.C. RESULTS AND DISCUSSION

V.C.1. Ordered Solvation Shells Revealed by VSFSS

A colloidal suspension of nanoZIF-8 in DMF (SEM particle size of 316 nm and hydrodynamic diameter of 357 nm) was studied by VSFSS in the carbonyl stretching region of DMF (1600 – 1900 cm^{-1}) in three different polarization combinations **(Figure V.1A)**. As a control, VSFS spectra of bulk DMF were collected in all polarization combinations **(Figure C4.A-C)**, indicating that solvent absorption does not impact spectral line-shapes reported here **(Figure C4.D)**. To test whether particle aggregates impact the observed sum frequency response, we pursued a concentration-dependent size and polydispersity analysis as summarized in **Figure C5**. The concentration of 5 mg/mL ZIF-8 in DMF was monodisperse and contained no aggregates. Fitting parameters are provided in **Tables C1-2**.

The *ssp* trace, which probes vibrational modes perpendicular to the interface reveals two prominent features at 1689 and 1774 cm^{-1}. The significant signal intensity in this region indicates a large population of DMF molecules at the nanoMOF interface and indicates a high degree of ordering, as compared to previous VSFSS experiments that report relatively low signal intensity in the C=O region.[16,303] The presence of two distinct features indicates two significantly different chemical environments of the DMF C=O mode, which corroborates previous reports purporting the existence of multiple solvation shells at conventional nanoparticle surfaces.[169] Because both features are blue-shifted relative to DMF in bulk solution, these spectra indicate the C=O bond of interfacial DMF strengthens upon association with the nanoparticle surface, as is consistent with coordination of DMF to Lewis acidic metal sites in the absence of π-back-bonding. To better understand the relative orientation of these vibrational modes, *ppp* and *sps* polarization combinations were employed. In *ppp*, the lower-frequency peak at 1689 cm^{-1} appears in higher intensity as compared to *ssp*, while the higher-frequency peak broadens and becomes less defined. On the other hand, in the *sps* polarization combination, the lower frequency peak disappears, while the higher frequency feature remains well-defined. Since we only observe the 1689 cm^{-1} feature under *ssp* polarization conditions, the C=O IR transition moment must be perpendicular to the nanoMOF surface **(Figure V.1A)**. We therefore assign the 1689 cm^{-1} feature to an ordered solvation shell of DMF molecules not directly bound to surface Zn^{2+} sites **(Figure V.1B-C)**. A perpendicular arrangement of the DMF dipole to the particle surface would prevent the oxygen

lone pairs on DMF to bind to surface Zn^{2+} sites. The increase in intensity of the 1689 cm^{-1} feature from *ssp* to *ppp* polarization can be attributed to an increase in specific tensor elements of $X^{(2)}_{\square}$ (from 1 to 4) probed in the experiment.[304] As observed in other interfacial systems, most commonly with any hydrophobic/water interface, the presence of charge at an interface induces restructuring

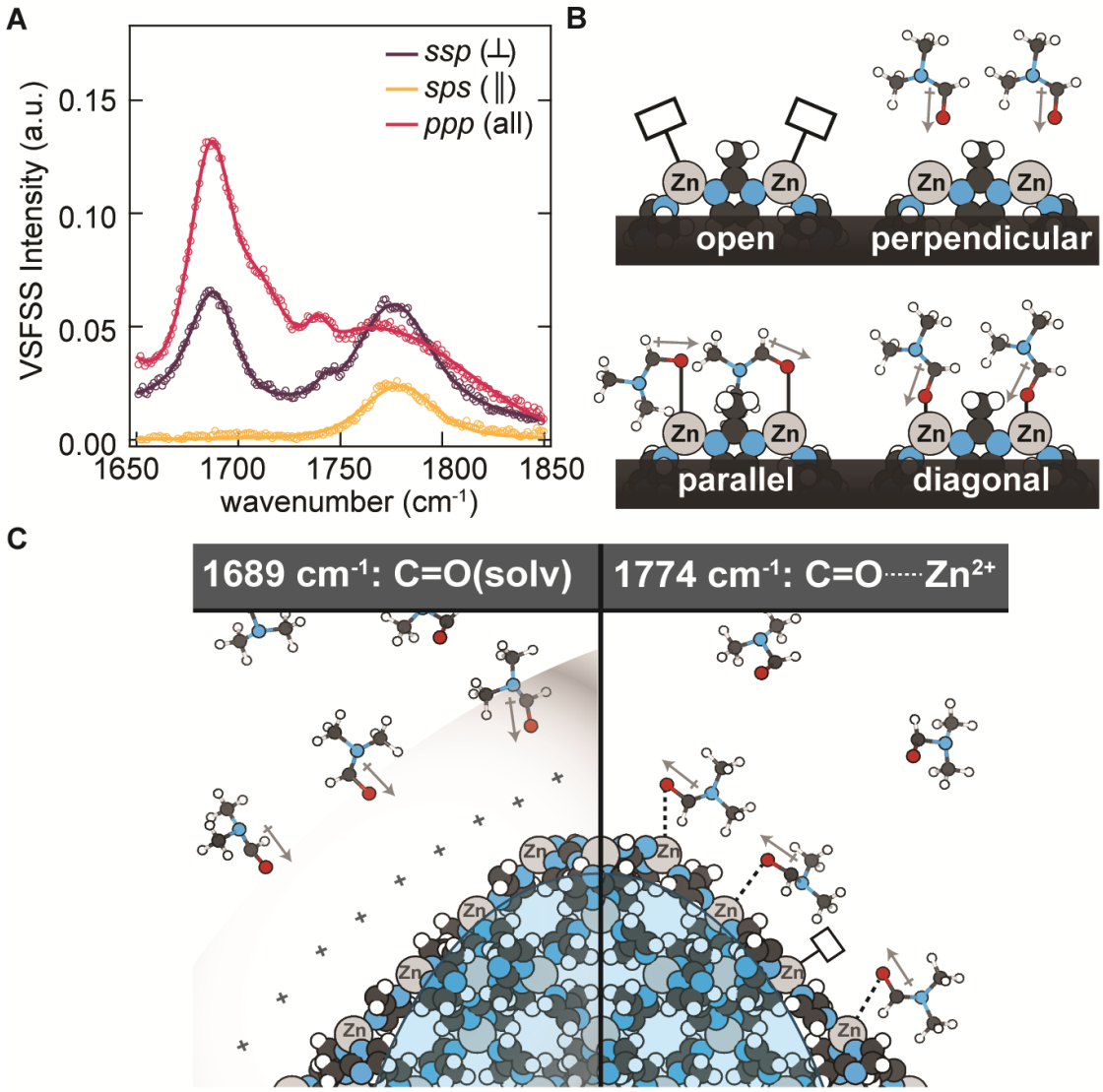

Figure V. 1 A) VSFSS measurements of nanoZIF-8 particles suspended in DMF taken in the C=O stretching region in various polarization combinations. Lettering corresponds to the polarizations of the sum frequency, visible, and IR pulses, respectively. B) Illustration of open metal sites on nanoZIF-8 and the orientation of carbonyl transition dipoles of DMF relative to the nanoMOF surface. **C)** Illustration of different solvent ordering environments (solvation shell and metal binding) at the nanoZIF-8 interface. In all VSFS spectra, open dots are raw data while lines represent fits.

of solvent molecules into a net orientation.[169,279,305] Indeed, the positive zeta potential of ~28 mV measured for these particles further supports the presence of a large surface charge and the presence of open metal sites.[306] We propose that this surface charge creates an electric field that aligns the dipoles of the DMF molecules in a perpendicular orientation. Previous studies have shown that colloidal mesoporous SiO_2 nanoparticles possess similar zeta potentials to ZIF-8 nanoparticles, but display significantly reduced populations of ordered interfacial solvent as compared to their solid-interface counterparts.[167,284] The highly ordered solvation shells around nanoMOFs, on the other hand, may arise from the presence of open metal sites at uncapped MOF surfaces.[306–308] In spite of low surface densities, the zeta potentials of MOF particles with high concentrations of missing linker defects, such as $Zr_6O_4(OH)_4$(terephthalate)$_6$ (UiO-66), approach values expected for nonporous metal particles.[309,310] The 1689 cm^{-1} solvation shell feature disappears in the *sps* polarization combination, as the interfacial electric field does not align the dipoles of DMF in a parallel fashion. A slight blue shift of the solvation shell DMF, as compared to the bulk DMF C=O mode typically occurring at 1677 cm^{-1} is due to enhancement of the solvent dielectric at a surface as compared to the bulk and is commonly observed in sum frequency experiments.[311,312] A weak feature at 1745 cm^{-1} is present in both *ssp* and *ppp* polarization schemes and can be attributed to DMF vibrational modes ordered *within* the cavity of ZIF-8, however ongoing experiments are in progress to assign the nature of this peak.

The polarization selectivity of VSFSS allows assignment of the feature at 1774 cm^{-1}. As this vibration appears in all polarization schemes, it corresponds to C=O modes that exist in a variety of orientations relative to the interface. Additionally, the significant blue-shift of this mode, relative to the bulk DMF C=O mode suggests a dative ligand-metal interaction. Therefore, we attribute this feature to C=O modes of DMF bound to open Zn sites **(Figure V.1C)**. DMF molecules pack around the Zn sites in directions, such as diagonal to the interface, that contain parallel and perpendicular contributions from each orientation **(Figure V.1B)**. As opposed to an ordered solvation shell, an ensemble of DMF molecules binding to Zn sites creates a feature present in all three polarization combinations. Previous reports from the MOF literature attest blue-shifting of C=O vibrational modes to when carbonyl or carboxylate groups donate lone-pair electron density to Lewis-acidic centers, such as Zn^{2+}.[313–315] While the blueshifts seen here far exceed shifts observed in bulk IR spectroscopy of C=O modes in MOFs, the interfacial environments of nanoZIF-8 vary significantly from the bulk. Interfaces, in general, present

complex chemical environments where pK_a values can shift 1-3 units more alkaline,[311] solvent dielectric constants alter by an order of magnitude,[316] sterically hindered cavities dictate reaction selectivity,[317] and molecules spontaneously undergo conformational changes.[318] Given that carbonyl modes provide sensitive probes to chemical environments for measuring changes in lipid conformation, protein structure, and ion-induced effects, it serves again here to report on the distinct chemical environments at the nanoMOF-solvent interface.[319,320]

To probe mixed solvation shells by VSFSS, we targeted perpendicular C=O modes (*ssp* polarization) of nanoZIF-8 suspended in 100% DMF, 50% DMF:50% H_2O, and 100% H_2O **(Figure V.2A)**. The 100% DMF trace shown in **Figure V.2** is the same as shown in **Figure V.1A**, with both DMF features present. When suspending nanoZIF-8 in a 50:50 mixture of DMF and water, however, the signal intensity of the lower-frequency feature (DMF solvation shell) reduces, and the higher-frequency (Zn binding) feature disappears completely. Size and zeta potential measurements were collected of these 316 nm ZIF-8 particle suspensions with mixed DMF/H_2O solvents to concurrently monitor stability (**Figure V.2B**)**.** With nanoZIF-8 suspended in 100% water or DMF, zeta potentials remain large and sizes at their smallest, indicating particle stabilization. For any mixture of DMF and water (25:75, 50:50, and 75:25), however, the hydrodynamic diameters increase and zeta potentials decrease. These results suggest that

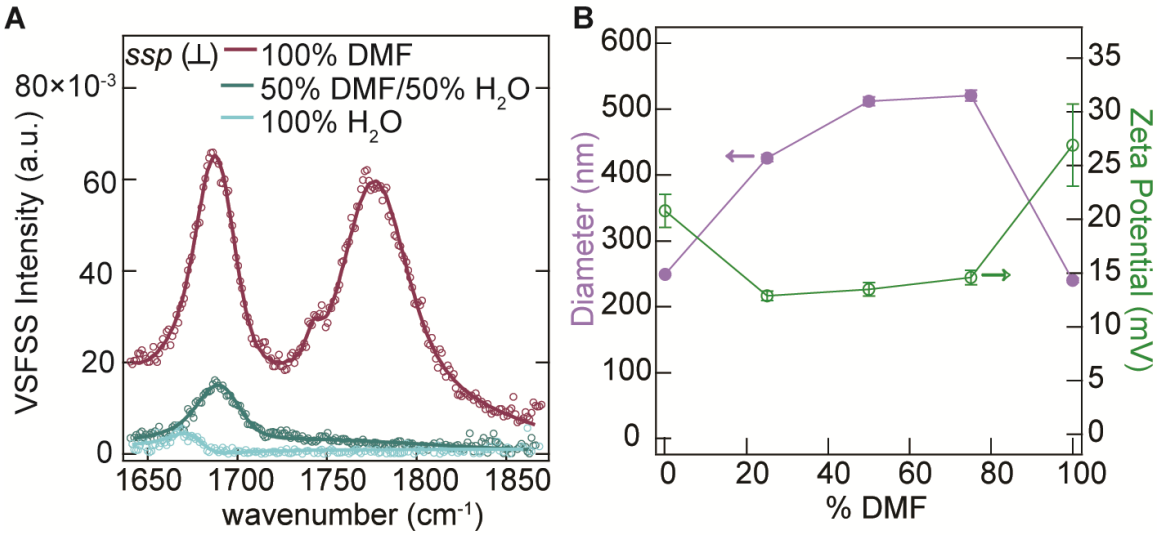

Figure V. 2 A) VSFSS measurements (ssp polarization) of nanoZIF-8 particles dispersed in 100% DMF, 100% water, and 50:50 mixture. Open dots are raw data while lines represent fits. B) Hydrodynamic diameter (purple, closed dots) and surface zeta potential (green, open dots) measurements of nanoZIF-8 colloids suspended in varying ratios of water and DMF.

competitive solvation between water and DMF increases the particle hydrodynamic radius and screens the interfacial charge. Competitive solvation has also been observed in bulk mixtures of DMF and water.[312,321] The reduction in the DMF solvation peak observed by VSFSS at 1692 cm^{-1} implies competitive solvation with H_2O reduces the population of DMF at the interface. The disappearance of the DMF-Zn binding feature at 1774 cm^{-1} also suggests H_2O out-competes DMF for binding with Zn. Finally, the spectrum corresponding to 100% H_2O lacks C=O modes, as expected. Instead, the spectrum contains a small feature at 1680 cm^{-1} attributable to a water bending mode and indicative of a water solvation shell around the MOF framework.[322,323]

V.C.2. Spontaneous Ordering within the ZIF-8 Nanoparticles

To investigate whether colloidal stability arises from excess linker binding to nanoZIF-8 open metal sites, VSFSS experiments were conducted in the C-H stretching region to detect 2-methylimidazolate ordered at the solvent-nanoparticle interface. In these experiments, deuterated DMF was used to shift the solvent C-H modes away from the frequency region of interest (2800 – 3000 cm^{-1}) and to isolate vibrational modes arising from the linker. **Figure V.3A** plots the resulting spectrum with a signal-to-noise typically expected for crystalline materials. Fitting parameters are provided in **Table C3**. From the spectrum in **Figure V.3A**, we attribute the peak at 2924 cm^{-1} to the CH_3 asymmetric stretch (plus symbol), and the feature at 2847 cm^{-1} corresponds a CH_3 Fermi resonance (open square symbol) **(Figure V.3B)**. The high intensity peak above 3000 cm^{-1} results from a combination of both the aromatic C-H asymmetric and symmetric stretches (asterisk symbol) **(Figure V.3B)**. While we were unable to resolve a CH_3 symmetric stretch, these peak assignments are consistent with bulk IR experiments **(Figure C3)** and recent literature[324,325] In fact, FT-IR studies into the gas sorption behavior of ZIF-8 are similarly unable to resolve the CH_s symmetric stretch of 2-methylimidazole.[326,327] A non-resonant peak is included in the fit at 2808 cm^{-1}, which becomes most prominent in measurements of nanoZIF-8 in H_2O, a higher dielectric solvent **(Figure C9)**. Non-resonant backgrounds are often observed in the spectra of substrates with complex or metallic compositions. As with these data, they often appear in the C-H stretching region and arise from inker-based electronic transitions that can be reduced by de-timing the visible pulse in the experiment.[328–331] This approach, however, resulted in poor resolution of the resonant CH modes, prompting us to report spectra from the coherent VSFSS measurement.

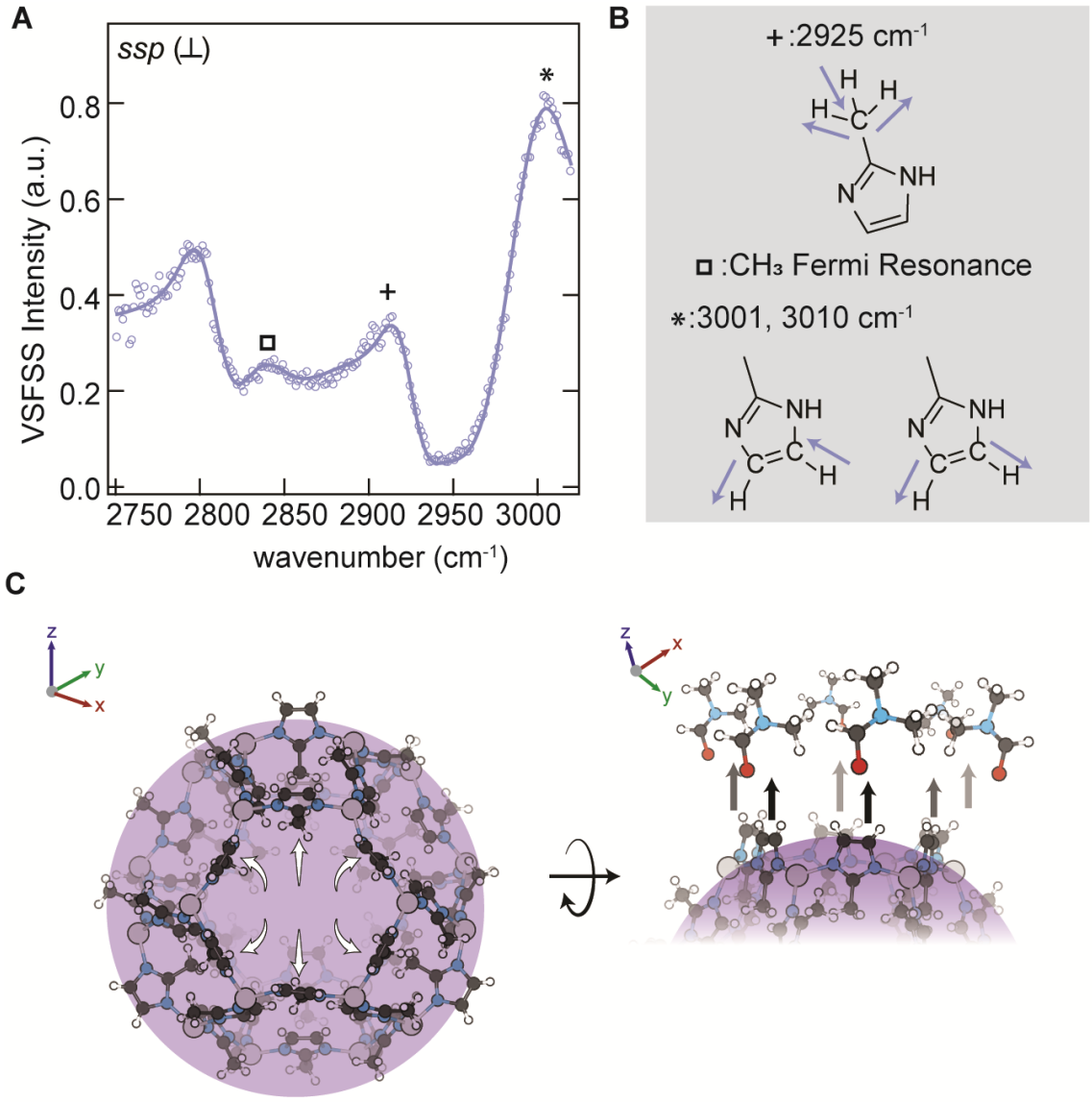

Figure V. 3 A) VSFSS measurements (ssp polarization) of nanoZIF-8 particles suspended in d-DMF taken in the C-H stretching region. Lines represent fits of the data. B) Illustrations of linker vibrational modes corresponding to symbols on peaks in A. C) Cartoon schematic demonstrating the rotational axis of 2-methylimidazole at the nanoZIF-8 interface at a top-down (left) and side view (right).

Due to the non-centrosymmetric space group of ZIF-8 ($I\bar{4}3m$), we considered whether the VSFSS response in the C-H region arises from the bulk response of the linker. However, previous reports have demonstrated that introduction of solvent or other guest molecules causes the framework to adopt a centrosymmetric structure due to linker rotation.[299,332] In addition, earlier investigations have also shown that ZIF-8 in a non-centrosymmetric conformation would be

VSFSS inactive because its only unique bulk nonlinear susceptibility tensor element, $X^{(2)}_{xyz}$, is null. Because the *ssp* polarization scheme used here probes the $X^{(2)}_{yyz}$ tensor element and reveals resonant vibrational modes, this intense C-H signal must arise from MOF linker spontaneously ordered at the ZIF-8 particle surface. Although we anticipated this spectrum to arise from excess ZIF-8 linker bound to the particle surface, ^{1}H NMR solution-state spectra of acid-digested particles and thermogravimetric analysis (TGA) were unable to detect excess 2-MIm (**Figure C6, C7**). Furthermore, if excess linker was present in quantities below the detection limit of these techniques (μmol concentrations for ^{1}H NMR and 0.1 μg masses for TGA), such quantities are unlikely to produce the observed signal. Therefore, this SFG signal must result from linker *within* the outermost layer of ZIF-8 nanoparticles, rather than excess linker as a capping ligand. To test whether 2-MIm binds to particle surfaces, we measured zeta potentials of ZIF-8 mixtures containing increasing quantities of additional 2-MIm, with the expectation that zeta potentials would decrease due to the presence of deprotonated imidazolate groups binding to Zn^{2+} sites. Instead, with just 25 equivalents per particle, zeta potentials increased from +10 mV to +40 mV (**Figure C8**) This result suggests that 2-MIm disrupts the DMF solvation shell that otherwise screens the positive Zn^{2+} charges from the Stern layer probed by zeta potential measurements. Instead of acting as surface capping ligands, excess 2-MIm disrupts the DMF solvation shell.

The ability to detect VSFSS signal for the 2-MIm C-H vibrational modes indicate a net ordering of the linker dipoles near the solvent-nanoparticle interface, possible only if 2-MIm can rotate into a thermodynamically stable configuration **(Figure V.3C)**. Computational studies and gas adsorption experiments have reported linker rotation for ZIF-8 about its M-N bond axis.[333,334] A significant consequence of this rotational freedom is that gas molecules larger than the pore size of ZIF-8 can fit inside the framework. This phenomenon implies linker molecules could rotate and therefore "open the gate" to these larger guests species.[335] Similarly, in our work, the ability of the 2-MIm linker to rotate permits the alignment of 2-MIm vibrational dipoles at the framework interface as shown by the VSFSS signal. VSFSS experiments probing the C-H modes on the surface of ZIF-8 were also performed in H_2O and show well-defined C-H vibrational modes attributed to the linker at similar frequencies to those seen for 2MIm in DMF **(Figure C9)**. While ZIF-8 is hydrophobic, likely a few water molecules enter the pores and nucleate around the metal sites, as shown by theory and experiments for other MOFs with hydrophobic cores.[336,337] In both

solvents studied, the rotational ability of 2-MIm promotes the filling of solvent within the porous framework.

V.D. CONCLUSIONS

This study reports interface-specific vibrational spectra of colloidal nanoparticles and the chemical insights they enable into the nature of solvation shells. Spectra reveal the presence of solvation shells around MOF ($Zn(2\text{-methylimidazolate})_2$) nanoparticles in aqueous, non-aqueous (DMF), and mixtures of solvent. Controlling the polarization of incident light probes the spatial arrangement of solvent molecules, while spectral shifts indicate the strength and orbital character of solvent-nanoparticle interactions. Differences between the spectra of these materials therefore uncover the microscopic details of material-specific solvation shells. Unexpectedly, VSFSS also revealed the vibrational signatures of the nanoparticle, in addition to solvent, providing direct evidence of spontaneous order-ng of molecular dipoles on either side of the nanoparticle-solvent interface. These results lay the groundwork for applying VSFSS as one of the only surface-specific techniques for understanding the interfacial chemistry of colloidal nanoparticles. Many avenues are available for further use of this tool to measure the surface of MOF nanoparticles. The following chapters contain unpublished work in progress that seeks to connect our fundamental microscopic understanding MOF interfaces with macroscopic properties of materials, such as membrane strength (Chapter VI) or critical aggregation concentration (Chapter VII).

CHAPTER VI: CHARACTERIZING THE MOF-POLYMER INTERFACE FOR IMPROVED MEMBRANE FORMULATION

This work is currently in preparation for submission. Ashley N. Mapile is credited with conceptualization, formal analysis, investigation, writing – original draft, writing – review and editing, and visualization. Michael A. Leroy synthesized the ZIF-8 nanoparticles and collected tensile strength measurements. Audrey M. Davenport collected SEM images. Collaborators from Boston University in the laboratory of Keith A. Brown collected force-probe AFM measurements. Lawrence F. Scatena assisted in writing – review and editing, supervision, and funding acquisition. Carl K. Brozek assisted in conceptualization, writing – review and editing, supervision and funding acquisition. Supplementary information for this chapter is provided in Appendix D.

VI.A. AN INTRODUCTION TO MIXED MATRIX MEMBRANES

Mixed-matrix membranes (MMMs), polymeric films with an inorganic filler, are promising alternatives for chemical separation traditionally achieved by distillation towers which are energy and space intensive or polymer membranes alone which lack chemical specificity. In particular, the incorporation of metal-organic framework (MOFs) into a polymer membrane allows for targeted gas separation, efficient recyclability, and tunability due to the multitude of inorganic and organic building blocks available.[338,339] However, the solution processibility necessary for incorporation into a polymeric membrane requires the formulation of colloidally stable nanoparticles of MOFs. We recently demonstrated that nanoparticles of $Fe(TA)_2$ (TA = 1,2,3-triazole) can be synthesized as small as 6 nm[340] and other common MOF nanoparticles, such as ZIF-8, exhibit unique colloidal stability despite having no capping ligands or surfactants at the surface.[160,341] Using the surface specificity of vibrational sum frequency scattering spectroscopy (VSFSS), we found that ordered solvation shells and solvent-metal binding at the nanoparticle surface contribute to this unique colloidal stability. With our recent efforts to create nanosized MOFs with impressive colloidal stability, we turn to understanding the interface between MOF nanoparticles and polymer membranes to better formulate robust MMMs.

A significant problem in formulation MMMs is that an interfacial void space is created between the inorganic filler and the polymer matrix. This open space reduces chemical separation efficiency and can eliminate the selectivity introduced by MOF nanoparticles. Previous work has filled the MOF-polymer void with surface functionalization that attempts to bridge the nanoMOF

surface to the polymer matrix with covalent chemical bonds. In practice, this can be achieved by post-synthetic functionalization of the MOF surface,[342,343] using an intrinsically porous polymer for the matrix,[344] or using an ionic liquid.[345] Usually, at least two or even three of these methods have to be used to efficiently fill the void space and in reality, scaling up these post synthetic procedures for industry relevance is challenging and time consuming. In addition, most studies analyze the final performance characteristics of the MMM rather than characterizing the interfacial dynamics that give rise to improved separations.

Beyond the practical necessity to fill the MOF-polymer void space, characterizing the surface interactions is of interest to create better MMM designs. Characterizing the surface interactions is very difficult experimentally due to the buried nature of the interface and the non-specific character of the surface interactions. Most of the previous work in this area is computational and observes weak, non-specific van der Waals interactions or hydrogen bonding between the polymer and the MOF nanoparticle.[346] In addition to characteristic void spaces at the interfaces, in some cases intercalation of the polymer into the MOF pore has also been observed which can lead to inefficient separation and clogging of the filtration channels.[159,347]

In this work, we propose interfacing ZIF-8 nanoparticles with a carbonyl-based polymeric binding agent at very low concentrations to achieve a continuous membrane without void spaces that exhibits improved mechanical strength and homogeneity as compared to traditional MMMs. We use ZIF-8 nanoparticles due to their open metal sites at the surface (**Figure VI.1**), impressive

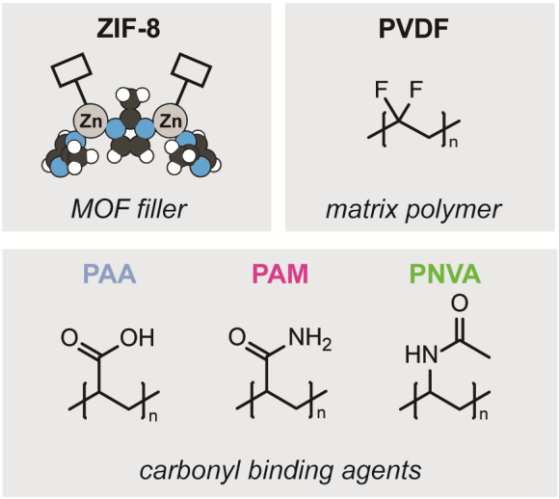

Figure VI. 1 Representation of the ZIF-8 nanocrystal surface and chemical structure of the polymers used for mixed-matrix membrane formation.

colloidal stability, and previously observed binding motifs exhibited between the C=O mode of DMF and Zn^{2+} surface sites suggesting other avenues for covalent binding at the surface. Carbonyl polymer binding agents of poly(acrylic acid) (PAA), poly(acrylamide) (PAM), and poly(N-vinyl acetamide) (PNVA) were chosen as these polymers closely resemble the binding agents used in paints.[348,349] In fact, the most common binding agents used in the formulation of white pigmented paint, for example, are acrylic polymer resins.[350] The chemical structure of these binding agents are shown in **Figure VI.1**.

With VSFSS we characterize the surface interactions between the ZIF-8 nanoparticle and the polymeric binding agent providing a fundamental understanding of the MOF-polymer interface in MMM. We find that the carbonyl mode on the binding polymer agent forms strong covalent bonds with open metal sites on the surface of ZIF-8 at a concentration as low as 250 ppm resulting in a well-ordered polymer layer at the nanoMOF surface. Complementary dynamic light scattering and zeta potential measurements help support the mechanism of binding at low concentrations by monitoring the polymer layering and reduction in surface charge. After deducing the mechanism of polymer binding at the nanoMOF interface, we employ this approach in formulating MMM films consisting of ZIF-8 nanoparticles, the carbonyl binding agent, and a commonly used polymer for membranes, polyvinylidene fluoride (PVDF, **Figure VI.1**). To demonstrate the robustness and mechanical stability of these films, we measure the homogeneity via SEM, the strength via tensile testing, and the interfacial interactions through force-probe AFM.

Ultimately, these results provide insight into forming strong MMMs with a low concentration of a binding agent that mimics technologies currently used for making paints. This formulation of ZIF-8 nanoparticles, carbonyl polymeric binder, and the polymer matrix uniformly disperses and holds the MOF nanoparticles in the polymer matrix. Unlike post-synthetic modification, this formulation can be easily scaled up and can likely be applied to other MOF nanoparticles with open metal sites at the surface. Future work involves tuning the molecular weight of these polymeric binders and introducing other dative binding mechanisms to determine the optimum packing of the binding agent at the interface for improved MMMs.

VI.B. MATERIALS AND METHODS

VI.B.1. Materials

All chemicals were used as purchased unless otherwise stated. Zinc nitrate hexahydrate (99%, metal basis, crystalline) was purchased from Thermo Fisher Scientific. 2-methylimidazole (99%) was obtained from Acros Organics. Methanol (certified ACS grade) and *N,N*-dimethylformamide (certified ACS grade) were supplied by Fisher Chemical. Poly(acrylic acid) (M_v~450,000) and poly(acrylamide) (M_n~40,000) were purchased from Sigma Aldrich. Poly(N-vinyl acetamide) was purchased from Polysciences. Polyvinylidene fluoride (Kynar HSV900) was purchased from PolyK Technologies. Deuterium oxide (99.9% D) was obtained from Cambridge Isotope Labs. pH was measured using MilliporeSigma MColorpHast pH strips.

All glassware used in VSFSS experiments was copiously cleaned in a concentrated sulfuric acid bath (98%, Sigma Aldrich) containing AlNOCHROMIX oxidizer (Godax Laboratories Inc.) for at least 24 hours before being rinsed with 18.2 MΩ-cm water for at least 2 minutes and then dried in an oven.

VI.B.2. Synthesis of nanoZIF-8

ZIF-8 nanoparticles (nanoZIF-8) were synthesized following a literature procedure. To synthesize the ~96 nm crystallite sized ZIF-8 particles used in this study, zinc nitrate hexahydrate (6.72 mmol) was dissolved in 137 mL of methanol and mixed with a solution of 2-methylimidazole (13.55 mmol) in 136 mL of methanol. The resulting solution was stirred at 500 rpm for 1 hour. After 1 hour, the resulting nanoparticles were centrifuged and washed with methanol three times before being dried at 100 ˚C under vacuum for 24 hours. Sample purity was verified by powder X-Ray diffraction (PXRD) with a Bruker D2 Phaser benchtop diffractometer.

VI.B.3. Formation of MMMs

Mixed matrix membranes were formed by dissolving 0.02 g of PVDF in 0.75 mL of DMF and mixing by sonication and vortexing. Meanwhile, 5 mg of ZIF-8 was dispersed in 0.25 mL of a stock solution (1000 ppm) of the carbonyl binding agent (PAA, PAM, or PNVA) and sonicated for 20 mins. Then, 1 mL of DMF was added to the MOF/binding agent mixture to give a final polymer concentration of 250 ppm. Once both solutions were completely dispersed, the MOF/binding agent mixture was added to the PVDF solution and sonicated. The mixture was then either drop casted

into a petri dish, heated at 60 ˚C for 1 hour, and released by acetone (for SEM measurements) or extruded into a Teflon mold and annealed by a hot plate for 20 minutes (for tensile strength testing).

VI.B.4. Dynamic Light Scattering and Zeta Potential

Hydrodynamic diameter (Z-average), polydispersity index (PDI), and zeta potential was measured with a Malvern Zetasizer Nano ZS. The size and PDI are reported from an average of at least three measurements while zeta potential values are an average of at least five measurements. Room temperature DLS and zeta potential measurements were collected by pipetting 1 mL of a 5 mg/mL ZIF-8 suspension into a quartz cuvette with dip cell for zeta potential.

VI.B.5. FT-IR Spectroscopy

FT-IR spectra were collected on a Thermo Fisher Nicolet 6700 FT-IR spectrometer using the Smart iTR diamond ATR accessory.

VI.B.6. Scanning Electron Microscopy

Imaging was performed using a Thermo Fisher Apreo 2 SEM instrument with 10.00 kV energy and 0.8 nA current. SEM samples were prepared by cutting a 1 mm square membrane and depositing it on a silicon substrate.

VI.C. RESULTS AND DISCUSSION

VI.C.1. Water Stability of ZIF-8 with Binding Agent

While previous work from this group suspended ZIF-8 nanoparticles in DMF, the VSFSS measurements in this study are conducted in D_2O to reduce solvent contributions from the region of interest, namely the C=O modes on the polymeric binding agents. However, due to the inherent hydrophobicity of ZIF-8 there are significant concerns about its long-term stability in water. Initial pH and visual analysis of the ZIF-8 colloids with either PAA, PAM, or PNVA in water were studied as a function of binding agent concentration (**Figure D1-2**). Additionally, even though VSFSS measurements were conducted on fresh samples, the crystalline structure of the colloids were measured after being dispersed in D_2O for 7 days (**Figure VI.2**).

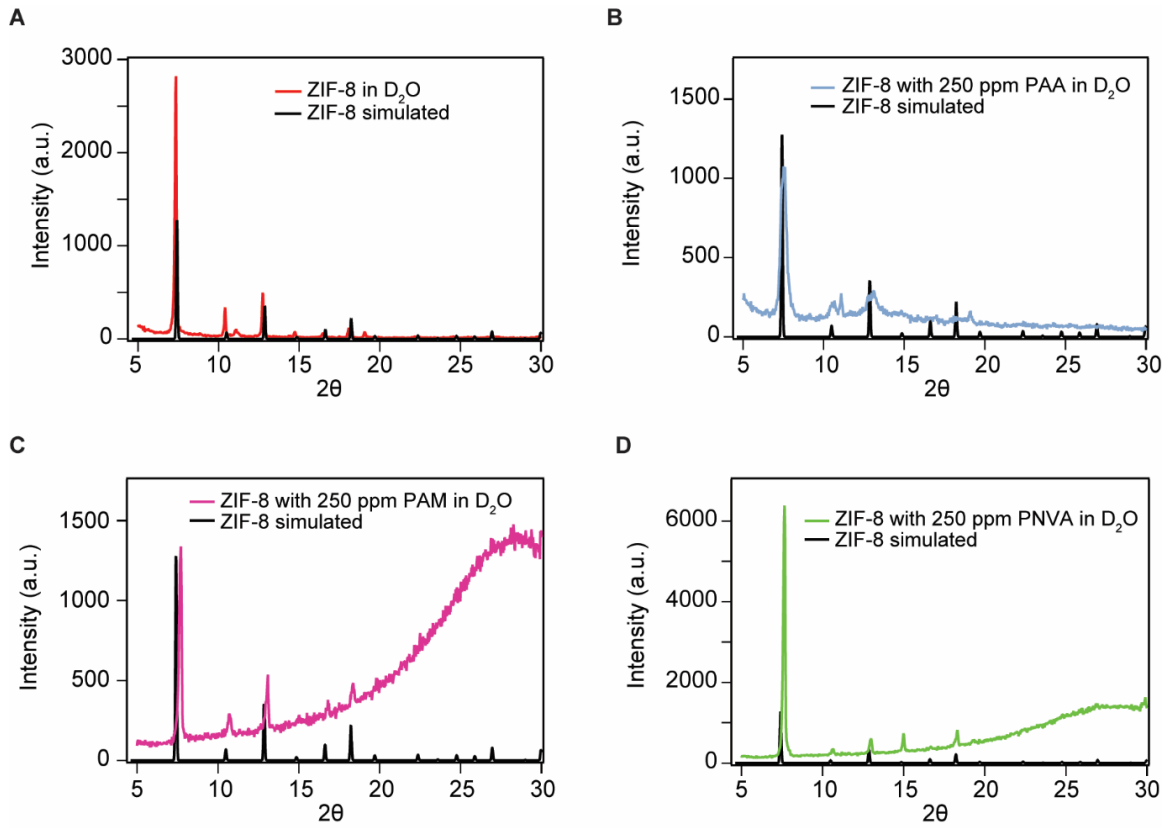

Figure VI. 2 PXRD patterns of A) ZIF-8 and ZIF-8 with 250 ppm B) poly(acrylic acid), C) poly(acrylamide), and D) poly(N-vinyl acetamide) suspended in D2O for seven days.

At a concentration of 5 mg/mL, ZIF-8 is known to degrade in water after 7 days as evidenced by the formation of a new crystallite phase in PXRD powder patterns.[159,160] Similar to literature, we observe the growth of a new phase as indicated by a small feature around 12°, in both the sample of ZIF-8 alone in D_2O (**Figure VI.2A**) and ZIF-8 with 250 ppm PAA (**Figure VI.2B**). However, with the addition of 250 ppm PAM and PNVA, the stability of ZIF-8 in D_2O improves, as no additional crystalline peaks are observed (**Figure VI.2C-D**).

The difference in colloid stability as a result of binding agent identity is explained by the ionic nature of the carbonyl polymers. PAA is ionic and has a pK_a of 4.5, indicating that at the natural pH of ZIF-8 in water (~9, **Figure D1**), some of the polymer is deprotonated. Previous work has found that ZIF-8 crystal edges are etched by acidic species.[351] In particular, sulfuric acid is known to degrade the ZIF-8 framework into $Zn(OH)_2$ clusters and free 2-methylimidazole.[352] We find that with increasing concentration of PAA up to 10,000 ppm we see a dramatic decrease in the pH of the colloid, from pH 9 to 5 (**Figure D1**), and a complete dissolution of the ZIF-8 framework

resulting in a clear solution (**Figure D2**). On the other hand, when adding the non-ionic polymers PAM and PNVA to the ZIF-8 solutions, a slight decrease in pH is observed but the colloids remain visually stable in solution (**Figure D2**). These results suggest that at low concentrations, especially for the non-ionic polymers, the binding agents act as a protective coating for the ZIF-8 frameworks in water. With acidic polymers, high concentrations cause the degradation of the framework.

As our VSFSS measurements in D_2O were collected on the same day of formation of the colloids we do not believe that any degradation has occurred. In fact, we will emphasize multiple times in this work that a lower concentration of binding agent is ideal for filling the void space between the ZIF-8 nanoparticles and the polymeric matrix, as initially evident by the ability of PAM and PNVA to form protective layers around ZIF-8 in water.

VI.C.2. Characterization of Colloids

The size and surface charge of ZIF-8 suspended in D_2O with varying amounts of binding agent was measured by dynamic light scattering (DLS) and zeta potential, respectively (**Figure VI.3**). Without polymeric binding agents, ZIF-8 colloids are approximately 200-300 nm in water. With the addition of only 250 ppm binding agent, the hydrodynamic diameter increased, regardless of polymer identity (**Figure VI.3A**). This increase in solvation shell diameter indicates that the polymer has layered on the ZIF-8 surface. As 500 ppm of polymer is added, the hydrodynamic

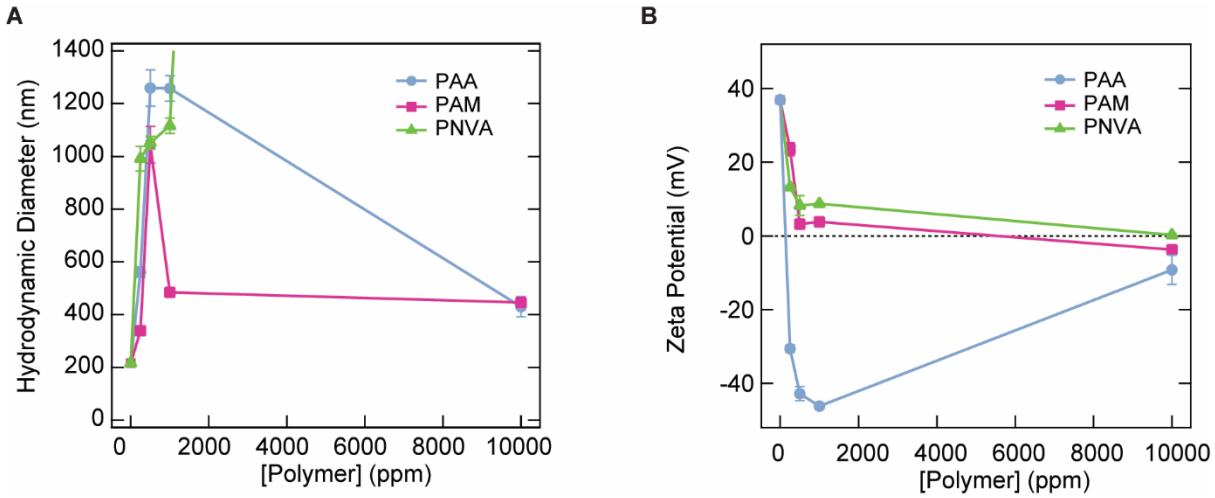

Figure VI. 3 A) Hydrodynamic diameter and B) Zeta potential of ZIF-8 colloids suspend in D2O with varying concentrations of PAA, PAM, and PNVA.

diameter increases further suggesting additional polymer layering. After 1000 ppm, the size trend deviates depending on the identity of the binding agent.

With 10,000 ppm PAA, the hydrodynamic diameter decreases to nearly 400 nm. While this size reduction could indicate the formation of a stable colloid, the pH and crystallite stability measured above indicate that instead, clusters of degraded framework give rise to the small particle size. For PAM, increasing concentration beyond 500 ppm causes little change to the hydrodynamic diameter suggesting that the surface becomes saturated with polymer and cannot accommodate additional layers. Interestingly, for PNVA, the hydrodynamic diameter increases dramatically with concentration, resulting in colloids outside of the regime that can be studied by VSFSS. Here, this ever-increasing size is attributed to favorable hydrogen bonding motifs achieved by PNVA that results in extended polymer layers beyond the surface. Spectroscopically, as described below, these additional layers are well-ordered due to the polymer geometry favoring hydrogen bonding between neighboring acetamide groups.[16]

Undercoordinated Zn^{2+} sites on the surface of ZIF-8 gives rise to a nearly 40 mV zeta potential when suspended in water. With only 250 ppm of binding agent, the zeta potential of the ZIF-8 surface is reduced as the polymer binds to the open metal sites (**Figure 3B**). For the acidic PAA, the zeta potential becomes negative confirming the presence of deprotonated acid at the surface. As higher amounts of PAA are added, we see a reduction in the magnitude of the zeta potential as charge screening is caused by additional polymer layers. At 10,000 ppm a zeta potential close to zero indicates poor colloidal stability and dissolution of the ZIF-8 framework. For PAM, with increasing concentration the zeta potential quickly approaches zero which initially indicates that PAM has completely charged screened the surface. However, with 10,000 ppm PAM the zeta potential becomes negative which is surprising given the non-ionic nature of the polymer. This negative surface charge could be due to extremely surface-active contaminants;[180] however, another explanation is that the resonance form of PAM is favored as the polymer layer extends into the bulk. In the resonance form, the negatively charged oxygen could be solvated in the water phase and give rise to the negative surface charge. VSFSS spectra below also support the presence of the PAM resonance form at the surface. For PNVA, commensurate with the ever-increasing hydrodynamic diameter, additional polymer layer causes charge screening at the surface and a reduction in the zeta potential magnitude. Ultimately, these measurements of the colloid size and

zeta potential indicate initial polymer at low concentrations and subsequent polymer layering, results that will be further analyzed by VSFSS and utilized in making robust MMMs.

VI.C.3. Ordered Polymer Layers Measured by VSFSS

Poly(acrylic acid)

To understand the molecular ordering of polymeric binding agents at the ZIF-8 surface, suspensions of ZIF-8 in D_2O with varying concentrations of binder were measured by VSFSS in the C=O stretching region (~1540 – 1720 cm^{-1}, **Figure VI.4**). Spectra were collected in *ssp* polarization, in which the presence of signal indicates both a population and net ordering of C=O transition dipole moments aligned perpendicularly to the nanoZIF-8 surface. ZIF-8 colloids were freshly prepared and sonicated on the same day as VSFSS measurements to ensure homogenous samples that maintained the crystalline structure. Fitting parameters are provided in **Tables D1-3**.

For ZIF-8 coated with poly(acrylic acid), a sharp feature is observed at ~ 1668 cm^{-1} (**Figure VI.4A**). Despite the C=O vibrational mode for PAA arising at ~1705 cm^{-1} in bulk FT-IR spectroscopy, no additional signals were measured in this spectral range even with the addition of PAA. As the ZIF-8 particles were synthesized in and washed with methanol before being suspended in water, no solvent contribution is expected in this region. Therefore, we assign the 37 cm^{-1} red-shifted feature at 1668 cm^{-1} to the C=O asymmetric stretch on PAA.

Carboxylic acids are known to have distinct asymmetric and symmetric carbonyl stretches in solution in which the vibrations occurs at higher and lower frequencies, respectively. The difference between the two modes is defined as the Δ_{ion}, which ranges anywhere from 150-200 cm^{-1} depending on the system. While we are unable to probe the symmetric stretch by VSFSS due to the low intensity of IR power in that region, the red-shifting of the asymmetric stretch provides insight into the binding mechanism exhibited by PAA at the Zn-rich nanoparticles surface. A decrease in the Δ_{ion}, as compared to a non-bound carboxylic acid, indicates a bidentate binding motif.[353] In our case, the red-shift of the asymmetric stretch is commensurate with a decrease in Δ_{ion}, suggesting that one Zn^{2+} atom on the surface is bound to two oxygen atoms on the carboxylic acid. This type of bidentate binding is enthalpically strong and resembles strong dative-type interactions present in other framework materials that utilize carboxylic acid linker units. Especially at 250 ppm, where the intensity of the feature is greatest, this red-shifted feature indicates strong covalent bonds formed between the ZIF-8 surface and PAA.

Surprisingly, with increasing concentration of PAA, the signal intensity and gaussian linewidth decrease (**Figure D3**). The amplitude from our fitting routine describes the population of vibrational modes in a net orientation while the linewidth indicates the distribution of chemical environments. In previous experiments analyzing the structure of PAA at the surface of nanoemulsions, the opposite trend was observed, in which nearly no signal was observed with 500 ppm PAA and a significant feature only became present at 1000 ppm PAA.[234] In this work, the decrease in amplitude and linewidth with increasing concentrations of PAA suggests that enthalpic polymer-surface interactions dominate at lower concentrations while enthalpically favored polymer-polymer interactions are preferred at higher concentrations. In other words, the C=O mode is well ordered at the surface in low concentrations due to the electric field and binding sites at the surface. With additional polymer layers, the driving force for C=O ordering is reduced and therefore, a lower population of the overall polymer concentration is bound and aligned at the surface. Instead, polymer-polymer van der Waals and hydrogen bonding interactions are favored as additional PAA is adsorbed to the surface. In a similar fashion to the observations made by dynamic light scattering, zeta potential, and PXRD, a low concentration of PAA is ideal to form strong dative bonds between the polymer while high concentrations degrades the framework.

Poly(acrylamide)

For ZIF-8 coated with PAM, a broad feature is observed around 1585 cm^{-1} (**Figure VI.4C**). This peak is fit to two vibrational modes, an N-H bend that occurs at 1580 cm^{-1} and the C=O stretch at 1584 cm^{-1}. In this system, the C=O stretch is 80 cm^{-1} red shifted from where it is to be expected in bulk FT-IR spectroscopy.[354] Unlike acrylic acid, bidentate binding is rarely exhibited by acrylamide units, therefore an alternative must explain this significant redshift. Red shifting of C=O modes indicative of weakening the C=O double bond character, however, as we and others have shown, Zn^{2+} is unlikely to π-backbond to carbonyl moieties due to its full d-orbital.[341,355] For Zn^{2+}, it is instead likely for the carbonyl group to donate lone-pair electron density to the Lewis-acid, resulting in a blue shift of the carbonyl.[313] Here, we suggest that the resonance form of poly(acrylamide) is favored in which the negatively charged oxygen is binding to the open Zn^{2+} sites at the surface resulting in an enthalpically favorable covalent bond. While the magnitude of this red shift is large, a red shift of over 20 cm^{-1} is observed for weak hydrogen bonds between acrylamide monomer units and water.[356] Coupling the strong dative interactions exhibited by O^{-}

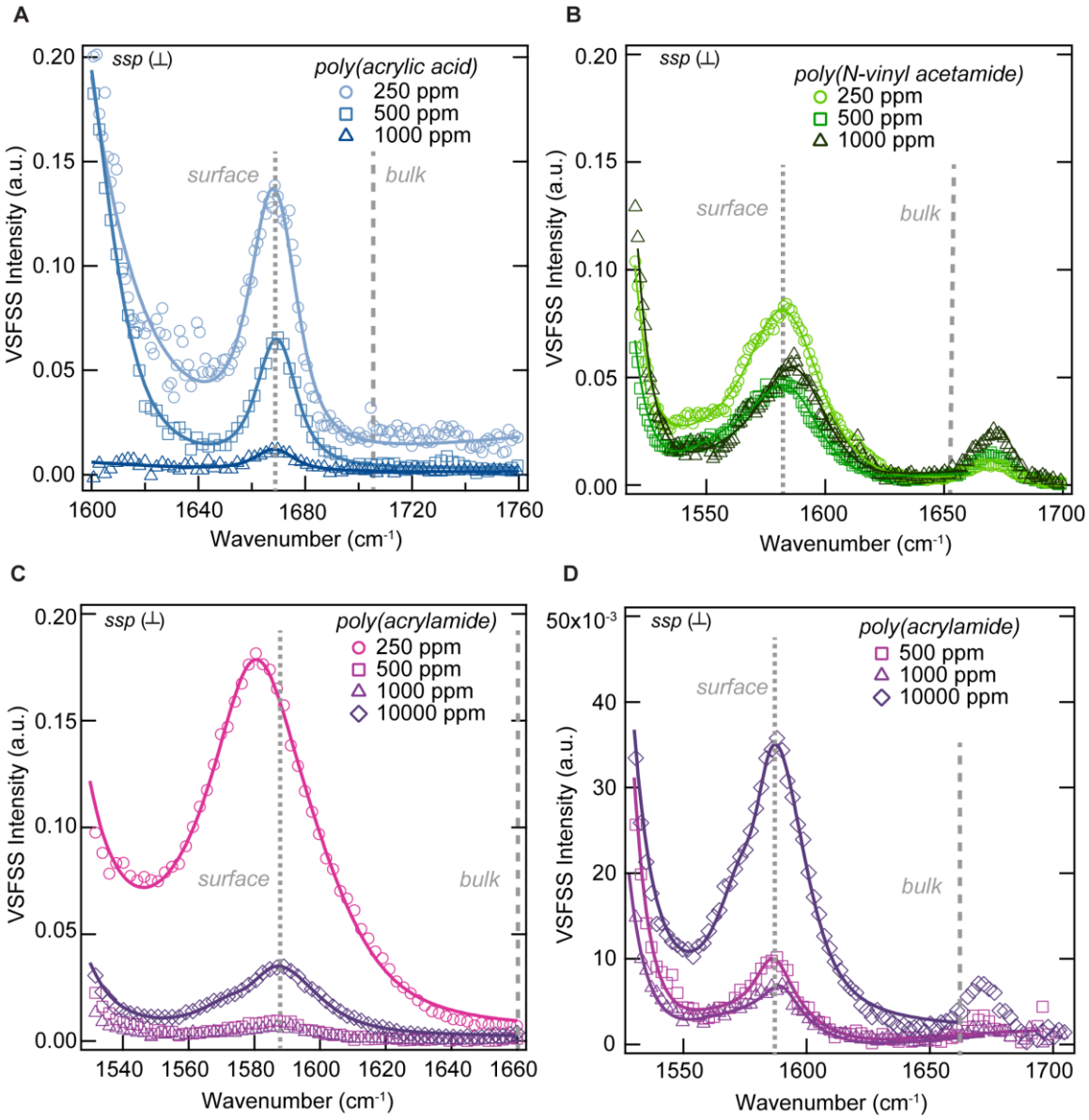

Figure VI. 4 VSFSS measurements (ssp polarization) of nanoZIF-8 particles suspended in D2O and coated with A) poly(acrylic acid), B) poly(N-vinyl acetamide), and C-D) poly(acrylamide). Lines represent fits of the data.

with a heavier Zn ion as compared to a hydrogen atom, with the known observation that electric fields at interfaces result in significantly shifted vibrational modes as opposed to the bulk, this red shift is justified.

When analyzing the amplitude and linewidth of PAM at the ZIF-8 interface, we notice that the linewidth is slightly broader than that of the PAA C=O mode (**Figure D3**), likely due to the resonance forms of PAM. At 250 ppm PAM, we see a very pronounced feature suggesting a large

population of ordered, bound C=O modes at the interface similar to what was observed with PAA. However, with the addition of PAM, despite initial decrease in signal from 250-1000 ppm PAM, an increase in intensity is observed with 10,000 ppm. Additionally, when expanding the spectral region of interest, a second, small feature is observed near 1670 cm^{-1} with only 10,000 ppm PAM (**Figure VI.4D**). This second peak is in a similar location to where the bulk C=O vibrational mode of PAM is expected to appear. Therefore, we conclude that at low concentrations (250 ppm), polymer layers close to the ZIF-8 surface are well aligned and bound to Zn^{2+} sites. At concentrations of 500 and 1000 ppm, the polymer layers favor interchain interactions that lead to a net disorder and a lower population of ordered C=O modes bound to the surface. At the highest concentration (10,000 ppm) the outer layer of polymer is now oriented and unbound to the surface, resulting in the presence of a feature assigned to bulk PAM. While the details of the binding mechanisms at higher concentrations of PAM are nuanced and interesting, we will focus in the following sections on leveraging low concentrations of PAM as a binding agent, as it is established that PAM alone does not form strong polymeric films.

Poly(N-vinyl acetamide)

ZIF-8 nanoparticles coated with PNVA exhibit a broad feature around ~1575 cm^{-1} (**Figure VI.4B**) which fit to an N-H bend at 1573 cm^{-1} and a C=O stretch at 1576 cm^{-1}. Here, the C=O stretch is 74 cm^{-1} red shifted to what is expected for bulk PNVA. Just like acrylamide, acetamide units are unlikely to participate in bidentate binding.[357] Therefore, we also attribute the significant red shift of the C=O mode to the resonance form of PNVA forming bonds between the O^- on the polymer and Zn^{2+} on the surface. In other metal frameworks made from bis(acetamide) ligands, a red shift is also observed between the free acetamide C=O stretch and the acetamide bound to the metal nodes.[358] Again, this significant red shift suggests very strong dative metal bonds at the interface of the ZIF-8 nanoparticle and PNVA, in a similar nature to ZIF-8 and PAM.

VSFSS measurements were not conducted on nanoZIF-8 particles coated with 10,000 ppm PNVA due to the size of the colloid being outside of the range of the measurement. However, we observe the presence and growth of a secondary peak at lower concentrations than those seen for PAM. This second feature occurs close to where the bulk C=O mode is expected at 1670 cm^{-1}, is present in all concentrations studied, and grows in intensity with increasing polymer concentration. This feature is assigned to C=O modes on PNVA that are not bound to the nanoparticle surface but

are instead in well-ordered layers that extend beyond the surface. Due to the geometry of PNVA, it is able to form well-ordered stacks at as additional polymer layers are added with H-bonding interactions occurring between neighboring acetamide groups.[16] These interchain interactions also contribute to the general invariance in peak amplitude and linewidth as a function of polymer concentration as nearly every polymer layer looks similar in terms of chemical environments (**Figure D3**). Ultimately, this molecular level perspective of the ZIF-8/polymer interface indicates that ultra-strong dative interactions between C=O modes on the polymer and open Zn^{2+} sites on the surface are optimum at low concentrations (250 ppm). In the following sections, we connect these microscopic properties to macroscopic characteristics of MMMs.

VI.C.4. Characterization of MMMs

(in progress)

MMMs consisting of 25 wt% ZIF-8 were formed with PVDF and the polymeric binding agent drop casted from DMF (**Figure VI.5A**). A film consisting of just PVDF was also formed for comparison. Transmittance FT-IR measurements (**Figure D4**) display the characteristic vibrational modes of PVDF, however, C=O stretching features from the binding agents were unable to be resolved to due the presence of residual DMF.

SEM images of the MMMs were collected to view the morphology and dispersion of the ZIF-8 particles in solution. **Figure VI.5B** displays a well-dispersed film using PAA as the binding agent where ZIF-8 nanoparticles of approximately 140 nm, with some pockets of aggregation. Current work in progress includes additional SEM images of all MMM formulations to determine the degree of homogenous dispersion as compared to films made without the polymeric binding

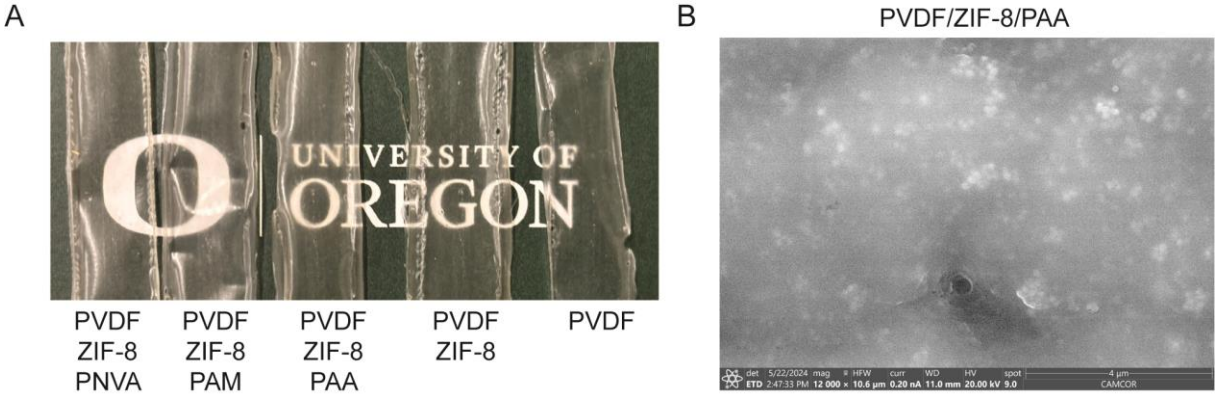

Figure VI. 5 A) Image of MMMs after drop casting. B) SEM image of membrane made with PVDF, ZIF-8, and PAA.

agent. Additionally, cross sectional SEM will provide insight into the morphology of the MMMs to evaluate their eventual performance as filter material, as suggested by previous literature.[338,344]

VI.C.5. Tensile Strength Testing

(in progress)

The mechanical strength of the MMMs is currently being measured at the Knight Campus at the University of Oregon. Rectangular pieces of membranes approximately 5 mm in width and 30 mm in length are stretched at a rate of 5 mm/min until fracture, in a similar procedure as found in literature.[359] These measurements will report on the Young's Modulus, tensile strength, and elongation at break. We hypothesize that MMMs made with polymeric binding agents will impart improved mechanical strength as compared to a membrane made of only ZIF-8 and PVDF, due to the strong dative binding interactions at the surface that ensure a homogenous distribution of ZIF-8 nanoparticles and fill the void space commonly left between the MOF surface and the supporting matrix.

VI.C.6. Force-Probe AFM

(in progress)

In a collaboration with the Brown Lab at Boston University, state-of-the-art force-probe atomic force microscopy (AFM) measurements are currently being conducted at the surface of polymer films and ZIF-8 crystals to determine the strength and type of interactions occurring at the interface in the solid state. Recently, the Brown group used this technique to measure the adhesion force between ZIF-8 and commonly used polymers for membranes, such as PVDF, poly(ethylene oxide) (PEO), polystyrene-block-polybutadiene-block-polystyrene (SBS), and polyisobutylene (PIB).[360] For PVDF, PEO, and SBS, the adhesion force between the MOF and the polymer was similar to that exhibited at the interface of a silica bead and the polymer. Using a silica bead as a non-porous comparison, suggested that PVDF, PEO, and SBS exhibit only solid-solid contact at the surface of the MOF crystallite. On the other hand, PIB exhibited adhesion forces with the MOF that deviated from that measured for the silica bead suggesting that additional forces besides solid-solid contact gives rise to the strong adhesion. The authors assigned this additional force to the ability of PIB to infiltrate into the pores of ZIF-8, due to it's small size and mobility in the form of a rubbery state at room temperature.

Due to the bulky, solid nature of the polymeric binding units at room temperature, we do not expect to see intercalation of the polymer into the ZIF-8 pores. Instead, we hypothesize that covalent bonds at the surface between the polymer film and the MOF surface will impart a significantly higher adhesion force as compared to PVDF at the ZIF-8 surface, which has only solid-solid contact adhesion. These results will provide another glimpse into the microscopic chemical interactions that give rise to strong MMMs.

VI.D. CONCLUSIONS

Using a wide range of surface-specific and bulk measurement techniques, we determined that a small concentration (250 ppm) of carbonyl polymer binding agent is sufficient, and ideal, to form robust MMMs. The incorporation of a polymeric binding agent to fill the void space between the inorganic filler and the polymer matrix, as opposed to post-synthetic modification or the use of ionic liquids, allows for industrially-relevant scale-up and future tunability depending on the MOF surface structure. For example, UiO-66 nanoparticles are known to have a negative zeta potential in water,[361,362] suggesting deprotonation of the benzene-1,4-dicarboxylic acid linker. Therefore, to fill the void space in a MMM made of UiO-66, cationic polymers such as poly(ethylamine) or imidazolium-based polymers can be used as low-concentration binding agents. This work also inspires core-shell or self-assembly design in which the chemistry of the MOF surface must be carefully characterized and utilized to grow additional units beyond the interface.

CHAPTER VII: ORDERED SOLVATION SHELLS AND THE STABILITY OF POROUS AND NON-POROUS COLLOIDS

(*in progress*)

While ZIF-8 nanoparticles provide a useful platform for studying solvation shells around nanoparticles with complex compositions and structural flexibility, we sought evidence for solvation shells around conventional semiconductor nanocrystals with both porous and nonporous structures. Due to their small sizes (sub-20 nm diameters), the large van der Waals energies of quantum dots necessitate surface capping ligands, but semiconductor nanocrystals larger than 50-100 nm remain colloidally stable without them.

We examined 21-nm TiO_2, 45-nm mesoporous SiO_2, and 200-nm Fe_2O_3 nanoparticles that swelled in solution to hydrodynamic diameters satisfying the size constraints of VSFSS. Like ZIF-8 nanoparticles, all materials remained colloidally stable for at least a week, as evidenced by DLS data summarized in **Figure E1**. Interestingly, zeta potential measurements indicated a nearly net-zero surface charge of TiO_2 and Fe_2O_3 particles, in contrast to the large positive charges of ZIF-8 (+32.7 mV) and the large negative charges of SiO_2 (-31.5 mV) that suggest the presence of open Zn^{2+} sites and deprotonated surface hydroxides, respectively.

To probe the origin of the differences in colloidal stability between ZIF-8, TiO_2, SiO_2, and Fe_2O_3 nanoparticles, colloidal suspensions of 5 mg/mL in DMF were studied by VSFSS in the carbonyl stretching region (1600 – 1900 cm^{-1}). Spectra were collected in the *ssp* polarization combination to focus on DMF vibrational modes perpendicular to the nanoparticle surface. **Figure VII.1** shows that unlike the two blue-shifted C=O stretches observed for ZIF-8, nanoparticles of TiO_2 and Fe_2O_3 produced a single feature at 1659 cm^{-1} and 1655 cm^{-1}, respectively, while hydrophilic SiO_2 displayed a peak at 1674 cm^{-1} —both red-shifted from bulk DMF. In the latter, the signal intensity exceeds that of TiO_2, but is lower than ZIF-8. A 20-fold scaling factor was necessary for visual comparison of Fe_2O_3 to the other nanoparticle systems.

The distinct spectral signatures of solvation shells around ZIF-8, TiO_2, SiO_2, and Fe_2O_3 particles supports prior studies into their surface composition, while providing microscopic insight into the interfacial orbital interactions. The redshifted C=O vibrational mode for Fe_2O_3, TiO_2, and SiO_2 (-22 cm^{-1}, –18 cm^{-1}, and –3 cm^{-1}, respectively, relative to the bulk DMF C=O frequency

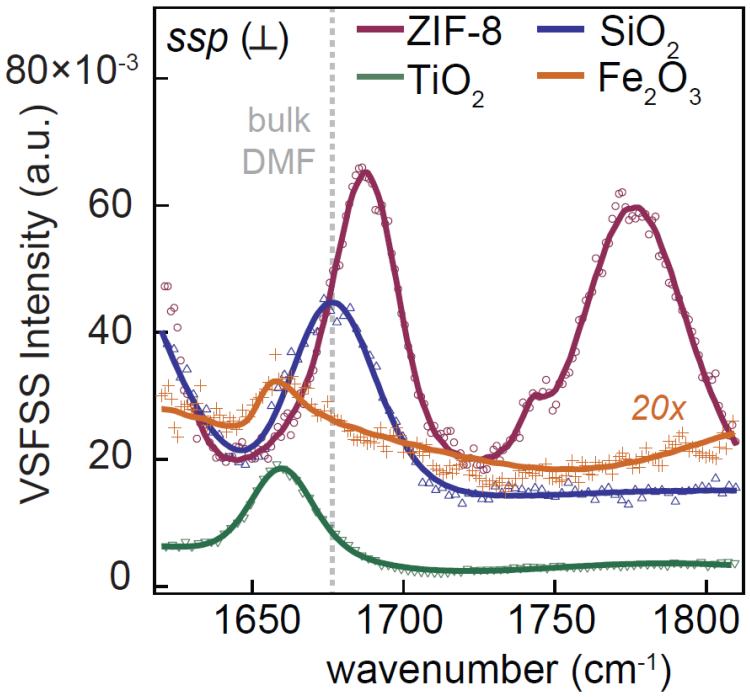

Figure VII. 1 VSFSS measurements (ssp polarization) of nanoparticles of ZIF-8, TiO2, mesoporous SiO2, and Fe2O3 (scaled by 20x) in DMF taken in the C=O stretching region. Lines represent fits of the data.

occurring at 1677 cm^{-1}), complements previous reports of hydrogen bonding between OH surface groups and DMF.[181] Due to the more negative surface charge of SiO_2, fewer protonated hydroxide groups would be expected to engage in H-bonding. This observation also accounts for the smaller redshift of the DMF C=O mode in the case of SiO_2. Unlike the purely electrostatic origin of the redshift in these two oxide systems, the blueshift of +12 cm^{-1} observed with ZIF-8 reflects a more coordinate covalent interaction between Zn^{2+} and the carbonyl oxygen of DMF. Specifically, the transfer of lone pairs from DMF removes formally non-bonding and anti-bonding electron density from the C–O vector, thereby strengthening the bond and increasing the C=O frequency. Additionally, the reduction in signal intensity for TiO_2 and Fe_2O_3 indicates a less ordered solvation shell resulting in weaker long-term colloidal stability as exhibited in **Figure E1**. This comparative analysis of correlating colloidal stability to surface-specific spectra features serves as a proof-of-concept for potential of VSFSS to probe wide-ranging phenomena occurring at colloidal nanoparticle interfaces.

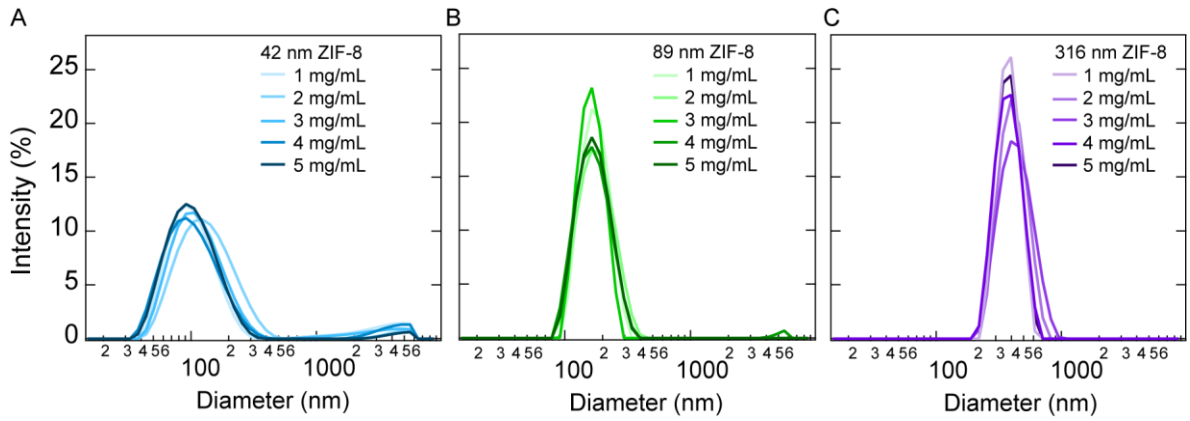

Figure VII. 2 Dynamic light scattering distribution curves of three different sizes of ZIF-8 suspended in DMF as a function of concentration.

Adam Mather is currently collecting data that will correlate the strength of the DMF solvation shell to a physical metric of colloidal stability, the critical aggregation concentration (CAC). Similar to critical micelle concentration (CMC), at which surfactants form micelles, the CAC for nanoparticles occurs when particles are no longer monodisperse in solution and form larger sized aggregates. The inspiration for this project arose from a reviewer concerned that our concentration of 5 mg/mL ZIF-8 in DMF was too large and likely contained aggregates. To address this comment, I measured size distribution curves of three different sizes of ZIF-8 suspended in DMF as a function of concentration (**Figure VII.2**). From 1-5 mg/mL no aggregation of the particles was observed. In fact, some size narrowing occurred with increasing concentration for the largest sized ZIF-8 nanoparticles.

We hypothesize that nanoparticles exhibiting stronger solvation shell, as evidenced by the large amplitude VSFSS signal, will display a higher CAC as the ordered solvation shell imparts colloidal stability. In particular, porous nanoparticles like ZIF-8 have less van der Waals attractive forces and stronger solvation shells as compared to nonporous nanoparticles (like TiO_2) and can therefore accommodate a greater concentration of nanoparticles before aggregation. This project addresses the vague associations between VSFSS signal and colloidal stability which is typically assumed but never tested. These results will provide insight into the relationship between ordered solvation shells and the colloidal stability of porous materials.

CHAPTER VIII: THE FUTURE OF VSFSS FOR PROBING UNIQUE MECHANISMS OF COLLOIDAL STABILITY

This dissertation described a variety of unique chemical systems that remain colloidally stable despite using mechanisms that cannot be explained by traditional DLVO theory alone. Functionalizing emulsions and MOF nanoparticles with polymeric layers, for example, provides a steric layer that can stabilize colloids with nearly zero surface charge. The discovery of ordered solvation shells for porous materials allows for further investigation into unconventional chemical ordering, such as solvent inside pores or ordered linker on the surface, that can give rise to colloidal stability. However, these physical insights would not have been possible without the surface specificity of VSFSS. The future of this scattering setup at the University of Oregon promises further investigation of the physical phenomena at buried interfaces that contributes to bulk properties of colloidal stability. The following paragraphs highlight some of the avenues for advancement of the laser setup and exciting new experiments.

Variable Temperature VSFSS

Understanding the temperature-dependent colloidal stability of nanoparticles is critical for their application in drug delivery systems, biosensing, and membrane filtration where temperatures can vary drastically.[363–366] Recent utilization of MOFs for water adsorption takes place in heating and cooling systems emphasizing the need for thermal stability.[367,368] Previous work from our lab has shown that optical shifts, phase transitions, metal-ligand binding strength, and molecular gaseous uptake in MOFs all vary with the influence of temperature.[369–373] In nanoMOFs, where surface-solvent or surface-substrate interaction dominate, these temperature-dependent behaviors are enhanced. We propose adapting the current VSFSS setup to study thermal-induced transitions occurring at nanoMOF surfaces. Expanding this system to perform temperature-dependent VSFS experiments involves few physical adjustments to the setup, centering around the sample cell holder. A custom-made sample cell from Quantum Northwest, already obtained by the Brozek group, will facilitate temperature-controlled measurements with a metallic cuvette holder and a single Peltier element.[374] Purging of the cell with N_2 gas will be necessary to prevent condensation of air on the cuvettes. As in previous VSFSS experiments, the front window of the cuvette will be CaF_2 and the back window will be quartz. Details regarding the experimental setup of the heating and cooling chambers are found from publications from the Roke lab.[375–377] Currently, the Scatena-

Brozek group is one of only five groups in the world that uses VSFSS.[378–381] Only the Roke group has provided evidence of temperature-dependent VSFS spectra, namely on frozen ice droplets in oil or oil droplets in frozen water. With the modification of our current setup to probe colloids at varying temperatures, we will provide fundamental insight to the impact of solvent thermodynamics and kinetics in the role of colloidal stability, variables previously unexplained by DLVO theory.

Complementary temperature-dependent size measurements of ZIF-8 in DMF been conducted in the cooling and heating directions to measure the ability of the colloid to return to its room temperature equilibrium state (**Figure VIII.1**). In the cooling direction, from 70 to 0 °C, very little change is observed in the hydrodynamic diameter and upon crossing the room temperature point (25 °C) the size closely resembles that of the colloid first upon formation (as indicated by the dotted line). However, in the heating direction nanoZIF-8 exhibits an irreversible aggregation feature. These preliminary results suggest unique solvent dependence to colloidal stability and that complex mechanisms of particle kinetics give rise to irreversible temperature variations. At higher temperatures, increased rates of collision would be expected to give rise to aggregated particles. Yet, the aggregation at lower temperatures could be explained by the reduced kinetic energy causing particles to adsorb to each other rather than face repulsion. Coupling these results with VT-VSFS will provide a picture of the molecular forces at interfaces that give rise to temperature-dependent colloidal behavior.

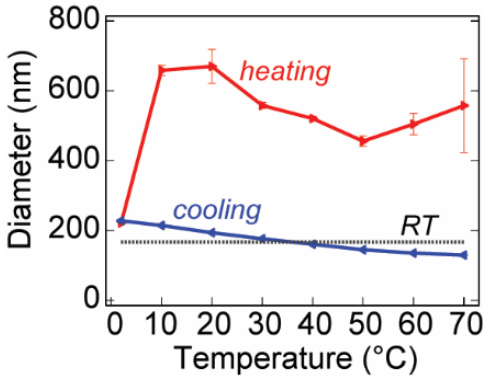

Figure VIII. 1 Temperature dependent hydrodynamic diameter of 5 mg/mL nanoZIF-8 in DMF.

nanoMOF Electrolyte-Resistance

With the utility of MOFs for a variety of storage, delivery, or filtration applications, nanoMOF particles prepared into membranes need to be colloidally stable against electrolytes. This is especially relevant in drug delivery systems where the wide variety of ions present in biological media can significantly impact nanoparticle colloidal stability.[291,382] Beyond their practical importance, significant interest lies in understanding the Hofmeister series for other materials besides proteins. Preliminary data of electrolyte titrations into solutions of $Cu(TA)_2$ suggest that nanoMOFs follow the Hofmeister series exhibited for proteins (**Figure VIII.2A**) but are still colloidally stable at the point of zero charge. In other words, $Cu(TA)_2$ nanoparticles maintain a small diameter in solutions of DMF despite having nearly 0 mV of electrostatic charge at the surface. These results are corroborated with VSFS spectra of ZIF-8 nanoparticles suspended in DMF with varying concentration of the bulky electrolyte, $TBAPF_6$ (**Figure VIII.2B**). From with the addition of 5 mM $TBAPF_6$, the same concentration used to reach the point of zero charge for $Cu(TA)_2$ nanoparticles, very little change in the zeta potential and VSFS spectra is observed, suggesting that the bulky electrolyte has little impact on the ZIF-8 surface at these concentrations. With even further addition of $TBAPF_6$, a charge inversion is passed between 7.5 mM and 10 mM. Despite this charge inversion, the ZIF-8 nanoparticles remained colloidally stable and were able

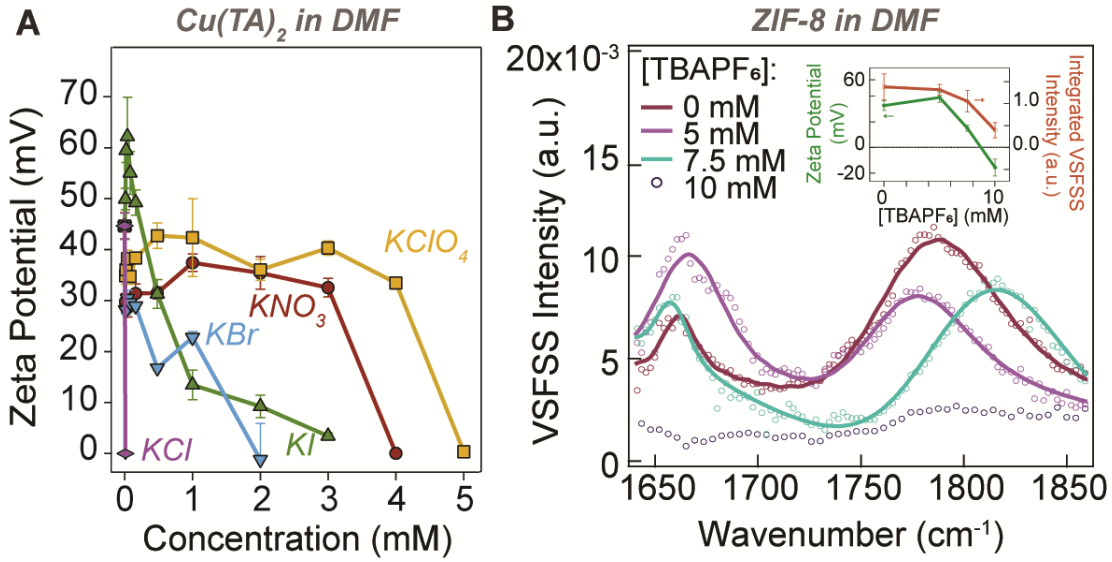

Figure VIII. 2 a) Zeta potential of Cu(TA)2 nanoparticles in DMF with varying amounts of electrolyte. b) VSFSS spectra of ZIF-8 nanoparticles with TBAPF6. Inset shows the zeta potential and integrated VSFSS area as a function of concentration.

to be measured by VSFSS, meaning they had a particle diameter that closely resembled that of ZIF-8 with 0 mM $TBAPF_6$.

Continuing to measure the influence of electrolyte addition on colloidal stability by both zeta potential and VSFSS which will provide insight into the surface charge and solvation shell ordering, respectively. In particular, we are interested in how small ions intercalate into the pores and alter the colloidal stability. These results will prove useful for applications of nanoMOFs in a variety of solutions that contain small ions. Probing specific ion interactions by using electrolytes in the Hofmeister series will bridge the knowledge gap between the solvation of pseudo porous materials like polymers and proteins with permanently porous materials, like nanoMOFs.

APPENDIX A: SUPPLEMENTARY INFORMATION FOR CHAPTER III

Percent Protonation Curve

The percent protonation of poly(acrylic-acid) (PAA) was calculated using:

$$\% \, Protonation = \frac{[H_3O^+]}{[H_3O^+] + K_a} \qquad (A1)$$

as a function of pH.[106] The known pK_a of PAA (~4.5) was used for the bulk % protonation curve.[187] To calculate the interfacial pK_a of PAA, the zeta potential (ZP) of *d*-hexadecane emulsions stabilized with 500 ppm PAA in D_2O was measured as a function of pH. Plotting the -log(ZP) as a function of pH results in two regimes, one with an appreciable slope and one relatively flat, where the intersection of those lines is defined as the surface pK_a (Figure A1).[206] For this system, a surface pK_a of 5.3 was measured, consistent with previous work that predicts dissociation at the surface to be more basic than in the bulk.

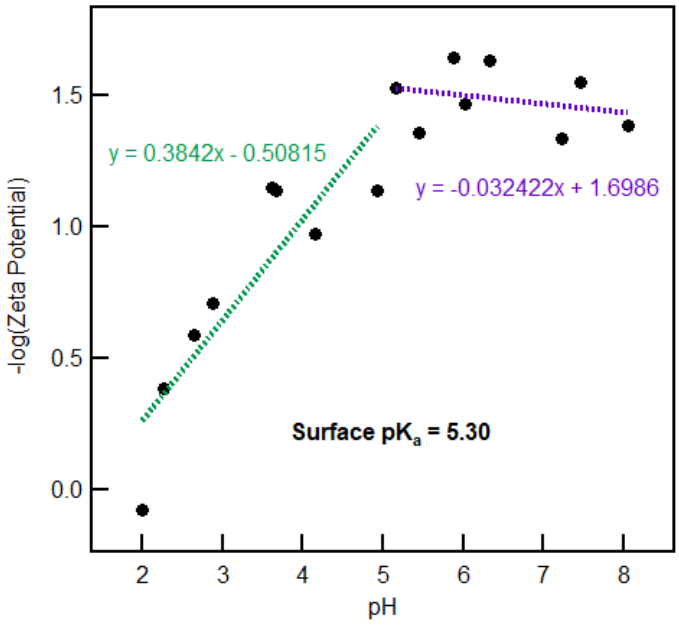

Figure A. 1 Zeta potential of 500 ppm PAA-stabilized d-hexadecane emulsions in water as a function of pH. Linear analyses define the two regimes, while the intersection of the lines provides the experimentally derived surface pKa.

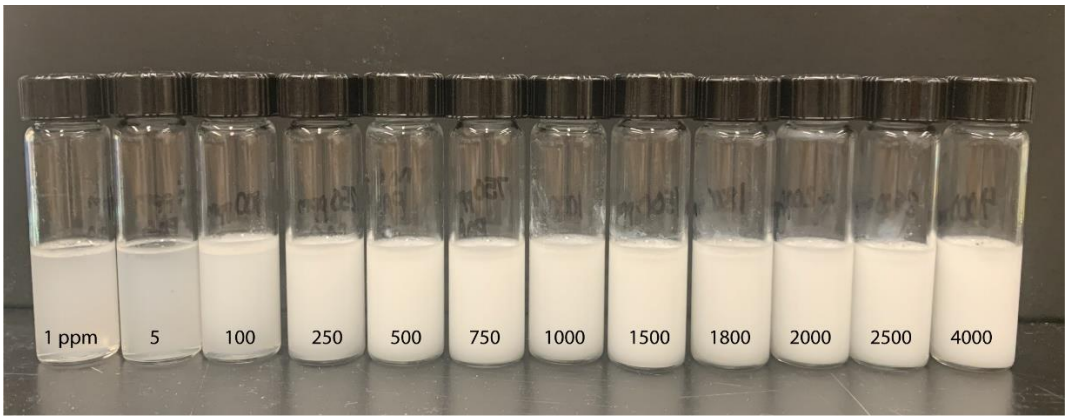

Figure A. 2 Visual representation of the time-dependent colloidal stability of PAA-coated emulsions prepared with varying concentrations of PAA in pH 4 conditions. This photo was taken 1 week after formation, demonstrating that emulsions prepared at and below ppm are unstable.

Table A. 1 Emulsion zeta potential (measured upon formation) and long-term stability as a function of PAA concentration. Stability was determined visually, as unstable colloids showed phase separation while stable colloids remained turbid.

[PAA] in emulsion (ppm)	Zeta Potential (mV)	Stable after 7 days?
1	-32.9 ± 1.7	No
5	-23.0 ± 0.9	No
100	-35.8 ± 0.4	No
250	-22.9 ± 0.6	No
500	-23.4 ± 0.4	Yes
750	-10 ± 1	Yes
1000	-9.5 ± 0.6	Yes
1500	-6.7 ± 0.3	Yes
2000	-4.6 ± 0.2	Yes
2500	-5.4 ± 0.5	Yes
4000	-3.7 ± 0.7	Yes

Surface Activity of PAA and PAA/Salt Mixtures

Pendant drop surface tensiometery was used to measure the surface pressure of PAA with and without added salt at the hexadecane/water interface. In the pendant drop method, the curvature of an oil droplet suspended in aqueous solution is fit to the Young-Laplace equation to determine the surface tension. Further details on the technique can be found elsewhere.[383]

PAA is surface active in all pH conditions (Figure S2). The natural pH of the aqueous polymer solution is pH 4, and DCl or NaOD is added to adjust the solution to acidic or basic conditions, respectively. While pendant drop surface tensiometery provides insight into PAA surface activity, it is not a direct measurement of polymer adsorption to the emulsion interface.

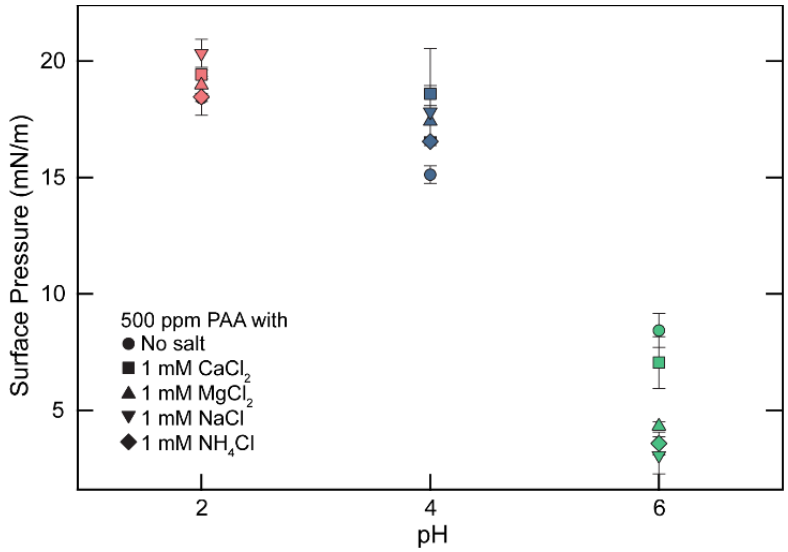

Figure A. 3 Equilibrium surface pressure of 500 ppm PAA with no salt (circles), 1 mM CaCl2 (squares), 1 mM MgCl2 (upward triangles), 1 mM NaCl (downward triangles), or 1 mM NH4Cl (diamonds) measured by pendant drop surface tensiometery at the hexadecane and water interface in varying pH conditions.

The polymer is most surface active at pH 2 and has very little surface population at pH 6. These results are consistent with previous studies of the interfacial behavior of PAA, where at pH 6, the polymer is significantly deprotonated and would prefer to be solvated in the aqueous phase.[191] In general, the addition of salt does not significantly increase nor decrease the population of PAA at the interface. An increase in surface pressure with the presence of salt could indicate that the polymer is layering at the interface while a decrease in surface pressure could suggest that the charged moieties of the polymer would rather interact with the cations in the bulk phase and is

desorbing from the interface. In this system however, neither of these trends are observed, allowing us to intuit that any changes in vibrational sum frequency scattering spectra can be attributed to molecular reorientation with negligible changes in surface population.

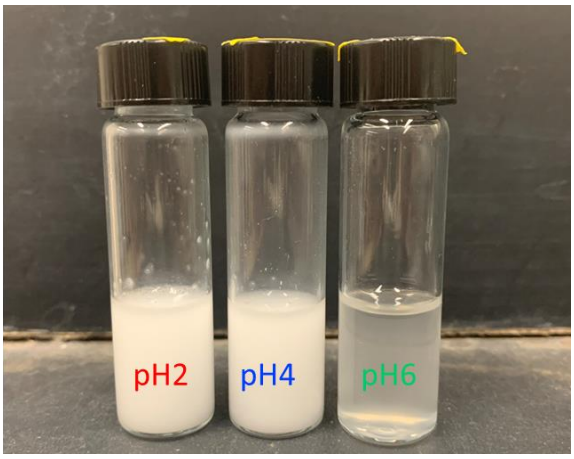

Figure A. 4 Visual representation of the time-dependent colloidal stability of emulsions stabilized with 500 ppm PAA prepared at pH 2, pH 4, and pH 6. After 1 week, pH 2 and pH 4 emulsions are still turbid while the pH 6 sample has phase separated.

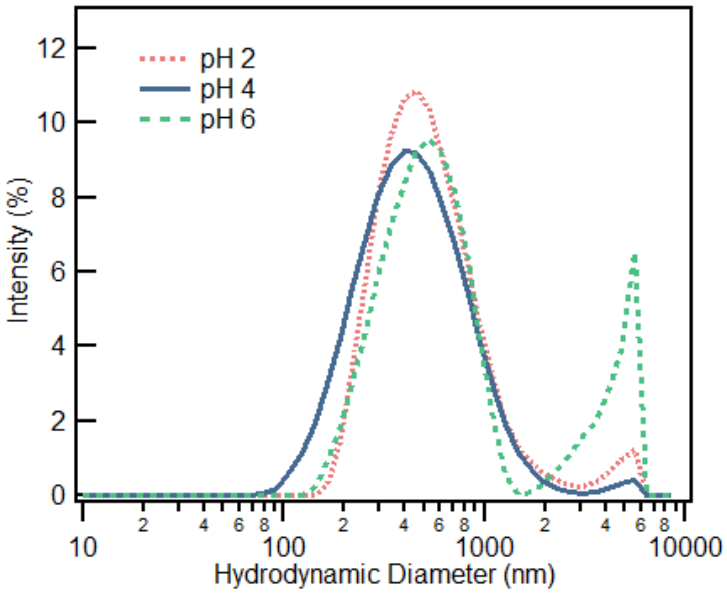

Figure A. 5 Hydrodynamic diameter distribution curves of colloids coated with 500 ppm PAA at pH 2, pH 4, and pH 6 demonstrating the monomodal nature of pH 2 and pH 4 emulsions and subsequently low polydispersity index.

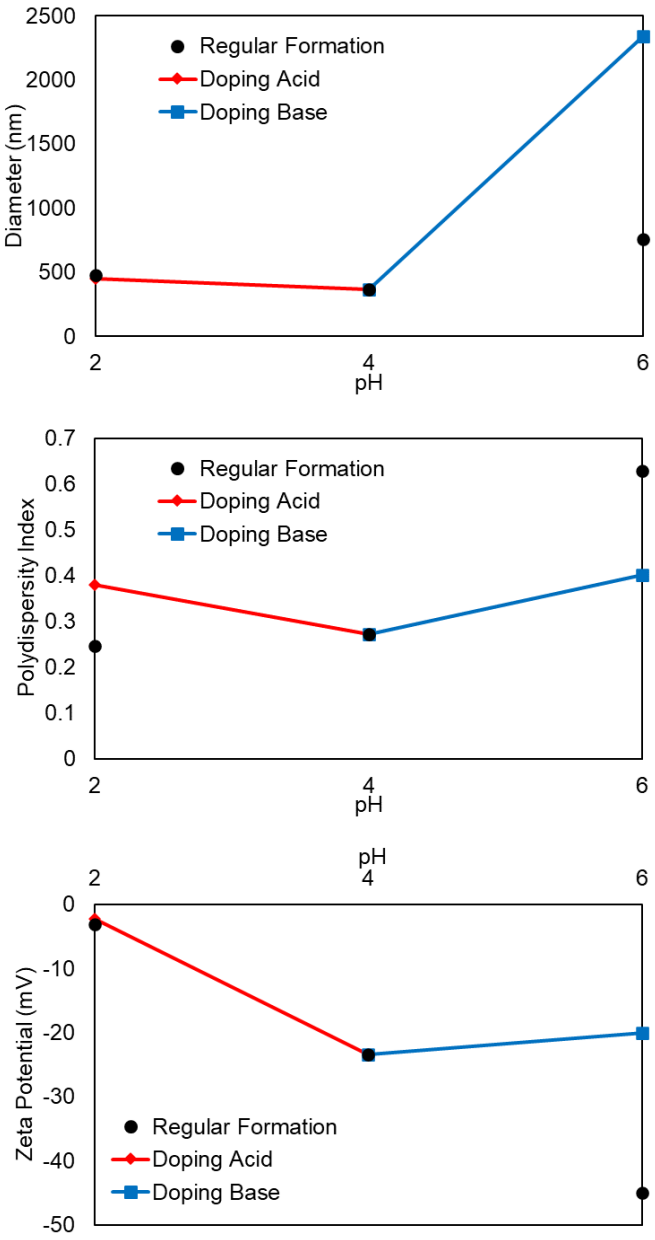

Figure A. 6 Dynamic light scattering and Zeta Potential measurements of hexadecane in water emulsions ultrasonicated with 500 ppm poly(acrylic acid). Regular formation describes droplets ultrasonicated with acid or base while the doping traces describe droplets initially prepared at the natural pH (4) with acid or base added after ultrasonication.

Table A. 2 Polydispersity index (PDI) values of all emulsion samples studied by VSFSS. All samples prepared at pH 2 and pH 4 are moderately polydisperse while all pH 6 samples are broadly polydisperse.

Sample Conditions		PDI
No salt	pH 2	0.247
	pH 4	0.272
	pH 6	0.628
1 mM $CaCl_2$	pH 2	0.279
	pH 4	0.225
	pH 6	0.375
1 mM $MgCl_2$	pH 2	0.281
	pH 4	0.275
	pH 6	0.901
3 mM NaCl	pH 2	0.276
	pH 4	0.255
	pH 6	0.915
3 mM NH_4Cl	pH 2	0.298
	pH 4	0.282
	pH 6	0.761

Calculation of Hydrophilic-Lipophilic Balance

The Hydrophlilic-Lipophilic Balance (HLB) describes the degree of water or oil solubility of a surfactant. A lower HLB value indicates better oil solubility (and can be better for forming water in oil emulsions), while a higher HLB value indicates better water solubility (ideal for oil in water emulsions).

Here we calculate HLB values for poly(acrylic acid) at pH 2, 4, 6 using the group numbers for hydrophilic moieties and the equation formulated by Davies.[223]

$$HLB = 7 + \sum_{i-1}^{m} H_i - n \times 0.475 \qquad (A2)$$

Where m is the number of hydrophilic groups in the molecule, H_i is the value of the i^{th} hydrophilic group (see table below), and n is the number of lipophilic groups in the molecule.

Group	Group Number
$-COO^-$	19.1
-COOH	2.1
Lipophilic group (i.e. CH, CH_2)	-0.475

To perform this calculation with pH in mind, we use the experimentally derived % protonation.

For example, the HLB for PAA at pH 4 (with 95.2% protonation) is calculated by:

$$HLB = 7 + \%prot\big(COOH - (2 \times 0.475)\big) + \%deprot\big(COO^{-} - (2 \times 0.475)\big) \qquad (A3)$$

$$HLB = 7 + 0.952\big(2.1 - (2 \times 0.475)\big) + 0.048\big(19.1 - (2 \times 0.475)\big) \qquad (A4)$$

The HLB values for the polymer at each pH is summarized in the table below. While the addition of salts cannot be directly included in the calculation of HLB, it is assumed that adding salts will reduce the HLB by reducing the hydrophilic character of the deprotonated carboxylic acid.

pH	HLB
2	8.17
4	8.97
6	22.3

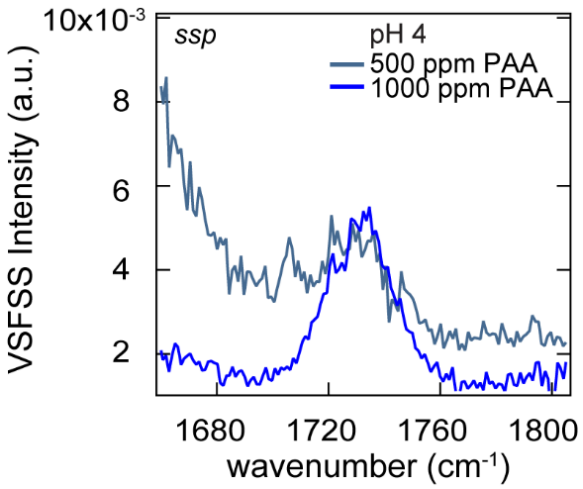

Figure A. 7 VSFSS measurements (ssp polarization) of d-hexadecane emulsions in D2O stabilized with 500 ppm and 1000 ppm PAA at pH 4 in the C=O stretching region.

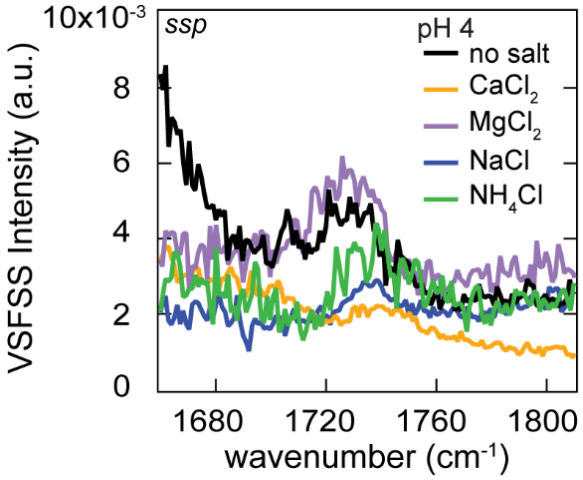

Figure A. 8 VSFSS measurements (ssp polarization) of d-hexadecane emulsions D2O stabilized with 500 ppm PAA with 2 mM ionic strength salt at pH 4 in C=O stretching region.

Table A. 3 Fitting parameters for CH spectra of d-hexadecane emulsions in water coated with 500 ppm PAA and no salt, corresponding to Figure III.3.

Alkane C-H Stretches, *ssp* polarization			
PAA concentration = 500 ppm **No Salt**			
Peak Assignment	**Parameters**	**pH 2**	**pH 4**
Methine Stretch	Amplitude	0.074 ± 0.002	0.133 ± 0.002
	Phase	0	0
	Lorentzian linewidth	2	2
	Peak position	2876.0 ± 0.9	2877.0 ± 0.6
	Gaussian linewidth	58.7 ± 0.9	53 ± 1
Methylene Symmetric Stretch	Amplitude	0.175 ± 0.003	0.260 ± 0.004
	Phase	0	0
	Lorentzian linewidth	2	2
	Peak position	2931.8 ± 0.3	2928.7 ± 0.3
	Gaussian linewidth	15.3 ± 0.3	16.4 ± 0.3
Methyl Symmetric Stretch Fermi Resonance and Methyl Bending Overtones	Amplitude	0.011 ± 0.08	0.014 ± 0.02
	Phase	0	0
	Lorentzian linewidth	2	2
	Peak position	2930 ± 2	2933 ± 2
	Gaussian linewidth	0.009 ± 0.001	2 ± 4
Non-resonant Contribution	Amplitude	0.009 ± 0.002	0.012 ± 0.002
	Phase	0	0

Table A. 4 Fitting parameters for C=O spectra of d-hexadecane emulsions in water coated with 500 ppm PAA and no salt, corresponding to Figure III.3.

C=O stretches, *ssp* polarization			
PAA concentration = 500 ppm **No Salt**			
Peak Assignment	**Parameters**	**pH 2**	**pH 4**
Background Peak 1	Amplitude	0.07 ± 0.01	0.17 ± 0.02
	Phase	3.14	3.14
	Lorentzian linewidth	10	10
	Peak position	1628 ± 0	1628 ± 11
	Gaussian linewidth	75 ± 4	27 ± 5
C=O Stretch	Amplitude		0.10 ± 0.01
	Phase		0
	Lorentzian linewidth		5
	Peak position		1735 ± 3
	Gaussian linewidth		19 ± 2
Background Peak 2	Amplitude	0.038 ± 0.003	0.07 ± 0.01
	Phase	3.14	3.14
	Lorentzian linewidth	10	10
	Peak position	1793 ± 0	1793 ± 5
	Gaussian linewidth	194 ± 82	27 ± 12
Non-resonant Contribution	Amplitude	0	0
	Phase	0	0

Table A. 5 Fitting parameters for spectra of d-hexadecane emulsions in water coated with 500 ppm PAA and 1 mM CaCl2, corresponding to Figure III.5.

Alkane C-H Stretches, *ssp* polarization			
PAA concentration = 500 ppm **$CaCl_2$ = 1 mM**			
Peak Assignment	**Parameters**	**pH 2**	**pH 4**
Methine Stretch	Amplitude	0.111 ± 0.007	0.162 ± 0.007
	Phase	0	0
	Lorentzian linewidth	2	2
	Peak position	2877.2 ± 0.4	2878.2 ± 0.8
	Gaussian linewidth	60.0 ± 0.5	55.0 ± 0.5
Methylene Symmetric Stretch	Amplitude	0.186 ± 0.003	0.280 ± 0.004
	Phase	0	0
	Lorentzian linewidth	2	2
	Peak position	2929 ± 2	2924.7 ± 0.9
	Gaussian linewidth	15.5 ± 0.2	17.1 ± 0.2
Methyl Symmetric Stretch Fermi Resonance and Methyl Bending Overtones	Amplitude	0.013 ± 0.061	0.075 ± 0.009
	Phase	0	0
	Lorentzian linewidth	2	2
	Peak position	2931.4 ± 0.1	2932.5 ± 0.2
	Gaussian linewidth	1 ± 5	65.9 ± 0.9
Non-resonant Contribution	Amplitude	0.009 ± 0.002	0.020 ± 0.002
	Phase	0	0

Table A. 6 Fitting parameters for spectra of d-hexadecane emulsions in water coated with 500 ppm PAA and 1 mM MgCl2, corresponding to Figure III.5.

Alkane C-H Stretches, *ssp* polarization			
PAA concentration = 500 ppm **$MgCl_2$ = 1 mM**			
Peak Assignment	**Parameters**	**pH 2**	**pH 4**
Methine Stretch	Amplitude	0.05 ± 0.01	0.061 ± 0.008
	Phase	0	0
	Lorentzian linewidth	2	2
	Peak position	2880 ± 2	2875.0 ± 0.7
	Gaussian linewidth	32 ± 4	55 ± 1
Methylene Symmetric Stretch	Amplitude	0.17 ± 0.02	0.11 ± 0.02
	Phase	0	0
	Lorentzian linewidth	2	2
	Peak position	2935 ± 2	2931 ± 1
	Gaussian linewidth	18.5 ± 0.9	17 ± 2
Methyl Symmetric Stretch Fermi Resonance and Methyl Bending Overtones	Amplitude	0.04 ± 0.02	0.026 ± 0.024
	Phase	0	0
	Lorentzian linewidth	2	2
	Peak position	2932.2 ± 0.7	2929.5 ± 0.8
	Gaussian linewidth	8 ± 2	9 ± 3
Non-resonant Contribution	Amplitude	0.007 ± 0.003	0.003 ± 0.002
	Phase	0	0

Table A. 7 Fitting parameters for spectra of d-hexadecane emulsions in water coated with 500 ppm PAA and 3 mM NaCl, corresponding to Figure III.5.

Alkane C-H Stretches, *ssp* polarization			
PAA concentration = 500 ppm **NaCl = 3 mM**			
Peak Assignment	**Parameters**	**pH 2**	**pH 4**
Methine Stretch	Amplitude	0.09 ± 0.1	0.080 ± 0.005
	Phase	0	0
	Lorentzian linewidth	2	2
	Peak position	2880 ± 1	2874.8 ± 0.9
	Gaussian linewidth	40 ± 3	50 ± 1
Methylene Symmetric Stretch	Amplitude	0.228 ± 0.004	0.187 ± 0.002
	Phase	0	0
	Lorentzian linewidth	2	2
	Peak position	2931.7 ± 0.6	2933.2 ± 0.4
	Gaussian linewidth	16.5 ± 0.2	16.1 ± 0.2
Methyl Symmetric Stretch Fermi Resonance and Methyl Bending Overtones	Amplitude	0.001 ± 0.002	0.05 ± 0.01
	Phase	0	0
	Lorentzian linewidth	2	2
	Peak position	2930 ± 2	2932.9 ± 0.2
	Gaussian linewidth	138 ± 10	66.7 ± 0.9
Non-resonant Contribution	Amplitude	0.002 ± 0.002	0.008 ± 0.002
	Phase	0	0

Table A. 8 Fitting parameters for spectra of d-hexadecane emulsions in water coated with 500 ppm PAA and 3 mM NH4Cl, corresponding to Figure III.5.

Alkane C-H Stretches, *ssp* polarization			
PAA concentration = 500 ppm **NH_4Cl = 3 mM**			
Peak Assignment	**Parameters**	**pH 2**	**pH 4**
Methine Stretch	Amplitude	0.075 ± 0.005	0.073 ± 0.01
	Phase	0	0
	Lorentzian linewidth	2	2
	Peak position	2878.1 ± 0.5	2877.7 ± 0.6
	Gaussian linewidth	54.6 ± 0.8	57.4 ± 0.9
Methylene Symmetric Stretch	Amplitude	0.130 ± 0.002	0.188 ± 0.002
	Phase	0	0
	Lorentzian linewidth	2	2
	Peak position	2932.9 ± 0.4	2932.4 ± 0.4
	Gaussian linewidth	15.6 ± 0.2	15.6 ± 0.2
Methyl Symmetric Stretch Fermi Resonance and Methyl Bending Overtones	Amplitude	0.047 ± 0.007	0.008 ± 0.01
	Phase	0	0
	Lorentzian linewidth	2	2
	Peak position	2936.1 ± 0.2	2939 ± 2
	Gaussian linewidth	70.5 ± 0.6	64 ± 8
Non-resonant Contribution	Amplitude	0.002 ± 0.002	0.0005 ± 0.002
	Phase	0	0

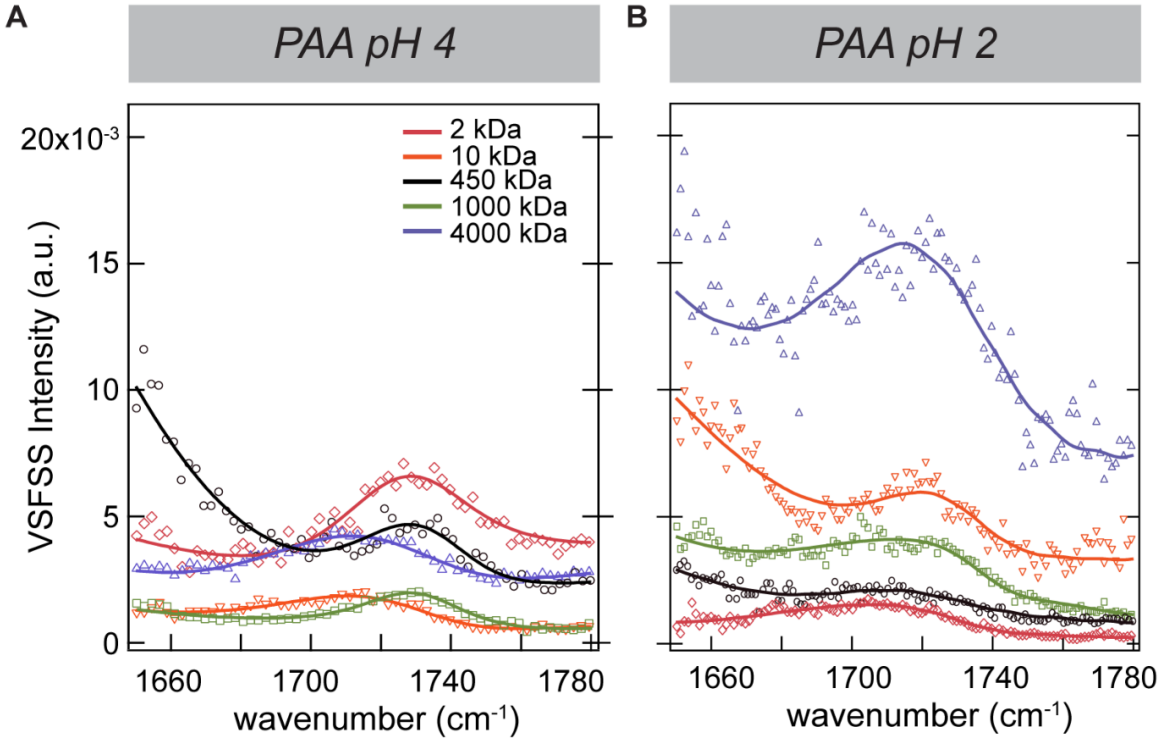

Figure B. 1 VSFSS measurements (ssp polarization) of D-hexadecane emulsions in D2O stabilized with 500 ppm PAA of varying molecular weight at pH 4 (A) and pH 2 (B) in the C=O stretching region. Solid lines represent fits of the data.

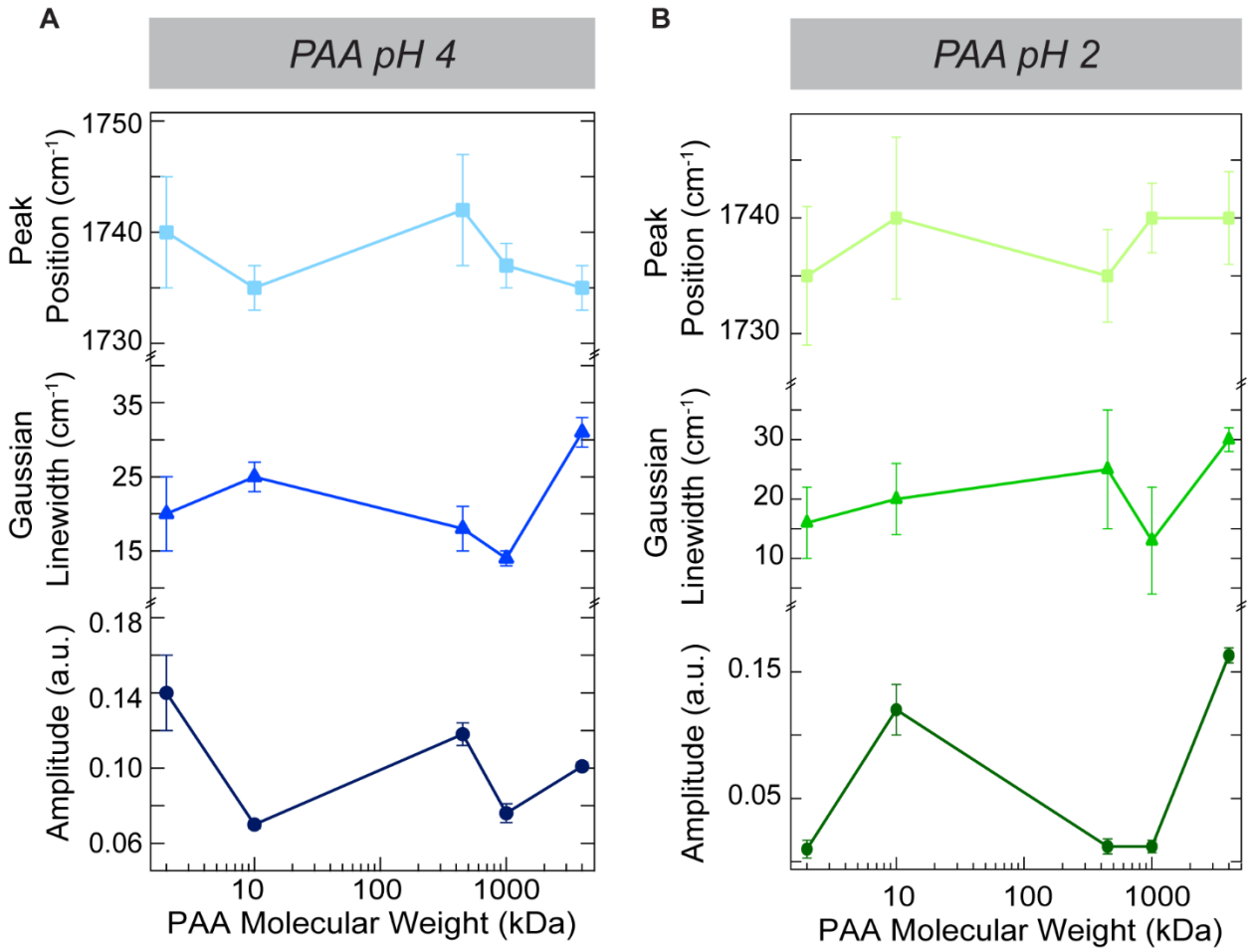

Figure B. 2 Fit parameter trends for VSFSS measurements of PAA of varying molecular weight at pH 4 (A) and pH 2 (B) in the C=O stretching region, corresponding to Figure B1.

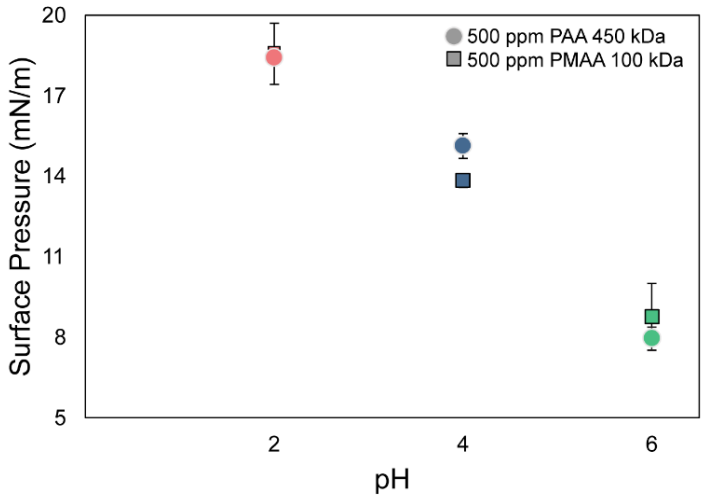

Figure B. 3 Equilibrium surface pressure of 500 ppm poly(acrylic acid) (circles) and 500 ppm poly(methacrylic acid) (squares) measured by pendant drop surface tensiometery at the hexadecane and water interface in varying pH conditions.

Table B. 1 Characteristics (diameter, polydispersity index, and zeta potential) of nanoemulsions formed with 500 ppm and 2687 ppm poly(methacrylic acid) (PMAA) at varying pH conditions.

[PMAA] (ppm)	*pH*	*Diameter (nm)*	*Polydispersity Index*	*Zeta Potential (mV)*
500	2	491.5	0.196	-4.21
	4	505.9	0.265	-8.47
	6	720.0	0.433	-23.4
2687	2	383.0	0.200	-1.71
	4	280.6	0.232	-5.33
	6	572.8	0.674	-44.0

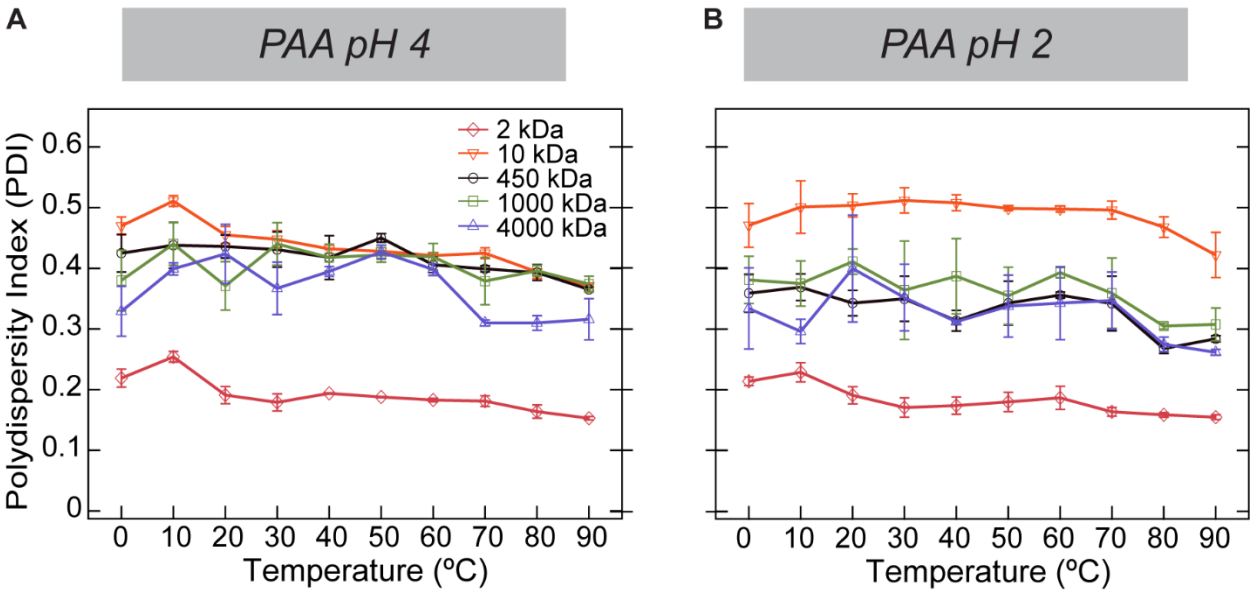

Figure B. 4 Polydispersity index (PDI) of nanoemulsions coated with 500 ppm PAA of varying molecular weight as a function of temperature at (A) pH 4 and (B) pH 2.

Table B. 2 Fitting parameters for C-H spectra of d-hexadecane emulsions in D2O coated with 500 ppm PAA with varying molecular weight, corresponding to Figure IV.3 and Figure IV.4.

Alkane C-H Stretches, *ssp* polarization						
PAA, pH 4						
Peak Assignment	**Parameters**	**2 kDa**	**10 kDa**	**450 kDa**	**1000 kDa**	**4000 kDa**
Methine Stretch	Amplitude	0.045 ± 0.001	0.0486 ± 0.0009	0.074 ± 0.002	0.073 ± 0.001	0.0544 ± 0.0009
	Phase	0	0	0	0	0
	Lorentzian linewidth	2	2	2	2	2
	Peak position	2868.2 ± 0.6	2873.3 ± 0.5	2871 ± 1	2865.3 ± 0.5	2870.7 ± 0.5
	Gaussian linewidth	62 ± 2	57.8 ± 0.8	42 ± 2	58.0 ± 0.8	60.0 ± 0.8
Methylene Symmetric Stretch	Amplitude	0.101 ± 0.001	0.105 ± 0.001	0.190 ± 0.003	0.156 ± 0.002	0.117 ± 0.001
	Phase	0	0	0	0	0
	Lorentzian linewidth	2	2	2	2	2
	Peak position	2931.1 ± 0.4	2930.9 ± 0.3	2931.5 ± 0.4	2928.0 ± 0.2	2930.6 ± 0.2
	Gaussian linewidth	15.8 ± 0.3	16.7 ± 0.2	17.1 ± 0.3	15.8 ± 0.2	15.7 ± 0.2
Non-resonant	Amplitude	0.003 ± 0.001	0.0031 ± 0.0007	0.010 ± 0.002	0.003 ± 0.001	0.0009 ± 0.0008
	Phase	0	0	0	0	0
pH 2						
Peak Assignment	**Parameters**	**2 kDa**	**10 kDa**	**450 kDa**	**1000 kDa**	**4000 kDa**
Methine Stretch	Amplitude	0.049 ± 0.003	0.04 ± 0.02	0.073 ± 0.002	0.194 ± 0.004	0.139 ± 0.003
	Phase	0	0	0	0	0
	Lorentzian linewidth	2	2	2	2	2
	Peak position	2871 ± 1	2871 ± 3	2872 ± 2	2872 ± 2	2871 ± 1
	Gaussian linewidth	134 ± 3	78 ± 5	60 ± 3	82 ± 4	111 ± 2
Methylene Symmetric Stretch	Amplitude	0.171 ± 0.004	0.17 ± 0.01	0.181 ± 0.004	0.460 ± 0.006	0.285 ± 0.005
	Phase	0	0	0	0	0
	Lorentzian linewidth	2	2	2	2	2
	Peak position	2932.7 ± 0.5	2933 ± 3	2932.0 ± 0.4	2929.3 ± 0.3	2931.9 ± 0.4
	Gaussian linewidth	14.3 ± 0.5	12 ± 1	15.4 ± 0.3	14.6 ± 0.2	14.9 ± 0.4
Non-resonant	Amplitude	0.003 ± 0.003	0.02 ± 0.01	0.012 ± 0.002	0.005 ± 0.004	0.004 ± 0.004
	Phase	0	0	0	0	0

Table B. 3 Fitting parameters for C=O spectra of d-hexadecane emulsions in D2O coated with 500 ppm PAA with varying molecular weight, corresponding to Figure B1.

C=O Stretches, *ssp* polarization						
PAA, pH 4						
Peak Assignment	**Parameters**	**2 kDa**	**10 kDa**	**450 kDa**	**1000 kDa**	**4000 kDa**
Background Peak 1	Amplitude	0.08 ± 0.01	0.046 ± 0.002	0.170 ± 0.007	0.17 ± 0.07	0.18 ± 0.08
	Phase	3.14	3.14	3.14	3.14	3.14
	Lorentzian linewidth	10	10	10	10	10
	Peak position	1555 ± 42	1593 ± 7	1603 ± 6	1527 ± 16	1479 ± 34
	Gaussian linewidth	90 ± 43	31 ± 6	46 ± 7	32 ± 6	65 ± 7
C=O Stretch	Amplitude	0.14 ± 0.02	0.070 ± 0.002	0.118 ± 0.006	0.076 ± 0.005	0.101 ± 0.002
	Phase	0	0	0	0	0
	Lorentzian linewidth	5	5	5	5	5
	Peak position	1740 ± 5	1735 ± 2	1742 ± 5	1737 ± 2	1735 ± 2
	Gaussian linewidth	20 ± 5	25 ± 2	18 ± 3	14 ± 1	31 ± 2
Background Peak 2	Amplitude	0.091 ± 0.005	0.0318 ± 0.0009	0.065 ± 0.008	0.12 ± 0.02	0.09 ± 0.01
	Phase	3.14	3.14	3.14	3.14	3.14
	Lorentzian linewidth	10	10	10	10	10
	Peak Position	1862 ± 25	1956 ± 39	1830 ± 40	2134 ± 95	1935 ± 50
	Gaussian linewidth	113 ± 32	427 ± 67	88 ± 40	255 ± 64	179 ± 37
Non-resonant	Amplitude	0.03 ± 0.01	0.019 ± 0.002	0.007 ± 0.006	0.05 ± 0.01	0.03 ± 0.02
	Phase	0	0	0	0	0

Table B3. *Continued from previous page*

PAA, pH 2						
Peak Assignment	**Parameters**	**2 kDa**	**10 kDa**	**450 kDa**	**1000 kDa**	**4000 kDa**
Background Peak 1	Amplitude	0.028 ± 0.003	0.13 ± 0.01	0.029 ± 0.007	0.03 ± 0.01	0.19 ± 0.01
	Phase	3.14	3.14	3.14	3.14	3.14
	Lorentzian linewidth	10	10	10	10	0
	Peak position	1694 ± 10	1583 ± 14	1721 ± 6	1705 ± 10	1577 ± 11
	Gaussian linewidth	50 ± 11	63 ± 17	44 ± 4	47 ± 17	25 ± 8
C=O Stretch	Amplitude	0.010 ± 0.007	0.12 ± 0.02	0.012 ± 0.006	0.012 ± 0.005	0.163 ± 0.006
	Phase	0	0	0	0	0
	Lorentzian linewidth	5	5	5	5	5
	Peak position	1735 ± 6	1740 ± 7	1735 ± 4	1740 ± 3	1740 ± 4
	Gaussian linewidth	16 ± 6	20 ± 6	25 ± 10	13 ± 9	30 ± 2
Background Peak 2	Amplitude	0.7 ± 0.2	0.4 ± 0.1	1.04 ± 0.07	1.1 ± 0.6	0.67 ± 0.05
	Phase	3.14	3.14	3.14	3.14	3.14
	Lorentzian linewidth	10	10	10	10	10
	Peak Position	2539 ± 257	2205 ± 189	2506 ± 65	2539 ± 550	2305 ± 45
	Gaussian linewidth	365 ± 117	270 ± 111	360 ± 31	378 ± 269	309 ± 28
Non-resonant	Amplitude	0.23 ± 0.06	0.12 ± 0.05	0.34 ± 0.02	0.4 ± 0.2	0.25 ± 0.02
	Phase	0	0	0	0	0

Table B. 4. Fitting parameters for C-H spectra of d-hexadecane emulsions in D2O coated with 500 ppm PMAA, corresponding to Figure IV.7A.

Alkane C-H Stretches, *ssp* polarization			
PMAA, 500 ppm			
Peak Assignment	**Parameters**	**pH 2**	**pH 4**
Polymer Endcap Methyl Stretch	Amplitude	0.054 ± 0.002	0.067 ± 0.004
	Phase	0	0
	Lorentzian linewidth	2	2
	Peak position	2887.0 ± 0.8	2890 ± 5
	Gaussian linewidth	121 ± 2	80 ± 8
Methyl Symmetric Stretch	Amplitude	0.097 ± 0.003	0.172 ± 0.005
	Phase	0	0
	Lorentzian linewidth	2	2
	Peak position	2939.8 ± 0.7	2937.1 ± 0.9
	Gaussian linewidth	22.1 ± 0.8	22.0 ± 0.6
Non-resonant	Amplitude	0.002 ± 0.002	0.003 ± 0.003
	Phase	0	0

Table B. 5 Fitting parameters for C=O spectra of d-hexadecane emulsions in D2O coated with 500 ppm PMAA, corresponding to Figure IV.7B.

C=O stretches, *ssp* polarization			
PMAA, 500 ppm			
Peak Assignment	**Parameters**	**pH 2**	**pH 4**
Background Peak	Amplitude	0.16 ± 0.01	0.047 ± 0.001
	Phase	0	0
	Lorentzian linewidth	5	5
	Peak position	1536 ± 13	1470 ± 7
	Gaussian linewidth	87 ± 9	242 ± 8
C=O Stretch	Amplitude	0.051 ± 0.002	0.0205 ± 0.0006
	Phase	0	0
	Lorentzian linewidth	5	5
	Peak position	1735.6 ± 0.6	1736.4 ± 0.6
	Gaussian linewidth	22 ± 1	21 ± 1
Non-resonant Contribution	Amplitude	0.121 ± 0.004	0.0699 ± 0.0006
	Phase	0	0

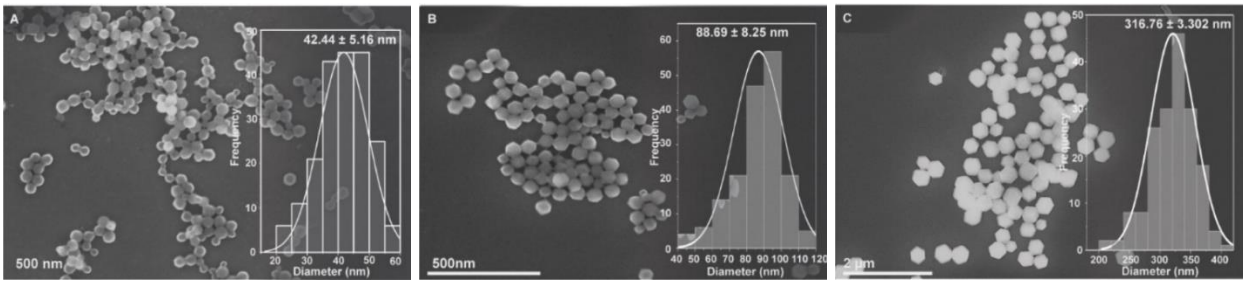

Figure C. 1 SEM images of ZIF-8 nanoparticles of a) 36 nm, b) 60 nm, and c) 96 nm crystallite size as determined by Scherrer analysis.

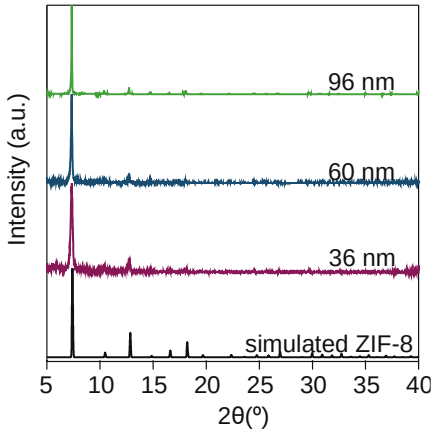

Figure C. 2 PXRD patterns of powder nanoZIF-8 synthesized for three different sizes. Expected reflections are shown as the bottom trace. Sizes are determined by Scherrer analysis.

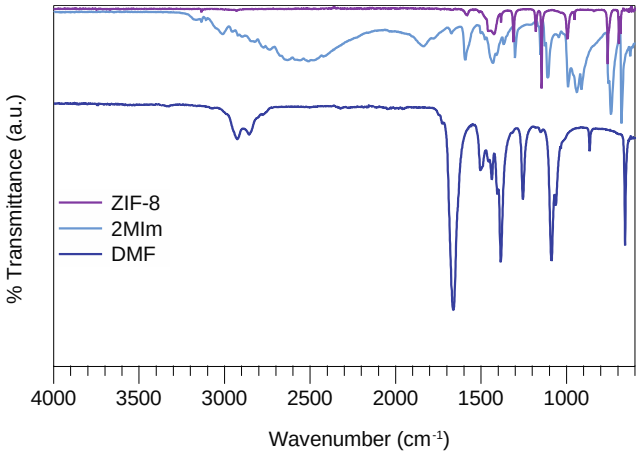

Figure C. 3 FT-IR spectra of neat DMF, powder 2-methylimidazole, and powder ZIF-8 (96 nm crystallite size).

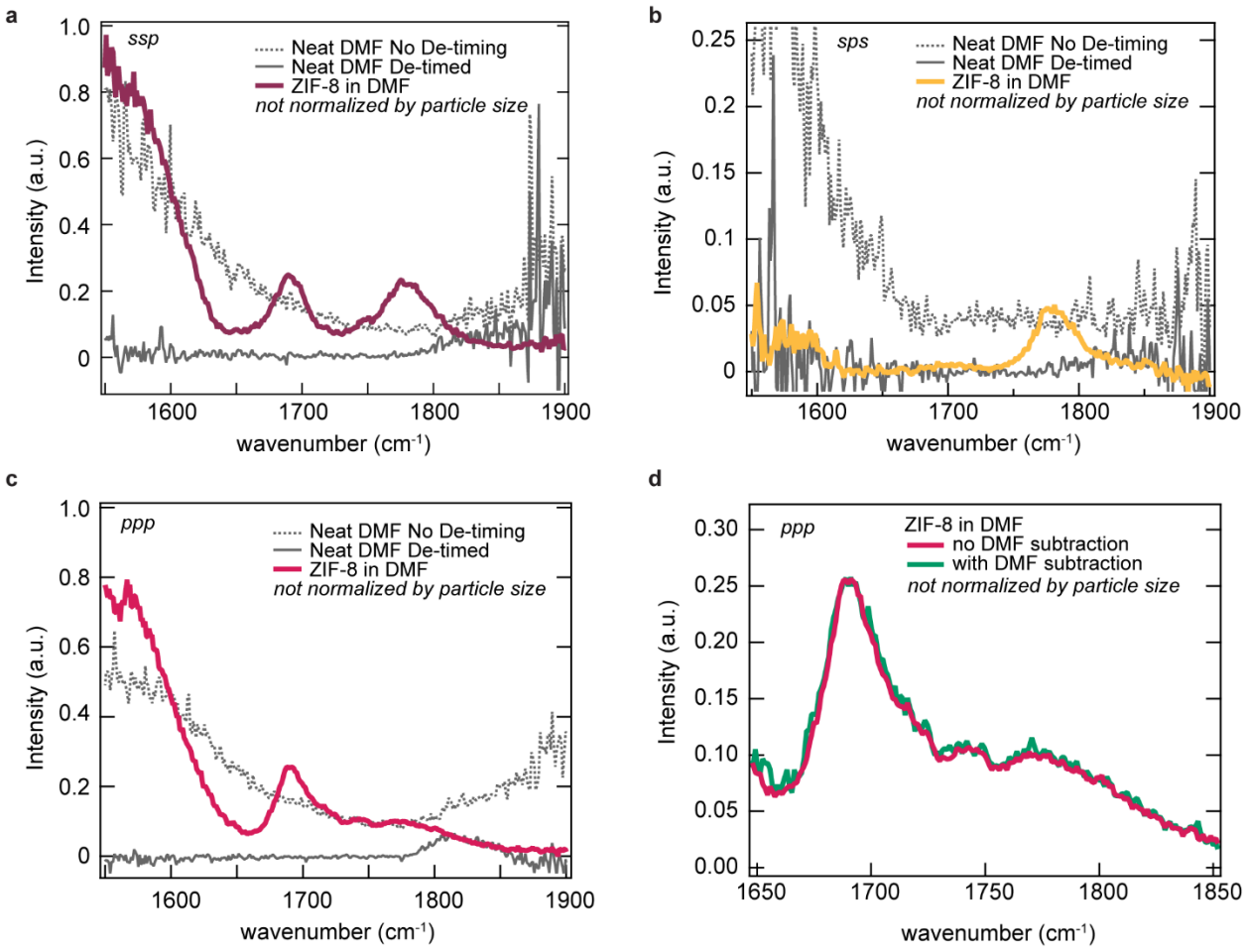

Figure C. 4 Impact of DMF absorption on VSFSS spectra. VSFSS measurements of neat DMF and nanoparticles of ZIF-8 suspended in DMF in the C=O stretching region for a) ssp b) sps and c) ppp polarization combinations. Panel D shows the impact of subtracting the neat DMF trace from the ZIF-8 in DMF response in *ppp*. These traces are not normalized by the particle size-dependent scattering pattern.

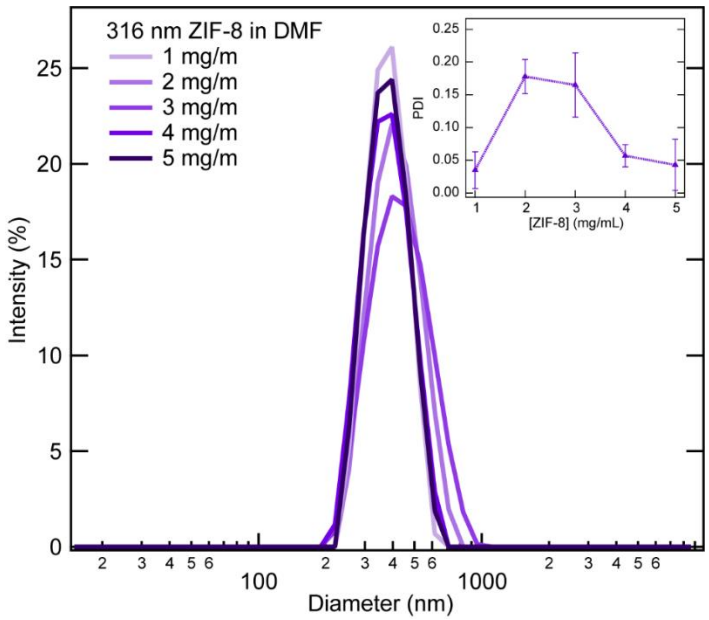

Figure C. 5 Size distribution curves of nanoZIF-8 particles in DMF as a function of concentration with polydispersity values provided inset.

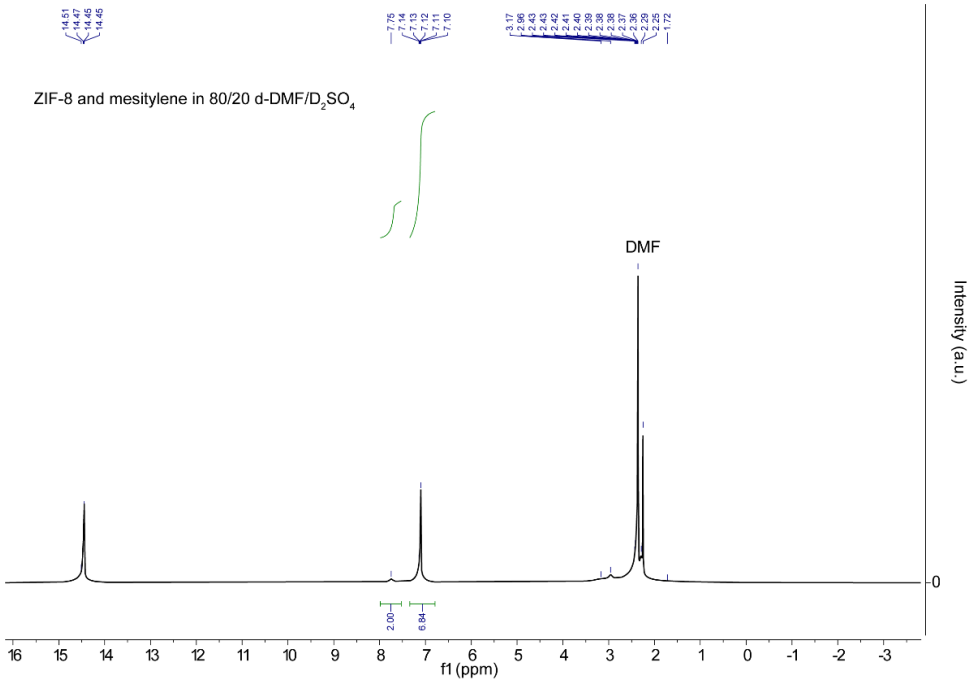

Figure C. 6 Acid digestion 1H NMR of nanoZIF-8 in an 80/20 mixture of d-DMF and D2SO4 with mesitylene internal standard performed on a Bruker AV-600 NMR.

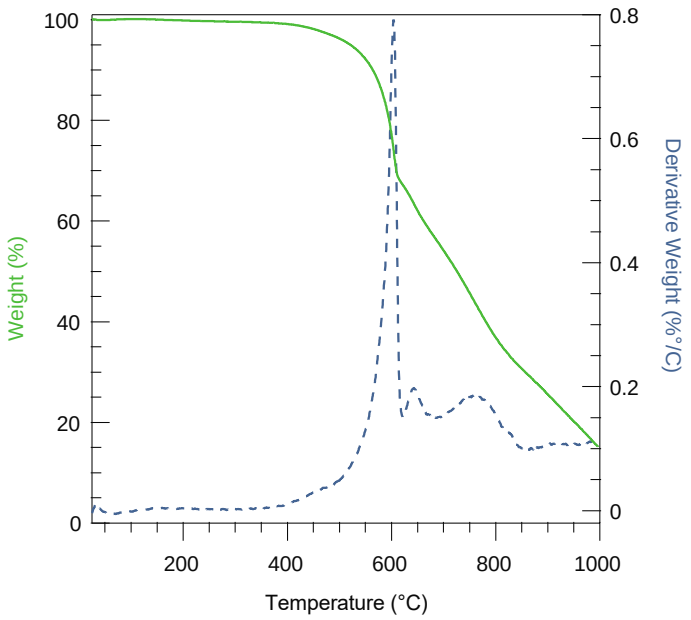

Figure C. 7 TGA trace of nanoZIF-8 under nitrogen at a heating rate of 10° per minute.

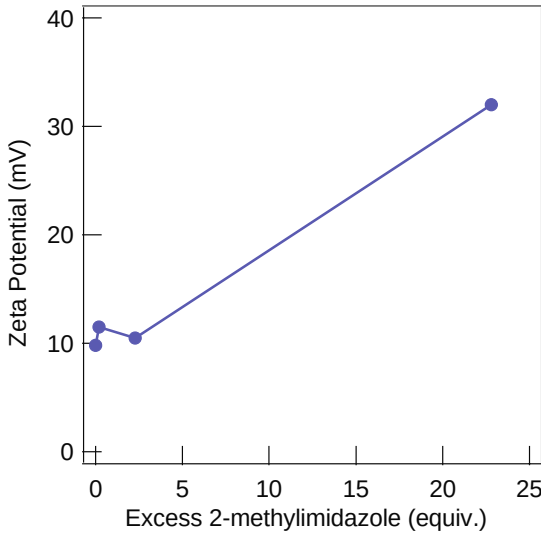

Figure C. 8 Surface zeta potential of nanoZIF-8 (1 mg/mL) with excess 2-methylimidazole. Equivalents of excess linker are defined per nanoZIF-8 concentration with respect to ZIF-8 particle molecular weight.

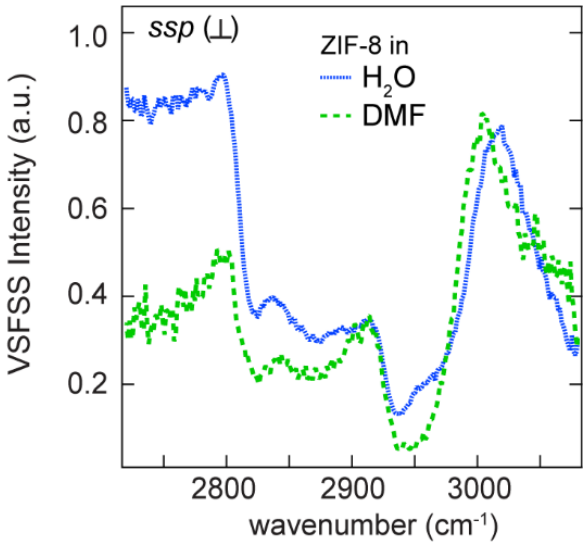

Figure C. 9 VSFSS measurements (ssp polarization) of nanoparticles of ZIF-8 suspended in H2O and d-DMF taken in the C-H stretching region.

Table C. 1 Fitting parameters for spectra of ZIF-8 nanoparticles dispersed in DMF measured in different polarization schemes, corresponding to Figure V.1A.

C=O Stretches: Mixed Polarizations				
96 nm crystalline diameter ZIF-8 in DMF				
Peak Assignment	**Parameters**	***ssp***	***ppp***	***sps***
Background Peak	Amplitude	0.387 ± 0.004	0.65 ± 0.07	
	Phase	0	0	
	Lorentzian linewidth	10	10	
	Peak position	1605.9 ± 0.4	1568.3 ±	
	Gaussian linewidth	16.7 ± 0.8	65 ± 7	
C=O Stretch	Amplitude	0.183 ± 0.003	0.27 ± 0.03	
	Phase	0	0	
	Lorentzian linewidth	5	5	
	Peak position	1689.3 ± 0.1	1688.4 ± 0.1	
	Gaussian linewidth	11.5 ± 0.3	10.0 ± 0.7	
C=O Stretch Shoulder 1	Amplitude	0.133 ± 0.002	0.15 ± 0.01	
	Phase	0	0	
	Lorentzian linewidth	5	5	
	Peak position	1712.8 ± 0.6	1708.6 ± 0.2	
	Gaussian linewidth	125 ± 2	18 ± 2	
C=O Stretch Shoulder 2	Amplitude	0.1 ± 0.1	0.07 ± 0.03	
	Phase	0	0	
	Lorentzian linewidth	5	5	
	Peak position	1742.7 ± 0.6	1740.1 ± 0.5	
	Gaussian linewidth	2 ± 2	3.9 ± 1.9	
C=O Stretch	Amplitude	0.174 ± 0.002	0.219 ± 0.003	0.205 ± 0.003
	Phase	0	0	0
	Lorentzian linewidth	5	5	5
	Peak position	1773.6 ± 0.2	1776.4 ± 0.3	1778.9 ± 0.3
	Gaussian linewidth	19.4 ± 0.4	77 ± 2	18.0 ± 0.5
Non-resonant Contribution	Amplitude	0.042 ± 0.002	0.21 ± 0.02	$9e^{-5}$ ± 0.002
	Phase	0	0	0

Table C. 2 Fitting parameters for spectra of ZIF-8 nanoparticles dispersed in varying solvents taken in ssp polarization, corresponding to Figure V.2A.

C=O Stretches: Mixed Solvents				
96 nm crystalline diameter ZIF-8, *ssp* polarization				
Peak Assignment	**Parameters**	**100% DMF**	**50% DMF/ 50% H_2O**	**100 % H_2O**
Background Peak	Amplitude	0.387 ± 0.004		
	Phase	0		
	Lorentzian linewidth	10		
	Peak position	1605.9 ± 0.7		
	Gaussian linewidth	16.7 ± 0.8		
C=O Stretch	Amplitude	0.183 ± 0.003	0.110 ± 0.003	
	Phase	0	0	
	Lorentzian linewidth	5	5	
	Peak position	1689.3 ± 2	1691.6 ± 0.3	
	Gaussian linewidth	11.5 ± 0.3	12.3 ± 0.6	
C=O Stretch Shoulder 1	Amplitude	0.133 ± 0.002		
	Phase	0		
	Lorentzian linewidth	5		
	Peak position	1712.8 ± 0.9		
	Gaussian linewidth	125 ± 2		
C=O Stretch Shoulder 2	Amplitude	0.1 ± 0.1		
	Phase	0		
	Lorentzian linewidth	5		
	Peak position	1742.7 ± 0.7		
	Gaussian linewidth	2 ± 2		
C=O Stretch	Amplitude	0.174 ± 0.002		
	Phase	0		
	Lorentzian linewidth	5		
	Peak position	1773.6 ± 0.3		
	Gaussian linewidth	19.4 ± 0.4		
H_2O Bend	Amplitude			0.09 ± 0.01
	Phase			0
	Lorentzian linewidth			5
	Peak position			1677 ± 1
	Gaussian linewidth			9 ± 2
Background Peak 2	Amplitude		0.056 ± 0.002	
	Phase		0	
	Lorentzian linewidth		5	
	Peak position		1731 ± 3	
	Gaussian linewidth		99 ± 10	
Non-resonant Contribution	Amplitude	0.042 ± 0.002	0.004 ± 0.002	0.03 ± 0.002
	Phase	0	0	0

Table C. 3 Fitting parameters for spectra of ZIF-8 nanoparticles dispersed in d-DMF taken in ssp polarization, corresponding to Figure 3A.

C-H Stretches: 2-Methylimidazole		
96 nm crystalline diameter ZIF-8 in d-DMF		
Peak Assignment	**Parameters**	***ssp***
Non-resonant Background Peak	Amplitude	0.252 ± 0.008
	Phase	0
	Lorentzian linewidth	2
	Peak position	2808.4 ± 0.3
	Gaussian linewidth	13.5 ± 0.6
CH_3 Fermi Resonance	Amplitude	0.065 ± 0.008
	Phase	0
	Lorentzian linewidth	2
	Peak position	2847 ± 2
	Gaussian linewidth	18 ± 3
CH_3 Asymmetric Stretch	Amplitude	0.28 ± 0.01
	Phase	0
	Lorentzian linewidth	2
	Peak position	2924.5 ± 0.4
	Gaussian linewidth	11.5 ± 0.7
Aromatic C-H Asymmetric Stretch	Amplitude	1.1 ± 0.6
	Phase	3.14
	Lorentzian linewidth	2
	Peak position	3001.3 ± 0.2
	Gaussian linewidth	32 ± 1
Aromatic C-H Symmetric Stretch	Amplitude	0.8 ± 0.6
	Phase	0
	Lorentzian linewidth	2
	Peak position	3010.2 ± 0.2
	Gaussian linewidth	26 ± 3
Non-resonant Contribution	Amplitude	0.584 ± 0.002
	Phase	0

APPENDIX D: SUPPLEMENTARY INFORMATION FOR CHAPTER VI

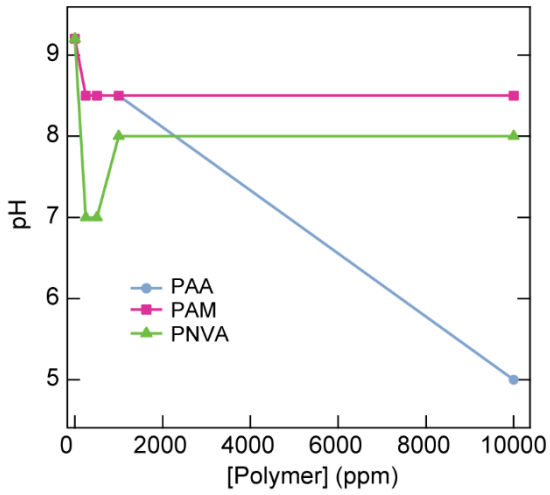

Figure D. 1 pH measurements of ZIF-8 suspended in D2O with PAA, PAM, and PNVA at varying concentrations.

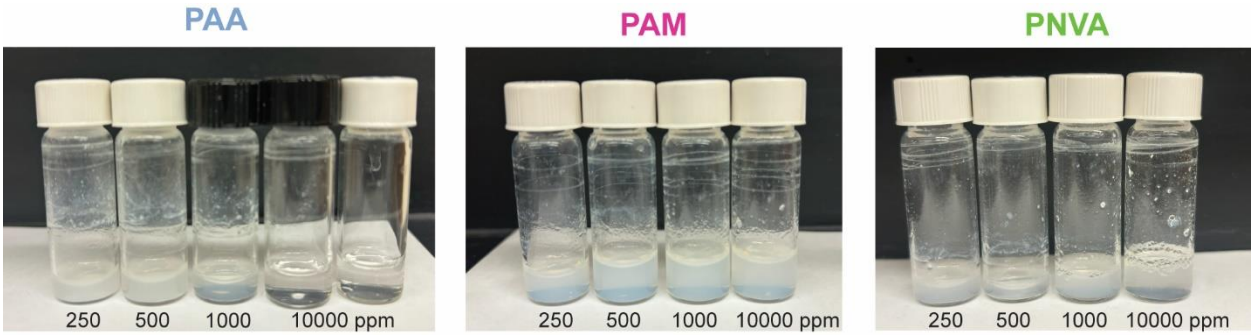

Figure D. 2 Pictures of ZIF-8 colloids suspended in D2O with varying concentrations of PAA (left), PAM (middle), and PNVA (right).

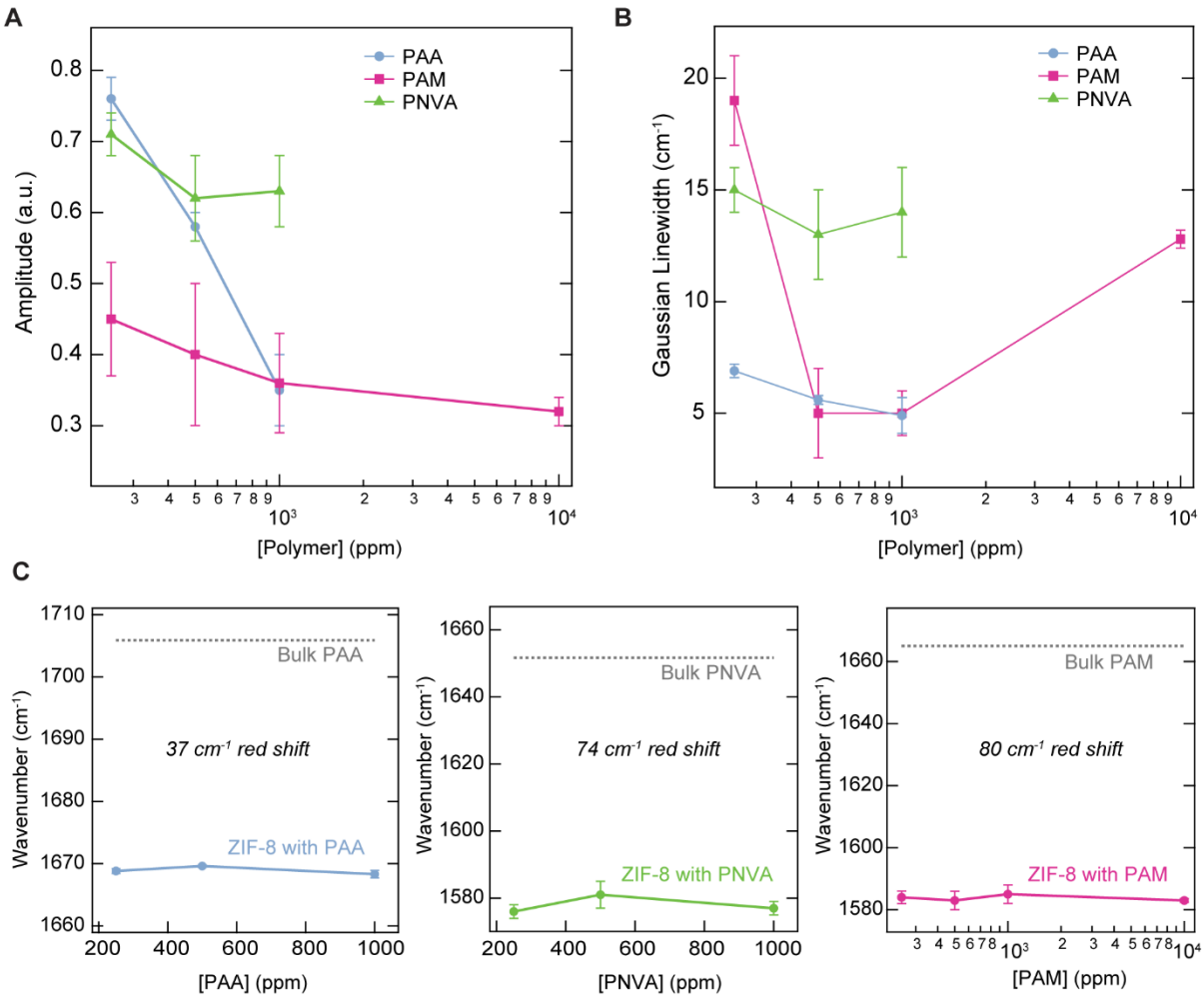

Figure D. 3 A) Amplitude, B) Gaussian linewidth, and C) peak position trends obtained from fitting VSFSS spectra as a function of polymer binding agent identity and concentration.

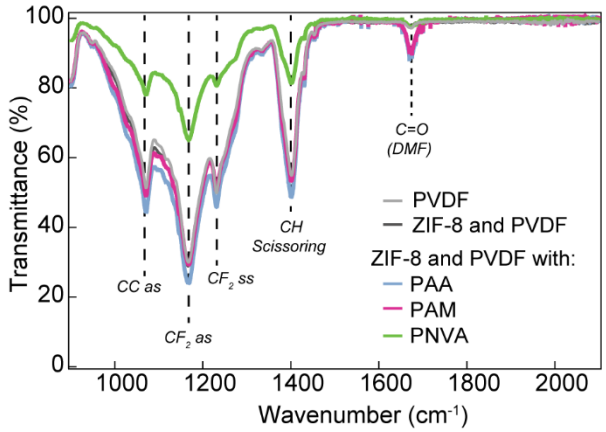

Figure D. 4 FT-IR spectra of polymeric membrane films.

Table D. 1 Fitting parameters for spectra of ZIF-8 nanoparticles dispersed in D2O with varying concentrations of poly(acrylic acid), corresponding to Figure VI.4A.

C=O Stretches, *ssp* polarization				
5 mg/mL ZIF-8 with poly(acrylic acid)				
Peak Assignment	**Parameters**	**250 ppm**	**500 ppm**	**1000 ppm**
Background Peak	Amplitude	1.7 ± 0.3	1.10 ± 0.03	0.29 ± 0.03
	Phase	0	0	0
	Lorentzian linewidth	10	10	10
	Peak position	1530 ± 6	1594.3 ± 0.8	1297 ± 59
	Gaussian linewidth	41 ± 3	10.3 ± 0.6	250 ± 42
C=O Stretch	Amplitude	0.76 ± 0.03	0.58 ± 0.02	0.35 ± 0.05
	Phase	3.14	3.14	3.14
	Lorentzian linewidth	5	5	5
	Peak position	1668.8 ± 0.4	1669.6 ± 0.2	1668.3 ± 0.6
	Gaussian linewidth	6.9 ± 0.3	5.6 ± 0.2	4.9 ± 0.8
Non-resonant	Amplitude	0.27 ± 0.02	0.076 ± 0.003	0.13 ± 0.01
	Phase	0	0	0

Table D. 2 Fitting parameters for spectra of ZIF-8 nanoparticles dispersed in D2O with varying concentrations of poly(acrylamide), corresponding to Figure VI.4C-D.

C=O Stretches, *ssp* polarization					
5 mg/mL ZIF-8 with poly(acrylamide)					
Peak Assignment	**Parameters**	**250 ppm**	**500 ppm**	**1000 ppm**	**10000 ppm**
Background Peak	Amplitude	17 ± 8	12 ± 4	14 ± 1	10 ± 2
	Phase	0	0	0	0
	Lorentzian linewidth	10	10	10	10
	Peak position	1515 ± 6	1519 ± 4	1510 ± 16	1520 ± 2
	Gaussian linewidth	0.6 ± 0.3	0.4 ± 0.1	0.5 ± 0.1	0.4 ± 0.1
N-H Bend	Amplitude	0.16 ± 0.07	0.08 ± 0.01	0.075 ± 0.005	0.12 ± 0.02
	Phase	3.14	0	0	0
	Lorentzian linewidth	5	5	5	5
	Peak position	1580.6 ± 0.9	1580 ± 3	1580 ± 2	1579 ± 0.5
	Gaussian linewidth	8 ± 3	33 ± 3	33 ± 2	4 ± 2
C=O Stretch	Amplitude	0.45 ± 0.08	0.4 ± 0.1	0.36 ± 0.07	0.32 ± 0.02
	Phase	3.14	3.14	3.14	3.14
	Lorentzian linewidth	5	5	5	5
	Peak position	1584 ± 2	1583 ± 3	1585 ± 3	1583.8 ± 0.6
	Gaussian linewidth	19 ± 2	5 ± 2	5 ± 1	12.8 ± 0.4
Non-resonant	Amplitude	0.06 ± 0.02	0.062 ± 0.007	0.068 ± 0.006	0.043 ± 0.004
	Phase	0	0	0	0

Table D. 3 Fitting parameters for spectra of ZIF-8 nanoparticles dispersed in D2O with varying concentrations of poly(N-vinyl acetamide), corresponding to Figure V.4B.

C=O Stretches, *ssp* polarization				
5 mg/mL ZIF-8 (large) with poly(N-vinyl acetamide)				
Peak Assignment	**Parameters**	**250 ppm**	**500 ppm**	**1000 ppm**
Background Peak	Amplitude	18 ± 9	19 ± 1	19 ± 6
	Phase	0	0	0
	Lorentzian linewidth	10	10	10
	Peak position	1512 ± 4	1513 ± 4	1510 ± 3
	Gaussian linewidth	0.4 ± 0.2	0.4 ± 0.2	0.4 ± 0.1
N-H Bend	Amplitude	0.25 ± 0.04	0.22 ± 0.07	0.26 ± 0.06
	Phase	0	0	0
	Lorentzian linewidth	5	5	5
	Peak position	1573 ± 3	1576 ± 3	1572 ± 2
	Gaussian linewidth	42 ± 4	33 ± 4	32 ± 2
C=O Stretch	Amplitude	0.71 ± 0.03	0.62 ± 0.06	0.63 ± 0.05
	Phase	3.14	3.14	3.14
	Lorentzian linewidth	5	5	5
	Peak position	1576 ± 2	1581 ± 4	1577 ± 2
	Gaussian linewidth	15 ± 1	13 ± 2	14 ± 2
Non-resonant	Amplitude	0.10 ± 0.01	0.11 ± 0.01	0.101 ± 0.008
	Phase	0	0	0

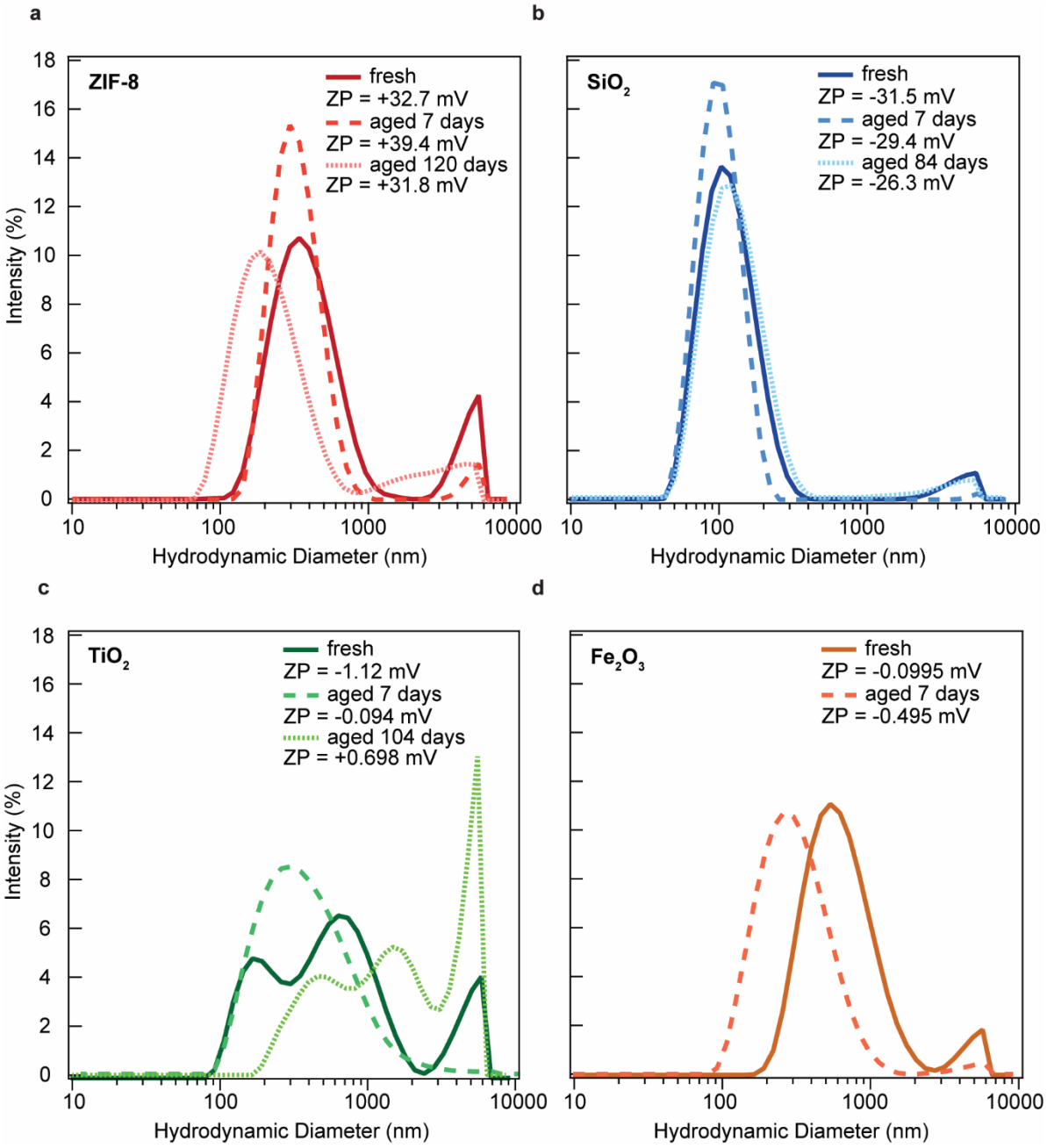

Figure E. 1 Dynamic light scattering curves measured at different time intervals of a) ZIF-8, b) mesoporous SiO2, c) TiO2, and d) Fe2O3 nanoparticles suspended in DMF at 5 mg/mL.

APPENDIX F: CALCULATION OF NANOPARTICLE SURFACE DENSITY

	ZIF-8	ZnO
Diameter (nm)	100	100
Molar ratio (metal:linker/oxide)	2:1	1:1
Density (g/cm^3)	0.95	5.61
Molecular weight (g/mol)	229.58	81.38
Surface density (atoms/nm^2)	*7*	*78*

We first calculate the moles of metal ions in the entire particle, in the interior, and at the surface:

Entire particle:

$$moles\ Zn^{2+} per\ particle = \frac{particle\ MW}{MW} \times metal\ molar\ ratio \quad (F1)$$

$$moles\ of\ Zn^{2+} per\ particle = \frac{4.97 \times 10^{-16} \frac{g}{particle}}{229.58 \frac{g}{mol}} \times 2 = 2.17 \times 10^{-18}\ mol \quad (F2)$$

where the particle molecular weight is dependent on the volume of the particle.
For a 100 nm particle:

$$particle\ MW = volume \times density \quad (F3)$$

$$particle\ MW = 5.23 \times 10^{-16}\ cm^3 \times 0.95 \frac{g}{cm^3} = 4.97 \times 10^{-16} \frac{g}{particle} \quad (F4)$$

Interior:

$$interior\ moles\ Zn^{2+} = \frac{moles\ of\ Zn^{2+}\ in\ particle}{1 + particle\ SA{:}V\ ratio} \quad (F5)$$

$$interior\ moles\ Zn^{2+} = \frac{2.04 \times 10^{-18}\ mol}{1 + 0.06} = 2.04 \times 10^{-18}\ mol \quad (F6)$$

Surface:

$$surface\ moles\ Zn^{2+} = moles\ of\ Zn^{2+} per\ particle - moles\ of\ interior\ Zn^{2+} \quad (F7)$$

$$surface\ moles\ Zn^{2+} = 2.17 \times 10^{-18}\ mol - 2.04 \times 10^{-18}\ mol = 1.22 \times 10^{-19}\ mol \quad (F8)$$

The same procedure is followed to calculate the moles of linker in the entire particle, in the interior, and at the surface.

$$moles\ linker\ per\ particle = \frac{particle\ MW}{MW} \times linker\ molar\ ratio = 4.33 \times 10^{-18}\ mol \quad (F9)$$

$$interior\ moles\ linker = \frac{moles\ of\ linker\ in\ particle}{1 + particle\ SA{:}V\ ratio} = 4.08 \times 10^{-18}\ mol \quad (F10)$$

$$surface\ moles\ linker = moles\ of\ linker\ per\ particle - moles\ of\ interior\ linker = 2.45 \times 10^{-19}\ mol \quad (F11)$$

Next, we calculate the total moles of surface atoms (metal and linker):

$$Moles\ of\ surface\ atoms = surface\ metal\ moles + surface\ linker\ moles \quad (F12)$$

$$Moles\ of\ surface\ atoms = 1.22 \times 10^{-19}\ mol + 2.45 \times 10^{-19}\ mol = 3.68 \times 10^{-19}\ mol \quad (F13)$$

We multiple by Avogadro's number and divide by the surface area to determine the number density of atoms at the surface:

$$number\ density = \frac{moles\ of\ surface\ atoms}{Surface\ Area} \times N_A \quad (F14)$$

$$\boldsymbol{number\ density = \frac{3.68 \times 10^{-19}\ mol}{31415.92\ nm^2}\ x\ N_A \approx 7\frac{atoms}{nm^2}} \quad (\boldsymbol{F15})$$

The same calculation can be carried out for ZnO nanoparticles but with different values for the density, molecular weight, and molar ratio. The "linker" values above will be attributed to oxygen atoms for ZnO.

$$moles\ of\ Zn^{2+} per\ particle = \frac{2.94 \times 10^{-15} \frac{g}{particle}}{81.38 \frac{g}{mol}} \times 1 = 3.61 \times 10^{-17}\ mol \quad (F16)$$

$$interior\ moles\ Zn^{2+} = \frac{3.61 \times 10^{-17}\ mol}{1 + 0.06} = 3.41 \times 10^{-17}\ mol \quad (F17)$$

$$surface\ moles\ Zn^{2+} = 2.17 \times 10^{-18}\ mol - 2.04 \times 10^{-18}\ mol = 2.04 \times 10^{-18}\ mol \quad (F18)$$

$$moles\ O^{2-}\ per\ particle = \frac{particle\ MW}{MW} \times linker\ molar\ ratio = 3.61 \times 10^{-17}\ mol \quad (F19)$$

$$interior\ moles\ O^{2-} = \frac{moles\ of\ O^{2-}\ in\ particle}{1 + particle\ SA{:}V\ ratio} = 3.41\ \times\ 10^{-17}\ mol \qquad (F20)$$

$$surface\ moles\ linker = \ moles\ of\ linker\ per\ particle - moles\ of\ interior\ linker = 2.04\ \times\ 10^{-18}\ mol \qquad (F21)$$

$$Moles\ of\ surface\ atoms = 1.22\ \times\ 10^{-19}\ mol + 2.45\ \times\ 10^{-19}\ mol = 4.09\ \times\ 10^{-18}\ mol \quad (F22)$$

$$\boldsymbol{number\ density = \frac{4.09\ \times\ 10^{-18}\ mol}{31415.92\ nm^2}\ x\ N_A\ \approx 78\frac{atom}{nm^2}} \qquad (\boldsymbol{F23})$$

APPENDIX G: VSFSS NORMALIZATION PROCEDURE

1. The non-resonant response from a $KNbO_3$ crystal is measured (**Figure G1**), providing the daily profile of the IR pulse. The only data processing that occurs to produce **Figure G1** is background subtraction.

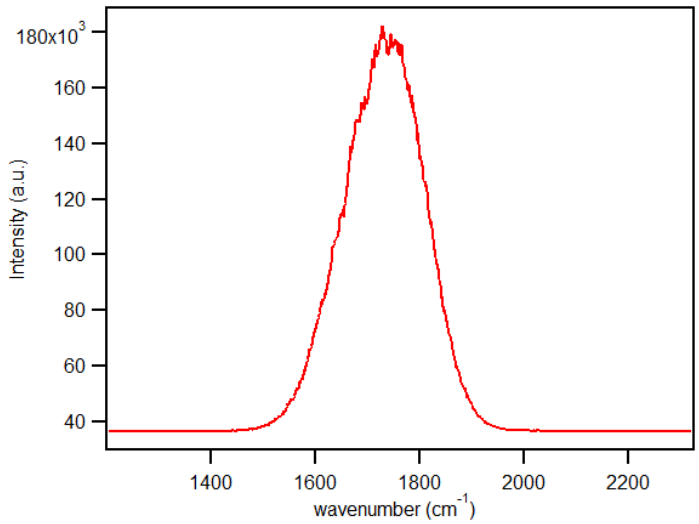

Figure G. 1 Non-resonant response from KNbO¬3 crystal measured in the C=O region.

2. The raw signal from colloidal nanoZIF-8 in DMF (example) is measured at the signal timing for 20 minutes (**Figure G2**).

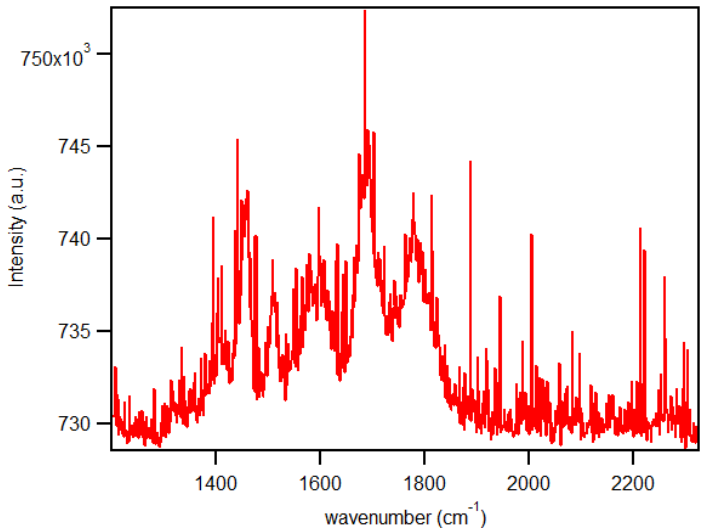

Figure G. 2 Raw signal obtained from one scan of colloidal nanoZIF-8 (96 nm diameter) in DMF.

Then, an average signal trace is created by averaging 2 signal scans subtracted by 2 background scans (**Figure G3**).

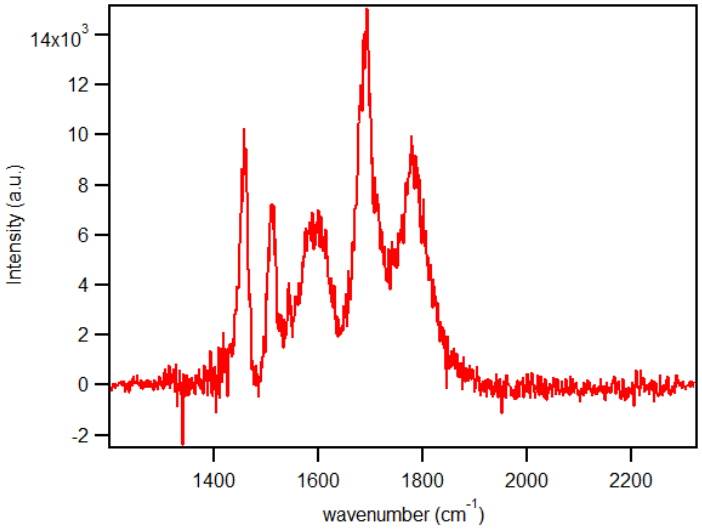

Figure G. 3 Average signal trace of colloidal nanoZIF-8 (97 nm diameter) in DMF.

Although our spectrometer measures features across this spectrum (1400-2200 cm^{-1}), we only consider features to be relevant within the range of our IR pulse (approximately determined from our $KNbO_3$ response, black trace, **Figure G4**). We've defined this range to be 1600-1850 cm^{-1}.

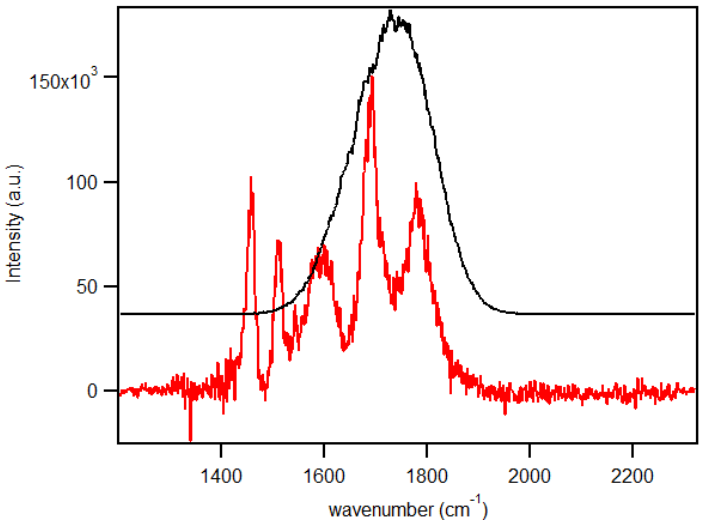

Figure G. 4 Averaged signal trace from colloidal ZIF-8 in DMF (10x, red) overlayed with the non-resonant response from KNbO3 (black).

The resulting average signal in this range is **Figure G5**:

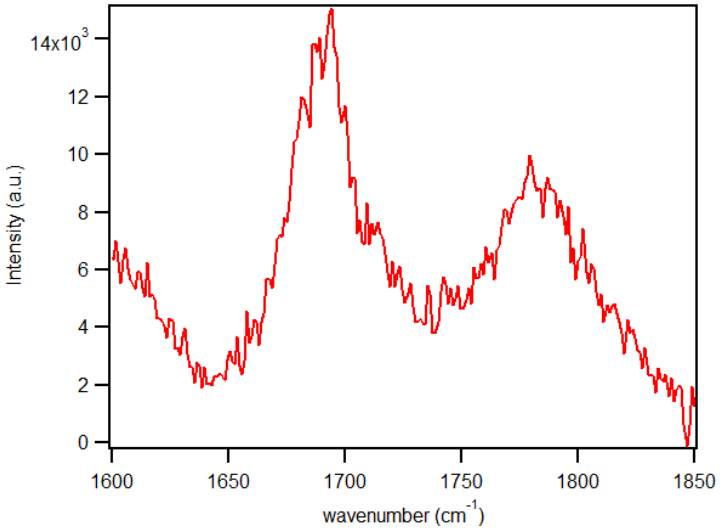

Figure G. 5 Averaged signal trace from colloidal ZIF-8 in DMF within the appropriate IR wavenumber range.

3. Next, we divide the averaged signal trace by the $KNbO_3$ reference to account for our IR pulse.

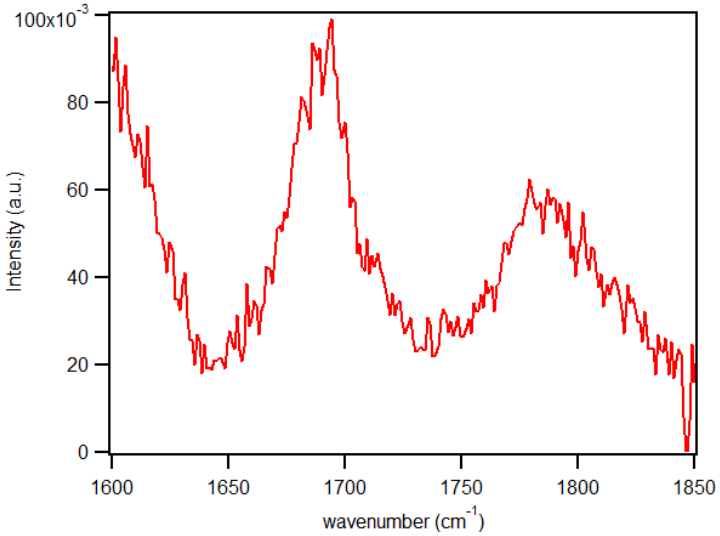

Figure G. 6 Signal trace from colloidal ZIF-8 in DMF normalized by KNbO¬3 response.

4. Finally, we divide by the scattering pattern produced by the average size of the particle measured. This factor accounts for the fraction of scattered signal that is collected from our lens (placed at 60° relative to the experimental plane). The scattering pattern is produced by the NLS software developed by Sylvie Roke.

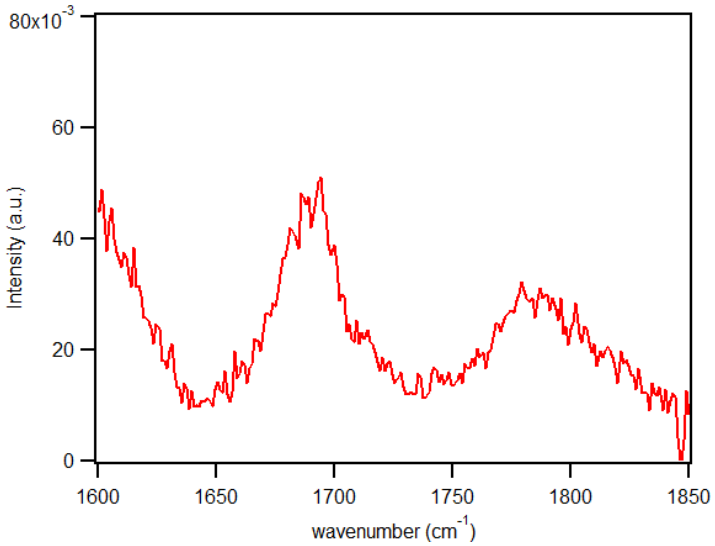

Figure G. 7 Completely normalized signal trace from colloidal ZIF-8 in DMF.

This process is repeated for at least 3 trials collected on different days and averaged to produce the spectra suitable for publication. That averaged spectrum is then fit using the parameters provided in the appendix tables.

APPENDIX H: DETERMINATION OF PARTICLE CONCENTRATION FOR VSFSS DETECTION LIMIT

In accordance with the comment published by Arianna Marchioro, Sylvie Roke, and others,[384] it is necessary to confirm that our particle concentration is above the detection limit for vibration sum frequency scattering.

For a suspension of ZIF-8 nanoparticles in DMF:

Total Concentration	0.005 g/mL
Density (ρ)	0.35 g/cm^3
Molecular Weight (MW)	227.58 g/mol
Particle Diameter (as determined by SEM)	316 nm
Particle Radius	158 nm

We calculate the # of particles in solution by:

$$Volume = \frac{4}{3}\pi R^3 = \mathbf{1.65219\ E^{-14}\ cm^3}$$

$$Particle\ MW = V\rho N_A = \mathbf{3481163376\ g/mol}$$

$$Particle\ Concentration = \frac{Total\ Concentration}{Particle\ MW} = \mathbf{1.4363\ E^{-12}\ mol/mL}$$

$$\#\ of\ Particles = Particle\ Concentration\ \times\ N_A = \mathbf{8.6465\ E^{11}\ particles/mL}$$

Therefore, for a 5 mg/mL solution of particles with a radius of **1.58 E^{-7} m**, our concentration of particles is **8.6465 E^{11} particles/mL.** This confirms our VSFS measurement is above the SNR = 1 detection limit. Our results are plotted onto **Figure H1** from the reference material.

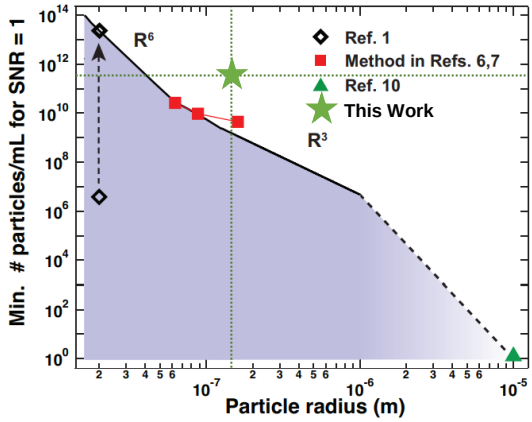

Figure H. 1 Signal-to-noise ratio given by the solid black line as a function of particle radius and concentration of particles for VSFSS experiments. Adapted from ref. 384

REFERENCES

(1) Derjaguin, B.; Landau, L. Theory of the Stability of Strongly Charged Lyophobic Sols and of the Adhesion of Strongly Charged Particles in Solutions of Electrolytes. *Progress in Surface Science* **1993**, *43* (1), 30–59. https://doi.org/10.1016/0079-6816(93)90013-L.

(2) Helmholtz, H. Ueber Einige Gesetze Der Vertheilung Elektrischer Ströme in Körperlichen Leitern Mit Anwendung Auf Die Thierisch-Elektrischen Versuche. *Annalen der Physik* **1853**, *165* (6), 211–233. https://doi.org/10.1002/andp.18531650603.

(3) Gouy, M. Sur la constitution de la charge électrique à la surface d'un électrolyte. *J. Phys. Theor. Appl.* **1910**, *9* (1), 457–468. https://doi.org/10.1051/jphystap:019100090045700.

(4) Chapman, D. L. LI. A Contribution to the Theory of Electrocapillarity. *The London, Edinburgh, and Dublin Philosophical Magazine and Journal of Science* **1913**, *25* (148), 475–481. https://doi.org/10.1080/14786440408634187.

(5) Stern, O. Zur Theorie Der Elektrolytischen Doppelschicht. *Zeitschrift für Elektrochemie und angewandte physikalische Chemie* **1924**, *30* (21–22), 508–516. https://doi.org/10.1002/bbpc.192400182.

(6) Verwey, E. J. W. Theory of the Stability of Lyophobic Colloids. *J. Phys. Chem.* **1947**, *51* (3), 631–636. https://doi.org/10.1021/j150453a001.

(7) Verwey, E. J. W.; Overbeek, J. Th. G. *Theory of the Stability of Lyophobic Colloids*; Elsevier: Amsterdam, 1948.

(8) Derjaguin, B. V.; Churaev, N. V.; Muller, V. M. The Derjaguin—Landau—Verwey—Overbeek (DLVO) Theory of Stability of Lyophobic Colloids. In *Surface Forces*; Derjaguin, B. V., Churaev, N. V., Muller, V. M., Eds.; Springer US: Boston, MA, 1987; pp 293–310. https://doi.org/10.1007/978-1-4757-6639-4_8.

(9) Trefalt, G.; Szilagyi, I.; Borkovec, M. Poisson–Boltzmann Description of Interaction Forces and Aggregation Rates Involving Charged Colloidal Particles in Asymmetric Electrolytes. *Journal of Colloid and Interface Science* **2013**, *406*, 111–120. https://doi.org/10.1016/j.jcis.2013.05.071.

(10) Trefalt, G.; Ruiz-Cabello, F. J. M.; Borkovec, M. Interaction Forces, Heteroaggregation, and Deposition Involving Charged Colloidal Particles. *J. Phys. Chem. B* **2014**, *118* (23), 6346–6355. https://doi.org/10.1021/jp503564p.

(11) Trefalt, G.; Cao, T.; Sugimoto, T.; Borkovec, M. Heteroaggregation between Charged and Neutral Particles. *Langmuir* **2020**, *36* (19), 5303–5311. https://doi.org/10.1021/acs.langmuir.0c00667.

(12) Obstbaum, T.; Sivan, U. Thermodynamics of Charge Regulation near Surface Neutrality. *Langmuir* **2022**, *38* (27), 8477–8483. https://doi.org/10.1021/acs.langmuir.2c01352.

(13) Russel, W. B.; Saville, D. A.; Schowalter, W. R. *Colloidal Dispersions*; Cambridge Monographs on Mechanics; Cambridge University Press: Cambridge, 1989. https://doi.org/10.1017/CBO9780511608810.

(14) Leckband, D.; Sivasankar, S. Forces Controlling Protein Interactions: Theory and Experiment. *Colloids and Surfaces B: Biointerfaces* **1999**, *14* (1), 83–97. https://doi.org/10.1016/S0927-7765(99)00027-2.

(15) Eom, N.; Parsons, D. F.; Craig, V. S. J. Roughness in Surface Force Measurements: Extension of DLVO Theory To Describe the Forces between Hafnia Surfaces. *J. Phys. Chem. B* **2017**, *121* (26), 6442–6453. https://doi.org/10.1021/acs.jpcb.7b03131.

(16) Tran, E.; Richmond, G. L. Interfacial Steric and Molecular Bonding Effects Contributing to the Stability of Neutrally Charged Nanoemulsions. *Langmuir* **2021**, *37* (43), 12643–12653. https://doi.org/10.1021/acs.langmuir.1c02020.
(17) Yang, L.; Wen, J. Can DLVO Theory Be Applied to MOF in Different Dielectric Solvents? *Microporous and Mesoporous Materials* **2022**, *343*, 112166. https://doi.org/10.1016/j.micromeso.2022.112166.
(18) Peng, B.; Liao, P.; Jiang, Y. A Meta-Analysis to Revisit the Property–Aggregation Relationships of Carbon Nanomaterials: Experimental Observations versus Predictions of the DLVO Theory. *Langmuir* **2024**, *40* (13), 7127–7138. https://doi.org/10.1021/acs.langmuir.4c00274.
(19) van Oss, C. J. Chapter Three - The Extended DLVO Theory. In *Interface Science and Technology*; van Oss, C. J., Ed.; The Properties of Water and their Role in Colloidal and Biological Systems; Elsevier, 2008; Vol. 16, pp 31–48. https://doi.org/10.1016/S1573-4285(08)00203-2.
(20) Boström, M.; Deniz, V.; Franks, G. V.; Ninham, B. W. Extended DLVO Theory: Electrostatic and Non-Electrostatic Forces in Oxide Suspensions. *Advances in Colloid and Interface Science* **2006**, *123–126*, 5–15. https://doi.org/10.1016/j.cis.2006.05.001.
(21) Buchcic, C.; Tromp, R. H.; Meinders, M. B. J.; Stuart, M. A. C. Harnessing the Advantages of Hard and Soft Colloids by the Use of Core–Shell Particles as Interfacial Stabilizers. *Soft Matter* **2017**, *13* (7), 1326–1334. https://doi.org/10.1039/C6SM02159J.
(22) Style, R. W.; Isa, L.; Dufresne, E. R. Adsorption of Soft Particles at Fluid Interfaces. *Soft Matter* **2015**, *11* (37), 7412–7419. https://doi.org/10.1039/C5SM01743B.
(23) Abate, A. R.; Han, L.; Jin, L.; Suo, Z.; Weitz, D. A. Measuring the Elastic Modulus of Microgels Using Microdrops. *Soft Matter* **2012**, *8* (39), 10032–10035. https://doi.org/10.1039/C2SM26108A.
(24) Tan, S.; Sherman, R. L.; Ford, W. T. Nanoscale Compression of Polymer Microspheres by Atomic Force Microscopy. *Langmuir* **2004**, *20* (17), 7015–7020. https://doi.org/10.1021/la049597c.
(25) Wennerström, H.; Vallina Estrada, E.; Danielsson, J.; Oliveberg, M. Colloidal Stability of the Living Cell. *Proceedings of the National Academy of Sciences* **2020**, *117* (19), 10113–10121. https://doi.org/10.1073/pnas.1914599117.
(26) Molina-Bolívar, J. A.; Galisteo-González, F.; Hidalgo-Alvarez, R. The Role Played by Hydration Forces in the Stability of Protein-Coated Particles: Non-Classical DLVO Behaviour. *Colloids and Surfaces B: Biointerfaces* **1999**, *14* (1), 3–17. https://doi.org/10.1016/S0927-7765(99)00020-X.
(27) Singh, R. S.; Hernandez, R. Modeling Soft Core-Shell Colloids Using Stochastic Hard Collision Dynamics. *Chemical Physics Letters* **2018**, *708*, 233–240. https://doi.org/10.1016/j.cplett.2018.08.032.
(28) Cao, W.; Xiang, C.; Yang, Y.; Chen, Q.; Chen, L.; Yan, X.; Qian, L. Highly Stable QLEDs with Improved Hole Injection via Quantum Dot Structure Tailoring. *Nat Commun* **2018**, *9* (1), 2608. https://doi.org/10.1038/s41467-018-04986-z.
(29) Park, Y.-S.; Lim, J.; Klimov, V. I. Asymmetrically Strained Quantum Dots with Non-Fluctuating Single-Dot Emission Spectra and Subthermal Room-Temperature Linewidths. *Nature Mater* **2019**, *18* (3), 249–255. https://doi.org/10.1038/s41563-018-0254-7.
(30) Everett, D. H. Manual of Symbols and Terminology for Physicochemical Quantities and Units, Appendix II: Definitions, Terminology and Symbols in Colloid and Surface

Chemistry. *Pure and Applied Chemistry* **1972**, *31* (4), 577–638. https://doi.org/10.1351/pac197231040577.
(31) Clarke, J. B.; Hastie, J. W.; Kihlborg, L. H. E.; Metselaar, R.; Thackeray, M. M. Definitions of Terms Relating to Phase Transitions of the Solid State (IUPAC Recommendations 1994). *Pure and Applied Chemistry* **1994**, *66* (3), 577–594. https://doi.org/10.1351/pac199466030577.
(32) *Standard Methods for the Examination of Water and Wastewater*, 23rd edition.; Bridgewater, L. L., Baird, R. B., Eaton, A. D., Rice, E. W., American Public Health Association, American Water Works Association, Water Environment Federation, Eds.; American Public Health Association: Washington, DC, 2017.
(33) Butler, B. A.; Ford, R. G. Evaluating Relationships between Total Dissolved Solids (TDS) and Total Suspended Solids (TSS) in a Mining-Influenced Watershed. *Mine Water Environ* **2018**, *37* (1), 18–30. https://doi.org/10.1007/s10230-017-0484-y.
(34) Beard, M. C.; Peng, X.; Hens, Z.; Weiss, E. A. Introduction to Special Issue: Colloidal Quantum Dots. *The Journal of Chemical Physics* **2020**, *153* (24), 240401. https://doi.org/10.1063/5.0039506.
(35) Bawendi, M. G.; Brus, L. E.; Yekimov, A. The Nobel Prize in Chemistry 2023.
(36) Rossetti, R.; Nakahara, S.; Brus, L. E. Quantum Size Effects in the Redox Potentials, Resonance Raman Spectra, and Electronic Spectra of CdS Crystallites in Aqueous Solution. *The Journal of Chemical Physics* **1983**, *79* (2), 1086–1088. https://doi.org/10.1063/1.445834.
(37) Cardellini, A.; Alberghini, M.; Rajan, A. G.; Misra, R. P.; Blankschtein, D.; Asinari, P. Multi-Scale Approach for Modeling Stability, Aggregation, and Network Formation of Nanoparticles Suspended in Aqueous Solutions. *Nanoscale* **2019**, *11* (9), 3979–3992. https://doi.org/10.1039/C8NR08782B.
(38) Zarghami, M. H.; Liu, Y.; Gibbs, M.; Gebremichael, E.; Webster, C.; Law, M. P-Type PbSe and PbS Quantum Dot Solids Prepared with Short-Chain Acids and Diacids. *ACS Nano* **2010**, *4* (4), 2475–2485. https://doi.org/10.1021/nn100339b.
(39) Bae, W. K.; Joo, J.; Padilha, L. A.; Won, J.; Lee, D. C.; Lin, Q.; Koh, W.; Luo, H.; Klimov, V. I.; Pietryga, J. M. Highly Effective Surface Passivation of PbSe Quantum Dots through Reaction with Molecular Chlorine. *J. Am. Chem. Soc.* **2012**, *134* (49), 20160–20168. https://doi.org/10.1021/ja309783v.
(40) Zhang, J.; Gao, J.; Miller, E. M.; Luther, J. M.; Beard, M. C. Diffusion-Controlled Synthesis of PbS and PbSe Quantum Dots with in Situ Halide Passivation for Quantum Dot Solar Cells. *ACS Nano* **2014**, *8* (1), 614–622. https://doi.org/10.1021/nn405236k.
(41) Kovalenko, M. V.; Scheele, M.; Talapin, D. V. Colloidal Nanocrystals with Molecular Metal Chalcogenide Surface Ligands. *Science* **2009**, *324* (5933), 1417–1420. https://doi.org/10.1126/science.1170524.
(42) Bederak, D.; Sukharevska, N.; Kahmann, S.; Abdu-Aguye, M.; Duim, H.; Dirin, D. N.; Kovalenko, M. V.; Portale, G.; Loi, M. A. On the Colloidal Stability of PbS Quantum Dots Capped with Methylammonium Lead Iodide Ligands. *ACS Appl. Mater. Interfaces* **2020**, *12* (47), 52959–52966. https://doi.org/10.1021/acsami.0c16646.
(43) Alam, A.-M.; Shon, Y.-S. Water-Soluble Noble Metal Nanoparticle Catalysts Capped with Small Organic Molecules for Organic Transformations in Water. *ACS Appl. Nano Mater.* **2021**, *4* (4), 3294–3318. https://doi.org/10.1021/acsanm.1c00335.

(44) Oh, E.; Delehanty, J. B.; Klug, C. A.; Susumu, K.; Algar, W. R.; Goswami, R.; Medintz, I. L. Utility of PEGylated Dithiolane Ligands for Direct Synthesis of Water-Soluble Au, Ag, Pt, Pd, Cu and AuPt Nanoparticles. *Chem. Commun.* **2018**, *54* (16), 1956–1959. https://doi.org/10.1039/C7CC08650D.
(45) Moore, T. L.; Urban, D. A.; Rodriguez-Lorenzo, L.; Milosevic, A.; Crippa, F.; Spuch-Calvar, M.; Balog, S.; Rothen-Rutishauser, B.; Lattuada, M.; Petri-Fink, A. Nanoparticle Administration Method in Cell Culture Alters Particle-Cell Interaction. *Sci Rep* **2019**, *9* (1), 900. https://doi.org/10.1038/s41598-018-36954-4.
(46) Moore, T. L.; Rodriguez-Lorenzo, L.; Hirsch, V.; Balog, S.; Urban, D.; Jud, C.; Rothen-Rutishauser, B.; Lattuada, M.; Petri-Fink, A. Nanoparticle Colloidal Stability in Cell Culture Media and Impact on Cellular Interactions. *Chem. Soc. Rev.* **2015**, *44* (17), 6287–6305. https://doi.org/10.1039/C4CS00487F.
(47) Arcudi, F.; Westmoreland, D. E.; Weiss, E. A. Colloidally Stable CdS Quantum Dots in Water with Electrostatically Stabilized Weak-Binding, Sulfur-Free Ligands. *Chemistry – A European Journal* **2019**, *25* (63), 14469–14474. https://doi.org/10.1002/chem.201903908.
(48) Owen, J. The Coordination Chemistry of Nanocrystal Surfaces. *Science* **2015**, *347* (6222), 615–616. https://doi.org/10.1126/science.1259924.
(49) Prather, K. V.; Stoffel, J. T.; Tsui, E. Y. Redox Reactions at Colloidal Semiconductor Nanocrystal Surfaces. *Chem. Mater.* **2023**, *35* (9), 3386–3403. https://doi.org/10.1021/acs.chemmater.3c00481.
(50) Sylvestre, J.-P.; Poulin, S.; Kabashin, A. V.; Sacher, E.; Meunier, M.; Luong, J. H. T. Surface Chemistry of Gold Nanoparticles Produced by Laser Ablation in Aqueous Media. *J. Phys. Chem. B* **2004**, *108* (43), 16864–16869. https://doi.org/10.1021/jp047134+.
(51) De Anda Villa, M.; Gaudin, J.; Amans, D.; Boudjada, F.; Bozek, J.; Evaristo Grisenti, R.; Lamour, E.; Laurens, G.; Macé, S.; Nicolas, C.; Papagiannouli, I.; Patanen, M.; Prigent, C.; Robert, E.; Steydli, S.; Trassinelli, M.; Vernhet, D.; Lévy, A. Assessing the Surface Oxidation State of Free-Standing Gold Nanoparticles Produced by Laser Ablation. *Langmuir* **2019**, *35* (36), 11859–11871. https://doi.org/10.1021/acs.langmuir.9b02159.
(52) Li, Z.; Ruiz, V. G.; Kanduč, M.; Dzubiella, J. Highly Heterogeneous Polarization and Solvation of Gold Nanoparticles in Aqueous Electrolytes. *ACS Nano* **2021**, *15* (8), 13155–13165. https://doi.org/10.1021/acsnano.1c02668.
(53) Chung, K.; Bang, J.; Thacharon, A.; Song, H. Y.; Kang, S. H.; Jang, W.-S.; Dhull, N.; Thapa, D.; Ajmal, C. M.; Song, B.; Lee, S.-G.; Wang, Z.; Jetybayeva, A.; Hong, S.; Lee, K. H.; Cho, E. J.; Baik, S.; Oh, S. H.; Kim, Y.-M.; Lee, Y. H.; Kim, S.-G.; Kim, S. W. Non-Oxidized Bare Copper Nanoparticles with Surface Excess Electrons in Air. *Nat. Nanotechnol.* **2022**, *17* (3), 285–291. https://doi.org/10.1038/s41565-021-01070-4.
(54) Johny, J.; van Halteren, C. E. R.; Zwiehoff, S.; Behrends, C.; Bäumer, C.; Timmermann, B.; Rehbock, C.; Barcikowski, S. Impact of Sterilization on the Colloidal Stability of Ligand-Free Gold Nanoparticles for Biomedical Applications. *Langmuir* **2022**, *38* (43), 13030–13047. https://doi.org/10.1021/acs.langmuir.2c01557.
(55) França, Á.; Pelaz, B.; Moros, M.; Sánchez-Espinel, C.; Hernández, A.; Fernández-López, C.; Grazú, V.; de la Fuente, J. M.; Pastoriza-Santos, I.; Liz-Marzán, L. M.; González-Fernández, Á. Sterilization Matters: Consequences of Different Sterilization Techniques on Gold Nanoparticles. *Small* **2010**, *6* (1), 89–95. https://doi.org/10.1002/smll.200901006.

(56) Scroccarello, A.; Álvarez-Diduk, R.; Della Pelle, F.; de Carvalho Castro e Silva, C.; Idili, A.; Parolo, C.; Compagnone, D.; Merkoçi, A. One-Step Laser Nanostructuration of Reduced Graphene Oxide Films Embedding Metal Nanoparticles for Sensing Applications. *ACS Sens.* **2023**, *8* (2), 598–609. https://doi.org/10.1021/acssensors.2c01782.
(57) Mastronardi, V.; Magliocca, E.; Gullon, J. S.; Brescia, R.; Pompa, P. P.; Miller, T. S.; Moglianetti, M. Ultrasmall, Coating-Free, Pyramidal Platinum Nanoparticles for High Stability Fuel Cell Oxygen Reduction. *ACS Appl. Mater. Interfaces* **2022**, *14* (32), 36570–36581. https://doi.org/10.1021/acsami.2c07738.
(58) Mazzotta, E.; Di Giulio, T.; Mastronardi, V.; Pompa, P. P.; Moglianetti, M.; Malitesta, C. Bare Platinum Nanoparticles Deposited on Glassy Carbon Electrodes for Electrocatalytic Detection of Hydrogen Peroxide. *ACS Appl. Nano Mater.* **2021**, *4* (8), 7650–7662. https://doi.org/10.1021/acsanm.1c00754.
(59) Sobhan, M. A.; Withford, M. J.; Goldys, E. M. Enhanced Stability of Gold Colloids Produced by Femtosecond Laser Synthesis in Aqueous Solution of CTAB. *Langmuir* **2010**, *26* (5), 3156–3159. https://doi.org/10.1021/la903088e.
(60) Li, Z.; Ruiz, V. G.; Kanduč, M.; Dzubiella, J. Ion-Specific Adsorption on Bare Gold (Au) Nanoparticles in Aqueous Solutions: Double-Layer Structure and Surface Potentials. *Langmuir* **2020**, *36* (45), 13457–13468. https://doi.org/10.1021/acs.langmuir.0c02097.
(61) Merk, V.; Rehbock, C.; Becker, F.; Hagemann, U.; Nienhaus, H.; Barcikowski, S. In Situ Non-DLVO Stabilization of Surfactant-Free, Plasmonic Gold Nanoparticles: Effect of Hofmeister's Anions. *Langmuir* **2014**, *30* (15), 4213–4222. https://doi.org/10.1021/la404556a.
(62) Oncsik, T.; Trefalt, G.; Borkovec, M.; Szilagyi, I. Specific Ion Effects on Particle Aggregation Induced by Monovalent Salts within the Hofmeister Series. *Langmuir* **2015**, *31* (13), 3799–3807. https://doi.org/10.1021/acs.langmuir.5b00225.
(63) Ziefuß, A. R.; Barcikowski, S.; Rehbock, C. Synergism between Specific Halide Anions and pH Effects during Nanosecond Laser Fragmentation of Ligand-Free Gold Nanoparticles. *Langmuir* **2019**, *35* (20), 6630–6639. https://doi.org/10.1021/acs.langmuir.9b00418.
(64) Lal, M.; Plummer, M.; Smith, W. Solvent Density Effects on the Solvation Behavior and Configurational Structure of Bare and Passivated 38-Atom Gold Nanoparticle in Supercritical Ethane. *J. Phys. Chem. B* **2006**, *110* (42), 20879–20888. https://doi.org/10.1021/jp0633650.
(65) Novelli, F.; Bernal Lopez, M.; Schwaab, G.; Roldan Cuenya, B.; Havenith, M. Water Solvation of Charged and Neutral Gold Nanoparticles. *J. Phys. Chem. B* **2019**, *123* (30), 6521–6528. https://doi.org/10.1021/acs.jpcb.9b02358.
(66) Huggins, M. L. Solutions of Long Chain Compounds. *The Journal of Chemical Physics* **1941**, *9* (5), 440. https://doi.org/10.1063/1.1750930.
(67) Flory, P. J. Thermodynamics of High Polymer Solutions. *The Journal of Chemical Physics* **1942**, *10* (1), 51–61. https://doi.org/10.1063/1.1723621.
(68) Dhabal, D.; Jiang, Z.; Pallath, A.; Patel, A. J. Characterizing the Interplay between Polymer Solvation and Conformation. *J. Phys. Chem. B* **2021**, *125* (20), 5434–5442. https://doi.org/10.1021/acs.jpcb.1c02191.

(69) Athawale, M. V.; Sarupria, S.; Garde, S. Enthalpy−Entropy Contributions to Salt and Osmolyte Effects on Molecular-Scale Hydrophobic Hydration and Interactions. *J. Phys. Chem. B* **2008**, *112* (18), 5661–5670. https://doi.org/10.1021/jp073485n.
(70) Dudowicz, J.; Freed, K. F.; Douglas, J. F. Theory of Competitive Solvation of Polymers by Two Solvents and Entropy-Enthalpy Compensation in the Solvation Free Energy upon Dilution with the Second Solvent. *The Journal of Chemical Physics* **2015**, *142* (21), 214906. https://doi.org/10.1063/1.4921373.
(71) Huang, Y.; Cheng, S. Chain Conformations and Phase Separation in Polymer Solutions with Varying Solvent Quality. *Journal of Polymer Science* **2021**, *59* (22), 2819–2831. https://doi.org/10.1002/pol.20210526.
(72) Siwy, Z.; Kosińska, I. D.; Fuliński, A.; Martin, C. R. Asymmetric Diffusion through Synthetic Nanopores. *Phys. Rev. Lett.* **2005**, *94* (4), 048102. https://doi.org/10.1103/PhysRevLett.94.048102.
(73) Martin, C. R.; Siwy, Z. S. Learning Nature's Way: Biosensing with Synthetic Nanopores. *Science* **2007**, *317* (5836), 331–332. https://doi.org/10.1126/science.1146126.
(74) Bush, S. N.; Ken, J. S.; Martin, C. R. The Ionic Composition and Chemistry of Nanopore-Confined Solutions. *ACS Nano* **2022**, *16* (5), 8338–8346. https://doi.org/10.1021/acsnano.2c02597.
(75) Budd, P. M.; Ghanem, B. S.; Makhseed, S.; McKeown, N. B.; Msayib, K. J.; Tattershall, C. E. Polymers of Intrinsic Microporosity (PIMs): Robust, Solution-Processable, Organic Nanoporous Materials. *Chem. Commun.* **2004**, No. 2, 230–231. https://doi.org/10.1039/B311764B.
(76) Wang, S.; Shi, K.; Tripathi, A.; Chakraborty, U.; Parsons, G. N.; Khan, S. A. Designing Intrinsically Microporous Polymer (PIM-1) Microfibers with Tunable Morphology and Porosity via Controlling Solvent/Nonsolvent/Polymer Interactions. *ACS Appl. Polym. Mater.* **2020**, *2* (6), 2434–2443. https://doi.org/10.1021/acsapm.0c00386.
(77) Wongwilawan, S.; Nguyen, T. S.; Nguyen, T. P. N.; Alhaji, A.; Lim, W.; Hong, Y.; Park, J. S.; Atilhan, M.; Kim, B. J.; Eddaoudi, M.; Yavuz, C. T. Non-Solvent Post-Modifications with Volatile Reagents for Remarkably Porous Ketone Functionalized Polymers of Intrinsic Microporosity. *Nat Commun* **2023**, *14* (1), 2096. https://doi.org/10.1038/s41467-023-37743-y.
(78) Wang, J.; Hou, T. Develop and Test a Solvent Accessible Surface Area-Based Model in Conformational Entropy Calculations. *J. Chem. Inf. Model.* **2012**, *52* (5), 1199–1212. https://doi.org/10.1021/ci300064d.
(79) Janjić, G. V.; Malkov, S. N.; Živković, M. V.; Zarić, S. D. What Are Preferred Water–Aromatic Interactions in Proteins and Crystal Structures of Small Molecules? *Phys. Chem. Chem. Phys.* **2014**, *16* (43), 23549–23553. https://doi.org/10.1039/C4CP00929K.
(80) Pal, P.; Chakraborty, S.; Jana, B. Number of Hydrogen Bonds per Unit Solvent Accessible Surface Area: A Descriptor of Functional States of Proteins. *J. Phys. Chem. B* **2022**, *126* (51), 10822–10833. https://doi.org/10.1021/acs.jpcb.2c05367.
(81) Hofmeister, F. Zur Lehre von der Wirkung der Salze. *Archiv f. experiment. Pathol. u. Pharmakol* **1888**, *24* (4), 247–260. https://doi.org/10.1007/BF01918191.
(82) Kunz, W.; Henle, J.; Ninham, B. W. 'Zur Lehre von Der Wirkung Der Salze' (about the Science of the Effect of Salts): Franz Hofmeister's Historical Papers. *Current Opinion in Colloid & Interface Science* **2004**, *9* (1), 19–37. https://doi.org/10.1016/j.cocis.2004.05.005.

(83) Buchecker, T.; Schmid, P.; Renaudineau, S.; Diat, O.; Proust, A.; Pfitzner, A.; Bauduin, P. Polyoxometalates in the Hofmeister Series. *Chem. Commun.* **2018**, *54* (15), 1833–1836. https://doi.org/10.1039/C7CC09113C.
(84) Rana, B.; Fairhurst, D. J.; Jena, K. C. Ion-Specific Water–Macromolecule Interactions at the Air/Aqueous Interface: An Insight into Hofmeister Effect. *J. Am. Chem. Soc.* **2023**, *145* (17), 9646–9654. https://doi.org/10.1021/jacs.3c00701.
(85) Judd, K. D.; Gonzalez, N. M.; Yang, T.; Cremer, P. S. Contact Ion Pair Formation Is Not Necessarily Stronger than Solvent Shared Ion Pairing. *J. Phys. Chem. Lett.* **2022**, *13* (3), 923–930. https://doi.org/10.1021/acs.jpclett.1c03576.
(86) Drexler, C. I.; Cracchiolo, O. M.; Myers, R. L.; Okur, H. I.; Serrano, A. L.; Corcelli, S. A.; Cremer, P. S. Local Electric Fields in Aqueous Electrolytes. *J. Phys. Chem. B* **2021**, *125* (30), 8484–8493. https://doi.org/10.1021/acs.jpcb.1c03257.
(87) Schwaab, G.; Sebastiani, F.; Havenith, M. Ion Hydration and Ion Pairing as Probed by THz Spectroscopy. *Angewandte Chemie International Edition* **2019**, *58* (10), 3000–3013. https://doi.org/10.1002/anie.201805261.
(88) Okur, H. I.; Hladílková, J.; Rembert, K. B.; Cho, Y.; Heyda, J.; Dzubiella, J.; Cremer, P. S.; Jungwirth, P. Beyond the Hofmeister Series: Ion-Specific Effects on Proteins and Their Biological Functions. *J. Phys. Chem. B* **2017**, *121* (9), 1997–2014. https://doi.org/10.1021/acs.jpcb.6b10797.
(89) Krishnamoorthy, A. N.; Holm, C.; Smiatek, J. Specific Ion Effects for Polyelectrolytes in Aqueous and Non-Aqueous Media: The Importance of the Ion Solvation Behavior. *Soft Matter* **2018**, *14* (30), 6243–6255. https://doi.org/10.1039/C8SM00600H.
(90) Miranda-Quintana, R. A.; Smiatek, J. Specific Ion Effects in Different Media: Current Status and Future Challenges. *J. Phys. Chem. B* **2021**, *125* (51), 13840–13849. https://doi.org/10.1021/acs.jpcb.1c07957.
(91) Mazzini, V.; Craig, V. S. J. What Is the Fundamental Ion-Specific Series for Anions and Cations? Ion Specificity in Standard Partial Molar Volumes of Electrolytes and Electrostriction in Water and Non-Aqueous Solvents. *Chem. Sci.* **2017**, *8* (10), 7052–7065. https://doi.org/10.1039/C7SC02691A.
(92) Yu, W.; Du, N.; Gu, Y.; Yan, J.; Hou, W. Specific Ion Effects on the Colloidal Stability of Layered Double Hydroxide Single-Layer Nanosheets. *Langmuir* **2020**, *36* (23), 6557–6568. https://doi.org/10.1021/acs.langmuir.0c01089.
(93) Han, X.; Goebl, J.; Lu, Z.; Yin, Y. Role of Salt in the Spontaneous Assembly of Charged Gold Nanoparticles in Ethanol. *Langmuir* **2011**, *27* (9), 5282–5289. https://doi.org/10.1021/la200459t.
(94) Abbas, S.; Yadav, I.; Kumar, S.; Aswal, V. K.; Kohlbrecher, J. Structure and Interaction in Pathway of Charged Nanoparticles Aggregation in Saline Water as Probed by Scattering Techniques. *Chemical Physics Letters* **2017**, *675*, 124–130. https://doi.org/10.1016/j.cplett.2017.03.024.
(95) John, V.; Arnosti, C.; Field, J.; Kujawinski, E.; McCormick, A. The Role of Dispersants in Oil Spill Remediation: Fundamental Concepts, Rationale for Use, Fate, and Transport Issues. *Oceanography* **2016**, *29* (3), 108–117.
(96) Attia, M. F.; Dieng, S. M.; Collot, M.; Klymchenko, A. S.; Bouillot, C.; Serra, C. A.; Schmutz, M.; Er-Rafik, M.; Vandamme, T. F.; Anton, N. Functionalizing Nanoemulsions with Carboxylates: Impact on the Biodistribution and Pharmacokinetics in Mice.

Macromolecular Bioscience **2017**, *17* (7), 1600471. https://doi.org/10.1002/mabi.201600471.
(97) Le Révérend, B. J. D.; Taylor, M. S.; Norton, I. T. Design and Application of Water-in-Oil Emulsions for Use in Lipstick Formulations. *Int J Cosmet Sci* **2011**, *33* (3), 263–268. https://doi.org/10.1111/j.1468-2494.2010.00624.x.
(98) Mason, T. G.; Wilking, J. N.; Meleson, K.; Chang, C. B.; Graves, S. M. Nanoemulsions: Formation, Structure, and Physical Properties. *J. Phys.: Condens. Matter* **2006**, *18* (41), R635–R666. https://doi.org/10.1088/0953-8984/18/41/R01.
(99) Kujawinski, E. B.; Reddy, C. M.; Rodgers, R. P.; Thrash, J. C.; Valentine, D. L.; White, H. K. The First Decade of Scientific Insights from the Deepwater Horizon Oil Release. *Nat Rev Earth Environ* **2020**, *1* (5), 237–250. https://doi.org/10.1038/s43017-020-0046-x.
(100) Gupta, A.; Eral, H. B.; Hatton, T. A.; Doyle, P. S. Nanoemulsions: Formation, Properties and Applications. *Soft Matter* **2016**, *12* (11), 2826–2841. https://doi.org/10.1039/C5SM02958A.
(101) McClements, D. J. Nanoemulsions versus Microemulsions: Terminology, Differences, and Similarities. *Soft Matter* **2012**, *8* (6), 1719–1729. https://doi.org/10.1039/C2SM06903B.
(102) Ding, B.; Ahmadi, S. H.; Babak, P.; Bryant, S. L.; Kantzas, A. On the Stability of Pickering and Classical Nanoemulsions: Theory and Experiments. *Langmuir* **2023**, *39* (20), 6975–6991. https://doi.org/10.1021/acs.langmuir.3c00133.
(103) Anton, N.; Vandamme, T. F. Nano-Emulsions and Micro-Emulsions: Clarifications of the Critical Differences. *Pharm Res* **2011**, *28* (5), 978–985. https://doi.org/10.1007/s11095-010-0309-1.
(104) Beaman, D. K.; Robertson, E. J.; Richmond, G. L. From Head to Tail: Structure, Solvation, and Hydrogen Bonding of Carboxylate Surfactants at the Organic–Water Interface. *J. Phys. Chem. C* **2011**, *115* (25), 12508–12516. https://doi.org/10.1021/jp202061y.
(105) Balzerowski, P.; Meister, K.; Versluis, J.; Bakker, H. J. Heterodyne-Detected Sum Frequency Generation Spectroscopy of Polyacrylic Acid at the Air/Water-Interface. *Phys. Chem. Chem. Phys.* **2016**, *18* (4), 2481–2487. https://doi.org/10.1039/C5CP06177F.
(106) Foster, M. J.; Carpenter, A. P.; Richmond, G. L. Dynamic Duo: Vibrational Sum Frequency Scattering Investigation of pH-Switchable Carboxylic Acid/Carboxylate Surfactants on Nanodroplet Surfaces. *J. Phys. Chem. B* **2021**, *125* (33), 9629–9640. https://doi.org/10.1021/acs.jpcb.1c05508.
(107) Zdrali, E.; Chen, Y.; Okur, H. I.; Wilkins, D. M.; Roke, S. The Molecular Mechanism of Nanodroplet Stability. *ACS Nano* **2017**, *11* (12), 12111–12120. https://doi.org/10.1021/acsnano.7b05100.
(108) Athas, J. C.; Jun, K.; McCafferty, C.; Owoseni, O.; John, V. T.; Raghavan, S. R. An Effective Dispersant for Oil Spills Based on Food-Grade Amphiphiles. *Langmuir* **2014**, *30* (31), 9285–9294. https://doi.org/10.1021/la502312n.
(109) Gebauer, J. S.; Malissek, M.; Simon, S.; Knauer, S. K.; Maskos, M.; Stauber, R. H.; Peukert, W.; Treuel, L. Impact of the Nanoparticle–Protein Corona on Colloidal Stability and Protein Structure. *Langmuir* **2012**, *28* (25), 9673–9679. https://doi.org/10.1021/la301104a.
(110) Vasti, C.; Bedoya, D. A.; Rojas, R.; Giacomelli, C. E. Effect of the Protein Corona on the Colloidal Stability and Reactivity of LDH-Based Nanocarriers. *J. Mater. Chem. B* **2016**, *4* (11), 2008–2016. https://doi.org/10.1039/C5TB02698A.

(111) Tengjisi; Hui, Y.; Fan, Y.; Zou, D.; Talbo, G. H.; Yang, G.; Zhao, C.-X. Influence of Nanoparticle Mechanical Property on Protein Corona Formation. *Journal of Colloid and Interface Science* **2022**, *606*, 1737–1744. https://doi.org/10.1016/j.jcis.2021.08.148.
(112) Ren, J.; Andrikopoulos, N.; Velonia, K.; Tang, H.; Cai, R.; Ding, F.; Ke, P. C.; Chen, C. Chemical and Biophysical Signatures of the Protein Corona in Nanomedicine. *J. Am. Chem. Soc.* **2022**, *144* (21), 9184–9205. https://doi.org/10.1021/jacs.2c02277.
(113) Chatterley, A. S.; Golbek, T. W.; Weidner, T. Measuring Protein Conformation at Aqueous Interfaces with 2D Infrared Spectroscopy of Emulsions. *J. Phys. Chem. Lett.* **2022**, *13* (31), 7191–7196. https://doi.org/10.1021/acs.jpclett.2c01324.
(114) Golbek, T. W.; Strunge, K.; Chatterley, A. S.; Weidner, T. Peptide Orientation at Emulsion Nanointerfaces Dramatically Different from Flat Surfaces. *J. Phys. Chem. Lett.* **2022**, *13* (46), 10858–10862. https://doi.org/10.1021/acs.jpclett.2c02870.
(115) Andersson, M. P.; Olsson, M. H. M.; Stipp, S. L. S. Predicting the pKa and Stability of Organic Acids and Bases at an Oil–Water Interface. *Langmuir* **2014**, *30* (22), 6437–6445. https://doi.org/10.1021/la5008318.
(116) Wellen, B. A.; Lach, E. A.; Allen, H. C. Surface pKa of Octanoic, Nonanoic, and Decanoic Fatty Acids at the Air–Water Interface: Applications to Atmospheric Aerosol Chemistry. *Phys. Chem. Chem. Phys.* **2017**, *19* (39), 26551–26558. https://doi.org/10.1039/C7CP04527A.
(117) Drummond, C. J.; Grieser, F.; Healy, T. W. Acid–Base Equilibria in Aqueous Micellar Solutions. Part 1.—'Simple' Weak Acids and Bases. *J. Chem. Soc., Faraday Trans. 1* **1989**, *85* (3), 521–535. https://doi.org/10.1039/F19898500521.
(118) Copp, S. M.; Hamblin, R. L.; Swingle, K.; Rai, D.; Urban, V. S.; Ivanov, S. A.; Montaño, G. A. Complex pH-Dependent Interactions between Weak Polyelectrolyte Block Copolymer Micelles and Molecular Fluorophores. *Langmuir* **2022**, *38* (6), 2038–2045. https://doi.org/10.1021/acs.langmuir.1c02889.
(119) Houska, M.; Brynda, E. Interactions of Proteins with Polyelectrolytes at Solid/Liquid Interfaces: Sequential Adsorption of Albumin and Heparin. *Journal of Colloid and Interface Science* **1997**, *188* (2), 243–250. https://doi.org/10.1006/jcis.1996.4576.
(120) Dickhaus, B. N.; Priefer, R. Determination of Polyelectrolyte pKa Values Using Surface-to-Air Tension Measurements. *Colloids and Surfaces A: Physicochemical and Engineering Aspects* **2016**, *488*, 15–19. https://doi.org/10.1016/j.colsurfa.2015.10.015.
(121) Rumyantsev, A. M.; Jackson, N. E.; de Pablo, J. J. Polyelectrolyte Complex Coacervates: Recent Developments and New Frontiers. *Annual Review of Condensed Matter Physics* **2021**, *12* (1), 155–176. https://doi.org/10.1146/annurev-conmatphys-042020-113457.
(122) Margossian, K. O.; Brown, M. U.; Emrick, T.; Muthukumar, M. Coacervation in Polyzwitterion-Polyelectrolyte Systems and Their Potential Applications for Gastrointestinal Drug Delivery Platforms. *Nat Commun* **2022**, *13* (1), 2250. https://doi.org/10.1038/s41467-022-29851-y.
(123) Sulatha, M. S.; Natarajan, U. Origin of the Difference in Structural Behavior of Poly(Acrylic Acid) and Poly(Methacrylic Acid) in Aqueous Solution Discerned by Explicit-Solvent Explicit-Ion MD Simulations. *Ind. Eng. Chem. Res.* **2011**, *50* (21), 11785–11796. https://doi.org/10.1021/ie2014845.
(124) Zhu, S.; Ye, Z.; Liu, Z.; Chen, Z.; Li, J.; Xiang, Z. Adsorption Characteristics of Polymer Solutions on Media Surfaces and Their Main Influencing Factors. *Polymers* **2021**, *13* (11), 1774. https://doi.org/10.3390/polym13111774.

(125) Kirchenbuechler, I.; Guu, D.; Kurniawan, N. A.; Koenderink, G. H.; Lettinga, M. P. Direct Visualization of Flow-Induced Conformational Transitions of Single Actin Filaments in Entangled Solutions. *Nat Commun* **2014**, *5* (1), 5060. https://doi.org/10.1038/ncomms6060.
(126) Stuart, M. A. C. Adsorbed Polymers in Colloidal Systems: From Statics to Dynamics. *Polym J* **1991**, *23* (5), 669–682. https://doi.org/10.1295/polymj.23.669.
(127) Welch, D.; Lettinga, M. P.; Ripoll, M.; Dogic, Z.; Vliegenthart, G. A. Trains, Tails and Loops of Partially Adsorbed Semi-Flexible Filaments. *Soft Matter* **2015**, *11* (38), 7507–7514. https://doi.org/10.1039/C5SM01457C.
(128) B. Davis, M. J.; Zuo, B.; D. Priestley, R. Competing Polymer–Substrate Interactions Mitigate Random Copolymer Adsorption. *Soft Matter* **2018**, *14* (35), 7204–7213. https://doi.org/10.1039/C8SM01433G.
(129) Schmüser, L.; Golbek, T. W.; Weidner, T. Windowless Detection Geometry for Sum Frequency Scattering Spectroscopy in the C–D and Amide I Regions. *Biointerphases* **2021**, *16* (1), 011201. https://doi.org/10.1116/6.0000419.
(130) Tang, C. Y.; Allen, H. C. Ionic Binding of Na+ versus K+ to the Carboxylic Acid Headgroup of Palmitic Acid Monolayers Studied by Vibrational Sum Frequency Generation Spectroscopy. *J. Phys. Chem. A* **2009**, *113* (26), 7383–7393. https://doi.org/10.1021/jp9000434.
(131) Rouquerol, J.; Avnir, D.; Fairbridge, C. W.; Everett, D. H.; Haynes, J. M.; Pernicone, N.; Ramsay, J. D. F.; Sing, K. S. W.; Unger, K. K. Recommendations for the Characterization of Porous Solids (Technical Report). *Pure and Applied Chemistry* **1994**, *66* (8), 1739–1758. https://doi.org/10.1351/pac199466081739.
(132) Natarajan, R.; Charmant, J. P. H.; Orpen, A. G.; Davis, A. P. Water Chains in Hydrophobic Crystal Channels: Nanoporous Materials as Supramolecular Analogues of Carbon Nanotubes. *Angewandte Chemie International Edition* **2010**, *49* (30), 5125–5129. https://doi.org/10.1002/anie.201002418.
(133) Hummer, G.; Rasaiah, J. C.; Noworyta, J. P. Water Conduction through the Hydrophobic Channel of a Carbon Nanotube. *Nature* **2001**, *414* (6860), 188–190. https://doi.org/10.1038/35102535.
(134) Shim, Y.; Kim, H. J. Solvation of Carbon Nanotubes in a Room-Temperature Ionic Liquid. *ACS Nano* **2009**, *3* (7), 1693–1702. https://doi.org/10.1021/nn900195b.
(135) Wang, X.; Fu, F.; Peng, K.; Huang, Q.; Li, W.; Chen, X.; Yang, Z. Understanding of Competitive Hydrogen Bond Behavior of Imidazolium-Based Ionic Liquid Mixture around Single-Walled Carbon Nanotubes. *J. Phys. Chem. C* **2020**, *124* (12), 6634–6645. https://doi.org/10.1021/acs.jpcc.9b11576.
(136) Shim, Y.; Jung, Y.; Kim, H. J. Carbon Nanotubes in Benzene: Internal and External Solvation. *Phys. Chem. Chem. Phys.* **2011**, *13* (9), 3969–3978. https://doi.org/10.1039/C0CP01845G.
(137) Hinkle, K. R.; Phelan, F. R. Jr. Solvation of Carbon Nanoparticles in Water/Alcohol Mixtures: Using Molecular Simulation To Probe Energetics, Structure, and Dynamics. *J. Phys. Chem. C* **2017**, *121* (41), 22926–22938. https://doi.org/10.1021/acs.jpcc.7b07769.
(138) Pramanik, C.; Gissinger, J. R.; Kumar, S.; Heinz, H. Carbon Nanotube Dispersion in Solvents and Polymer Solutions: Mechanisms, Assembly, and Preferences. *ACS Nano* **2017**, *11* (12), 12805–12816. https://doi.org/10.1021/acsnano.7b07684.

(139) Heinz, H.; Pramanik, C.; Heinz, O.; Ding, Y.; Mishra, R. K.; Marchon, D.; Flatt, R. J.; Estrela-Lopis, I.; Llop, J.; Moya, S.; Ziolo, R. F. Nanoparticle Decoration with Surfactants: Molecular Interactions, Assembly, and Applications. *Surface Science Reports* **2017**, *72* (1), 1–58. https://doi.org/10.1016/j.surfrep.2017.02.001.
(140) Jiang, H.; Cai, Q.; Mateti, S.; Yu, Y.; Zhi, C.; Chen, Y. Boron Nitride Nanosheet Dispersion at High Concentrations. *ACS Appl. Mater. Interfaces* **2021**, *13* (37), 44751–44759. https://doi.org/10.1021/acsami.1c11795.
(141) Smith McWilliams, A. D.; Martínez-Jiménez, C.; Matatyaho Ya'akobi, A.; Ginestra, C. J.; Talmon, Y.; Pasquali, M.; Martí, A. A. Understanding the Exfoliation and Dispersion of Hexagonal Boron Nitride Nanosheets by Surfactants: Implications for Antibacterial and Thermally Resistant Coatings. *ACS Appl. Nano Mater.* **2021**, *4* (1), 142–151. https://doi.org/10.1021/acsanm.0c02437.
(142) Li, D.; Müller, M. B.; Gilje, S.; Kaner, R. B.; Wallace, G. G. Processable Aqueous Dispersions of Graphene Nanosheets. *Nature Nanotech* **2008**, *3* (2), 101–105. https://doi.org/10.1038/nnano.2007.451.
(143) Ma, H.; Shen, Z.; Ben, S. Understanding the Exfoliation and Dispersion of MoS2 Nanosheets in Pure Water. *Journal of Colloid and Interface Science* **2018**, *517*, 204–212. https://doi.org/10.1016/j.jcis.2017.11.013.
(144) Kim, J.; Kwon, S.; Cho, D.-H.; Kang, B.; Kwon, H.; Kim, Y.; Park, S. O.; Jung, G. Y.; Shin, E.; Kim, W.-G.; Lee, H.; Ryu, G. H.; Choi, M.; Kim, T. H.; Oh, J.; Park, S.; Kwak, S. K.; Yoon, S. W.; Byun, D.; Lee, Z.; Lee, C. Direct Exfoliation and Dispersion of Two-Dimensional Materials in Pure Water via Temperature Control. *Nat Commun* **2015**, *6* (1), 8294. https://doi.org/10.1038/ncomms9294.
(145) Schoeman, B. J.; Sterte, J.; Otterstedt, J.-E. Colloidal Zeolite Suspensions. *Zeolites* **1994**, *14* (2), 110–116. https://doi.org/10.1016/0144-2449(94)90004-3.
(146) Lam, C. H.; Chi, H.-Y.; Hsu, S.-M.; Li, Y.-S.; Lee, W.-Y.; Cheng, I.-C.; Kang, D.-Y. Surfactant-Mediated Self-Assembly of Nanocrystals to Form Hierarchically Structured Zeolite Thin Films with Controlled Crystal Orientation. *RSC Adv.* **2017**, *7* (77), 49048–49055. https://doi.org/10.1039/C7RA10679C.
(147) Hsu, W.-J.; Huang, P.-S.; Huang, Y.-C.; Hu, S.-W.; Tsao, H.-K.; Kang, D.-Y. Zeolite-Based Antifogging Coating via Direct Wet Deposition. *Langmuir* **2019**, *35* (7), 2538–2546. https://doi.org/10.1021/acs.langmuir.8b03738.
(148) Gözcü, O.; Kayacı, H. U.; Dou, Y.; Zhang, W.; Hedin, N.; Jasso-Salcedo, A. B.; Kaiser, A.; Çınar Aygün, S. Colloidal Stabilization of Submicron-Sized Zeolite NaA in Ethanol–Water Mixtures for Nanostructuring into Thin Films and Nanofibers. *Langmuir* **2023**, *39* (1), 192–203. https://doi.org/10.1021/acs.langmuir.2c02241.
(149) Cai, Q.; Luo, Z.-S.; Pang, W.-Q.; Fan, Y.-W.; Chen, X.-H.; Cui, F.-Z. Dilute Solution Routes to Various Controllable Morphologies of MCM-41 Silica with a Basic Medium. *Chem. Mater.* **2001**, *13* (2), 258–263. https://doi.org/10.1021/cm990661z.
(150) Nooney, R. I.; Thirunavukkarasu, D.; Chen, Y.; Josephs, R.; Ostafin, A. E. Synthesis of Nanoscale Mesoporous Silica Spheres with Controlled Particle Size. *Chem. Mater.* **2002**, *14* (11), 4721–4728. https://doi.org/10.1021/cm0204371.
(151) Kobler, J.; Möller, K.; Bein, T. Colloidal Suspensions of Functionalized Mesoporous Silica Nanoparticles. *ACS Nano* **2008**, *2* (4), 791–799. https://doi.org/10.1021/nn700008s.

(152) Möller, K.; Kobler, J.; Bein, T. Colloidal Suspensions of Nanometer-Sized Mesoporous Silica. *Advanced Functional Materials* **2007**, *17* (4), 605–612. https://doi.org/10.1002/adfm.200600578.
(153) Pyo, C. E.; Chang, J. H. Hydrophobic Mesoporous Silica Particles Modified With Nonfluorinated Alkyl Silanes. *ACS Omega* **2021**, *6* (24), 16100–16109. https://doi.org/10.1021/acsomega.1c01981.
(154) Sabuncu, S.; Montoya Mira, J.; Quentel, A.; Gomes, M. M.; Civitci, F.; Fischer, J. M.; Yildirim, A. Protein-Coated Biodegradable Gas-Stabilizing Nanoparticles for Cancer Therapy and Diagnosis Using Focused Ultrasound. *Advanced Materials Interfaces* **2023**, *10* (2), 2201543. https://doi.org/10.1002/admi.202201543.
(155) Yamamoto, E.; Shimojima, A.; Wada, H.; Kuroda, K. Mesoporous Silica Nanoparticles with Dispersibility in Organic Solvents and Their Versatile Surface Modification. *Langmuir* **2020**, *36* (20), 5571–5578. https://doi.org/10.1021/acs.langmuir.0c00729.
(156) Schneid, A. D. C.; Silveira, C. P.; Galdino, F. E.; Ferreira, L. F.; Bouchmella, K.; Cardoso, M. B. Colloidal Stability and Redispersibility of Mesoporous Silica Nanoparticles in Biological Media. *Langmuir* **2020**, *36* (39), 11442–11449. https://doi.org/10.1021/acs.langmuir.0c01571.
(157) Wang, A.; Barcus, K.; Cohen, S. M. Quantifying Ligand Binding to the Surface of Metal–Organic Frameworks. *J. Am. Chem. Soc.* **2023**, *145* (30), 16821–16827. https://doi.org/10.1021/jacs.3c04892.
(158) Erdosy, D. P.; Wenny, M. B.; Cho, J.; DelRe, C.; Walter, M. V.; Jiménez-Ángeles, F.; Qiao, B.; Sanchez, R.; Peng, Y.; Polizzotti, B. D.; de la Cruz, M. O.; Mason, J. A. Microporous Water with High Gas Solubilities. *Nature* **2022**, *608* (7924), 712–718. https://doi.org/10.1038/s41586-022-05029-w.
(159) DelRe, C.; Hong, H.; Wenny, M. B.; Erdosy, D. P.; Cho, J.; Lee, B.; Mason, J. A. Design Principles for Using Amphiphilic Polymers To Create Microporous Water. *J. Am. Chem. Soc.* **2023**, *145* (36), 19982–19988. https://doi.org/10.1021/jacs.3c06627.
(160) LeRoy, M. A.; Perera, A. S.; Lamichhane, S.; Mapile, A. N.; Khaliq, F.; Kadota, K.; Zhang, X.; Ha, S.; Fisher, R.; Wu, D.; Risko, C.; Brozek, C. K. Colloidal Stability and Solubility of Metal–Organic Framework Particles. *Chem. Mater.* **2024**, *36* (8), 3673–3682. https://doi.org/10.1021/acs.chemmater.3c03191.
(161) Romero-Angel, M.; Castells-Gil, J.; Rubio-Giménez, V.; Ameloot, R.; Tatay, S.; Martí-Gastaldo, C. Surfactant-Assisted Synthesis of Titanium nanoMOFs for Thin Film Fabrication. *Chem. Commun.* **2021**, *57* (72), 9040–9043. https://doi.org/10.1039/D1CC02828F.
(162) Zheng, G.; Chen, Z.; Sentosun, K.; Pérez-Juste, I.; Bals, S.; Liz-Marzán, L. M.; Pastoriza-Santos, I.; Pérez-Juste, J.; Hong, M. Shape Control in ZIF-8 Nanocrystals and Metal nanoparticles@ZIF-8 Heterostructures. *Nanoscale* **2017**, *9* (43), 16645–16651. https://doi.org/10.1039/C7NR03739B.
(163) Mapile, A. N.; LeRoy, M. A.; Fabrizio, K.; Scatena, L. F.; Brozek, C. K. The Surface of Colloidal Metal–Organic Framework Nanoparticles Revealed by Vibrational Sum Frequency Scattering Spectroscopy. *ACS Nano* **2024**. https://doi.org/10.1021/acsnano.4c03758.
(164) Wang, S.; Park, S. S.; Buru, C. T.; Lin, H.; Chen, P.-C.; Roth, E. W.; Farha, O. K.; Mirkin, C. A. Colloidal Crystal Engineering with Metal–Organic Framework Nanoparticles and DNA. *Nat Commun* **2020**, *11* (1), 2495. https://doi.org/10.1038/s41467-020-16339-w.

(165) Ding, S.; Zhang, Y.; Lou, F.; Aslam, M. K.; Sun, Y.; Li, M.; Duan, J.; Li, Y.; Chen, S. "Uncapped" Metal–Organic Framework (MOF) Dispersions Driven by O_2 Plasma towards Superior Oxygen Evolution Electrocatalysis. *J. Mater. Chem. A* **2022**, *10* (39), 20813–20818. https://doi.org/10.1039/D2TA05387J.
(166) Jongert, T. K.; Slowinski, I. A.; Dao, B.; Cortez, V. H.; Gredig, T.; Plascencia, N. D.; Tian, F. Zeta Potential and Size Analysis of Zeolitic Imidazolate Framework-8 Nanocrystals Prepared by Surfactant-Assisted Synthesis. *Langmuir* **2024**, *40* (12), 6138–6148. https://doi.org/10.1021/acs.langmuir.3c03193.
(167) Yakin, F. E.; Barisik, M.; Sen, T. Pore Size and Porosity Dependent Zeta Potentials of Mesoporous Silica Nanoparticles. *J. Phys. Chem. C* **2020**, *124* (36), 19579–19587. https://doi.org/10.1021/acs.jpcc.0c04602.
(168) Chen, C.-Y.; Hsieh, M.-J.; Raj, A.; Peng, W.-C.; Hamaguchi, H.; Chuang, W.-T.; Wang, X.; Wang, C.-L. Missing Piece in Colloidal Stability─Morphological Factor of Hydrophobic Nanoparticles. *Langmuir* **2023**, *39* (8), 2922–2931. https://doi.org/10.1021/acs.langmuir.2c02582.
(169) Zobel, M.; Neder, R. B.; Kimber, S. A. J. Universal Solvent Restructuring Induced by Colloidal Nanoparticles. *Science* **2015**, *347* (6219), 292–294. https://doi.org/10.1126/science.1261412.
(170) Zobel, M. Observing Structural Reorientations at Solvent–Nanoparticle Interfaces by X-Ray Diffraction – Putting Water in the Spotlight. *Acta Crystallogr A Found Adv* **2016**, *72* (6), 621–631. https://doi.org/10.1107/S2053273316013516.
(171) Thomä, S. L. J.; Krauss, S. W.; Eckardt, M.; Chater, P.; Zobel, M. Atomic Insight into Hydration Shells around Facetted Nanoparticles. *Nat Commun* **2019**, *10* (1), 995. https://doi.org/10.1038/s41467-019-09007-1.
(172) Israelachvili, J. N.; McGuiggan, P. M. Forces Between Surfaces in Liquids. *Science* **1988**, *241* (4867), 795–800. https://doi.org/10.1126/science.241.4867.795.
(173) Israelachvili, J. N.; Wennerstroem, H. Entropic Forces between Amphiphilic Surfaces in Liquids. *J. Phys. Chem.* **1992**, *96* (2), 520–531. https://doi.org/10.1021/j100181a007.
(174) Roke, S.; Roeterdink, W. G.; Wijnhoven, J. E. G. J.; Petukhov, A. V.; Kleyn, A. W.; Bonn, M. Vibrational Sum Frequency Scattering from a Submicron Suspension. *Phys. Rev. Lett.* **2003**, *91* (25), 258302. https://doi.org/10.1103/PhysRevLett.91.258302.
(175) Shen, Y. R. Surface Properties Probed by Second-Harmonic and Sum-Frequency Generation. *Nature* **1989**, *337* (6207), 519–525. https://doi.org/10.1038/337519a0.
(176) Gragson, D. E.; Richmond, G. L. Comparisons of the Structure of Water at Neat Oil/Water and Air/Water Interfaces As Determined by Vibrational Sum Frequency Generation. *Langmuir* **1997**, *13* (18), 4804–4806. https://doi.org/10.1021/la970497z.
(177) Scatena, L. F.; Brown, M. G.; Richmond, G. L. Water at Hydrophobic Surfaces: Weak Hydrogen Bonding and Strong Orientation Effects. *Science* **2001**, *292* (5518), 908–912. https://doi.org/10.1126/science.1059514.
(178) Wang, H.; Xu, Q.; Liu, Z.; Tang, Y.; Wei, G.; Shen, Y. R.; Liu, W.-T. Gate-Controlled Sum-Frequency Vibrational Spectroscopy for Probing Charged Oxide/Water Interfaces. *J. Phys. Chem. Lett.* **2019**, *10* (19), 5943–5948. https://doi.org/10.1021/acs.jpclett.9b01908.
(179) Rehl, B.; Ma, E.; Parshotam, S.; DeWalt-Kerian, E. L.; Liu, T.; Geiger, F. M.; Gibbs, J. M. Water Structure in the Electrical Double Layer and the Contributions to the Total Interfacial Potential at Different Surface Charge Densities. *J. Am. Chem. Soc.* **2022**, *144* (36), 16338–16349. https://doi.org/10.1021/jacs.2c01830.

(180) Carpenter, A. P.; Tran, E.; Altman, R. M.; Richmond, G. L. Formation and Surface-Stabilizing Contributions to Bare Nanoemulsions Created with Negligible Surface Charge. *Proc Natl Acad Sci USA* **2019**, *116* (19), 9214–9219. https://doi.org/10.1073/pnas.1900802116.
(181) Pullanchery, S.; Kulik, S.; Rehl, B.; Hassanali, A.; Roke, S. Charge Transfer across C–H···O Hydrogen Bonds Stabilizes Oil Droplets in Water. *Science* **2021**, *374* (6573), 1366–1370. https://doi.org/10.1126/science.abj3007.
(182) Bain, C. D.; Davies, P. B.; Ong, T. Hui.; Ward, R. N.; Brown, M. A. Quantitative Analysis of Monolayer Composition by Sum-Frequency Vibrational Spectroscopy. *Langmuir* **1991**, *7* (8), 1563–1566. https://doi.org/10.1021/la00056a003.
(183) *NLS-Simulate. Get the software safely and easily.* Software Informer. https://nls-simulate.software.informer.com/ (accessed 2022-06-06).
(184) Beer, A. G. F. de; Roke, S.; Dadap, J. I. Theory of Optical Second-Harmonic and Sum-Frequency Scattering from Arbitrarily Shaped Particles. *J. Opt. Soc. Am. B, JOSAB* **2011**, *28* (6), 1374–1384. https://doi.org/10.1364/JOSAB.28.001374.
(185) Tran, E.; Jones, K. K.; Cano, G. A.; Moore, F. G.; Scatena, L. F. Spectroscopic Studies of Zwitterionic DDAPS at Planar and Droplet Oil/Water Interfaces. *J. Phys. Chem. B* **2022**, *126* (39), 7720–7730. https://doi.org/10.1021/acs.jpcb.2c02664.
(186) Tanaka, N.; Kitano, H.; Ise, N. Raman Spectroscopic Study of Hydrogen Bonding in Aqueous Carboxylic Acid Solutions. 3. Polyacrylic Acid. *Macromolecules* **1991**, *24* (10), 3017–3019. https://doi.org/10.1021/ma00010a060.
(187) Swift, T.; Swanson, L.; Geoghegan, M.; Rimmer, S. The pH-Responsive Behaviour of Poly(Acrylic Acid) in Aqueous Solution Is Dependent on Molar Mass. *Soft Matter* **2016**, *12* (9), 2542–2549. https://doi.org/10.1039/C5SM02693H.
(188) Mintis, D. G.; Mavrantzas, V. G. Effect of pH and Molecular Length on the Structure and Dynamics of Short Poly(Acrylic Acid) in Dilute Solution: Detailed Molecular Dynamics Study. *J. Phys. Chem. B* **2019**, *123* (19), 4204–4219. https://doi.org/10.1021/acs.jpcb.9b01696.
(189) Chollakup, R.; Beck, J. B.; Dirnberger, K.; Tirrell, M.; Eisenbach, C. D. Polyelectrolyte Molecular Weight and Salt Effects on the Phase Behavior and Coacervation of Aqueous Solutions of Poly(Acrylic Acid) Sodium Salt and Poly(Allylamine) Hydrochloride. *Macromolecules* **2013**, *46* (6), 2376–2390. https://doi.org/10.1021/ma202172q.
(190) Gong, Z.; Zacharia, N. S.; Vogt, B. D. Sodium Dodecyl Sulfate Modulates the Structure and Rheological Properties of Pluronic F108–Poly(Acrylic Acid) Coacervates). *Soft Matter* **2022**, *18* (2), 340–350. https://doi.org/10.1039/D1SM01273H.
(191) Beaman, D. K.; Robertson, E. J.; Richmond, G. L. Unique Assembly of Charged Polymers at the Oil−Water Interface. *Langmuir* **2011**, *27* (6), 2104–2106. https://doi.org/10.1021/la104390u.
(192) Beaman, D. K.; Robertson, E. J.; Richmond, G. L. Ordered Polyelectrolyte Assembly at the Oil-Water Interface. *Proceedings of the National Academy of Sciences* **2012**, *109* (9), 3226–3231. https://doi.org/10.1073/pnas.1200244109.
(193) Beaman, D. K.; Robertson, E. J.; Richmond, G. L. Metal Ions: Driving the Orderly Assembly of Polyelectrolytes at a Hydrophobic Surface. *Langmuir* **2012**, *28* (40), 14245–14253. https://doi.org/10.1021/la302917p.

(194) Robertson, E. J.; Richmond, G. L. Molecular Insights in the Structure and Layered Assembly of Polyelectrolytes at the Oil/Water Interface. *J. Phys. Chem. C* **2014**, *118* (49), 28331–28343. https://doi.org/10.1021/jp5068022.
(195) Phan, H. T.; Haes, A. J. What Does Nanoparticle Stability Mean? *J. Phys. Chem. C* **2019**, *123* (27), 16495–16507. https://doi.org/10.1021/acs.jpcc.9b00913.
(196) Hunter, S. J.; Armes, S. P. Pickering Emulsifiers Based on Block Copolymer Nanoparticles Prepared by Polymerization-Induced Self-Assembly. *Langmuir* **2020**, *36* (51), 15463–15484. https://doi.org/10.1021/acs.langmuir.0c02595.
(197) Chen, K.; Wang, S.; Guo, X. Confinement Effect on the Aqueous Behaviors of Free Poly(Acrylic Acid) and Poly(Acrylic Acid) Grafted on a Nanoparticle Surface. *Colloid Polym Sci* **2019**, *297* (9), 1223–1231. https://doi.org/10.1007/s00396-019-04541-2.
(198) Tran, E.; Carpenter, A. P.; Richmond, G. L. Probing the Molecular Structure of Coadsorbed Polyethylenimine and Charged Surfactants at the Nanoemulsion Droplet Surface. *Langmuir* **2020**, *36* (31), 9081–9089. https://doi.org/10.1021/acs.langmuir.0c01095.
(199) Fan, Y. L.; Tan, C. H.; Lui, Y.; Zudhistira, D.; Loo, S. C. J. Mechanistic Formation of Drug-Encapsulated Janus Particles through Emulsion Solvent Evaporation. *RSC Adv.* **2018**, *8* (29), 16032–16042. https://doi.org/10.1039/C8RA02271B.
(200) Nandy, M.; Lahiri, B. B.; Philip, J. Probing Concentration and Time Dependent Conformational Changes in Poly Acrylic Acid Stabilized Magnetic Nanoemulsion Using Magnetic Chaining-Based Inter-Droplet Force Measurement. *Colloid and Interface Science Communications* **2022**, *47*, 100592. https://doi.org/10.1016/j.colcom.2022.100592.
(201) Han, S.; An, H.; Tao, H.; Li, L.; Qi, Y.; Ma, Y.; Li, X.; Wang, R.; Zhang, J. Advanced Emulsions via Noncovalent Interaction-Mediated Interfacial Self-Assembly. *Chem. Commun.* **2018**, *54* (25), 3174–3177. https://doi.org/10.1039/C8CC00016F.
(202) Liu, D.; Zhang, Z.; Zhang, K.; Li, Y.; Song, D.-P. Host-Guest Interaction Mediated Interfacial Co-Assembly of Cyclodextrin and Bottlebrush Surfactants for Precisely Tunable Photonic Supraballs. *Small n/a* (n/a), 2312099. https://doi.org/10.1002/smll.202312099.
(203) Krężel, A.; Bal, W. A Formula for Correlating pKa Values Determined in D2O and H2O. *Journal of Inorganic Biochemistry* **2004**, *98* (1), 161–166. https://doi.org/10.1016/j.jinorgbio.2003.10.001.
(204) Goldburg, W. I. Dynamic Light Scattering. *American Journal of Physics* **1999**, *67* (12), 1152–1160. https://doi.org/10.1119/1.19101.
(205) Clogston, J. D.; Patri, A. K. Zeta Potential Measurement. *Methods Mol Biol* **2011**, *697*, 63–70. https://doi.org/10.1007/978-1-60327-198-1_6.
(206) Xi, W.; Haes, A. J. Elucidation of HEPES Affinity to and Structure on Gold Nanostars. *J. Am. Chem. Soc.* **2019**, *141* (9), 4034–4042. https://doi.org/10.1021/jacs.8b13211.
(207) Roger, K.; Cabane, B. Why Are Hydrophobic/Water Interfaces Negatively Charged? *Angewandte Chemie International Edition* **2012**, *51* (23), 5625–5628. https://doi.org/10.1002/anie.201108228.
(208) Barany, S. Polymer Adsorption and Electrokinetic Potential of Dispersed Particles in Weak and Strong Electric Fields. *Advances in Colloid and Interface Science* **2015**, *222*, 58–69.

(209) Ostolska, I.; Wiśniewska, M. Application of the Zeta Potential Measurements to Explanation of Colloidal Cr2O3 Stability Mechanism in the Presence of the Ionic Polyamino Acids. *Colloid Polym Sci* **2014**, *292* (10), 2453–2464. https://doi.org/10.1007/s00396-014-3276-y.
(210) Nobbmann, U. *Polydispersity – what does it mean for DLS and chromatography? - Materials Talks*. https://www.materials-talks.com/polydispersity-what-does-it-mean-for-dls-and-chromatography/ (accessed 2024-01-29).
(211) Rolland, M.; Truong, N. P.; Parkatzidis, K.; Pilkington, E. H.; Torzynski, A. L.; Style, R. W.; Dufresne, E. R.; Anastasaki, A. Shape-Controlled Nanoparticles from a Low-Energy Nanoemulsion. *JACS Au* **2021**, *1* (11), 1975–1986. https://doi.org/10.1021/jacsau.1c00321.
(212) To, D.; Kali, G.; Haddadzadegan, S.; Jörgensen, A. M.; Nigl, K.; Ricci, F.; Bernkop-Schnürch, A. Power-Up for Mucoadhesiveness: Two Generations of Thiolated Surfactants for Enhanced Sticky Nanoemulsions. *ACS Biomater. Sci. Eng.* **2023**, *9* (12), 6797–6804. https://doi.org/10.1021/acsbiomaterials.3c01207.
(213) Guo, Y.; Zhang, X.; Wang, X.; Zhang, L.; Xu, Z.; Sun, D. Nanoemulsions Stable against Ostwald Ripening. *Langmuir* **2024**, *40* (2), 1364–1372. https://doi.org/10.1021/acs.langmuir.3c03019.
(214) Chen, M.; Liu, X.; Fahr, A. Skin Penetration and Deposition of Carboxyfluorescein and Temoporfin from Different Lipid Vesicular Systems: In Vitro Study with Finite and Infinite Dosage Application. *International Journal of Pharmaceutics* **2011**, *408* (1), 223–234. https://doi.org/10.1016/j.ijpharm.2011.02.006.
(215) Danaei, M.; Dehghankhold, M.; Ataei, S.; Hasanzadeh Davarani, F.; Javanmard, R.; Dokhani, A.; Khorasani, S.; Mozafari, M. R. Impact of Particle Size and Polydispersity Index on the Clinical Applications of Lipidic Nanocarrier Systems. *Pharmaceutics* **2018**, *10* (2), 57. https://doi.org/10.3390/pharmaceutics10020057.
(216) Meng, R.; Wang, C.; Jin, J.; Wang, R.; Deng, L. Self-Assembly of Hydrophobically Associating Amphiphilic Polymer with Surfactant and Its Effect on Nanoemulsion. *Colloids and Surfaces A: Physicochemical and Engineering Aspects* **2022**, *642*, 128599. https://doi.org/10.1016/j.colsurfa.2022.128599.
(217) Estabrook, D. A.; Ennis, A. F.; Day, R. A.; Sletten, E. M. Controlling Nanoemulsion Surface Chemistry with Poly(2-Oxazoline) Amphiphiles. *Chem. Sci.* **2019**, *10* (14), 3994–4003. https://doi.org/10.1039/C8SC05735D.
(218) Hunter, S. J.; Cornel, E. J.; Mykhaylyk, O. O.; Armes, S. P. Effect of Salt on the Formation and Stability of Water-in-Oil Pickering Nanoemulsions Stabilized by Diblock Copolymer Nanoparticles. *Langmuir* **2020**, *36* (51), 15523–15535. https://doi.org/10.1021/acs.langmuir.0c02742.
(219) Dong, J.; Ozaki, Y.; Nakashima, K. FTIR Studies of Conformational Energies of Poly(Acrylic Acid) in Cast Films. *Journal of Polymer Science Part B: Polymer Physics* **1997**, *35* (3), 507–515. https://doi.org/10.1002/(SICI)1099-0488(199702)35:3<507::AID-POLB9>3.0.CO;2-O.
(220) Hu, D.; Yang, Z.; Chou, K. C. Interactions of Polyelectrolytes with Water and Ions at Air/Water Interfaces Studied by Phase-Sensitive Sum Frequency Generation Vibrational Spectroscopy. *J. Phys. Chem. C* **2013**, *117* (30), 15698–15703. https://doi.org/10.1021/jp404308g.

(221) Valley, N. A.; Robertson, E. J.; Richmond, G. L. Twist and Turn: Effect of Stereoconfiguration on the Interfacial Assembly of Polyelectrolytes. *Langmuir* **2014**, *30* (47), 14226–14233. https://doi.org/10.1021/la5037629.
(222) Kang, Y.; Zhao, X.; Han, X.; Ji, X.; Chen, Q.; Pasch, H.; Lederer, A.; Liu, Y. Conformation and Persistence Length of Chitosan in Aqueous Solutions of Different Ionic Strengths via Asymmetric Flow Field-Flow Fractionation. *Carbohydrate Polymers* **2021**, *271*, 118402. https://doi.org/10.1016/j.carbpol.2021.118402.
(223) Davies, J. T. A QUANTITATIVE KINETIC THEORY OF EMULSION TYPE. I. PHYSICAL CHEMISTRY OF THE EMULSIFYING AGENT. *Gas/Liquid and Liquid/Liquid Interfaces. Proceedings of 2nd International Congress Surface Activity* **1957**, 426–438.
(224) de Beer, A. G. F.; Roke, S. Nonlinear Mie Theory for Second-Harmonic and Sum-Frequency Scattering. *Phys. Rev. B* **2009**, *79* (15), 155420. https://doi.org/10.1103/PhysRevB.79.155420.
(225) Fahr, A.; Liu, X. Drug Delivery Strategies for Poorly Water-Soluble Drugs. *Expert Opinion on Drug Delivery* **2007**, *4* (4), 403–416. https://doi.org/10.1517/17425247.4.4.403.
(226) Wilson, B.; Geetha, K. M. Lipid Nanoparticles in the Development of mRNA Vaccines for COVID-19. *Journal of Drug Delivery Science and Technology* **2022**, *74*, 103553. https://doi.org/10.1016/j.jddst.2022.103553.
(227) Pourjavadi, A.; Amin, S. S.; Hosseini, S. H. Delivery of Hydrophobic Anticancer Drugs by Hydrophobically Modified Alginate Based Magnetic Nanocarrier. *Ind. Eng. Chem. Res.* **2018**, *57* (3), 822–832. https://doi.org/10.1021/acs.iecr.7b04050.
(228) Yilmaz, G.; Demir, B.; Timur, S.; Becer, C. R. Poly(Methacrylic Acid)-Coated Gold Nanoparticles: Functional Platforms for Theranostic Applications. *Biomacromolecules* **2016**, *17* (9), 2901–2911. https://doi.org/10.1021/acs.biomac.6b00706.
(229) Hogarth, C.; Arnold, K.; McLauchlin, A.; P. Rannard, S.; Siccardi, M.; O. McDonald, T. Evaluating the Impact of Systematic Hydrophobic Modification of Model Drugs on the Control, Stability and Loading of Lipid-Based Nanoparticles. *Journal of Materials Chemistry B* **2021**, *9* (48), 9874–9884. https://doi.org/10.1039/D1TB02297K.
(230) Chen, L.-H.; Doyle, P. S. Design and Use of a Thermogelling Methylcellulose Nanoemulsion to Formulate Nanocrystalline Oral Dosage Forms. *Advanced Materials* **2021**, *33* (29), 2008618. https://doi.org/10.1002/adma.202008618.
(231) Handa, M.; Ujjwal, R. R.; Vasdev, N.; Flora, S. J. S.; Shukla, R. Optimization of Surfactant- and Cosurfactant-Aided Pine Oil Nanoemulsions by Isothermal Low-Energy Methods for Anticholinesterase Activity. *ACS Omega* **2021**, *6* (1), 559–568. https://doi.org/10.1021/acsomega.0c05033.
(232) Huo, Q.; Gao, Y.; Wu, W.; Hu, S.; Dong, E.; Zhang, Y.; Tian, Y.; Huang, Y.; Quan, P.; Liu, D. Plugging the Leak of Nanoparticles by Interfacial Polymer Adsorption Enables an Efficient Protein and Peptide Encapsulation. *Advanced Functional Materials* **2024**, *34* (6), 2310146. https://doi.org/10.1002/adfm.202310146.
(233) Miao, Y.; Li, L.; Wang, Y.; Wang, J.; Zhou, Y.; Guo, L.; Zhao, Y.; Nie, D.; Zhang, Y.; Zhang, X.; Gan, Y. Regulating Protein Corona on Nanovesicles by Glycosylated Polyhydroxy Polymer Modification for Efficient Drug Delivery. *Nat Commun* **2024**, *15* (1), 1159. https://doi.org/10.1038/s41467-024-45254-7.

(234) Mapile, A. N.; Scatena, L. F. Stabilizing Strands: Exploring the Kinetic Stability of Polymer-Coated Emulsions with Surface Specific Spectroscopy. *Colloids and Surfaces A: Physicochemical and Engineering Aspects* **2024**, *697*, 134414. https://doi.org/10.1016/j.colsurfa.2024.134414.
(235) Wang, R.; Wei, Q.; Sheng, W.; Yu, B.; Zhou, F.; Li, B. Driving Polymer Brushes from Synthesis to Functioning. *Angewandte Chemie International Edition* **2023**, *62* (27), e202219312. https://doi.org/10.1002/anie.202219312.
(236) Li, D.; Xu, L.; Wang, J.; Gautrot, J. E. Responsive Polymer Brush Design and Emerging Applications for Nanotheranostics. *Advanced Healthcare Materials* **2021**, *10* (5), 2000953. https://doi.org/10.1002/adhm.202000953.
(237) Patel, A.; Mohanan, A.; Ghosh, S. Effect of Protein Type, Concentration and Oil Droplet Size on the Formation of Repulsively Jammed Elastic Nanoemulsion Gels. *Soft Matter* **2019**, *15* (47), 9762–9775. https://doi.org/10.1039/C9SM01650C.
(238) Bochenek, S.; Rudov, A. A.; Sassmann, T.; Potemkin, I. I.; Richtering, W. Influence of Architecture on the Interfacial Properties of Polymers: Linear Chains, Stars, and Microgels. *Langmuir* **2023**, *39* (50), 18354–18365. https://doi.org/10.1021/acs.langmuir.3c02470.
(239) Seong, H.-G.; Jin, Z.; Chen, Z.; Hu, M.; Emrick, T.; Russell, T. P. Bottlebrush Block Copolymers at the Interface of Immiscible Liquids: Adsorption and Lateral Packing. *J. Am. Chem. Soc.* **2024**, *146* (19), 13000–13009. https://doi.org/10.1021/jacs.3c13817.
(240) Effenberg, C.; Gaitzsch, J. Stretched or Wrinkled? Looking into the Polymer Conformation within Polymersome Membranes. *Soft Matter* **2024**. https://doi.org/10.1039/D4SM00239C.
(241) Carrillo, J.-M. Y.; Chen, Z.; Premadasa, U. I.; Steinmetz, C.; Coughlin, E. B.; Doughty, B.; Russell, T. P.; Sumpter, B. G. Assembly of Polyelectrolyte Star Block Copolymers at the Oil–Water Interface. *Nanoscale* **2023**, *15* (3), 1042–1052. https://doi.org/10.1039/D2NR05113C.
(242) Morozova, T. I.; García, N. A.; Barrat, J.-L.; Luengo, G. S.; Léonforte, F. Adsorption and Desorption of Polymers on Bioinspired Chemically Structured Substrates. *ACS Appl. Mater. Interfaces* **2021**, *13* (25), 30086–30097. https://doi.org/10.1021/acsami.1c07425.
(243) Qiao, H.; Wu, B.; Sun, S.; Wu, P. Entropy-Driven Design of Highly Impact-Stiffening Supramolecular Polymer Networks with Salt-Bridge Hydrogen Bonds. *J. Am. Chem. Soc.* **2024**, *146* (11), 7533–7542. https://doi.org/10.1021/jacs.3c13392.
(244) Kawaguchi, M.; Takahashi, A. Molecular Weight Dependence of the Thickness of the Polystyrene Layer Adsorbed onto a Metal Surface in Good Solvent Conditions. *Macromolecules* **1983**, *16* (9), 1465–1469. https://doi.org/10.1021/ma00243a010.
(245) Xu, J.; Bai, L.; Ren, W.; Zhu, H.; Zhou, X.; Zhang, C.; Wang, X. Flattened Chains Dominate the Adsorption Dynamics of Loosely Adsorbed Chains on Modified Planar Substrates. *Soft Matter* **2024**, *20* (1), 201–211. https://doi.org/10.1039/D3SM01339A.
(246) de Lima, B. M.; Hayes, P. L.; Wood-Adams, P. M. Influence of Polymer Molecular Weight on Chain Conformation at the Polystyrene/Silver Interface. *Langmuir* **2021**, *37* (33), 10036–10045. https://doi.org/10.1021/acs.langmuir.1c01211.
(247) Moll, C. J.; Giubertoni, G.; van Buren, L.; Versluis, J.; Koenderink, G. H.; Bakker, H. J. Molecular Structure and Surface Accumulation Dynamics of Hyaluronan at the Water–Air Interface. *Macromolecules* **2021**, *54* (18), 8655–8663. https://doi.org/10.1021/acs.macromol.1c00366.

(248) Cavallaro, G.; Lazzara, G.; Milioto, S. Aqueous Phase/Nanoparticles Interface: Hydroxypropyl Cellulose Adsorption and Desorption Triggered by Temperature and Inorganic Salts. *Soft Matter* **2012**, *8* (13), 3627–3633. https://doi.org/10.1039/C2SM07021A.
(249) Dong, R.; Lindau, M.; Ober, C. K. Dissociation Behavior of Weak Polyelectrolyte Brushes on a Planar Surface. *Langmuir* **2009**, *25* (8), 4774–4779. https://doi.org/10.1021/la8039384.
(250) Wang, J.; Chen, C.; Buck, S. M.; Chen, Z. Molecular Chemical Structure on Poly(Methyl Methacrylate) (PMMA) Surface Studied by Sum Frequency Generation (SFG) Vibrational Spectroscopy. *J. Phys. Chem. B* **2001**, *105* (48), 12118–12125. https://doi.org/10.1021/jp013161d.
(251) Wang, J.; Woodcock, S. E.; Buck, S. M.; Chen, C.; Chen, Z. Different Surface-Restructuring Behaviors of Poly(Methacrylate)s Detected by SFG in Water. *J. Am. Chem. Soc.* **2001**, *123* (38), 9470–9471. https://doi.org/10.1021/ja0164071.
(252) Valley, N. A.; Richmond, G. L. Solvation Station: Microsolvation for Modeling Vibrational Sum-Frequency Spectra of Acids at Aqueous Interfaces. *J. Chem. Theory Comput.* **2015**, *11* (10), 4780–4790. https://doi.org/10.1021/acs.jctc.5b00484.
(253) Mieras, H. J. M. A.; Rijn, C. F. H. V. Elastic Behaviour of Low Molecular Weight Polystyrenes. *Nature* **1969**, *224* (5215), 165–166. https://doi.org/10.1038/224165a0.
(254) M. Saffer, E.; A. Lackey, M.; M. Griffin, D.; Kishore, S.; N. Tew, G.; R. Bhatia, S. SANS Study of Highly Resilient Poly(Ethylene Glycol) Hydrogels. *Soft Matter* **2014**, *10* (12), 1905–1916. https://doi.org/10.1039/C3SM52395K.
(255) Deplancke, T.; Lame, O.; Rousset, F.; Seguela, R.; Vigier, G. Mechanisms of Chain Reentanglement during the Sintering of UHMWPE Nascent Powder: Effect of Molecular Weight. *Macromolecules* **2015**, *48* (15), 5328–5338. https://doi.org/10.1021/acs.macromol.5b00618.
(256) Kida, T.; Hiejima, Y.; Nitta, K. Microstructural Interpretation of Influences of Molecular Weight on the Tensile Properties of High-Density Polyethylene Solids Using Rheo-Raman Spectroscopy. *Macromolecules* **2021**, *54* (1), 225–234. https://doi.org/10.1021/acs.macromol.0c02124.
(257) Hoeve, C. A. J.; DiMarzio, E. A.; Peyser, P. Adsorption of Polymer Molecules at Low Surface Coverage. *The Journal of Chemical Physics* **1965**, *42* (7), 2558–2563. https://doi.org/10.1063/1.1696332.
(258) Garcés, J. L.; Koper, G. J. M.; Borkovec, M. Ionization Equilibria and Conformational Transitions in Polyprotic Molecules and Polyelectrolytes. *J. Phys. Chem. B* **2006**, *110* (22), 10937–10950. https://doi.org/10.1021/jp060684i.
(259) Chowdhury, A. U.; Taylor, G. J.; Bocharova, V.; Sacci, R. L.; Luo, Y.; McClintic, W. T.; Ma, Y.-Z.; Sarles, S. A.; Hong, K.; Collier, C. P.; Doughty, B. Insight into the Mechanisms Driving the Self-Assembly of Functional Interfaces: Moving from Lipids to Charged Amphiphilic Oligomers. *J. Am. Chem. Soc.* **2020**, *142* (1), 290–299. https://doi.org/10.1021/jacs.9b10536.
(260) Araiza-Calahorra, A.; Sarkar, A. Designing Biopolymer-Coated Pickering Emulsions to Modulate *in Vitro* Gastric Digestion: A Static Model Study. *Food Funct.* **2019**, *10* (9), 5498–5509. https://doi.org/10.1039/C9FO01080G.
(261) Xu, J.; Liu, Y.; He, J.; Zhang, R.; Zuo, B.; Wang, X. Surface Structures of Poly(Methyl Methacrylate) Films Influenced by Chain Entanglement in the Corresponding Film-

Formation Solution. *Soft Matter* **2014**, *10* (44), 8992–9002. https://doi.org/10.1039/C4SM01743A.
(262) Tran, E.; Mapile, A. N.; Richmond, G. L. Peeling Back the Layers: Investigating the Effects of Polyelectrolyte Layering on Surface Structure and Stability of Oil-in-Water Nanoemulsions. *Journal of Colloid and Interface Science* **2021**, *599*, 706–716. https://doi.org/10.1016/j.jcis.2021.04.115.
(263) Peplowski, L.; Szczesny, R.; Skowronski, L.; Krupka, A.; Smokal, V.; Derkowska-Zielinska, B. Vibrational Spectroscopy Studies of Methacrylic Polymers Containing Heterocyclic Azo Dyes. *Vibrational Spectroscopy* **2022**, *120*, 103377. https://doi.org/10.1016/j.vibspec.2022.103377.
(264) Zhang, F.; Li, Z.; Duan, Y.; Abbas, A.; Mundaca-Uribe, R.; Yin, L.; Luan, H.; Gao, W.; Fang, R. H.; Zhang, L.; Wang, J. Gastrointestinal Tract Drug Delivery Using Algae Motors Embedded in a Degradable Capsule. *Science Robotics* **2022**, *7* (70), eabo4160. https://doi.org/10.1126/scirobotics.abo4160.
(265) Byrne, J.; Huang, H.-W.; McRae, J. C.; Babaee, S.; Soltani, A.; Becker, S. L.; Traverso, G. Devices for Drug Delivery in the Gastrointestinal Tract: A Review of Systems Physically Interacting with the Mucosa for Enhanced Delivery. *Advanced Drug Delivery Reviews* **2021**, *177*, 113926. https://doi.org/10.1016/j.addr.2021.113926.
(266) Bolla, P. K.; Rodriguez, V. A.; Kalhapure, R. S.; Kolli, C. S.; Andrews, S.; Renukuntla, J. A Review on pH and Temperature Responsive Gels and Other Less Explored Drug Delivery Systems. *Journal of Drug Delivery Science and Technology* **2018**, *46*, 416–435. https://doi.org/10.1016/j.jddst.2018.05.037.
(267) Karimi, M.; Sahandi Zangabad, P.; Ghasemi, A.; Amiri, M.; Bahrami, M.; Malekzad, H.; Ghahramanzadeh Asl, H.; Mahdieh, Z.; Bozorgomid, M.; Ghasemi, A.; Rahmani Taji Boyuk, M. R.; Hamblin, M. R. Temperature-Responsive Smart Nanocarriers for Delivery Of Therapeutic Agents: Applications and Recent Advances. *ACS Appl. Mater. Interfaces* **2016**, *8* (33), 21107–21133. https://doi.org/10.1021/acsami.6b00371.
(268) Zyuzin, M. V.; Honold, T.; Carregal-Romero, S.; Kantner, K.; Karg, M.; Parak, W. J. Influence of Temperature on the Colloidal Stability of Polymer-Coated Gold Nanoparticles in Cell Culture Media. *Small* **2016**, *12* (13), 1723–1731. https://doi.org/10.1002/smll.201503232.
(269) Sabattié, E. F. D.; Tasche, J.; Wilson, M. R.; Skoda, M. W. A.; Hughes, A.; Lindner, T.; Thompson, R. L. Predicting Oligomer/Polymer Compatibility and the Impact on Nanoscale Segregation in Thin Films. *Soft Matter* **2017**, *13* (19), 3580–3591. https://doi.org/10.1039/C7SM00048K.
(270) Schirò, G.; Fichou, Y.; Gallat, F.-X.; Wood, K.; Gabel, F.; Moulin, M.; Härtlein, M.; Heyden, M.; Colletier, J.-P.; Orecchini, A.; Paciaroni, A.; Wuttke, J.; Tobias, D. J.; Weik, M. Translational Diffusion of Hydration Water Correlates with Functional Motions in Folded and Intrinsically Disordered Proteins. *Nat Commun* **2015**, *6* (1), 6490. https://doi.org/10.1038/ncomms7490.
(271) Bellissent-Funel, M.-C.; Hassanali, A.; Havenith, M.; Henchman, R.; Pohl, P.; Sterpone, F.; van der Spoel, D.; Xu, Y.; Garcia, A. E. Water Determines the Structure and Dynamics of Proteins. *Chem. Rev.* **2016**, *116* (13), 7673–7697. https://doi.org/10.1021/acs.chemrev.5b00664.
(272) Silvera Batista, C. A.; Larson, R. G.; Kotov, N. A. Nonadditivity of Nanoparticle Interactions. *Science* **2015**, *350* (6257), 1242477. https://doi.org/10.1126/science.1242477.

(273) Thomä, S. L. J.; Krauss, S. W.; Eckardt, M.; Chater, P.; Zobel, M. Atomic Insight into Hydration Shells around Facetted Nanoparticles. *Nat Commun* **2019**, *10* (1), 995. https://doi.org/10.1038/s41467-019-09007-1.
(274) Calvin, J. J.; Brewer, A. S.; Alivisatos, A. P. The Role of Organic Ligand Shell Structures in Colloidal Nanocrystal Synthesis. *Nat Synth* **2022**, *1* (2), 127–137. https://doi.org/10.1038/s44160-022-00025-4.
(275) Israelachvili, J.; Wennerström, H. Role of Hydration and Water Structure in Biological and Colloidal Interactions. *Nature* **1996**, *379* (6562), 219–225. https://doi.org/10.1038/379219a0.
(276) Petersen, N.; Girard, M.; Riedinger, A.; Valsson, O. The Crucial Role of Solvation Forces in the Steric Stabilization of Nanoplatelets. *Nano Lett.* **2022**, *22* (24), 9847–9853. https://doi.org/10.1021/acs.nanolett.2c02848.
(277) Valtiner, M.; Banquy, X.; Kristiansen, K.; Greene, G. W.; Israelachvili, J. N. The Electrochemical Surface Forces Apparatus: The Effect of Surface Roughness, Electrostatic Surface Potentials, and Anodic Oxide Growth on Interaction Forces, and Friction between Dissimilar Surfaces in Aqueous Solutions. *Langmuir* **2012**, *28* (36), 13080–13093. https://doi.org/10.1021/la3018216.
(278) Bischoff, M.; Biriukov, D.; Předota, M.; Marchioro, A. Second Harmonic Scattering Reveals Ion-Specific Effects at the SiO2 and TiO2 Nanoparticle/Aqueous Interface. *J. Phys. Chem. C* **2021**, *125* (45), 25261–25274. https://doi.org/10.1021/acs.jpcc.1c07191.
(279) Bischoff, M.; Kim, N. Y.; Joo, J. B.; Marchioro, A. Water Orientation at the Anatase TiO2 Nanoparticle Interface: A Probe of Surface pKa Values. *J. Phys. Chem. Lett.* **2022**, 8677–8683. https://doi.org/10.1021/acs.jpclett.2c02453.
(280) Murota, K.; Saito, T. Pore Size Effects on Surface Charges and Interfacial Electrostatics of Mesoporous Silicas. *Phys. Chem. Chem. Phys.* **2022**, *24* (30), 18073–18082. https://doi.org/10.1039/D2CP02520E.
(281) Sen, T.; Barisik, M. Internal Surface Electric Charge Characterization of Mesoporous Silica. *Sci Rep* **2019**, *9* (1), 137. https://doi.org/10.1038/s41598-018-36487-w.
(282) Salis, A.; Parsons, D. F.; Boström, M.; Medda, L.; Barse, B.; Ninham, B. W.; Monduzzi, M. Ion Specific Surface Charge Density of SBA-15 Mesoporous Silica. *Langmuir* **2010**, *26* (4), 2484–2490. https://doi.org/10.1021/la902721a.
(283) Abendroth, R. P. Surface Charge Development of Porous Silica in Aqueous Solution. *J. Phys. Chem.* **1972**, *76* (18), 2547–2549. https://doi.org/10.1021/j100662a012.
(284) Chen, C.-Y.; Hsieh, M.-J.; Raj, A.; Peng, W.-C.; Hamaguchi, H.; Chuang, W.-T.; Wang, X.; Wang, C.-L. Missing Piece in Colloidal Stability─Morphological Factor of Hydrophobic Nanoparticles. *Langmuir* **2023**, *39* (8), 2922–2931. https://doi.org/10.1021/acs.langmuir.2c02582.
(285) Farha, O. K.; Eryazici, I.; Jeong, N. C.; Hauser, B. G.; Wilmer, C. E.; Sarjeant, A. A.; Snurr, R. Q.; Nguyen, S. T.; Yazaydın, A. Ö.; Hupp, J. T. Metal–Organic Framework Materials with Ultrahigh Surface Areas: Is the Sky the Limit? *J. Am. Chem. Soc.* **2012**, *134* (36), 15016–15021. https://doi.org/10.1021/ja3055639.
(286) Marshall, C. R.; Timmel, E. E.; Staudhammer, S. A.; Brozek, C. K. Experimental Evidence for a General Model of Modulated MOF Nanoparticle Growth. *Chemical Science* **2020**, *11* (42), 11539–11547. https://doi.org/10.1039/d0sc04845c.

(287) Marshall, C. R.; Staudhammer, S. A.; Brozek, C. K. Size Control over Metal–Organic Framework Porous Nanocrystals. *Chem. Sci.* **2019**, *10* (41), 9396–9408. https://doi.org/10.1039/C9SC03802G.
(288) Marshall, C. R.; Dvorak, J. P.; Twight, L. P.; Chen, L.; Kadota, K.; Andreeva, A. B.; Overland, A. E.; Ericson, T.; Cozzolino, A. F.; Brozek, C. K. Size-Dependent Properties of Solution-Processable Conductive MOF Nanocrystals. *J. Am. Chem. Soc.* **2022**, *144* (13), 5784–5794. https://doi.org/10.1021/jacs.1c10800.
(289) Troyano, J.; Carné-Sánchez, A.; Avci, C.; Imaz, I.; Maspoch, D. Colloidal Metal–Organic Framework Particles: The Pioneering Case of ZIF-8. *Chem. Soc. Rev.* **2019**, *48* (23), 5534–5546. https://doi.org/10.1039/C9CS00472F.
(290) Fonseca, J.; Meng, L.; Imaz, I.; Maspoch, D. Self-Assembly of Colloidal Metal–Organic Framework (MOF) Particles. *Chem. Soc. Rev.* **2023**, *52* (7), 2528–2543. https://doi.org/10.1039/D2CS00858K.
(291) Rojas, S.; Carmona, F. J.; Maldonado, C. R.; Horcajada, P.; Hidalgo, T.; Serre, C.; Navarro, J. A. R.; Barea, E. Nanoscaled Zinc Pyrazolate Metal–Organic Frameworks as Drug-Delivery Systems. *Inorg. Chem.* **2016**, *55* (5), 2650–2663. https://doi.org/10.1021/acs.inorgchem.6b00045.
(292) Carey, C. A.; Devlin, A. M.; Matzger, A. J. Dual Modification of MOFs Improves Dispersion and Ionic Conductivity of Mixed Matrix Membranes. *ACS Materials Lett.* **2023**, 159–164. https://doi.org/10.1021/acsmaterialslett.3c01304.
(293) Yadav, P.; Kumari, S.; Yadav, A.; Bhardwaj, P.; Maruthi, M.; Chakraborty, A.; Kanoo, P. Biocompatible Drug Delivery System Based on a MOF Platform for a Sustained and Controlled Release of the Poorly Soluble Drug Norfloxacin. *ACS Omega* **2023**, *8* (31), 28367–28375. https://doi.org/10.1021/acsomega.3c02418.
(294) Tong, P.-H.; Zhu, L.; Zang, Y.; Li, J.; He, X.-P.; D. James, T. Metal–Organic Frameworks (MOFs) as Host Materials for the Enhanced Delivery of Biomacromolecular Therapeutics. *Chemical Communications* **2021**, *57* (91), 12098–12110. https://doi.org/10.1039/D1CC05157A.
(295) Lin, R.; Hernandez, B. V.; Ge, L.; Zhu, Z. Metal Organic Framework Based Mixed Matrix Membranes: An Overview on Filler/Polymer Interfaces. *J. Mater. Chem. A* **2018**, *6* (2), 293–312. https://doi.org/10.1039/C7TA07294E.
(296) Datta, S. J.; Mayoral, A.; Murthy Srivatsa Bettahalli, N.; Bhatt, P. M.; Karunakaran, M.; Carja, I. D.; Fan, D.; Graziane M. Mileo, P.; Semino, R.; Maurin, G.; Terasaki, O.; Eddaoudi, M. Rational Design of Mixed-Matrix Metal-Organic Framework Membranes for Molecular Separations. *Science* **2022**, *376* (6597), 1080–1087. https://doi.org/10.1126/science.abe0192.
(297) Bordenyuk, A. N.; Weeraman, C.; Yatawara, A.; Jayathilake, H. D.; Stiopkin, I.; Liu, Y.; Benderskii, A. V. Vibrational Sum Frequency Generation Spectroscopy of Dodecanethiol on Metal Nanoparticles. *J. Phys. Chem. C* **2007**, *111* (25), 8925–8933. https://doi.org/10.1021/jp069062n.
(298) Watson, B. R.; Ma, Y.-Z.; Cahill, J. F.; Doughty, B.; Calhoun, T. R. Probing Ligand Removal and Ordering at Quantum Dot Surfaces Using Vibrational Sum Frequency Generation Spectroscopy. *Journal of Colloid and Interface Science* **2019**, *537*, 389–395. https://doi.org/10.1016/j.jcis.2018.11.011.

(299) Wagner, J. C.; Hunter, K. M.; Paesani, F.; Xiong, W. Water Capture Mechanisms at Zeolitic Imidazolate Framework Interfaces. *J. Am. Chem. Soc.* **2021**, *143* (50), 21189–21194. https://doi.org/10.1021/jacs.1c09097.
(300) Cravillon, J.; Münzer, S.; Lohmeier, S.-J.; Feldhoff, A.; Huber, K.; Wiebcke, M. Rapid Room-Temperature Synthesis and Characterization of Nanocrystals of a Prototypical Zeolitic Imidazolate Framework. *Chem. Mater.* **2009**, *21* (8), 1410–1412. https://doi.org/10.1021/cm900166h.
(301) Stetefeld, J.; McKenna, S. A.; Patel, T. R. Dynamic Light Scattering: A Practical Guide and Applications in Biomedical Sciences. *Biophys Rev* **2016**, *8* (4), 409–427. https://doi.org/10.1007/s12551-016-0218-6.
(302) Kaszuba, M.; Corbett, J.; Watson, F. M.; Jones, A. High-Concentration Zeta Potential Measurements Using Light-Scattering Techniques. *Philos Trans A Math Phys Eng Sci* **2010**, *368* (1927), 4439–4451. https://doi.org/10.1098/rsta.2010.0175.
(303) Foster, M. J.; Carpenter, A. P.; Richmond, G. L. Dynamic Duo: Vibrational Sum Frequency Scattering Investigation of pH-Switchable Carboxylic Acid/Carboxylate Surfactants on Nanodroplet Surfaces. *J. Phys. Chem. B* **2021**, *125* (33), 9629–9640. https://doi.org/10.1021/acs.jpcb.1c05508.
(304) Lambert, A. G.; Davies, P. B.; Neivandt, D. J. Implementing the Theory of Sum Frequency Generation Vibrational Spectroscopy: A Tutorial Review. *Applied Spectroscopy Reviews* **2005**, *40* (2), 103–145. https://doi.org/10.1081/ASR-200038326.
(305) Shen, Y. R.; Ostroverkhov, V. Sum-Frequency Vibrational Spectroscopy on Water Interfaces: Polar Orientation of Water Molecules at Interfaces. *Chem. Rev.* **2006**, *106* (4), 1140–1154. https://doi.org/10.1021/cr040377d.
(306) Zhang, C.; Han, C.; Sholl, D. S.; Schmidt, J. R. Computational Characterization of Defects in Metal–Organic Frameworks: Spontaneous and Water-Induced Point Defects in ZIF-8. *J. Phys. Chem. Lett.* **2016**, *7* (3), 459–464. https://doi.org/10.1021/acs.jpclett.5b02683.
(307) Möslein, A. F.; Donà, L.; Civalleri, B.; Tan, J.-C. Defect Engineering in Metal–Organic Framework Nanocrystals: Implications for Mechanical Properties and Performance. *ACS Appl. Nano Mater.* **2022**, *5* (5), 6398–6409. https://doi.org/10.1021/acsanm.2c00493.
(308) Oh, S.; Lee, S.; Lee, G.; Oh, M. Enhanced Adsorption Capacity of ZIF-8 for Chemical Warfare Agent Simulants Caused by Its Morphology and Surface Charge. *Sci Rep* **2023**, *13* (1), 12250. https://doi.org/10.1038/s41598-023-39507-6.
(309) Morris, W.; Wang, S.; Cho, D.; Auyeung, E.; Li, P.; Farha, O. K.; Mirkin, C. A. Role of Modulators in Controlling the Colloidal Stability and Polydispersity of the UiO-66 Metal–Organic Framework. *ACS Appl. Mater. Interfaces* **2017**, *9* (39), 33413–33418. https://doi.org/10.1021/acsami.7b01040.
(310) Ibrahim, A. H.; El-Mehalmey, W. A.; Haikal, R. R.; Safy, M. E. A.; Amin, M.; Shatla, H. R.; Karakalos, S. G.; Alkordi, M. H. Tuning the Chemical Environment within the UiO-66-NH2 Nanocages for Charge-Dependent Contaminant Uptake and Selectivity. *Inorg. Chem.* **2019**, *58* (22), 15078–15087. https://doi.org/10.1021/acs.inorgchem.9b01611.
(311) Andino, R. S.; Liu, J.; Miller, C. M.; Chen, X.; Devlin, S. W.; Hong, M. K.; Rajagopal, R.; Erramilli, S.; Ziegler, L. D. Anomalous pH-Dependent Enhancement of p-Methyl Benzoic Acid Sum-Frequency Intensities: Cooperative Surface Adsorption Effects. *J. Phys. Chem. A* **2020**, *124* (16), 3064–3076. https://doi.org/10.1021/acs.jpca.9b10809.
(312) Koverga, V.; Juhász, Á.; Dudariev, D.; Lebedev, M.; Idrissi, A.; Jedlovszky, P. Local Structure of DMF–Water Mixtures, as Seen from Computer Simulations and Voronoi

Analysis. *J. Phys. Chem. B* **2022**, acs.jpcb.2c02235. https://doi.org/10.1021/acs.jpcb.2c02235.
(313) Koch, D.; Chen, Y.; Golub, P.; Manzhos, S. Revisiting π Backbonding: The Influence of d Orbitals on Metal–CO Bonds and Ligand Red Shifts. *Phys. Chem. Chem. Phys.* **2019**, *21* (37), 20814–20821. https://doi.org/10.1039/C9CP04624K.
(314) Kawasaki, H.; Yamamoto, H.; Fujimori, H.; Arakawa, R.; Iwasaki, Y.; Inada, M. Stability of the DMF-Protected Au Nanoclusters: Photochemical, Dispersion, and Thermal Properties. *Langmuir* **2010**, *26* (8), 5926–5933. https://doi.org/10.1021/la9038842.
(315) Mittal, A.; Gandhi, S.; Roy, I. Mechanistic Interaction Studies of Synthesized ZIF-8 Nanoparticles with Bovine Serum Albumin Using Spectroscopic and Molecular Docking Approaches. *Sci Rep* **2022**, *12* (1), 10331. https://doi.org/10.1038/s41598-022-14630-y.
(316) Sorenson, S. A.; Patrow, J. G.; Dawlaty, J. M. Solvation Reaction Field at the Interface Measured by Vibrational Sum Frequency Generation Spectroscopy. *J. Am. Chem. Soc.* **2017**, *139* (6), 2369–2378. https://doi.org/10.1021/jacs.6b11940.
(317) Yin, F.; Hu, P.; Ma, Y.-H.; Luo, Y.; Wang, C.; Zhu, W.; Lu, X. Polar Solvents Induce Sum Frequency Generation Activity for Multiwalled Carbon Nanotubes. *Langmuir* **2021**, *37* (21), 6540–6548. https://doi.org/10.1021/acs.langmuir.1c00825.
(318) Wang, Z.; Lin, H.; Zhang, X.; Li, J.; Chen, X.; Wang, S.; Gong, W.; Yan, H.; Zhao, Q.; Lv, W.; Gong, X.; Xiao, Q.; Li, F.; Ji, D.; Zhang, X.; Dong, H.; Li, L.; Hu, W. Revealing Molecular Conformation–Induced Stress at Embedded Interfaces of Organic Optoelectronic Devices by Sum Frequency Generation Spectroscopy. *Science Advances* **2021**, *7* (16), eabf8555. https://doi.org/10.1126/sciadv.abf8555.
(319) Dreier, L. B.; Bonn, M.; Backus, E. H. G. Hydration and Orientation of Carbonyl Groups in Oppositely Charged Lipid Monolayers on Water. *J. Phys. Chem. B* **2019**, *123* (5), 1085–1089. https://doi.org/10.1021/acs.jpcb.8b12297.
(320) Li, X.; Roiaz, M.; Pramhaas, V.; Rameshan, C.; Rupprechter, G. Polarization-Dependent SFG Spectroscopy of Near Ambient Pressure CO Adsorption on Pt(111) and Pd(111) Revisited. *Top Catal* **2018**, *61* (9–11), 751–762. https://doi.org/10.1007/s11244-018-0949-7.
(321) Tomar, D.; Rana, B.; Jena, K. C. The Structure of Water–DMF Binary Mixtures Probed by Linear and Nonlinear Vibrational Spectroscopy. *J. Chem. Phys.* **2020**, *152* (11), 114707. https://doi.org/10.1063/1.5141757.
(322) Vinaykin, M.; Benderskii, A. V. Vibrational Sum-Frequency Spectrum of the Water Bend at the Air/Water Interface. *J. Phys. Chem. Lett.* **2012**, *3* (22), 3348–3352. https://doi.org/10.1021/jz3014776.
(323) Seki, T.; Yu, C.-C.; Chiang, K.-Y.; Tan, J.; Sun, S.; Ye, S.; Bonn, M.; Nagata, Y. Disentangling Sum-Frequency Generation Spectra of the Water Bending Mode at Charged Aqueous Interfaces. *J. Phys. Chem. B* **2021**, *125* (25), 7060–7067. https://doi.org/10.1021/acs.jpcb.1c03258.
(324) Santo, A. D.; Pérez, H.; Echeverría, G. A.; Piro, O. E.; Iglesias, R. A.; Carbonio, R. E.; Altabef, A. B.; Gil, D. M. Exploring Weak Intermolecular Interactions in Thiocyanate-Bonded Zn(II) and Cd(II) Complexes with Methylimidazole: Crystal Structures, Hirshfeld Surface Analysis and Luminescence Properties. *RSC Adv.* **2018**, *8* (42), 23891–23902. https://doi.org/10.1039/C8RA04452J.
(325) Zhang, Y.; Jia, Y.; Li, M.; Hou, L. Influence of the 2-Methylimidazole/Zinc Nitrate Hexahydrate Molar Ratio on the Synthesis of Zeolitic Imidazolate Framework-8 Crystals

at Room Temperature. *Sci Rep* **2018**, *8* (1), 9597. https://doi.org/10.1038/s41598-018-28015-7.
(326) Hu, Y.; Kazemian, H.; Rohani, S.; Huang, Y.; Song, Y. In Situ High Pressure Study of ZIF-8 by FTIR Spectroscopy. *Chem. Commun.* **2011**, *47* (47), 12694. https://doi.org/10.1039/c1cc15525c.
(327) Hu, Y.; Liu, Z.; Xu, J.; Huang, Y.; Song, Y. Evidence of Pressure Enhanced CO2 Storage in ZIF-8 Probed by FTIR Spectroscopy. *J. Am. Chem. Soc.* **2013**, *135* (25), 9287–9290. https://doi.org/10.1021/ja403635b.
(328) Curtis, A. D.; Reynolds, S. B.; Calchera, A. R.; Patterson, J. E. Understanding the Role of Nonresonant Sum-Frequency Generation from Polystyrene Thin Films. *J. Phys. Chem. Lett.* **2010**, *1* (16), 2435–2439. https://doi.org/10.1021/jz100883z.
(329) Backus, E. H. G.; Garcia-Araez, N.; Bonn, M.; Bakker, H. J. On the Role of Fresnel Factors in Sum-Frequency Generation Spectroscopy of Metal–Water and Metal-Oxide–Water Interfaces. *J. Phys. Chem. C* **2012**, *116* (44), 23351–23361. https://doi.org/10.1021/jp306273d.
(330) Wallentine, S.; Bandaranayake, S.; Biswas, S.; Baker, L. R. Plasmon-Resonant Vibrational Sum Frequency Generation of Electrochemical Interfaces: Direct Observation of Carbon Dioxide Electroreduction on Gold. *J. Phys. Chem. A* **2020**, *124* (39), 8057–8064. https://doi.org/10.1021/acs.jpca.0c04268.
(331) Li, B.; Ma, Y.; Han, X.; Hu, P.; Lu, X. Enhanced Sum Frequency Generation for Monolayers on Au Relative to Silica: Local Field Factors and SPR Effect. *Langmuir* **2023**, *39* (1), 659–667. https://doi.org/10.1021/acs.langmuir.2c03016.
(332) Van Cleuvenbergen, S.; Stassen, I.; Gobechiya, E.; Zhang, Y.; Markey, K.; De Vos, D. E.; Kirschhock, C.; Champagne, B.; Verbiest, T.; van der Veen, M. A. ZIF-8 as Nonlinear Optical Material: Influence of Structure and Synthesis. *Chem. Mater.* **2016**, *28* (9), 3203–3209. https://doi.org/10.1021/acs.chemmater.6b01087.
(333) Zhou, W.; Wu, H.; Udovic, T. J.; Rush, J. J.; Yildirim, T. Quasi-Free Methyl Rotation in Zeolitic Imidazolate Framework-8. *J. Phys. Chem. A* **2008**, *112* (49), 12602–12606. https://doi.org/10.1021/jp807033m.
(334) Kolokolov, D. I.; Stepanov, A. G.; Jobic, H. Mobility of the 2-Methylimidazolate Linkers in ZIF-8 Probed by 2H NMR: Saloon Doors for the Guests. *J. Phys. Chem. C* **2015**, *119* (49), 27512–27520. https://doi.org/10.1021/acs.jpcc.5b09312.
(335) Fairen-Jimenez, D.; Moggach, S. A.; Wharmby, M. T.; Wright, P. A.; Parsons, S.; Düren, T. Opening the Gate: Framework Flexibility in ZIF-8 Explored by Experiments and Simulations. *J. Am. Chem. Soc.* **2011**, *133* (23), 8900–8902. https://doi.org/10.1021/ja202154j.
(336) Rieth, A. J.; Hunter, K. M.; Dincă, M.; Paesani, F. Hydrogen Bonding Structure of Confined Water Templated by a Metal-Organic Framework with Open Metal Sites. *Nat Commun* **2019**, *10* (1), 4771. https://doi.org/10.1038/s41467-019-12751-z.
(337) Valentine, M. L.; Yin, G.; Oppenheim, J. J.; Dincă, M.; Xiong, W. Ultrafast Water H-Bond Rearrangement in a Metal–Organic Framework Probed by Femtosecond Time-Resolved Infrared Spectroscopy. *J. Am. Chem. Soc.* **2023**, *145* (21), 11482–11487. https://doi.org/10.1021/jacs.3c01728.
(338) C. Moreton, J.; S. Denny, M.; M. Cohen, S. High MOF Loading in Mixed-Matrix Membranes Utilizing Styrene/Butadiene Copolymers. *Chemical Communications* **2016**, *52* (100), 14376–14379. https://doi.org/10.1039/C6CC07329H.

(339) Lin, R.; Hernandez, B. V.; Ge, L.; Zhu, Z. Metal Organic Framework Based Mixed Matrix Membranes: An Overview on Filler/Polymer Interfaces. *J. Mater. Chem. A* **2018**, *6* (2), 293–312. https://doi.org/10.1039/C7TA07294E.
(340) Marshall, C. R.; Dvorak, J. P.; Twight, L. P.; Chen, L.; Kadota, K.; Andreeva, A. B.; Overland, A. E.; Ericson, T.; Cozzolino, A. F.; Brozek, C. K. Size-Dependent Properties of Solution-Processable Conductive MOF Nanocrystals. *J. Am. Chem. Soc.* **2022**, *144* (13), 5784–5794. https://doi.org/10.1021/jacs.1c10800.
(341) Mapile, A. N.; LeRoy, M. A.; Fabrizio, K.; Scatena, L. F.; Brozek, C. K. The Surface of Colloidal Metal–Organic Framework Nanoparticles Revealed by Vibrational Sum Frequency Scattering Spectroscopy. *ACS Nano* **2024**, *18* (20), 13406–13414. https://doi.org/10.1021/acsnano.4c03758.
(342) Venna, S. R.; Lartey, M.; Li, T.; Spore, A.; Kumar, S.; Nulwala, H. B.; Luebke, D. R.; Rosi, N. L.; Albenze, E. Fabrication of MMMs with Improved Gas Separation Properties Using Externally-Functionalized MOF Particles. *J. Mater. Chem. A* **2015**, *3* (9), 5014–5022. https://doi.org/10.1039/C4TA05225K.
(343) Wang, Z.; Ren, H.; Zhang, S.; Zhang, F.; Jin, J. Polymers of Intrinsic Microporosity/Metal–Organic Framework Hybrid Membranes with Improved Interfacial Interaction for High-Performance CO2 Separation. *J. Mater. Chem. A* **2017**, *5* (22), 10968–10977. https://doi.org/10.1039/C7TA01773A.
(344) Wu, W.-N.; Mizrahi Rodriguez, K.; Roy, N.; Teesdale, J. J.; Han, G.; Liu, A.; Smith, Z. P. Engineering the Polymer–MOF Interface in Microporous Composites to Address Complex Mixture Separations. *ACS Appl. Mater. Interfaces* **2023**, *15* (45), 52893–52907. https://doi.org/10.1021/acsami.3c11300.
(345) Lin, R.; Ge, L.; Diao, H.; Rudolph, V.; Zhu, Z. Ionic Liquids as the MOFs/Polymer Interfacial Binder for Efficient Membrane Separation. *ACS Appl. Mater. Interfaces* **2016**, *8* (46), 32041–32049. https://doi.org/10.1021/acsami.6b11074.
(346) Semino, R.; Ramsahye, N. A.; Ghoufi, A.; Maurin, G. Microscopic Model of the Metal–Organic Framework/Polymer Interface: A First Step toward Understanding the Compatibility in Mixed Matrix Membranes. *ACS Appl. Mater. Interfaces* **2016**, *8* (1), 809–819. https://doi.org/10.1021/acsami.5b10150.
(347) Semino, R.; Moreton, J. C.; Ramsahye, N. A.; Cohen, S. M.; Maurin, G. Understanding the Origins of Metal–Organic Framework/Polymer Compatibility. *Chem. Sci.* **2018**, *9* (2), 315–324. https://doi.org/10.1039/C7SC04152G.
(348) Koleske, J. V.; Friel, J. M.; Nungesser, E. Acrylic Polymers as Coatings Binders. In *Paint and Coating Testing Manual: 15th. Edition of the Gardner-Sward Handbook*; Koleske, J. V., Ed.; ASTM International: 100 Barr Harbor Drive, PO Box C700, West Conshohocken, PA 19428-2959, 2012; pp 49-49–16. https://doi.org/10.1520/MNL12186M.
(349) Alvarez, V.; Paulis, M. Effect of Acrylic Binder Type and Calcium Carbonate Filler Amount on the Properties of Paint-like Blends. *Progress in Organic Coatings* **2017**, *112*, 210–218. https://doi.org/10.1016/j.porgcoat.2017.07.023.
(350) Lichtarowicz, M. *Paints*. https://www.essentialchemicalindustry.org/materials-and-applications/paints.html (accessed 2024-07-05).
(351) Avci, C.; Ariñez-Soriano, J.; Carné-Sánchez, A.; Guillerm, V.; Carbonell, C.; Imaz, I.; Maspoch, D. Post-Synthetic Anisotropic Wet-Chemical Etching of Colloidal Sodalite ZIF Crystals. *Angewandte Chemie International Edition* **2015**, *54* (48), 14417–14421. https://doi.org/10.1002/anie.201507588.

(352) Pang, S. H.; Han, C.; Sholl, D. S.; Jones, C. W.; Lively, R. P. Facet-Specific Stability of ZIF-8 in the Presence of Acid Gases Dissolved in Aqueous Solutions. *Chem. Mater.* **2016**, *28* (19), 6960–6967. https://doi.org/10.1021/acs.chemmater.6b02643.
(353) Nakamoto, K. *Infrared and Raman Spectra of Inorganic and Coordination Compounds*, 1st ed.; John Wiley & Sons, Ltd, 2008. https://doi.org/10.1002/9780470405840.
(354) Girma, K. B.; Lorenz, V.; Blaurock, S.; Edelmann, F. T. Coordination Chemistry of Acrylamide. *Coordination Chemistry Reviews* **2005**, *249* (11), 1283–1293. https://doi.org/10.1016/j.ccr.2005.01.028.
(355) Frenking, G.; Fernández, I.; Holzmann, N.; Pan, S.; Krossing, I.; Zhou, M. Metal–CO Bonding in Mononuclear Transition Metal Carbonyl Complexes. *JACS Au* **2021**, *1* (5), 623–645. https://doi.org/10.1021/jacsau.1c00106.
(356) Myshakina, N. S.; Ahmed, Z.; Asher, S. A. Dependence of Amide Vibrations on Hydrogen Bonding. *J. Phys. Chem. B* **2008**, *112* (38), 11873–11877. https://doi.org/10.1021/jp8057355.
(357) Xu, N.; Guan, Y.; Nguyen, N.; Lingafelt, C.; Powell, D. R.; Richter-Addo, G. B. Interactions of Acetamide and Acrylamide with Heme Models: Synthesis, Infrared Spectra, and Solid State Molecular Structures of Five- and Six-Coordinate Ferric Porphyrin Derivatives. *Journal of Inorganic Biochemistry* **2019**, *194*, 160–169. https://doi.org/10.1016/j.jinorgbio.2019.03.003.
(358) Liu, M.; McGillicuddy, R. D.; Vuong, H.; Tao, S.; Slavney, A. H.; Gonzalez, M. I.; Billinge, S. J. L.; Mason, J. A. Network-Forming Liquids from Metal–Bis(Acetamide) Frameworks with Low Melting Temperatures. *J. Am. Chem. Soc.* **2021**, *143* (7), 2801–2811. https://doi.org/10.1021/jacs.0c11718.
(359) Aguilar-Lugo, C.; Lee, W. H.; Miguel, J. A.; de la Campa, J. G.; Prádanos, P.; Bae, J. Y.; Lee, Y. M.; Álvarez, C.; Lozano, Á. E. Highly Permeable Mixed Matrix Membranes of Thermally Rearranged Polymers and Porous Polymer Networks for Gas Separations. *ACS Appl. Polym. Mater.* **2021**, *3* (10), 5224–5235. https://doi.org/10.1021/acsapm.1c01012.
(360) M. Palomba, J.; Saygin, V.; A. Brown, K. Experimental Observation of Metal–Organic Framework–Polymer Interaction Forces and Intercalation. *Chemical Communications* **2023**, *59* (3), 290–293. https://doi.org/10.1039/D2CC06381F.
(361) Azhar, M. R.; Abid, H. R.; Periasamy, V.; Sun, H.; Tade, M. O.; Wang, S. Adsorptive Removal of Antibiotic Sulfonamide by UiO-66 and ZIF-67 for Wastewater Treatment. *Journal of Colloid and Interface Science* **2017**, *500*, 88–95. https://doi.org/10.1016/j.jcis.2017.04.001.
(362) Jarai, B. M.; Stillman, Z.; Attia, L.; Decker, G. E.; Bloch, E. D.; Fromen, C. A. Evaluating UiO-66 Metal–Organic Framework Nanoparticles as Acid-Sensitive Carriers for Pulmonary Drug Delivery Applications. *ACS Appl. Mater. Interfaces* **2020**, *12* (35), 38989–39004. https://doi.org/10.1021/acsami.0c10900.
(363) Thananukul, K.; Kaewsaneha, C.; Opaprakasit, P.; Zine, N.; Elaissari, A. Biodegradable Porous Micro/Nanoparticles with Thermoresponsive Gatekeepers for Effective Loading and Precise Delivery of Active Compounds at the Body Temperature. *Sci Rep* **2022**, *12* (1), 10906. https://doi.org/10.1038/s41598-022-15069-x.
(364) Johnson, L.; M. Gray, D.; Niezabitowska, E.; O. McDonald, T. Multi-Stimuli-Responsive Aggregation of Nanoparticles Driven by the Manipulation of Colloidal Stability. *Nanoscale* **2021**, *13* (17), 7879–7896. https://doi.org/10.1039/D1NR01190A.

(365) Schmid, A. J.; Dubbert, J.; Rudov, A. A.; Pedersen, J. S.; Lindner, P.; Karg, M.; Potemkin, I. I.; Richtering, W. Multi-Shell Hollow Nanogels with Responsive Shell Permeability. *Sci Rep* **2016**, *6* (1), 22736. https://doi.org/10.1038/srep22736.
(366) L. Moore, T.; Rodriguez-Lorenzo, L.; Hirsch, V.; Balog, S.; Urban, D.; Jud, C.; Rothen-Rutishauser, B.; Lattuada, M.; Petri-Fink, A. Nanoparticle Colloidal Stability in Cell Culture Media and Impact on Cellular Interactions. *Chemical Society Reviews* **2015**, *44* (17), 6287–6305. https://doi.org/10.1039/C4CS00487F.
(367) *Cooling homes without warming the planet – MIT Department of Chemistry*. https://chemistry.mit.edu/chemistry-news/cooling-homes-without-warming-the-planet/ (accessed 2024-02-15).
(368) *Catalyzing Commercialization: Affordable and Sustainable Cooling Using Metal-Organic Frameworks*. https://www.aiche.org/resources/publications/cep/2020/september/catalyzing-commercialization-affordable-and-sustainable-cooling-using-metal-organic-frameworks (accessed 2024-02-15).
(369) Fabrizio, K.; Brozek, C. K. Size-Dependent Thermal Shifts to MOF Nanocrystal Optical Gaps Induced by Dynamic Bonding. *Nano Lett.* **2023**, *23* (3), 925–930. https://doi.org/10.1021/acs.nanolett.2c04286.
(370) Andreeva, A. B.; Le, K. N.; Chen, L.; Kellman, M. E.; Hendon, C. H.; Brozek, C. K. Soft Mode Metal-Linker Dynamics in Carboxylate MOFs Evidenced by Variable-Temperature Infrared Spectroscopy. *J. Am. Chem. Soc.* **2020**, *142* (45), 19291–19299. https://doi.org/10.1021/jacs.0c09499.
(371) Grzywa, M.; Röß-Ohlenroth, R.; Muschielok, C.; Oberhofer, H.; Błachowski, A.; Żukrowski, J.; Vieweg, D.; von Nidda, H.-A. K.; Volkmer, D. Cooperative Large-Hysteresis Spin-Crossover Transition in the Iron(II) Triazolate [Fe(Ta)2] Metal–Organic Framework. *Inorg. Chem.* **2020**, *59* (15), 10501–10511. https://doi.org/10.1021/acs.inorgchem.0c00814.
(372) Kim, D.; Park, J.; Kim, Y. S.; Lah, M. S. Temperature Dependent CO2 Behavior in Microporous 1-D Channels of a Metal-Organic Framework with Multiple Interaction Sites. *Sci Rep* **2017**, *7* (1), 41447. https://doi.org/10.1038/srep41447.
(373) Rahman, S.; Arami-Niya, A.; Yang, X.; Xiao, G.; Li, G. (Kevin); May, E. F. Temperature Dependence of Adsorption Hysteresis in Flexible Metal Organic Frameworks. *Commun Chem* **2020**, *3* (1), 1–6. https://doi.org/10.1038/s42004-020-00429-3.
(374) *Find a Product - Quantum Northwest*. Quantum Northwest - The largest selection of peltier based cuvette holders on earth! https://qnw.com/product-dispatch/ (accessed 2024-02-15).
(375) Smit, W. J.; Smolentsev, N.; Versluis, J.; Roke, S.; Bakker, H. J. Freezing Effects of Oil-in-Water Emulsions Studied by Sum-Frequency Scattering Spectroscopy. *The Journal of Chemical Physics* **2016**, *145* (4), 044706. https://doi.org/10.1063/1.4959128.
(376) Smolentsev, N.; Smit, W. J.; Bakker, H. J.; Roke, S. The Interfacial Structure of Water Droplets in a Hydrophobic Liquid. *Nat Commun* **2017**, *8* (1), 15548. https://doi.org/10.1038/ncomms15548.
(377) Kovacik, F.; Okur, H. I.; Smolentsev, N.; Scheu, R.; Roke, S. Hydration Mediated Interfacial Transitions on Mixed Hydrophobic/Hydrophilic Nanodroplet Interfaces. *The Journal of Chemical Physics* **2018**, *149* (23), 234704. https://doi.org/10.1063/1.5035161.

(378) Pullanchery, S.; Zhang, L.; Kulik, S.; Roke, S. Interfacial Inversion, Interference, and IR Absorption in Vibrational Sum Frequency Scattering Experiments. *J. Phys. Chem. B* **2023**, *127* (30), 6795–6803. https://doi.org/10.1021/acs.jpcb.3c02727.
(379) Johansson, P. K.; Castner, D. G. Vibrational Sum-Frequency Scattering as a Sensitive Approach to Detect Structural Changes in Collagen Fibers Treated with Surfactants. *Langmuir* **2019**, *35* (24), 7848–7857. https://doi.org/10.1021/acs.langmuir.9b00412.
(380) Brown, J. B.; Qian, Y.; Huang-Fu, Z.-C.; Zhang, T.; Wang, H.; Rao, Y. In Situ Probing of the Surface Properties of Droplets in the Air. *Langmuir* **2023**, *39* (31), 10724–10743. https://doi.org/10.1021/acs.langmuir.3c00875.
(381) Golbek, T. W.; Weidner, T. Peptide Orientation Strongly Affected by the Nanoparticle Size as Revealed by Sum Frequency Scattering Spectroscopy. *J. Phys. Chem. Lett.* **2023**, *14* (44), 9819–9823. https://doi.org/10.1021/acs.jpclett.3c01751.
(382) Gao, J.; Chu, W.; Ding, X.; Ding, L.; Guo, Q.; Fu, Y. Degradation Kinetic Studies of BSA@ZIF-8 Nanoparticles with Various Zinc Precursors, Metal-to-Ligand Ratios, and pH Conditions. *ACS Omega* **2023**, *8* (47), 44601–44610. https://doi.org/10.1021/acsomega.3c04973.
(383) Berry, J. D.; Neeson, M. J.; Dagastine, R. R.; Chan, D. Y. C.; Tabor, R. F. Measurement of Surface and Interfacial Tension Using Pendant Drop Tensiometry. *Journal of Colloid and Interface Science* **2015**, *454*, 226–237. https://doi.org/10.1016/j.jcis.2015.05.012.
(384) Marchioro, A.; Golbek, T. W.; Chatterley, A. S.; Weidner, T.; Roke, S. A Discrepancy of 107 in Experimental and Theoretical Density Detection Limits of Aerosol Particles by Surface Nonlinear Light Scattering. *Commun Chem* **2023**, *6* (1), 1–4. https://doi.org/10.1038/s42004-023-00903-8.